UNIVERSITY OF LEEDS

Analysis of Atmospheric Methane Across Different Spatial and Temporal Scales

Emily Dowd

Submitted in accordance with the requirements for the degree of Doctor of Philosophy

The University of Leeds

Faculty of Environment

School of Earth and Environment

July 26, 2024

Author Contributions & Intellectual Property

Paper 1:

Dowd, E., Wilson, C., Chipperfield, M. P., Gloor, E., Manning, A., and Doherty, R.: Decreasing seasonal cycle amplitude of methane in the northern high latitudes being driven by lower-latitude changes in emissions and transport, Atmos. Chem. Phys., 23, 7363–7382, https://doi.org/10.5194/acp-23-7363-2023, 2023

Emily Dowd - conceptualisation, methodology, forward modelling, formal analysis, visualisation and investigation, and writing (original and review) with the help and guidance of Chris Wilson, Martyn Chipperfield, Emanuel Gloor, Alistair Manning and Ruth Doherty

Supervision - Chris Wilson, Martyn Chipperfield, Emanuel Gloor, Alistair Manning and Ruth Doherty

Atmospheric Inversions - Chris Wilson

Paper 2 (draft):

Emily Dowd - implementation of legacy code and model development, testing methodology, formal analysis, visualisations and investigation with the guidance of Chris Wilson, Martyn Chipperfield, Emanuel Gloor and Ruth Doherty

Supervision - Chris Wilson, Martyn Chipperfield, Emanuel Gloor, Alistair Manning and Ruth Doherty

Paper 3:

Dowd, E., Manning, A. J., Orth-Lashley, B., Girard, M., France, J., Fisher, R. E.,

Lowry, D., Lanoisellé, M., Pitt, J. R., Stanley, K. M., O'Doherty, S., Young, D., Thistlethwaite, G., Chipperfield, M. P., Gloor, E., and Wilson, C.: First validation of high-resolution satellite-derived methane emissions from an active gas leak in the UK, Atmos. Meas. Tech., 17, 1599–1615, https://doi.org/10.5194/amt-17-1599-2024, 2024

Emily Dowd - conceptualisation, methodology, dispersion modelling, formal analysis, visualisations and investigation with the help and guidance of Alistair Manning, Chris Wilson, Martyn Chipperfield and Emanuel Gloor.

Supervision - Alistair Manning, Chris Wilson, Martyn Chipperfield, Emanuel Gloor

Bryn Orth-Lashley and Marianne Girard - Satellite data processing, emission estimations and satellite description

James France, Rebecca Fisher, Dave Lowry - Mobile survey data collection and emission estimation, emission estimation description

Mathias Lanoiselle- Isotope analysis

Joseph R. Pitt, Kieran M. Stanely, Simon O'Doherty and Dickon Young - UK DECC Network observations

Acknowledgements

I'd like to extend my sincere thanks to my supervisors Chris Wilson, Martyn Chipperfield, Emanuel Gloor, Alistair Manning and Ruth Doherty for all your help and guidance throughout my PhD. I'd like to especially thank Chris Wilson for the immense amount of support in starting a PhD during lockdown and navigating many hurdles.

Alongside this, I would like to thank the SENSE CDT for making my PhD experience the best it could be. From weeks of EO training, field work at Firbush and a week at ESA, the experiences and amazing people I met along the way. I would also like to thank Bryony, Calum and Morag for embarking on our SatSchool journey together and the SENSE CDT for their immense support of the project. I would also like to thank Anna and Adina for being awesome role models in the EO sphere and providing invaluable advice throughout my PhD.

Thank you to all the members of Team TOMCAT that I have had the pleasure of working with throughout my time at Leeds. Particularly to Matilda, Ailish, Carlo, Xin and Yang who were great office mates.

I would like to thank Alistair for hosting me at the Met Office and your support with NAME. I would like to thank James, Rebecca and Dave at Royal Holloway, University of London for collaborating and contributing to our gas leak study.

Thank you to the ESA Science Hub, particularly Christian, Daniele and Ed, for hosting me and supporting with my work using TROPOMI.

Finally, I would like to thank my friends and family, especially my mum and dad, and most of all Sam for their unconditional support these last four years.

This project was funded by the Natural Environment Research Council (NERC) SENSE CDT studentship (NE/T00939X/1)

Abstract

Global trends of atmospheric methane (CH_4) are poorly understood due to uncertainties surrounding its sources and sinks. Atmospheric CH_4 has a 20-year global warming potential 80 times greater than CO_2, but a shorter lifetime of approximately 9 years. Therefore, it presents a good short-term opportunity to mitigate the human impact on climate change whilst CO_2 emissions are reduced. This research exploits observations and models across different spatial and temporal scales to address important knowledge gaps in atmospheric CH_4. Specifically, this thesis explores global changes in the seasonal cycle amplitude of CH_4, develops and demonstrates the capability of a new regional "nested grid" 3-D chemical transport model, and quantifies emission estimates of a satellite-detected UK gas leak.

Long-term surface-based observations showed a decrease of 4ppb in the seasonal cycle amplitude (SCA) in the northern high latitudes (NHLs; 60°N-90°N) between 1995-2020. Global chemical transport modelling shows that the largest contributor to this SCA change was from well-mixed CH_4, as well as changes in emissions from Canada, Middle East and Europe. These results highlight that changes in the observed NHL seasonal cycle can indicate changes in emissions in local and non-local regions.

For studies on a finer spatial scale, a new high resolution regional model "nested" in TOMCAT called ZOOMCAT was developed and tested. Two case studies were simulated in ZOOMCAT over Europe in 2020. One which simulated the Nord Stream pipeline gas leak, which provided much more spatial detail in plume transport compared to TOMCAT. The lack of improvement in ZOOMCAT when compared with TOMCAT and tall tower observations of CH_4 in these case studies highlighted the importance of input meteorology.

On the metre-scale resolution, emissions from a 2023 gas leak near Cheltenham, UK were detected by tasking GHGSat. The satellite-derived emission estimates were evaluated using a

surface-based mobile survey and were found to broadly agree. This work also demonstrated that the UK tall tower network in this case was too sparse to quantify fugitive emissions on this scale using inverse modelling techniques. The total CH_4 leaked over the 11-week period is estimated to be 1,393,392 kg, equivalent to emissions from the average annual electricity consumption of 7,500 homes.

Contents

List of Figures

List of Tables

Chapter 1

Introduction

1.1 Motivation

Atmospheric methane (CH_4) is the second most important anthropogenic greenhouse gas in our atmosphere after carbon dioxide (CO_2). It has a 20-year global warming potential (GWP) 82 times greater than CO_2 (Forster et al., 2023). Despite its large GWP, its lifetime in the atmosphere is approximately 9 years, so it presents a good opportunity to reduce the human impact on climate change on a relatively short time scale (Prather et al., 2012). Global concentrations of CH_4 have been rising since atmospheric observations began in the 1980s with a global mean value reaching 1930 ppb in March 2024 (Lan et al., 2024). CH_4 exhibits a strong annual cycle in most locations due to the seasonal variation of its sources, sinks and transport (e.g the Intertropical Convergence Zone (ITCZ) in the tropics). There is an imbalance in the sources and sinks, leading to local and global changes (i.e. increases) of CH_4 concentrations over time. However, these variations of CH_4 are not fully understood, predominately due to uncertainties in the drivers of the sources and sinks of CH_4.

Atmospheric CH_4 has a mixture of natural and anthropogenic sources. The largest natural sources are wetlands and other major sources include fossil fuels, agriculture and waste. It is not fully understood how emissions from wetlands react to changes in climate variables, such as precipitation and temperature, which contributes to the uncertainty of the CH_4 budget (Poulter et al., 2017; Saunois et al., 2020; Peng et al., 2022). The main sink of CH_4 in the atmosphere, the hydroxyl radical (OH), also adds uncertainty to the CH_4 budget. This is because the lifetime of OH is $\sim$1 s and is therefore difficult to observe over a large scale and for long periods of time

(Stone et al., 2012; Lelieveld et al., 2016).

A further large contributing factor to the uncertainty in the CH_4 budget is the lack of long-term high spatial resolution observations of CH_4, particularly in regions of large and variable CH_4 emissions, such as wetland regions in the tropics (Dlugokencky et al., 2019; Feng et al., 2022). CH_4 can be measured by several different methods, including surface-based observations such as flask observations, tall tower networks and mobile surveys (Dlugokencky et al., 2019; Stanley et al., 2018; Lowry et al., 2020). CH_4 can also be observed by satellites, which measure concentrations from kilometre scales down to metre scales (Parker et al., 2011; Hu et al., 2018; Jervis et al., 2021). Satellite observations provide a range of spatial resolutions which can capture concentrations from area sources or point sources (Jacob et al., 2022). These different observation methods cover a range of different spatial and temporal scales, all of which are useful for determining changes in atmospheric CH_4.

The longest-standing observation network is managed by the National Oceanic and Atmospheric Administration's (NOAA) Global Monitoring Laboratory (GML). It has 90 surface observation sites worldwide but with far more sites situated in the northern hemisphere compared to the southern hemisphere. The coverage of these sites is poor around the tropics where CH_4 emissions are most uncertain and variable (Wilson et al., 2021; Feng et al., 2022). Satellites have been observing CH_4 since 2003 and are able to fill the gaps left by the NOAA network (Frankenberg et al., 2005). Satellite observations have the capability to detect sources of CH_4 that are not sufficiently characterised by surface observations. For example, satellite observations from the Scanning Imaging Absorption Spectrometer for Atmospheric Cartography (SCIAMACHY) and the Greenhouse Gases Observing Satellite (GOSAT) have improved our understanding of CH_4, particularly around the tropics (Frankenberg et al., 2011; Parker et al., 2018).

In 2017 a new high-resolution Tropospheric Monitoring Instrument (TROPOMI) was launched on Sentinel-5P (Hu et al., 2018). TROPOMI provides global CH_4 observations at a higher spatial and temporal resolution than earlier satellites, such as GOSAT which was launched in 2009 (Parker et al., 2011). GOSAT has a pixel size of 10 km in diameter with a return time of 3 days, whereas TROPOMI has a pixel size of 5.5 km $\times$ 7 km and a return time of 1 day (Parker et al., 2011; Hu et al., 2018; Lorente et al., 2023). The high-resolution data has already been shown to be advantageous in detecting anthropogenic emissions of CH_4. One of the first examples illustrating the benefits of the higher spatial resolution retrievals was when

TROPOMI detected CH_4 emissions from a natural gas well blowout in Ohio in 2018. This leak was estimated to be equivalent to one quarter of the entire state's reported annual oil and gas CH_4 emissions (Pandey et al., 2019). The instrument has continued to detect large emissions from a number of different anthropogenic sources across the globe (e.g. Schuit et al., 2023). TROPOMI is also used by the United Nations Environment Programme (UNEP) International Methane Emissions Observatory (IMEO) to identify CH_4 hot spots. These studies highlight the importance of high-resolution global monitoring satellite CH_4 observations for quantifying the methane budget.

In addition to the kilometre-scale global monitoring satellites, high-resolution imaging spectrometers such as the satellite constellation, GHGSat, are becoming important tools for detecting and monitoring point source emissions of CH_4. The GHGSat satellites can detect point source emissions at a spatial resolution of 25 m $\times$ 25 m with a theoretical detection limit of 100 kg CH_4 h^{-1} (Jervis et al., 2021; Jacob et al., 2022). GHGSat has demonstrated the ability to detect and quantify emission rates of various point source emissions such as landfill sites, coal mining and natural gas pipelines (ESA, 2021; GHGSat, 2023a; GHGSat, 2023b). CH_4 hot spots detected by TROPOMI can be used as targets for high-resolution satellites, such as GHGSat, to determine the exact location of the large emission. By detecting and monitoring CH_4 at this scale, we obtain a better understanding of the extent to which point sources are contributing to anthropogenic emissions. In this thesis, TROPOMI is referred to as high-resolution on a global monitoring scale and GHGSat is referred to as high-resolution on a point source scale. Figure 1.1 shows the spatial resolution and time scales of different observation methods, highlighting how each method is beneficial for improving our understanding of changes in atmospheric CH_4.

In addition to observations, chemical transport models (CTMs) such as TOMCAT (Chipperfield, 2006) can help us understand what might be driving changes in atmospheric CH_4 and test different scenarios. Models allow us to simulate CH_4 globally throughout the whole atmosphere, giving a complete overview of changes in CH_4 in a way observations cannot. However, the resolution of TOMCAT, for example, is currently too coarse to simulate the spatial detail observed by satellite data, such as TROPOMI. Therefore, higher resolution models are beneficial for detailed modelling and analysis when comparing to high-resolution satellite data.

The overarching aim of this thesis is to take advantage of the range of available observations and models to investigate global, regional and point source changes of atmospheric CH_4. To do

this I use the long-term NOAA network to investigate large-scale changes in the seasonal cycle of CH_4 across the globe. I have developed a nested grid model in TOMCAT to improve the model's spatial capability required for analysis with new high-resolution observation datasets, such as TROPOMI. Finally, I use a targeted imaging satellite and surface-based mobile surveys to validate satellite-derived emission estimates of a point source and to demonstrate the need for multi-scale observations to monitor fugitive emissions in the UK. This research employs observations and models across different spatial and temporal scales to fill some important gaps in our knowledge of what is driving changes in atmospheric CH_4.

1.2 Thesis Aims

The aim of this thesis is to demonstrate how we need to take advantage of observations and models across different spatial and temporal scales to improve our understanding of changes in atmospheric CH_4. This will be achieved through three key aims:

- Investigate where the seasonal cycle amplitude of atmospheric CH_4 is changing across the globe and if so, determine the causes.
- Develop a nested grid model for the TOMCAT chemical transport model in order to investigate changes in CH_4 concentrations over Europe during 2020 with high-resolution comparisons with TROPOMI retrievals.
- Validate high-resolution satellite-derived emission estimates of CH_4 from a point source.

1.3 Thesis Layout

Chapter 2 gives an introduction of atmospheric CH_4, its sources and sinks, and how it is observed and modelled. Chapter 3 provides a description of the different observations and models used in this thesis. Chapter 4 explores the long-term changes in the SCA of CH_4 using the NOAA surface observation network and the TOMCAT chemical transport model. Chapter 5 describes a new nested grid model for the TOMCAT and demonstrates its capability to compare with TROPOMI observations. Chapter 6 takes advantage of GHGSat's metre-scale resolution to detect a CH_4 point source and models the satellite data in the Met Office's Numerical Atmospheric-dispersion Modelling Environment (NAME). The thesis concludes with a summary of the thesis and future work in Chapter 7 and conclusions in Chapter 8.

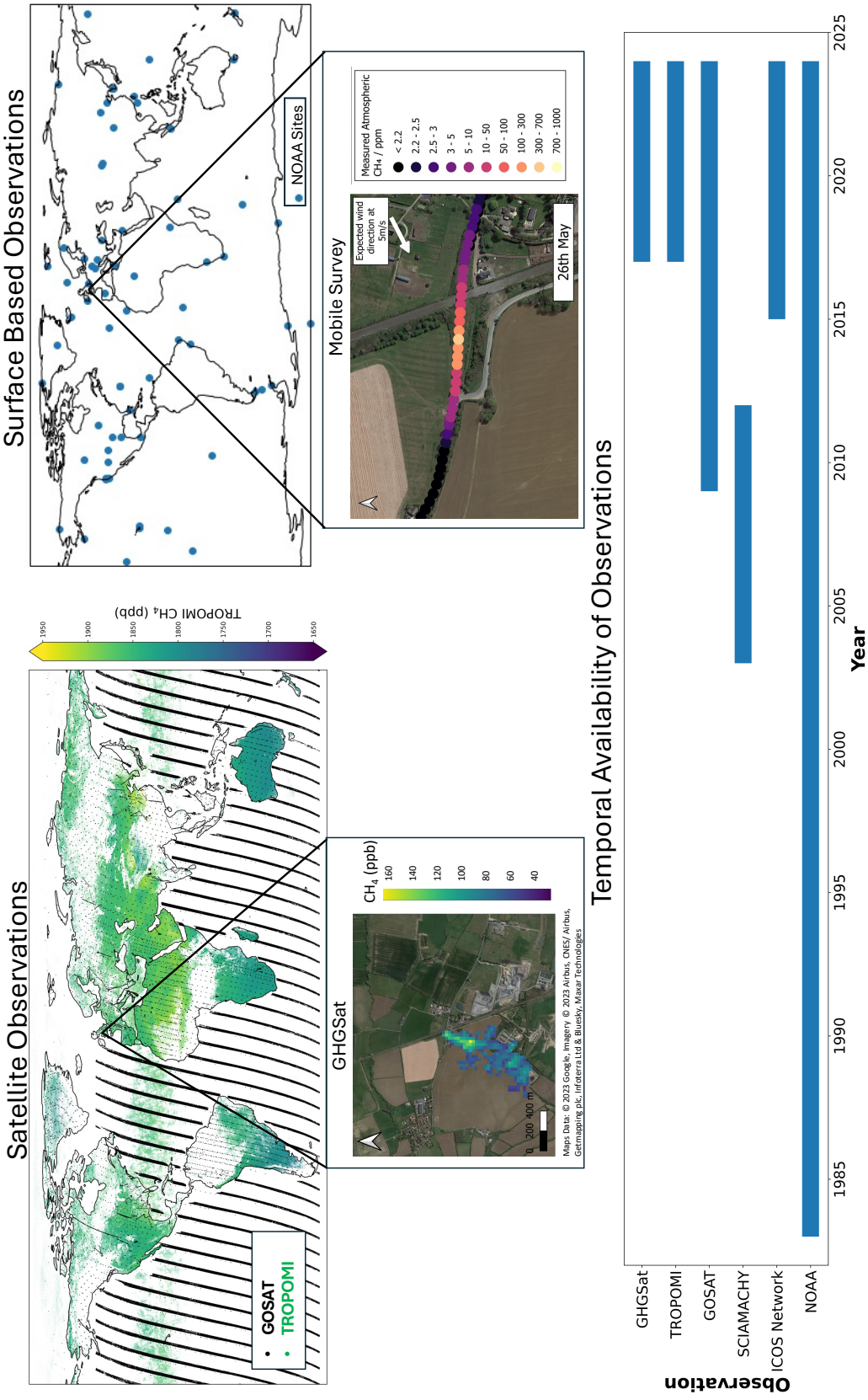

Figure 1.1: Summary of spatial coverage and temporal availability of different observation types for atmospheric CH_4.

Chapter 2

Atmospheric Methane

2.1 Introduction

This chapter provides background on atmospheric CH_4, the CH_4 budget, global trends and the processes in the atmosphere that need to be considered when simulating atmospheric constituents. Section 2.2 describes the structure of the atmosphere and its processes. Section 2.3 introduces atmospheric CH_4 and the impact it has on the Earth's surface energy balance. Section 2.4 describes the CH_4 budget, including details of its sources and sinks. Section 2.5 describes the trends of atmospheric CH_4 and the conflicting conclusions regarding what drives the global trends. The chapter concludes by describing how atmospheric CH_4 is observed (Section 2.6) and modelled (Section 2.7), both of which are important methods for investigating changes in atmospheric CH_4.

2.2 The Atmosphere

2.2.1 The Structure of the Atmosphere

The atmosphere is a layered mixture of gases which surrounds the surface of the Earth. It contains a number of different chemical species and is important for sustaining life on Earth. The atmosphere is mostly made up of nitrogen (78.08%), oxygen (20.95%), argon (0.94%), water vapour and a small proportion contains low concentrations of other "trace" gases (NOAA, 2024b). Despite making up a small fraction of the atmosphere, trace gases, such as CH_4, are important for the Earth's energy balance and changes in concentrations can have an impact on

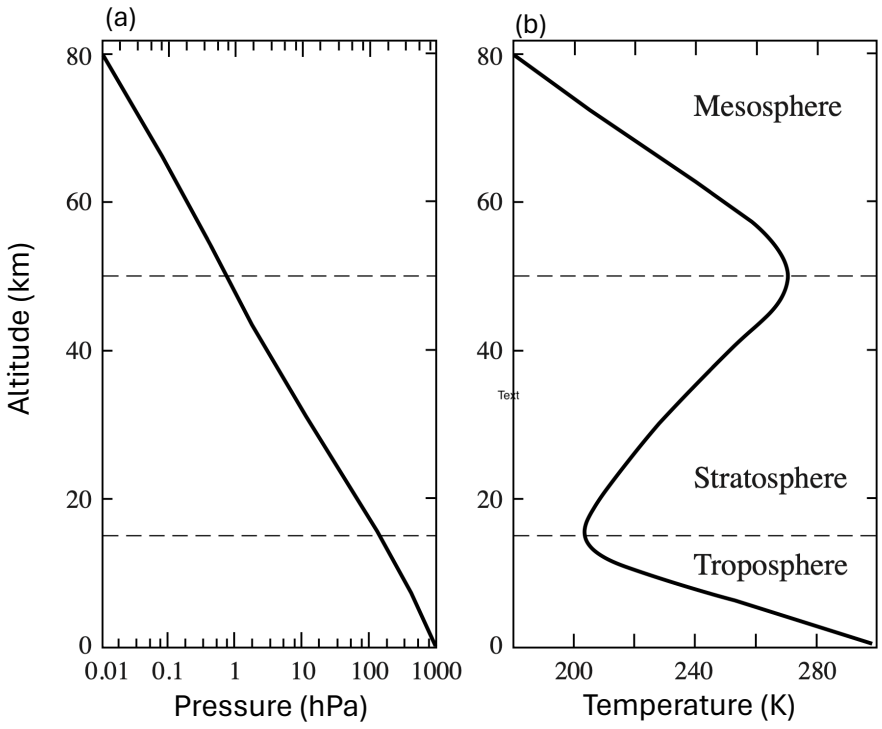

Figure 2.1: Mean atmospheric pressure with altitude (a) and mean atmospheric temperature with altitude (b) at 30°N in March. Figure adapted from Jacob (1999).

climate change. Notably, CH_4 is an important greenhouse gas.

The atmosphere is made up of five major layers. The troposphere is the layer closest to the surface and extends from the surface to approximately 8-18 km, depending on the latitude and season. It contains most the of the atmosphere and as a result, most of the greenhouse gas effect happens there. It also has its own chemistry regime and transport patterns. In the troposphere, temperature decreases with height, see Figure 2.1. Within the troposphere there is a small section, closest to the surface, called the planetary boundary layer (PBL). The PBL is characterised by turbulent and rapid mixing of air due to friction from the orography. The height of PBL changes with the temperature of the Earth's surface, varying from roughly 1-3 km in altitude (Jacob, 1999), which can impact the time it takes for species to be transported into the free troposphere above.

The layer above the troposphere is the stratosphere which extends from the tropopause (top of the troposphere) to approximately 50 km in altitude. The temperature in the stratosphere increases with height due to absorption of solar radiation by ozone (O_3). The layers above the stratosphere are the mesosphere and thermosphere. The troposphere and stratosphere make up 99.9% of the total atmospheric mass. CH_4 is emitted in the troposphere and transported into

the stratosphere. In this thesis I predominantly focus on CH_4 in the troposphere.

2.2.2 Atmospheric Transport

Chemical species in the atmosphere are transported and mixed throughout the atmosphere by atmospheric transport. The main processes are: advection, convection and boundary layer mixing. Chemical species are also transported through long-range transport such as meridonial or interhemispheric transport (described below).

Advection is the transport of chemical species due to winds. Wind is the movement of air caused by differences in atmospheric pressure, which arise from differences in temperature. The advection of a species can be described by the continuity equation, in Eulerian or Lagrangian form. The Eulerian continuity equation shows the conservation of mass:

$$\frac{\partial n}{\partial t} = -\nabla \cdot (n\boldsymbol{U}) \tag{2.1}$$

where $n(\boldsymbol{X}, t)$ is number density of a species in a fixed frame of reference and $\boldsymbol{U} = (u, v, w)$ is the local wind velocity vector. Equation 2.1 shows the number density of a species over time is conserved, assuming no emissions or loss. The Eulerian case considers chemical species in a fixed frame of reference, represented as a 3D grid, and therefore has a fixed coordinate system. Equation 2.1 can be integrated to obtain the concentration field of any given species. In the Lagrangian case, the continuity equation for the concentration field $n(\mathbf{X}, t)$ with a source field $P(\mathbf{X}, t)$ is defined as:

$$n(\mathbf{X}, t) = \int_{atm} Q(\mathbf{X_0}, t_0|\mathbf{X}, t) n(\mathbf{X_0}, t_0) dx_0 dy_0 dz_0 + \int_{atm} \int_{to}^{t} Q(\mathbf{X}', t'|\mathbf{X}, t) P(\mathbf{X}', t') dx' dy' dz' dt' \tag{2.2}$$

where the transition probability density $Q(\mathbf{X_0}, t_0|\mathbf{X}, t)$ is defined as the probability that the particle will have moved from location $\mathbf{X_0}$, starting at time t_0 to be within a volume (dx, dy, dz) centred at location $\mathbf{X}$ at time t (Jacob, 1999). Here the transport of the particle is described by a transition probability density Q instead of the wind velocity $\mathbf{U}$ (Jacob, 1999). Q accounts for turbulence, therefore the turbulent transport flux does not need to be parameterised. The Lagrangian case treats chemical species as a number of particles that move relative to the frame

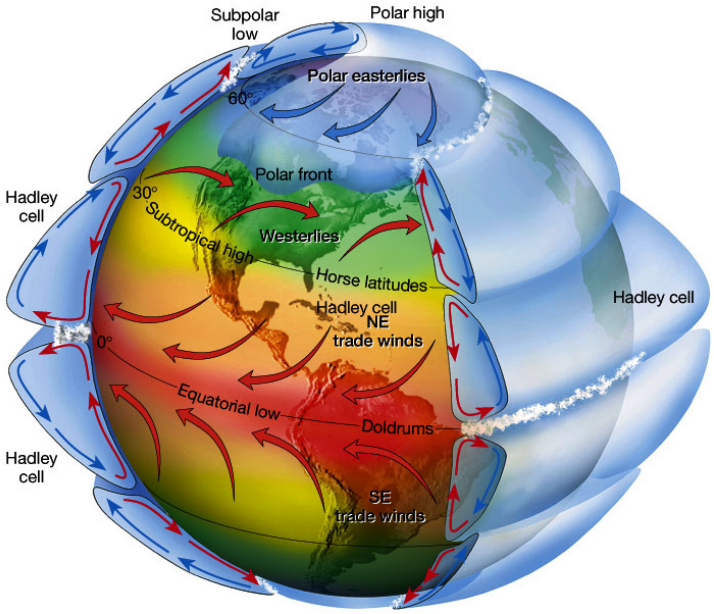

Figure 2.2: General circulation diagram, depicting the Hadley Cell (Figure by Lutgens and Tarbuck (2001)).

of reference of local flow.

Convection is the vertical transport of mass through heating, moisture, wind and orography. There are two types of convection. There is buoyant convection, which is solely driven by buoyancy forces, and forced convection, which is a combination of buoyancy and mechanical forcing. An example of forced convection is the heat exchange between the ground and the air leading to convection. Convection can occur in dry or moist conditions. Moist convection occurs when the air is saturated. Transport models used in this thesis have a relatively coarse spatial resolution and therefore have to parameterise processes such as convection.

The general circulation model describes large scale transport and wind flow patterns from the equator to the poles, see Figure 2.2. The Hadley Cell describes the transport of air from the equator. The air is heated at the equator, lofted through convection and then the air is advected polewards, deflected and accelerated by the Coriolis force and breaks down into an unstable flow and sinks at approximately 30°. Atmospheric convection occurs prominently at the equator due to the large amount of heating from the sun and the high moisture content at this latitude.

Horizontal transport in the troposphere occurs at different rates. Figure 2.3 shows the typical time scales for horizontal transport in the troposphere. Timescales range from approximately 2 weeks for zonal transport and up to ∼1 year for interhemispheric transport (Jacob, 1999). Vertical transport to different layers of the atmosphere also occurs at different rates. Figure

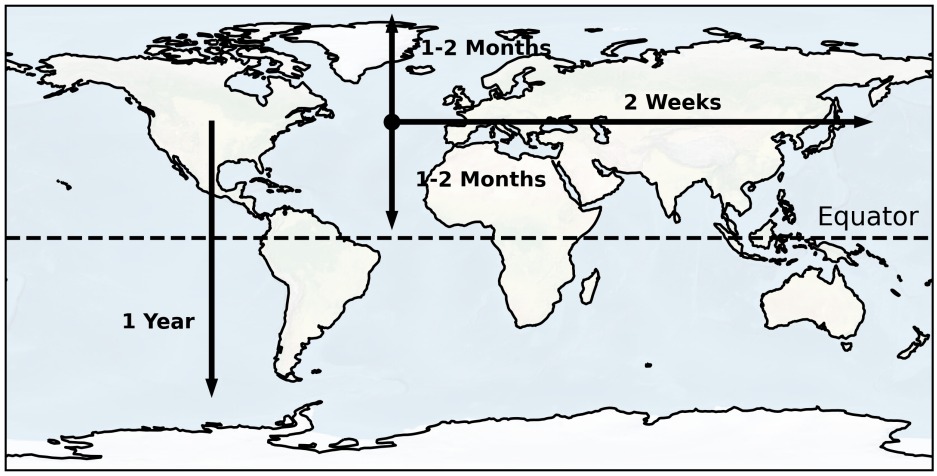

Figure 2.3: Typical time scales for horizontal transport in the troposphere. Figure adapted from Jacob (1999)

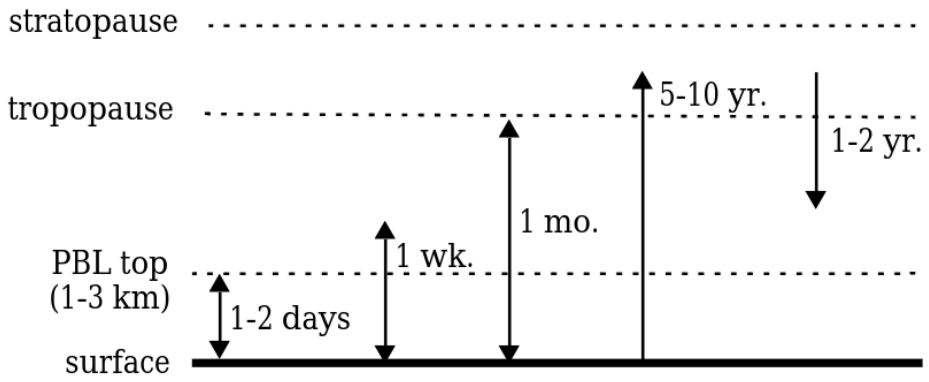

Figure 2.4: Typical time scales for vertical transport. Figure from Jacob (1999)

2.4 shows the characteristic time scales for vertical transport. Time scales range from 1-2 days for mixing withing PBL and up to 1-2 years for air to be transported from the stratosphere to the troposphere (Jacob, 1999). Air is generally transported from the troposphere to the stratosphere at the tropics and then is transported polewards before descending in the mid- and high-latitudes. This is known as the Brewer-Dobson circulation (Butchart, 2014), see Figure 2.5.

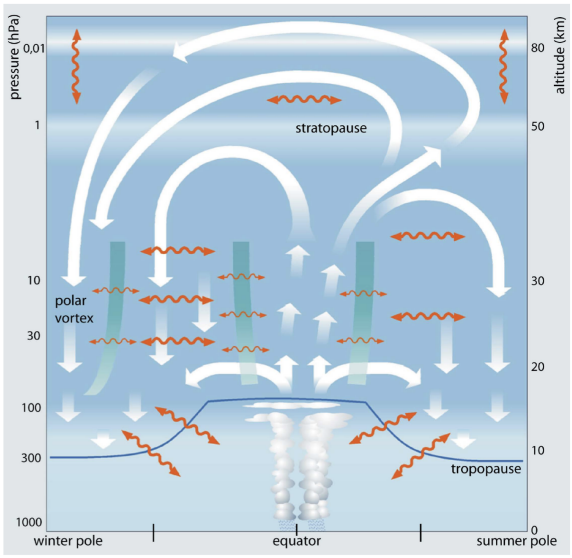

Figure 2.5: Schematic of the Brewer-Dobson circulation, shown by the white arrows. The orange arrows represents two-way mixing processes. Figure taken from Bönisch et al. (2011).

2.3 Atmospheric Methane

Methane (CH_4) is one of the most important greenhouse gases in our atmosphere. A greenhouse gas is a chemical which traps outgoing infrared radiation from the Earth's surface and radiates it back to Earth, resulting in the warming of the Earth's atmosphere. CH_4 is produced and emitted by a mixture of natural and anthropogenic sources. The anthropogenic emissions of CH_4 have contributed 23% to the additional radiative forcing in the troposphere since 1750 (Saunois et al., 2020). Radiative forcing is the net change in the energy balance of the Earth system, driven by factors which influence the energy balance such as greenhouse gas concentrations (Myhre et al., 2013). The global warming potential (GWP) is defined as the amount of energy the emissions of 1 tonne of gas will absorb over a given period of time, relative to CO_2. The GWP of CH_4 decreases relative to CO_2 due to its lifetime in the atmosphere; for example, the 100-year GWP for CH_4 is 29 times bigger than CO_2. CH_4 also has a 20-year GWP 82 times greater than carbon dioxide (CO_2) (Forster et al., 2023). Table 2.1 shows a comparison of the main greenhouse gases GWP and Radiative Efficiencies.

Global concentrations of CH_4 have been rising quickly in the past decade and our understanding of what is driving the increase remains incomplete. Natural sources, such as wetlands, contribute to the uncertainty of the CH_4 budget (Saunois et al., 2020). However anthropogenic sources, such as fossil fuels, present an opportunity to mitigate the human contribution to climate change on a relatively short timescale, since CH_4 has a much shorter atmospheric lifetime than

Table 2.1: Main greenhouses gases and their lifetimes.

Chemical Species	Lifetime (years)	Radiative Efficiency (W m^{-2} ppb^{-1})	20-Year GWP	Reference
Carbon Dioxide (CO_2)	-	1.33	1	Forster et al. (2023)
Methane (CH_4)	9	5.7	82.5	Prather et al. (2012) Forster et al. (2023)
Nitrous Oxide (N_2O)	109	208	273	Forster et al. (2023)

CO_2. CH_4 has a lifetime of approximately 9 years (Prather et al., 2012), whereas CO_2 has a significantly longer lifetime of 100s to 1000s of years (Joos et al., 2013). Many studies have been carried out to determine what is driving the recent global trends of CH_4 but these studies have led to conflicting conclusions resulting in a complex picture of the CH_4 budget (e.g. Rigby et al., 2017; McNorton et al., 2018; Feng et al., 2023; Peng et al., 2022).

The next two sections will describe the CH_4 budget and the recent global trends of atmospheric CH_4, highlighting the complexities inhibiting our understanding of CH_4.

2.4 Methane Budget

In order to identify the drivers of the trends in atmospheric CH_4, an understanding of the mechanisms that produce and destroy CH_4 is needed. The two main uncertainties in the CH_4 budget are the distribution and magnitude of CH_4 sources and the scale of the removal of CH_4 in the atmosphere due to the short-lived hydroxyl radical (OH). The most recent assessment of the global CH_4 budget was completed by the Global Carbon Project in 2020 (Saunois et al., 2020). The Global Carbon Project was established in 2001 and aims to provide improved and up-to-date estimates of the global CH_4 budget. The most recent budget covers 2008-2017. The study combines top-down studies and bottom-up estimates to provide the most comprehensive estimate of the sources and sinks of atmospheric CH_4. Top-down studies combine atmospheric observations, such as surface flask measurements and satellite observations, and inverse modelling. Bottom-up estimates include process-based models for estimating land surface emissions and atmospheric chemistry, data driven extrapolations and inventories of anthropogenic emissions (Saunois et al., 2020). The global emissions of CH_4 between 2008 and 2017 are estimated to be 572 [550-594] Tg CH_4 yr^{-1} from atmospheric inversions and 359 [336-376] Tg CH_4 yr^{-1} of the total emissions have been attributed to anthropogenic sources. However, bottom-up methods provide a larger estimate of global emissions of 737 [597-881] Tg CH_4 yr^{-1} and this is due

to larger estimates of natural emissions from wetlands and inland water systems (Saunois et al., 2020). The emission estimate values reported in Saunois et al. (2020) give an uncertainty range which corresponds to the minimum and maximum estimates of the model ensemble. The large uncertainty in the emission estimates, particularly between bottom-up estimates and top-down estimates, suggests that some bottom-up emissions are over-estimated (Saunois et al., 2020). Bottom-up estimates are often larger than top-down estimates for CH_4 and this is likely due to the larger and uncertain natural emissions, from wetlands and water systems, being double counted (Saunois et al., 2020).

The largest natural sources of CH_4 are wetlands, which contribute 149 [102-182] Tg CH_4 yr^{-1} from bottom-up estimates. Other natural sources of CH_4 include wild animals, termites and oceans. The largest anthropogenic source of CH_4, as categorised by the Global Carbon Project, is agriculture and waste which contribute 206 [191-223] Tg CH_4 yr^{-1}, according to bottom-up estimates. However, these two source categories are in fact quite distinct. Other anthropogenic sources include fossil fuels and biomass burning. The main sink of CH_4 is the reaction with hydroxyl radical (OH) in the atmosphere. Other sinks of CH_4 include loss in the stratosphere due to excited oxygen atoms ($O(^1D)$) and chlorine (Cl), and soil uptake. It is estimated that 595 [489-749] Tg CH_4 yr^{-1} is removed through chemical reactions in the atmosphere. The differences in bottom-up and top-down estimates can be seen in Figure 2.6.

The following sections will provide information on how CH_4 is emitted from different sources. It will also describe the uncertainty surrounding these estimates.

2.4.1 Natural Sources

2.4.1.1 Wetlands

Wetlands are the largest and most uncertain natural source of CH_4 and contribute 20-40% of global emissions (Kirschke et al., 2013; Parker et al., 2018). Wetlands are ecosystems with permanently or seasonally water saturated or inundated soils (Pandey et al., 2021). These include peatlands, bogs, fens, swamps, marshes or floodplains. Bogs in forested or non-forested areas are usually associated with waterlogging or freeze-thaw cycles and occur predominantly in boreal regions. Swamps are most common in the tropics and the seasonal inundation is due to precipitation driven increases in river and lake levels (Matthews and Fung, 1987). CH_4 is emitted from wetlands by anaerobic decomposition of organic material in wetland soils (Pandey et al.,

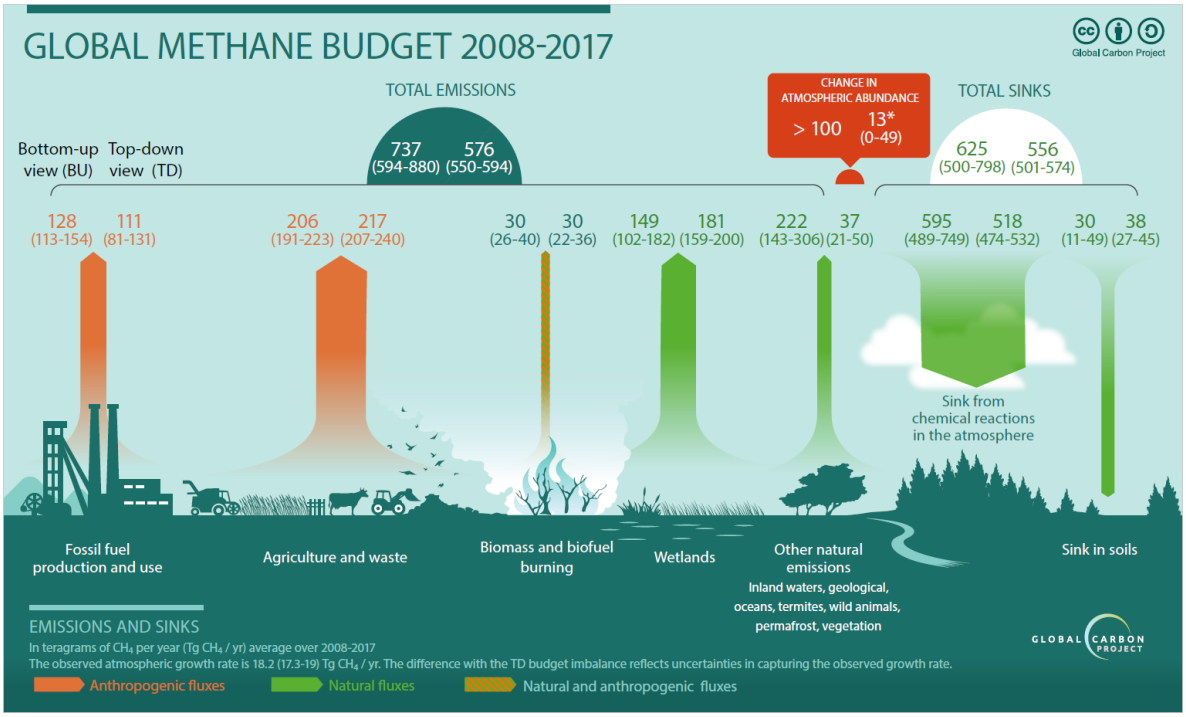

Figure 2.6: Global CH_4 budget for 2008-2017. Bottom-up (left) and top-down (right) estimates for are given for each source and sink category in Tg CH_4 yr^{-1} (Saunois et al., 2020).

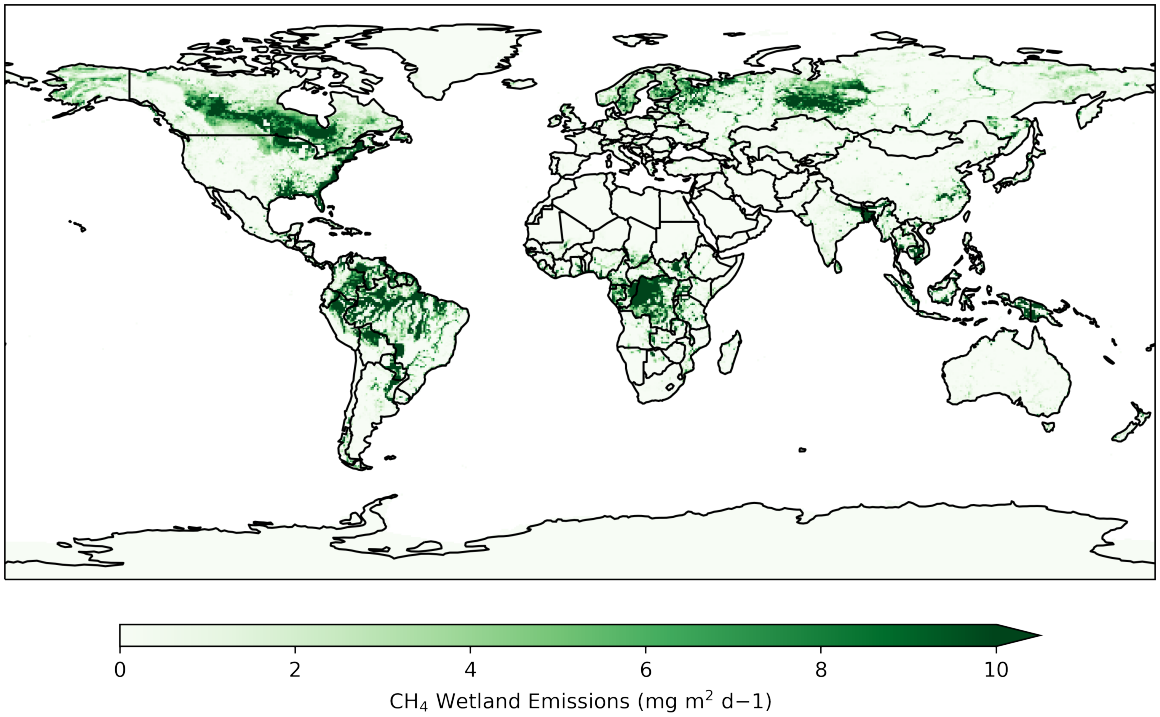

Figure 2.7: Mean CH_4 emissions (mg m^2 d^{-1}) from wetlands between 2001-2019, data from Bloom et al. (2021).

2021). The amount of CH_4 emitted from wetlands is dependent on a number of environmental and ecological factors which include; temperature, precipitation, moisture and vegetation characteristics (Matthews and Fung, 1987; Pandey et al., 2021).

Wetlands are distributed across the globe with large emissions from the Amazon Basin, Central Africa and the Arctic. Figure 2.7 shows the distribution of CH_4 emissions from wetlands as estimated by the WetCHARTs model ensemble (Bloom et al., 2021). Chapter 3, Section 3.3.2 provides further details about WetCHARTs. It is possible that wetland emissions are over estimated in emission datasets due to double counting wetlands or inland water estuaries, or classifying a rice paddy as a wetland. Double counting of wetlands can occur in part due to the definition of wetlands (e.g wetlands and lakes) and limitations of remote sensing techniques used to classify wetlands (Saunois et al., 2020).

2.4.1.2 Wild Ruminants and Termites

Wild ruminants, such as buffalo and deer, naturally emit CH_4 through the microbial fermentation of ingested food in their gut (Pérez-Barbería, 2017). It is estimated that wild animals emit 1.1-2.7 Tg yr^{-1}, which is smaller than the previously estimated (15 Tg yr^{-1}) due to the wild ruminant population being previously over estimated (Pérez-Barbería, 2017). However, there is uncertainty in the world's wild ruminant animal population which could lead to discrepancies in the CH_4 emission estimates.

Termites are another natural source of CH_4, emitting CH_4 through anaerobic decomposition of plant biomass in their gut (Nauer et al., 2018). They are mostly situated in the tropical and subtropical latitudes and their emissions vary in different ecosystems (Abe et al., 2000; Kirschke et al., 2013). A lack of field observations of termite biomass and emissions contribute to the uncertainty in emissions estimates. Saunois et al. (2020) report a value of 9 [3-15] Tg yr^{-1} from termites. A study carried out by Nauer et al. (2018) found that 20-80% of termite-produced CH_4 was being mitigated by methanogenic bacteria within the termite mound walls and the soil beneath, before being emitted into the atmosphere. Although this study was carried out using field measurements from North Australia, it highlights the uncertainty in the emission estimates and that further research is needed to gain a better understanding of the global emissions of CH_4 from termites.

2.4.1.3 Oceans

CH_4 is also emitted from the ocean by several mechanisms. These include production from anoxic marine sediments or thawing sub-sea permafrost, in situ production in the water column, leaks from geological marine seepage and emission from destabilisation of marine hydrates (Weber et al., 2019). CH_4 is emitted into the atmosphere by diffusive gas transfer and ebullition across the air-sea interface (Weber et al., 2019). Weber et al. (2019) find that the flux of global ocean CH_4 emissions is dominated by shallow near-shore environments, where CH_4 released from the sea floor can reach the atmosphere before oxidation. The combined emissions of the different oceanic fluxes amounts to 13 [9-22] Tg yr^{-1}, however these emissions are uncertain due to sparse observational constraints (Saunois et al., 2020).

2.4.2 Anthropogenic Sources

2.4.2.1 Agriculture and Waste

In the Global CH_4 Budget, by Saunois et al. (2020), the largest anthropogenic emissions are from the combination of agriculture and waste (206 [191-223] Tg yr^{-1}). The agricultural sector includes emissions from livestock and rice cultivation (131 Tg yr^{-1}) and the waste sector includes emissions from waste management (65 Tg yr^{-1}, Saunois et al. (2020)). Like wild animals, domestic livestock such as cattle, sheep, buffalo and goats emit CH_4 via anaerobic activity in their digestive system. The emissions of CH_4 from domestic livestock varies in different countries due to different living conditions and feed types (Chang et al., 2019). Domestic livestock also produce manure which decomposes anaerobically, producing CH_4. However different manure compositions from animal diet, type of animal and the different management systems, such as slurry treated in ponds or solid manure deposited on pasture, produce varying amounts of CH_4 emissions (Saunois et al., 2020). Increasing numbers of domestic livestock means that estimated emissions have increased from 103 Tg yr^{-1} (between 2000-2009) to 111 [106-116] Tg yr^{-1} (Saunois et al., 2020).

Rice cultivation is another large emitter of CH_4. Rice paddies are fields of shallow water where anaerobic decomposition results in CH_4 production. The largest emissions from rice cultivation are found in Asia, where China and India account for 30-50% of global emissions (Saunois et al., 2020). Emissions from rice cultivation have decreased in recent decades and this is due to changes in agricultural practices, decrease in cultivation area and northward shift of rice

cultivation since 1970s in China (Chen et al., 2013). The rice paddies in northern regions of China emit less CH_4 than those in the south due to water saving practices during the growing season, and irrigation practices during the non-rice crop growing season (Chen et al., 2013). Southwestern rice paddies have a drying crop or fallow after the growing season which account for 11-65 % of the of CH_4 emissions from year round flooded paddies (Chen et al., 2013). The global emission of CH_4 from rice cultivation is estimated to be 30 [25-38] Tg yr^{-1} (Saunois et al., 2020).

Waste management such as managed and unmanaged landfills and wastewater handling are sources of CH_4 categorised under agriculture and waste. They emit CH_4 through anaerobic decomposition of organic material and the amount of CH_4 emitted is dependent on pH, moisture and temperature (Saunois et al., 2020). The estimate of CH_4 emissions from waste management is 65 [60-69] Tg yr^{-1} (Saunois et al., 2020), however global emission estimates rely on national reporting according to IPCC guidelines, which recommend a first order decay model based on disposal mass and age of the landfill (Wang et al., 2024). This method does not take into account the geographical location, waste composition and potential climate change impacts from changes in temperature and moisture. A study by Wang et al. (2024) makes a correction for waste composition, moisture and temperature in their emission estimation, concluding that emissions from individual landfills have been underestimated by up to 200%. These results show that environmental factors should be considered made when estimating landfill emissions of CH_4 (Wang et al., 2024).

2.4.2.2 Fossil Fuels

Fossil fuel production and use is another anthropogenic source of CH_4. Emissions related to fossil fuels come from the exploitation, transportation and usage of coal, oil and natural gas (Saunois et al., 2020). During coal mining, CH_4 is released from ventilation shafts. Natural gas is mostly made up of CH_4 and is released into the atmosphere through planned and fugitive emissions during drilling, extraction, transportation, storage and end use of natural gas. CH_4 can also be released through incomplete combustion of gas flares. Smaller emissions also come from the production of chemicals and metals, fossil fuel fires and transport. The global emissions from these sources are estimated to be 128 [113-154] Tg yr^{-1}, an increase in emissions from estimates between 2000-2009 (112 Tg yr^{-1}). This is due to an increase in emissions from coal due to revised emission factors for coal mines in China and an increase in the number of coal

mines which are accounted for in the estimation. Emissions from oil and gas have have increased due to an increase in production.

Global CH_4 emissions estimates from oil and natural gas vary by approximately 20 Tg yr^{-1} due to different methods for quantifying emissions and represent approximately 63% of the total fossil fuel CH_4 emissions. Several studies suggest that CH_4 emissions from oil and gas are underestimated by emission inventories and, for example, fugitive emissions from "super-emitters" contribute approximately 60% of the total oil and gas sector in the US, despite not being included in the emission inventories (Zavala-Araiza et al., 2015b; Lauvaux et al., 2022). A super-emitter is loosely defined in a number of ways. Zavala-Araiza et al. (2015a) define a super-emitting site as one with the highest proportional loss rates (methane emitted relative to methane produced). The US Environmental Protection Agency (EPA) define it as a source that is emitting CH_4 above 100 kg h^{-1} (EPA, 2022). Super-emitters are concentrated point sources, which are difficult to account for in emission inventories because they are often unplanned or occur under abnormal conditions and are not limited to the oil and gas sector (Schuit et al., 2023). Other examples of super-emitters include coal mines and landfills. Satellites have become an important tool in detecting and quantifying CH_4 from super-emitters, however these emission estimates are yet to be formally included in emission inventories.

2.4.2.3 Biomass Burning

Biomass burning is categorised under anthropogenic emissions by the Global Carbon Project, although emission estimates include a mixture of natural and anthropogenic biomass burning (Saunois et al., 2020). Biomass burning in forests, savannahs, grasslands, peatlands, and biofuels emit CH_4 under incomplete combustion. The amount of CH_4 emitted depends on the amount of biomass, burning conditions and the type of material that is being burned (Saunois et al., 2020). Biomass and biofuel burning emissions are estimated to be 30 [26-40] Tg yr^{-1}, of which 30-50% is biofuel burning (Saunois et al., 2020). The range in emission estimates is partly due to uncertainties in burnt area estimates, emission factors, combustion factors and the inter-annual variability in emissions due to El Niño-Southern Oscillation (ENSO) driven changes in rainfall (Worden et al., 2017). ENSO encompasses two phenomena: El Niño which is the warming of the upper ocean in the tropical eastern Pacific lasting over five months, and the Southern Oscillation is a widespread inter-annual variation in atmospheric sea-level pressure (Wang et al., 1999a). It is measured as an index, typically between 5°N -5°S for an area in the central Pacific

(Wang et al., 1999a). ENSO has an impact on global temperature and precipitation (Lin and Qian, 2019).

2.4.2.4 Other Sources

In addition to the sources described above, there a number of other small sources which contribute to the CH_4 budget. These include geological sources, permafrost soils and vegetation. The geological emissions come from CH_4 that is produced by the Earth's crust and travels through fractured rocks and tectonic faults to reach the atmosphere. Geological emissions are estimated to contribute 43-50 Tg yr^{-1} (Etiope et al., 2019). The thaw of permafrost soils can lead to direct and indirect emissions of CH_4. CH_4 is directly emitted into the atmosphere when CH_4 contained within the soil is released through thawing. CH_4 is released indirectly through methanogenesis when the organic matter is released through thawing and through changes in hydrology. Permafrost thaw is estimated to contribute approximately 1 Tg yr^{-1} (Saunois et al., 2020). Finally, CH_4 can also be emitted from vegetation through several pathways. One example is that plants draw up CH_4 produced by anoxic soils and release CH_4 into the atmosphere (Covey and Megonigal, 2019). Estimates of how much CH_4 is released from vegetation are very uncertain.

2.4.3 Sinks

Atmospheric CH_4 can be removed by a number of different processes. The main sink of atmospheric CH_4 is tropospheric loss via reaction with the hydroxyl radical (OH) (Rigby et al., 2017). However, CH_4 also undergoes reactions with the electronically excited oxygen ($O(^1D)$), Cl and OH in the stratosphere. This section provides details on the chemical reactions of CH_4 in the atmosphere and and soil uptake.

2.4.3.1 Tropospheric Loss

Approximately 85% of CH_4 is removed from the troposphere through the reaction with OH. OH is produced in a reaction between O_3, ultraviolet light and water vapour. The reactions are shown in Equations 2.3 and 2.4.

$$O_3 + h\nu \rightarrow O(^1D) + O_2 \qquad \lambda < 315nm \tag{2.3}$$

$$O(^1D) + H_2O \rightarrow 2OH \tag{2.4}$$

O_3 reacts with ultraviolet (UV) light to produce $O(^1D)$ and an oxygen molecule (O_2). $O(^1D)$ then reacts with water vapour in the atmosphere to produce OH. The global distribution of tropospheric OH is dependent on latitude, where higher abundances are seen in the tropics and lower abundances occur over the poles (Lelieveld et al., 2016). The distribution of OH also has a seasonal cycle due the production of OH being reliant on the amount of UV light, for example there are higher abundances of OH in the hemispheric summertime, see Figure 2.8.

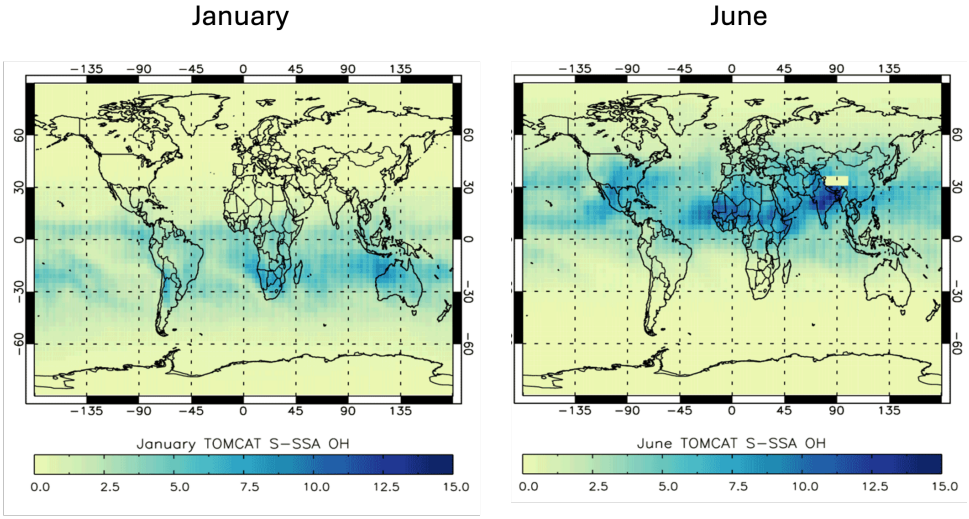

Figure 2.8: OH concentrations from a satellite derived steady state approximation ($\times 10^6$ molec. cm^{-3}) averaged over 600-700hPa by Pimlott et al. (2022). The figures show the distribution of abundances in January and June. Figure adapted from Pimlott et al. (2022).

$$CH_4 + OH \rightarrow H_2O + CH_3 \tag{2.5}$$

$$net: CH_4 + 10O_2 \rightarrow CO_2 + H_2O + 5O_3 + 2OH \tag{2.6}$$

Equation 2.5 shows that CH_4 is removed by reacting with OH to produce methyl (CH_3). CH_3 rapidly reacts with water vapour to create the methylperoxy radical (CH_3O_2). Then CH_3O_2 goes through a number of reactions to eventually produce CO_2 and O_3 (Jacob, 1999). The net reaction is shown by Equation 2.6. The amount of CH_4 removed from the atmosphere is dependent on the quantity of OH present. The tropospheric loss of CH_4 from OH is estimated

to be 553 [476-677] Tg yr^{-1} (Saunois et al., 2020).

Tropospheric OH has a lifetime of 1-2 seconds making it difficult to directly observe. Therefore it is not possible to obtain global OH concentrations from observations. Instead, global concentrations of OH are estimated using global models. OH concentrations are predominantly estimated by an inversion of methyl chloroform (MCF) which relies on two important factors; concentrations and emissions of MCF are well observed and the main sink of MCF is OH (Zhao et al., 2019). OH can also be estimated using atmospheric chemistry models, which relies on chemical transport and chemistry schemes (Zhao et al., 2019). Zhao et al. (2019) find that different estimates of OH can result in a difference of 19% in simulated CH_4 when compared with observations, highlighting the need for improved estimates of OH for CH_4 model simulations.

More recently, OH has been estimated using satellite data from Infrared Atmospheric Sounding Interferometer (IASI) on board ESA's MetOp-A satellite and a simplified steady state approximation (Pimlott et al., 2022). This simplified steady state approximation contains one source term based on Equations 2.3 and 2.4 and three sink terms based on the reaction of OH with CH_4, CO and O_3. Despite being able to model and estimate OH on a global scale there is still uncertainty surrounding the quantity and spatial distribution of OH. Studies have conflicting conclusions on OH variability. For example Rigby et al. (2017) and Turner et al. (2017) find a declining trend in OH from 2004 but Zhao et al. (2019) find an increasing trend between 2004 and 2010. However, studies by Patra et al. (2021) and Naus et al. (2021) find small annual variability on OH. More recently, Pimlott et al. (2022) find that between 2008 and 2017 global annual mean anomalies derived from the simplified steady state approximation and IASI retrievals are variable, ranging from -3.1% to +4.7%. These studies highlight the large uncertainties in estimating OH concentrations and as a result, OH concentrations are a large uncertainty in the CH_4 budget.

CH_4 also reacts with Cl in the troposphere. Estimates of how much Cl contributes to the sink of CH_4 in the troposphere are variable and uncertain. Studies have shown Cl can remove up to 37 Tg yr^{-1} (Allan et al., 2007) but also removes as little as 1 Tg yr^{-1} (Gromov et al., 2018). Saunois et al. (2020) emphasise the need for further work to estimate the Cl impact in the troposphere and estimate that it removes approximately 11 [1–35] Tg yr^{-1} of CH_4.

2.4.3.2 Stratospheric Loss

CH_4 is also removed from the atmosphere via chemical reactions in the stratosphere. CH_4 is transported into the stratosphere via slow ascent and then transported to higher latitudes and altitudes by the Brewer-Dobson circulation (see Figure 2.5; Saunois et al. (2020)). CH_4 is destroyed through reactions with $O(^1D)$, chlorine (Cl) and OH (Le Texier et al., 1988). The reactions are shown in Equations 2.7 and 2.8. When CH_4 reacts with $O(^1D)$ in the stratosphere it mainly leads to methyl (CH_3) formation, which reacts with O_2 or atomic oxygen, but can also lead to formaldehyde (CH_2O) formation (Le Texier et al., 1988). Similarly, when CH_4 reacts with Cl it produces CH_3 and hydrogen chloride (HCl).

$$\begin{aligned} CH_4 + O(^1D) &\rightarrow CH_3 + OH \\ &\rightarrow CH_2O + H_2 \end{aligned} \tag{2.7}$$

$$CH_4 + Cl \rightarrow CH_3 + HCl \tag{2.8}$$

The mean stratospheric loss of CH_4 is estimated to be 31 [12-37] Tg yr^{-1} (Saunois et al., 2020), which is a much smaller contribution than from the tropospheric OH sink. There are large uncertainties in stratospheric loss of CH_4 due to uncertainties in the inter-annual variability of stratospheric transport and CH_4's chemical interactions and feedbacks with stratospheric O_3 (Portmann et al., 2012; Saunois et al., 2020). For example, CH_4 reacts with stratospheric Cl producing HCl, which suppresses O_3 depletion (Portmann et al., 2012). Global tropospheric and stratospheric loss of CH_4 are both difficult to measure directly because of the short lifetime of OH, adding to the uncertainties in the CH_4 budget. The total chemical loss of CH_4 in the atmosphere is estimated to be 595 [489-749] Tg yr^{-1} (Saunois et al., 2020).

2.4.3.3 Soil Uptake

CH_4 is also removed from the atmosphere via soil uptake. Unsaturated oxic soils contain methanotrophic bacteria, which consume CH_4 as a source of energy (Dutaur and Verchot, 2007). The estimate of uptake by soils is 30 [11-49] Tg yr^{-1} (Saunois et al., 2020).

2.5 Trends of Atmospheric Methane

The uncertainties in both the sources and sinks of CH_4 make it difficult to attribute changes in global atmospheric CH_4 concentrations. The next section will discuss the recent trends in global CH_4 concentrations and what could be driving them.

2.5.1 Global Variations

Atmospheric CH_4 exhibits a seasonal cycle due to the seasonality of its sources and sinks. The seasonal cycle of CH_4 in the northern hemisphere, for example, has a peak during spring and a trough in summer. There is an imbalance between the sources and sinks, causing the global concentrations of CH_4 to increase from year to year. Atmospheric CH_4 concentrations have been rising since pre-industrial times, however there has not been a continuous rise (see Figure 2.9). There was a stagnation of global growth between 1999 and 2006, where the global growth rate slowed to 0.6 ppb yr^{-1} (Dlugokencky et al., 2011; McNorton et al., 2016). The global growth rate resumed in 2007 at a rate of 4.9 ppb yr^{-1} (Nisbet et al., 2016; McNorton et al., 2016) and accelerated in 2014 to 12.7 ppb yr^{-1} (Nisbet et al., 2019). In 2020, the global annual increase was the largest on record at 15.15 ppb, however this record was surpassed in 2021 with a global increase of 17.92 ppb, see Figure 2.9 (Lan et al., 2024). Global concentrations of CH_4 also exhibit inter-annual variations (IAV). The IAV is mostly driven by natural variation in global emissions and meteorology, but the exact mechanisms that drive the IAV are not fully understood (Rowlinson et al., 2019).

The causes of the recent global variations of CH_4 have not been resolved. This includes the slow global growth between 1999 and 2006. At the time it appeared that CH_4 could have been approaching long-term steady state due to its sources and sinks being in balance, or only a more temporary pause to the increasing trend. During 2007, the global concentrations began to increase again but due to the lack of observational data it is difficult to be conclusive on what caused this hiatus period (Dlugokencky et al., 2003; Dlugokencky et al., 2011). Studies by Rigby et al. (2017) and Zhao et al. (2019) find increases in OH during the hiatus period. Estimates of OH come with large uncertainties and these results highlight the complexity of understanding the role of OH during the hiatus period. In addition to changes in the OH sink, changes were observed in wetland emissions. Poulter et al. (2017) found in their bottom-up model that there was an increase in boreal wetland emissions by 1.2 Tg yr^{-1} between 2000-2012

but there was a decrease of 0.9 Tg yr^{-1} in tropical wetlands. It was also shown that the IAV of wetland emissions during 2000-2006 was smaller than 2007-2012. In addition to changes in natural sources, it is possible that a reduction in fossil fuel emissions between 1998-2002 from the oil industry could also have been a factor in the early years of the period of slow growth (Crippa et al., 2020a). These results give indication of what was happening during the period of slow growth but do not provide a definitive answer. Many studies have investigated this period of slow growth, however without better constraints on the sinks, it is difficult to draw firm conclusions about the sources. After that period, the main focus of most atmospheric CH_4 studies was on the rise of CH_4 in 2007.

A number of studies have investigated the increase in global growth from 2007 onwards and there have been conflicting results regarding what was responsible for the rise in concentrations. Nisbet et al. (2016) used $\delta^{13}C$ isotope ratios to investigate the rise in CH_4 from 2007 to 2013. $\delta^{13}C_{CH_4}$ is a measure of the ratio of $^{13}C/^{12}C$ in CH_4 (Nisbet et al., 2016). The source sector of CH_4 can be determined by $\delta^{13}C_{CH_4}$ because ^{13}C is slightly heavier than ^{12}C. Biogenic emissions, such as those from wetlands, agriculture and landfills, have less ^{13}C than emissions

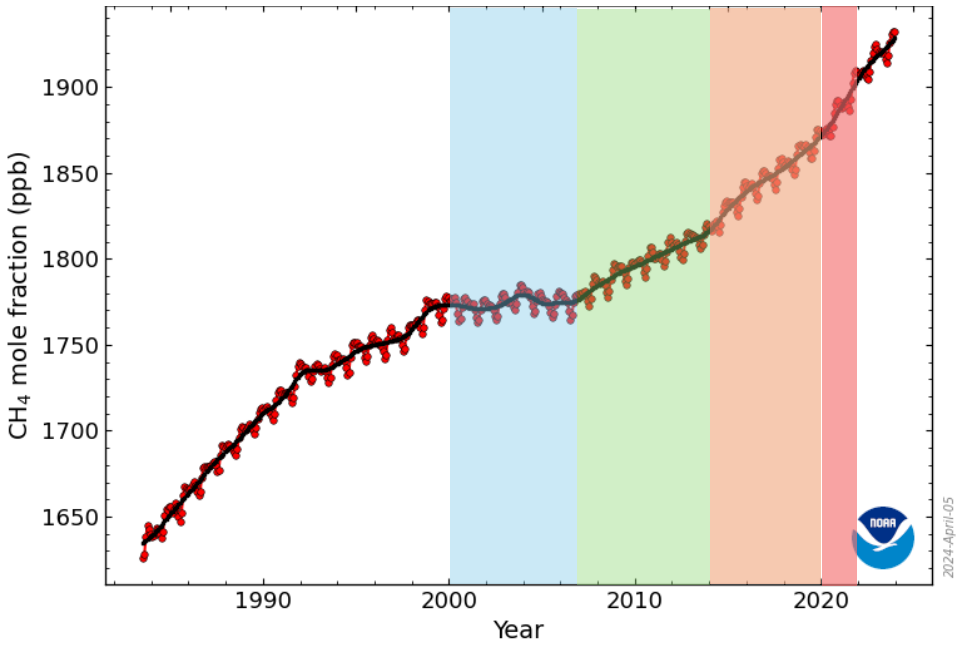

Figure 2.9: Globally averaged, monthly mean atmospheric CH_4 concentrations (red line) and long term trend (black line) from NOAA's Global Monitoring Laboratory. The blue shading highlights the stagnation of growth between 1999-2006. The green shading shows when the growth rate resumed in 2007 and the orange shading shows when the growth rate accelerated in 2014. The red shading shows the large growth rates in 2020 and 2021. Figure adapted from eslr.noaa.gov (NOAA, 2024c)

from fossil fuels, resulting in a more negative $\delta^{13}C_{CH_4}$ from these sources. Nisbet et al. (2016) found that the growth of CH_4 was dominated by biogenic emissions (e.g wetlands or biomass burning), suggesting that CH_4 emissions are responding to sustained changes in precipitation and temperature in the tropics. OH is estimated to have varied by less than 1% globally between 2006-2008 and the isotopic shift to larger biogenic emissions suggests that changes in emissions caused the increase in CH_4 concentrations in 2007. In contrast, Rigby et al. (2017) found a 60-70% probability that a decline in OH contributed to the rise in CH_4 concentrations. These conflicting results add to the complicated picture but McNorton et al. (2018) found that a combination of sources and sinks led to the rise in 2007. They show a decrease in the mean OH concentration and increase in CH_4 emissions from the energy sector over Africa, Middle East, Southern Asia and Oceania and increase in wetland emissions from Eurasia.

Another acceleration of global growth was observed in 2014. Nisbet et al. (2019) found that CH_4 grew by 12.7 ppb in 2014 and observed strong increases in 2015 (10.1 ppb), 2016 (7.0 ppb) and 2017 (7.7 ppb). The study could not be definitive in its conclusions due to lack of observational data. However, they concluded that the rise of CH_4 during 2014-2017 was likely due to a change in biogenic, thermogenic (e.g geological emissions) and pyrogenic sources, especially in the tropics and subtropics, or a decline in OH. These results emphasise the need for increased spatial and temporal observations of CH_4. It was observed that the strong growth of CH_4 coincided with years of exceptional warmth (2014-2016). The temperature dependence of microbial CH_4 emissions suggests that this increased warmth could have contributed to the increase in CH_4. Similarly, biogenic sources could have been responding to increased warmth over Amazonia and increased rainfall over equatorial Africa during the strong El Niño year 2015-2016.

In 2020 and in 2021 NOAA's surface observation network observed the largest annual increases on record (15.15 ppb and 17.92 ppb respectively, Lan et al. (2024)). 2020 was a unique year due to reduced economic activity due to the global pandemic. These large rises in global CH_4 are very recent and still need to be fully investigated but studies have found that natural sources are becoming large contributors to the large increase in global CH_4 concentrations (Wilson et al., 2021; Feng et al., 2022). Feng et al. (2022) used satellite data and atmospheric inversions to investigate CH_4 from 2010-2019 and find that tropical emissions are responsible for 80% of the observed global atmospheric growth rate. The rise in tropical emissions has been linked to large

changes in sea surface temperature in tropical oceans and regional variations in temperature and precipitation over tropical South America and tropical Africa. A study by Lunt et al. (2021) has shown the large role that East Africa has in the global CH_4. Lunt et al. (2021) showed that precipitation anomalies during the short rainy season (October-December) over South Sudan led to CH_4 emissions, equivalent to over a quarter of the growth in global emissions in 2019. The study also highlighted that these precipitation anomalies continued into 2020. The impact of these precipitation anomalies in East Africa is shown by Feng et al. (2023), who concludes that this region is partially responsible for the large rise of CH_4 along with tropical Asia and tropical south America. Feng et al. (2023) finds positive correlations between tropical CH_4 emissions anomalies and ground water, derived from the Gravity Recovery and Climate Experiment Follow-on (GRACE-FO) satellite liquid water equivalent depth, which emphasises the role of wetlands in the global CH_4 budget.

2.5.2 Seasonal Cycle

Section 2.5.1 briefly introduced the seasonal cycle of CH_4 and how it influences the global annual increase of atmospheric CH_4. Emissions of CH_4 from sources such as wetlands vary seasonally with changes in soil moisture content and temperature, and biomass burning emissions vary with wet and dry seasons (Dlugokencky et al., 1997). The main sink of CH_4, the reaction with OH, also varies seasonally as the production of OH is dependent on solar radiation intensity (Lelieveld et al., 2016). Investigating whether the seasonal cycle amplitude and phase of atmospheric CH_4 has a persistent change is important, as it can indicate a change in magnitude or phasing of its sources and sinks. These changes in the seasonal cycle will then be displayed in the global annual trends of CH_4. A study by Dlugokencky et al. (1997) investigated whether the amplitude of the CH_4 seasonal cycle was changing during 1983-1994. They found no significant trend in the seasonal cycle amplitude and suggested that further analysis is needed over a longer time series. Since that study, there has been little to no investigation into long-term changes of the CH_4 seasonal cycle.

2.5.3 Interannual Variations

Global CH_4 concentrations also exhibit IAV within long-term trends, however the exact mechanisms that drive the IAV are not fully understood. Wetland emissions are thought to be a large contributor to the IAV of CH_4 with anomalies driven by ENSO (Zhang et al., 2018). ENSO

was described in Section 2.4.2.3. However, it is not known to what extent the increase in global CH_4 concentrations during ENSO are from wetlands and how much wetlands contribute to the IAV. Zhang et al. (2018) found during the 2015-2016 ENSO that wetlands responded differently during different times within the El Niño phase. For example, wetland emissions decreased in the later stages of El Niño due to higher temperatures and decreased wetland extent. During the 1997-1998 El Niño, Rowlinson et al. (2019) found larger than usual emissions from biomass burning increased the lifetime of CH_4. CO emissions from biomass burning react with OH, the main tropospheric sink for CO and CH_4, reducing the concentration of OH and in turn increasing the lifetime of CH_4. These two studies highlight how the different ENSO years have different factors that influence the IAV of atmospheric CH_4.

2.6 Atmospheric Methane Measurements

Observations are needed to determine the trends in atmospheric CH_4. Atmospheric CH_4 can be measured by a number of different methods. There are advantages and disadvantages to the different observation methods, depending on the source type and spatial and temporal range. The NOAA network, tall tower networks and global monitoring satellites can provide long term observations on the order of days to years. These observations are used to identify changes in global CH_4 concentrations and quantify emissions using inverse modelling. More recently, large point source emissions have been detected by hyperspectral imaging spectrometer satellites, such as the GHGSat satellite constellation. These satellite constellations are able to identify and quantify emissions from large emitters at a metre-scale resolution. This section will describe the key CH_4 observation methods and their spatial and temporal scales. Full details of how observations used in this thesis are taken will be described in Chapter 3.

2.6.1 Surface Observations

NOAA Earth System Research Laboratories (ESRL) provide long-term weekly flask samples of CH_4 from a large number of observation sites across the globe (Dlugokencky et al., 2019). The observations began in 1983 and 36 sites were set up between 1983-1992. The network has now expanded to 90 sites and observations continue to be collected. Figure 2.10 shows the spatial coverage of NOAA's observation sites, with a disproportionate number of sites situated in the Northern Hemisphere compared with the Southern Hemisphere. There is poor spatial coverage,

particularly in the tropics, where the largest natural sources of CH_4 are situated. In addition to poor spatial coverage, not all of these sites have regular observations, limiting the number of sites which can be used for long term studies. Despite this being a valuable record of long term CH_4 observations, other observations are required to fill in the gaps in spatial coverage in order to fully understand global CH_4 and the CH_4 budget.

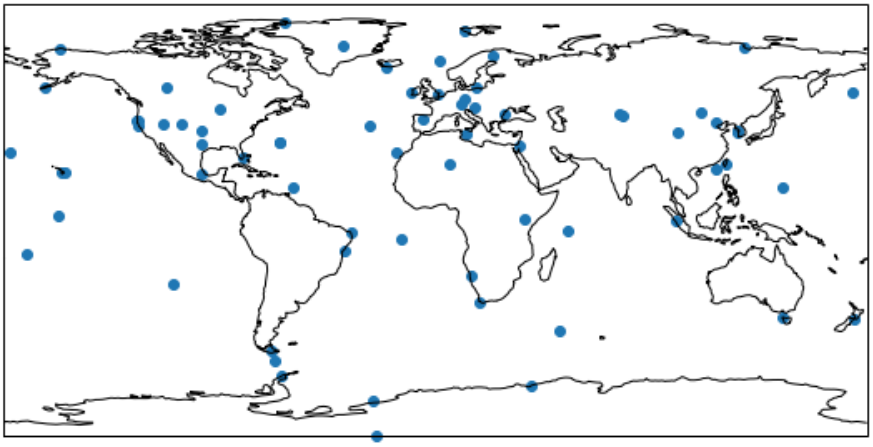

Figure 2.10: A map showing the locations of the current NOAA ESRL CH_4 observation sites, excluding observations taken on cruises (Dlugokencky et al., 2019).

CH_4 is also observed on tall towers, where instruments are placed at different heights along a mast. There are several tall tower networks around the globe. These include the NOAA tall tower network situated in the United States (Andrews et al., 2023), Japan–Russia Siberian Tall Tower Inland Observation Network (JR-STATION) (Sasakawa et al., 2010), the Integrated Carbon Observation System (ICOS) tall tower network over mainland Europe (Couret and Schmidt, 2023) and the UK Deriving Emissions linked to Climate Change (DECC) network (Stanley et al., 2018). Observations from tall towers began in the 1990s as part of national and international campaigns. Tall tower observations provide information on local and regional CH_4 concentrations. This is because the observations are taken at various heights above the surface, capturing a range of CH_4 concentrations over a wider area than surface observations. The measurements taken on tall towers also reduce the complex signal between sources and sinks observed at the surface (Gerbig et al., 2009; Stanley et al., 2018).

Surface based mobile surveys are another method to detect point source emissions of CH_4. This type of survey involves making transects of a plume of CH_4 emitted from a point source. The transects are made using a car with absorption spectrometers onboard. These types of observations provide information on point sources, which can be used to determine the flux

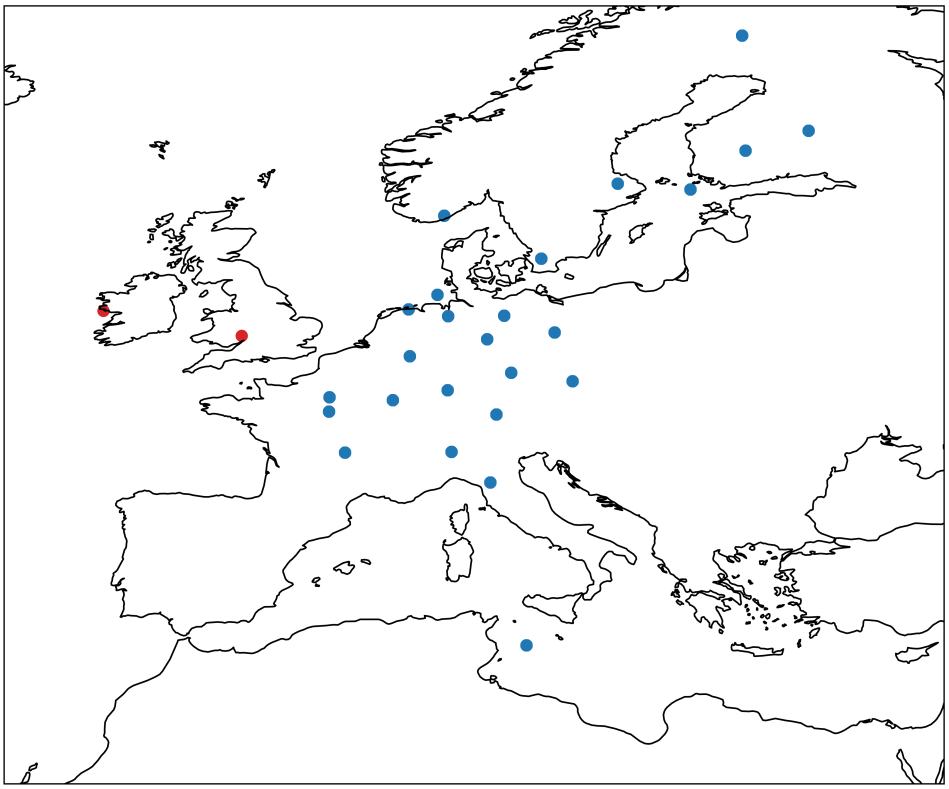

Figure 2.11: A map showing the locations of the tall tower sites from the ICOS network (blue) and UK DECC netowrk (red) used in this thesis.

of the sources. An example of using a surface based mobile survey include quantifying CH_4 from a UK biogas plant (Bakkaloglu et al., 2021). In addition to surface based mobile surveys, unmanned aerial vehicle (UAV)/drone and aircraft surveys can capture CH_4 concentrations over both natural and anthropogenic sources (Shaw et al., 2021; Allen, 2023). Some examples of studies which use UAV or airborne observations include the quantification of net methane fluxes from European Arctic wetlands (Barker et al., 2021) and quantifying methane emissions from a UAV survey of a UK landfill (Yong et al., 2024). In this thesis, a surface-based mobile survey is used to validate satellite derived emission estimates. A description of the instruments used and the survey details can be found in Chapter 3, Section 3.1.1.3 and Chapter 6.

The total column of CH_4 in the atmosphere can also be observed from the surface. The Total Carbon Column Observing Network (TCCON) is one network which provides these observations. It is a network of approximately 18 ground-based Fourier Transform spectrometers which are important for validating satellite observations (Wunch et al., 2011). Figure 2.12 shows the distribution of the TCCON network and the lack of sites in the tropics where large and variable CH_4 sources are situated. The TCCON network has been used to validate GOSAT and

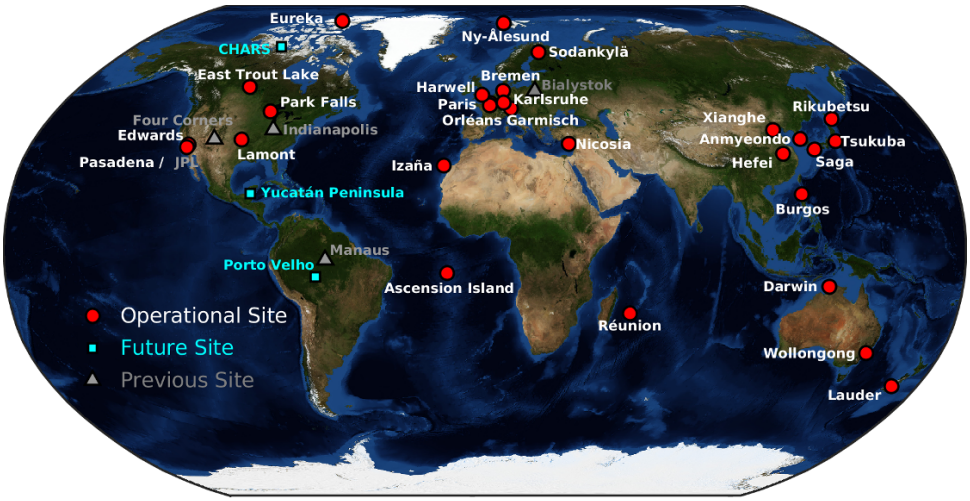

Figure 2.12: A map showing the locations of the TCCON sites. Figure by TCCON (2023).

TROPOMI CH_4 observations. These two satellites are described in Section 2.6.2.

The research in this thesis takes advantage of several surface-based observation types. These include flask, tall tower and surface-based mobile survey measurements. The full details of the surface measurements used in this study can be found in Chapter 3. These observations provide information from long term changes in global CH_4 to temporary point sources of CH_4. However, the spatial and temporal coverage of these observations are variable depending on whether global trends or point sources are being investigated.

2.6.2 Satellite Measurements

Satellite observations have the capacity to obtain global coverage of atmospheric CH_4. The different satellites which measure CH_4 are summarised in Table 2.2. There are advantages and disadvantages to observing CH_4 via satellite when compared to surface observations. Observing CH_4 by satellite provides global coverage at a higher spatial resolution than surface observations but the temporal resolution can vary at particular locations, depending on the satellite repeat time and cloud coverage during the overpass. The satellite era does not extend as far back in time as the surface flask observations and the mission lifetime can limit long term observations. However, some satellite missions exceed their mission lifetimes. For example, GOSAT which had a planned mission lifetime of 5 years has been collecting data for 15 years. Satellites which retrieve CH_4 rely on the reflected sunlight from the Earth's surface to make measurements. This means that measurements can only be taken during the day, and it can be challenging to retrieve measurements over the ocean due the surface reflectivity. Instruments onboard these

satellites focus on the shortwave infrared (SWIR) where the vertical sensitivity of the measurement is evenly distributed throughout the troposphere, providing good sensitivity towards the surface, where CH_4 is emitted. The sensitivity of the retrieval as a function of altitude is called an averaging kernel. Satellite observations are also sensitive to cloud cover in the retrieval (e.g full cloud cover, partial cloud cover or high cirrus clouds). Systematic errors can arise from inaccurate spectroscopic data used in the retrieval to obtain total column average CH_4 and instrument degradation over time (Jacob et al., 2016). Satellite observations provide extra spatial and temporal coverage that NOAA's surface observations do not have and provide an aerial view of global CH_4. These observations are invaluable for investigating changes in atmospheric CH_4, particularly in areas that are difficult to observe from the surface but they do have some limitations. For example, extensive cloud coverage over Amazonia, an area which emits approximately 49 Tg yr^{-1}, makes it very difficult for satellites to observe in this region (Wilson et al., 2021).

CH_4 has been observed from space by satellites since 2003 and these instruments provide global observations of CH_4 concentrations. The first satellite that retrieved CH_4 was SCIAMACHY, which provided data between 2003 and 2012 with a pixel size of 30 km $\times$ 60 km, giving full global coverage every 6 days (Frankenberg et al., 2005). Inaccuracies in the water vapour spectroscopy led to SCIAMACHY's retrieval substantially overestimating CH_4 over scenes containing large amounts of water vapour (Frankenberg et al., 2008). GOSAT has been providing observations since 2009 with a pixel size of 10 km in diameter and global coverage every 3 days, improving on the spatial and temporal resolution of SCIAMACHY and with a lower bias (Parker et al., 2011). Despite SCIAMACHY having large systematic biases, the observations provided by the instrument and GOSAT have improved our understanding of atmospheric CH_4, particularly over the tropics (Frankenberg et al., 2011; Parker et al., 2018).

On 13^{th} October 2017 TROPOMI was launched on Sentinel 5P in a Sun-synchronous orbit and with an expected mission lifetime of 7 years. TROPOMI has a ground pixel of 3.5/7 km $\times$ 7 km at sub-satellite point (Hu et al., 2018). TROPOMI initially measured CH_4 with a ground pixel of 7 km $\times$ 7 km but was upgraded to 5.5 km $\times$ 7 km in 2019 (Hu et al., 2018; Lorente et al., 2021). It provides daily, near full surface coverage of CH_4 observations, which is a significant improvement on the previous satellite, GOSAT (see Figure 2.13). Further details on TROPOMI can be found in Chapter 3.

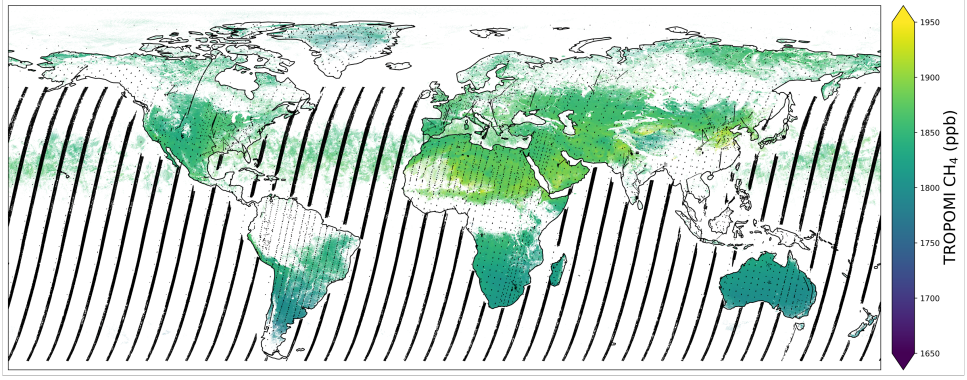

Figure 2.13: Difference in spatial coverage between TROPOMI (colour map) and GOSAT (black) satellite observations averaged over June 2020 (Parker et al., 2011; Schneising et al., 2023).

In addition to global monitoring satellites, which measure CH_4 on the kilometre-scale, there are satellites which can measure large point sources of CH_4 on the metre-scale. These include Landsat-8, WorldView-3, Sentinel-2, GHGSat, PRISMA, EnMAP and EMIT. Of these, the GHGSat satellite constellation of 10 SmallSats (satellites $<$ 180 kg) has the second highest spatial resolution and lowest detection threshold after WorldView-3. GHGSat has a spatial resolution of 25 m $\times$ 25 m and a detection threshold of 100 kg h^{-1} (Jervis et al., 2021). The spatial resolution of GHGSat means it can detect CH_4 emissions at specific facilities, although the satellite needs to be tasked to detect CH_4 over specific locations. The GHGSat constellation has a repeat observation time of approximately 1-2 days and more satellites are being launched meaning that the repeat time will likely improve in the future. Observations on this scale have only been available in recent years and an open question remains as to how this information can be optimally fed into atmospheric inversions and emission inventories.

Table 2.2 gives a summary of the satellites currently in orbit and their spatial and temporal resolutions. There are a range of satellites which measure CH_4 across different spatial and temporal scales, capturing the breadth of CH_4 sources. In this study I take advantage of the spatial resolution of TROPOMI when testing a newly developed nested grid model for TOMCAT (see Chapter 5). The GHGSat constellation is also used to monitor a point source of CH_4 in the UK (see Chapter 6). These studies capture local and regional changes over different timescales by taking advantage of different satellite platforms. Chapter 3 provides further details on how CH_4 is observed through the different observation types used in this study.

Table 2.2: Current satellite instruments which observe atmospheric CH_4 and their detection limits if they are able to observe point sources of CH_4. This table has been adapted from Jacob et al. (2022).

Satellite	Pixel Size	Return Time (days)	Mission Years	Detection Limit (kg h^{-1})	References
Area flux mappers					
SCIAMACHY	30 km × 60 km	6	2003 - 2012	-	Frankenberg et al. (2005)
GOSAT	10 km diameter	3	2009 - present	-	Parker et al. (2011)
Sentinel-5P/TROPOMI	3.5/7 km × 7 km	1	2014 - present	25 000	Lorente et al. (2021), Lauvaux et al. (2022)
Point source imagers					
Landsat-8	30 m × 30 m	16	2013 - present	1800-25000	Varon et al. (2021), Ehret et al. (2022)
WorldView-3	3.7 m × 3.7 m	< 1	2014 - present	< 100	Sánchez-García et al. (2022)
Sentinel-2	20 m × 20 m	2-5	2015 - present	1800-25000	Varon et al. (2021), Ehret et al. (2022)
GHGSat	25 m × 25 m	1-7	2016 - present	100	Jervis et al. (2021)
PRISMA	30 m × 30 m	4	2019 - present	500-2000	Guanter et al. (2021)
EnMAP	30 m × 30 m	4	2022 - present	-	Cusworth et al. (2019)
EMIT	60 m × 60 m	9	2022 - present	-	Cusworth et al. (2019)

2.7 Modelling Methane

2.7.1 Forward Modelling

There are a wide range of methods to investigate global trends in atmospheric CH_4. It is not possible to observe CH_4 continuously and with full global coverage. Therefore, a large number of studies use chemical transport modelling to determine what could be driving trends in CH_4. Chemical transport models which simulate atmospheric constituents and their concentrations consider four main processes: emissions, chemistry, transport and deposition. Atmospheric transport (described in Section 2.2.2) in the model, such as advection and convection, are parameterised because these processes happen on a smaller spatial scale compared to the model grid. There are two types of model, Lagrangian models and Eulerian models.

Chemical transport models are generally Eulerian and some examples include GEOS-Chem, TM5 and TOMCAT (Bey et al., 2001; Huijnen et al., 2010; Chipperfield, 2006). They are driven by meteorological reanalysis, which facilitates comparison with satellite data. GEOS-Chem's global configuration is generally run at a resolution 4°× 5° or 2°× 2.5° and is forced by Goddard Earth Observing System (GEOS) at the NASA Global Modeling Assimilation Office (GMAO) (Philip et al., 2016). TM5 has a resolution of 6°× 4° or 3°× 2° and is forced by the European Centre for Medium-Range Weather Forecasts (ECMWF) reanalyses, such as ERA5 (Hersbach et al., 2020). Similarly, TOMCAT can be run at a horizontal resolution of 5.6°× 5.6° up to ∼1.125°× 1.125° and uses meteorology from ECMWF. All of these models are generally

run at a coarser resolution than the horizontal resolution of their associated meteorology. This is because modelling chemical species at high resolution on a global scale is computationally expensive. However, with the improvements in resolution of satellite data on the <10 km to metre-scale, the model resolution is often too coarse to enable effective comparisons between the model and the observations. For example the highest horizontal resolution of TOMCAT is $\sim 1.125° \times 1.125°$, which is approximately 100 km × 100 km at the equator. This resolution is too coarse to capture the spatial detail and changes in atmospheric CH_4 observed by high-resolution satellite observations, such as TROPOMI.

In order to investigate areas of interest at higher resolution, and at a lower computational cost, a nested grid can be used within a Eulerian model. With a nested grid the area of interest is simulated at a high resolution, often surrounded by a region of intermediate resolution, but the rest of the world is simulated at a lower resolution. A nested grid is advantageous for analysing CH_4 at local scales since observations at a higher resolution are being provided by global monitoring satellites (see Section 2.6.2). There are two types of nested grid, one-way or two-way, which have already been included in other CTMs for example in GEOS-Chem and TM5 (Wang et al., 2004; Huijnen et al., 2010).

In a one-way nested grid the information from the coarse grid is fed into the higher resolution grid, without information flowing in the other direction. Wang et al. (2004) developed a one-way nested grid for GEOS-Chem to investigate CO over Asia. The results from the coarse model simulation were used to define the boundary conditions for the nested grid. The boundary conditions are set in a buffer zone, which separates the high and low resolution areas of the model. Wang et al. (2004) found that the nested grid model was in good agreement with observations of CO and captures more detail of the variability of CO shown by observations when compared with the coarser model.

A two-way nested grid model allows information to be communicated from the coarser grid to the higher resolution grid and vise versa. Krol et al. (2005) developed a two-way nested chemical-transport for the CTM Tracer Model 5 (TM5). In one-way nesting it is possible for loss of information to occur during the exchange of tracer mass between the coarser model and nested grid boundary. The two-way model avoids this loss due to calculations being done "online" (e.g. transport and chemistry occurs at the same time in each model grid). Krol et al. (2005) developed several predefined nested regions over Europe, North America, Africa and Asia

in order to cover global hot spots of atmospheric chemistry. Krol et al. (2005) defined these regions as areas with high emission rates of ozone precursors (e.g Nitrogen dioxide (NO_2)). The study showed that the nested grid model cells were more representative of local observations. Peters et al. (2004) also evaluated the TM5 nested grid and found that it performs well in global and regional transport and can output signals seen in CO_2. However the model produces biases in the vertical mixing scheme where it fails to distribute surface mixing ratios fast enough and it overestimates the meridional gradient, meaning further development and validation of this model is needed.

These studies show that nested grid models are beneficial when modelling chemical species because they produce more representative results, when compared with observations. In this study, a nested grid for TOMCAT has been developed to investigate the changes in CH_4 over Europe, see Chapter 3 for the full TOMCAT model description and Chapter 5 for details on the nested grid model: ZOOMCAT.

In addition to Eulerian chemical transport models, there are also Lagrangian atmospheric dispersion models. An example of a Lagrangian dispersion model is the UK Met Office's Numerical Atmospheric Dispersion Modelling Environment (NAME). NAME simulates the transport and dispersion of chemical species through the atmosphere (Jones et al., 2007). The model was originally developed as a nuclear accident model in response to Chernobyl nuclear disaster and is now used in a number of applications such as routine forecasting applications, scientific research and policy support work. The model is predominantly used at the Met Office for operational purposes but has been used in scientific reports and studies such as Kendall et al. (2019) and Heard et al. (2012). It is driven by the Met Office's Numerical Weather Prediction (NWP) meteorology from the 1.5 km $\times$ 1.5 km resolution UKV model (Davies et al., 2005; Bush et al., 2023). Due to the Lagrangian nature of the model, NAME has the flexibility to alter the domain and resolution of the model. The combination of high-resolution UKV meteorology and NAME's horizontal resolution means that it can simulate point sources of CH_4 observed by point source imaging satellites such as GHGSat. In this study NAME is used to estimate emissions of a point source of CH_4 observed by GHGSat and validate satellite derived emission estimates. Full details of the NAME model can be found in Chapter 3 and details of the study can be found in Chapter 6.

2.7.2 Inverse Modelling

Forward modelling of atmospheric CH_4 is an important tool for investigating change in global trends. In order to represent the chemical composition of the atmosphere in a model, such as TOMCAT, the model inputs such as meteorology, chemical reaction rates and emissions of species need to be accurate. However, there are uncertainties around the spatial and temporal variation of surface fluxes of trace gases, such as CH_4.

Inverse modelling combines chemical transport modelling and data assimilation techniques to provide optimised emissions estimates. This technique has been used in a number of studies to investigate variations of atmospheric CH_4. For example, Bousquet et al. (2011) used inverse modelling to investigate CH_4 variability between 2006-2008. This study found tropical and temperate latitudes to be dominant drivers of the observed CH_4 increase in this period, despite the limited observations in the tropics to constrain the model (Bousquet et al., 2011; Houweling et al., 2017). Inversions using satellite data have also confirmed and emphasised the importance of tropical emissions in the CH_4 budget (Wilson et al., 2021; Houweling et al., 2017).

There are a number of inverse modelling techniques. In this study four-dimensional variational (4D-Var) techniques are used in order to deal with the large amount of data available from satellite observations (Houweling et al., 2017). Chapter 3 provides a brief introduction on inverse modelling theory and a full description of the inverse model used in this study.

2.8 Methane Across Different Spatial and Temporal Scales

This chapter has described the CH_4 budget and the recent global trends of atmospheric CH_4. To understand what is driving the recent global trends, changes in the sources and sinks of CH_4 need to be identified. As described in Section 2.4.3, it is difficult to directly observe the main sink of CH_4, OH, and this therefore contributes a large uncertainty to the CH_4 budget. However, there are several methods (described in Section 2.6), which can measure atmospheric CH_4. These observations, combined with computer models, mean it is possible to attribute changes in atmospheric CH_4 to different regions and even source type.

Long term surface observations are limited in their global distribution, particularly around the tropics where there are large and variable natural sources of CH_4. However, satellites have the ability to detect large area sources down to temporary super-emitters and can provide

global coverage of CH_4 concentrations. These observations are valuable in consolidating the CH_4 budget, together with computer models to fill in the gaps between observations across the different spatial and temporal scales.

In this study, I have taken advantage of both observations and models to investigate changes in CH_4 across different spatial and temporal scales. Long term surface observations and a global chemical transport model are used to investigate changes in the seasonal cycle of CH_4. I have developed a nested grid model for TOMCAT to compare with satellite data over regional scales. Finally, I have validated satellite derived emission estimates of a large point source using observations and models on metre-scales.

Chapter 3

Datasets and Models

This chapter provides an overview of the key datasets and models used in this thesis. The chapter begins by describing the different observations (Section 3.1) used in this thesis and then goes on to describe the models (Section 3.2) and associated emission inventories (Section 3.3) used to simulate CH_4.

3.1 Observations

In this thesis I take advantage of several different types of observations to investigate changes in atmospheric CH_4, all which have been briefly introduced in Chapter 2. This section will describe how the different measurements are made and comment on their strengths and weaknesses. The surface flask observations provided by NOAA are used in Chapter 4 and the UK DECC network and mobile surveys are used in Chapter 6. I also use satellite data from TROPOMI in Chapter 5 and GHGSat satellite observations in Chapter 6. Further details on how these observations are used in each study are documented in the result sections of Chapters 4-6.

3.1.1 Surface-Based Observations

3.1.1.1 NOAA Network

The NOAA surface network includes observations from fixed sites and measurements taken on board ships in the Pacific Ocean (Dlugokencky et al., 2019). In this thesis, only observations from fixed sites between 1983-2020 are used. Fixed sites are selected because the sampling location and conditions (e.g local orography) are consistent.

The observations are collected approximately weekly in glass flasks. Samples are then sent for analysis at the NOAA GML by gas chromatography with flame ionisation or by Cavity Ring-Down spectroscopy (CRDS). Measurements taken between 1983-2019 use the gas chromatography method, where aliquots of sample and standard gas are injected into a gas chromatograph and the CH_4 is separated out from other species by using packed columns and then detected by flame ionisation. In 1991, changes to the analysis procedure were made which improved the repeatability of the measurements from 3 ppb to 1-2 ppb (Dlugokencky et al., 2019). In 2019 the analysis method was changed to CRDS. This method determines the concentration of a species by passing pulses of light through the sample and determining its rate of absorption (Berden et al., 2000). This method has improved the repeatability of the measurement to approximately 0.2 ppb. The spatial and temporal resolution of the NOAA surface network is described in Chapter 2, Section 2.6.1. The NOAA network has been used in a wide range of studies (e.g Dlugokencky et al., 1997; McNorton et al., 2018; Nisbet et al., 2019)

3.1.1.2 UK DECC Network

The UK DECC network measures CH_4 at up to six sites, including four on tall towers, across the UK and Ireland. The location of the sites used in this study are shown in Chapter 2, Figure 2.11. At these sites CH_4 is measured by CRDS at different inlet heights. The heights of the inlets vary at each site, ranging from 45-222 m above ground level (a.g.l.). The instrument is calibrated using both a standard of approximately ambient mole fraction and a set of calibration standards which range above and below ambient mole fractions (Stanley et al., 2018). The calibrant and standard gases used in the CRDS at all sites are of natural composition. The standard gas is measured daily to assess linear instrumental drift. The instrument has a repeatability of 0.3 ppb (Stanley et al., 2018). The UK DEEC network also measures other atmsopheric constituents and has been used in studies to verify bottom-up estimates of UK CH_4 emissions (Stanley et al., 2018) and monitoring of hydrofluorocarbons in the UK (Manning et al., 2021).

The DECC Network sites used in this study are Mace Head (MHD) on the west coast of Ireland and Ridge Hill (RGL) in central-western England, with observations taken between March 2022 and June 2023. At MHD the inlet is located at 10 m a.g.l. with measurements taken every 20 minutes using Gas Chromatography Flame Ionisation (GC-FID). CRDS data at MHD are also available through the ICOS network. At RGL the inlets are located at 45 and 90 m a.g.l. with measurements reported every minute (Stanley et al., 2018) using a CRDS. Full details of each

observation site used in this study can be found in Chapter 6.

3.1.1.3 Mobile Surveys

Mobile surveys can be used to observe and estimate emissions from point sources of CH_4. In this study I collaborated with Royal Holloway, University of London to carry out a ground-based mobile survey in May and June 2023, to verify satellite observations of CH_4. The mobile laboratory is on board a hybrid car and contains a suite of cavity-enhanced laser absorption spectrometers. These instruments can measure CH_4, CO_2, ethane (C_2H_6) and CH_4 isotopes (δ^{13}C-CH_4). The instruments include: Picarro G2311-f (10 Hz CH_4 and CO_2), LI-COR LI-7810 (1 Hz CH_4 and CO_2), LGR UMEA, i.e. Ultraportable Methane/Ethane Analyser (1 Hz CH_4 and C_2H_6), and Picarro G2210-i (1 Hz CH_4, CO_2, C_2H_6 100 and δ^{13}C-CH_4). Air is pumped to the instruments from inlets on the roof of the vehicle, next to the inlets are a sonic anemometer (Campbell CSAT3B 3-D) and a GPS receiver.

There is also another inlet which is connected to a diaphragm pump to fill 3 L foil bags with air which can later be analysed by isotope ratio mass spectrometry (Fisher et al., 2006). Royal Holloway have conducted a number of surveys which have been used to investigate point sources of CH_4 (e.g. Lowry et al., 2020; Bakkaloglu et al., 2021). Full details of how the mobile survey was carried out to generate the data for use in this thesis can be found in Chapter 6.

3.1.2 Satellite Datasets

This thesis also takes advantage of satellite retrievals of CH_4 to investigate changes in concentrations on a global and point-source scale. TROPOMI and GHGSat satellite retrievals are described in the following sections.

3.1.2.1 TROPOMI

TROPOMI, onboard Sentinel-5P, is the main global satellite dataset used in this thesis. It improves on the spatial and temporal resolution of GOSAT, providing higher detail on regional and point sources. TROPOMI provides near-global coverage of CH_4 every day with limitations over water, cloudy locations and high-latitudes (Hu et al., 2018; Lorente et al., 2022). It has two spectrometer modules where the first uses ultraviolet (UV), visible and NIR spectral bands and the second contains SWIR spectral bands around 2.3μm (Hu et al., 2018). A small fraction

(4.4%) of light in the detection contains stray light and this can be corrected for, according to Tol et al. (2018).

There are two main retrieval algorithm groups who extract CH_4 column data from TROPOMI. The first one is Netherlands Institute for Space Research (SRON) which uses a full-physics retrieval method and the second is the University of Bremen which uses a Weighting Function Modified Differential Optical Absorption Spectroscopy (WFM-DOAS) algorithm. The following paragraphs will give a brief description of each method.

The retrieval algorithm by SRON determines concentrations of CH_4 by retrieving the reflected radiances of the absorption of solar light by CH_4. In order to get an accurate retrieval, the light path through the atmosphere needs to be known. However, scattering by cirrus clouds and aerosols can modify the light path, leading to retrieval errors. The full-physics method is used to minimise the errors in the light path by simultaneously retrieving CH_4 column concentrations and the scattering properties of the atmosphere (Hu et al., 2018). The fitted parameters are the partial CH_4 column in 12 atmospheric layers, the total columns of water vapour and CO, two scattering parameters, surface albedo and wavelength shifts in Earth radiance and solar irradiance spectra (Hu et al., 2018). The molecular absorption features are calculated using spectroscopic databases for CO and CH_4. The mean bias between TROPOMI and GOSAT is 13.6 ppb and the standard deviation is 19.6 ppb. These differences could be attributed GOSAT's latitudinally-varying bias, with a negative bias in southerly latitudes when compared with observations (Hu et al., 2018; Parker et al., 2011). Hu et al. (2018) also finds TROPOMI observations are lower than GOSAT over the tropics and this could be due to errors in water vapour spectroscopy in TROPOMI's 2.3 μm region. This is because the spectroscopy in the 2.3 μm region is not as well established as the 1.6 μm region used in GOSAT.

Further work has been done by Lorente et al. (2021) to improve the SRON retrieval algorithm for CH_4 observations from TROPOMI. The improved TROPOMI retrieval algorithm show good agreement with TCCON (-3.4 $\pm$ 5.6 ppb) which is within the mission requirements of a precision and accuracy of 1% (Lorente et al., 2021; Lorente et al., 2023). However, there are some larger differences with GOSAT (-10.3 $\pm$ 6.8 ppb, (Lorente et al., 2021)). Lorente et al. (2023) also corrected artefacts found in the retrievals caused by spectral features of surfaces such as carbonated rocks, leading to false anomalies of up to 20-30 ppb. The most challenging areas for the retrieval algorithm are scenes with low and high albedo, although

the a posteriori correction accounts for most of the bias. TROPOMI also overestimates XCH_4 in snow-covered scenes (Lorente et al., 2021). Further investigation is needed to understand whether it is the instrument or retrieval algorithm which is contributing to the biases in high and low albedo areas. However, lack of data in high albedo scenes and observation sites in the southern hemisphere hinder this.

The second retrieval algorithm was developed by Schneising et al. (2019) at the University of Bremen using a WFM-DOAS algorithm. This algorithm uses a linear least-squares method which is based on fitting the logarithm of a linearised radiative transfer model and a low-order polynomial to the logarithm of the ratio of nadir radiance and solar irridiance spectrum (observed sun-normalised radiance; Buchwitz et al. (2006)). The linearised radiative transport model includes the components of the vertical columns of all trace gases which have absorption lines in the select spectral fitting window (Buchwitz et al., 2006). The radiative transfer model used for retrieving CH_4 by Schneising et al. (2019) is SCIATRAN. The retrieval algorithm also uses a machine learning-based data quality filter which is based on a random forest classifier to reduce any remaining systematic errors. A random forest classifier is made up of multiple decision trees which use randomness to create an uncorrelated forest of decision trees to obtain a single result (Schneising et al., 2019). In this case decision trees are trained on variables which are related to surface albedo variations (e.g apparent albedo and solar zenith angle). The training data set also contains measurements based on cloud information from the Visible Infrared Imaging Radiometer suite (VIIRS) on Suomi NPP. An additional filter is applied to retrievals which deviate relative to a climatological value, they are are then adjusted with an accumulative increase based on globally averaged NOAA surface measurements of CH_4 until the time of measurement. Schneising et al. (2019) also found a systemic albedo dependence where there is an underestimation of CH_4 over dark surfaces and have added a correction for this using a shallow machine learning method on the systematic errors caused by surface albedo.

The Bremen algorithm has better coverage of retrieved CH_4 than the SRON algorithm and when compared with TCCON observations it has a higher correlation of 0.91 for CH_4. A study by Hachmeister et al. (2022) highlights features that appear in CH_4 concentrations from both retrieval algorithms around coastal regions, with biases around $\pm$ 50-100 ppb. Hachmeister et al. (2022) found the features are more pronounced in the operational retrieval algorithm and correlate with differences in the digital elevation model (DEM) used. This study highlights

the importance of having the most up-to-date DEM in the TROPOMI retrieval algorithms to remove any bias caused by topography, as a result, the SRON and University of Bremen algorithms have updated their DEMs.

In this thesis, Chapter 5 uses the University of Bremen WFM-DOAS v1.8 algorithm because it provides better spatial coverage than the SRON retrieval algorithm.

3.1.2.2 GHGSat

Chapter 6 uses GHGSat enhanced CH_4 retrievals and satellite-derived emissions estimates to quantify a gas leak in the UK. GHGSat is a constellation of SmallSats in low Earth orbit at approximately 500 km in altitude. Each satellite has a wide angle Fabry-Pérot imaging spectrometer with sensitivity in the SWIR (1630-1675 nm) onboard. The instrument retrieves the vertical column density of CH_4 and detects concentration enhancements above background at targeted locations. CH_4 absorption lines are resolved for each pixel in a 12 km $\times$ 12 km field of view with a spatial resolution of 25 m and a spectral resolution of 0.3 nm. The satellites have a detection limit of 100 kg h^{-1} (50% probability at a wind speed of 3 ms^{-1}) and the images are processed through GHGSat's proprietary toolchain.

The satellite constellation has been tested through controlled releases of CH_4. This is when a source is released at a specified rate and the satellite measures the source, with an estimated release rate being determined from the observations. Sherwin et al. (2023) conducted single-blind validation tests with a variety of satellites, including GHGSat. GHGSat performed well and detected an emission rate of 3800 kg h^{-1} for a source released at 4000 kg h^{-1}. GHGSat also detected the smallest release in the study at 197 [187,208] kg h^{-1} for a source released at 200 kg h^{-1}. GHGSat has also been tested over a mixture of surface types and was found to have a column precision of $\sim$2% of background CH_4 column density (MacLean et al., 2024; Jacob et al., 2022). Chapter 6 contains the full details of how GHGSat was used to quantify and validate a point source of CH_4 in the UK.

3.2 Atmospheric Modelling

This section describes the chemical transport models used in this thesis.

3.2.1 TOMCAT Model Description

TOMCAT is a Eulerian three-dimensional (3D) chemical transport model (CTM) and was first described by Chipperfield et al. (1993). It was created in the early 1990s to study the polar stratosphere. TOMCAT was originally two separate models known as TOMCAT and SLIMCAT, which were used for modelling the troposphere and stratosphere respectively, but were later combined into one model and named TOMCAT (Chipperfield, 2006). The model has been used and validated in a number of studies, including studies of atmospheric CH_4 (e.g. McNorton et al., 2018; Wilson et al., 2021). The model contains separate atmospheric transport and chemistry schemes which are run sequentially (i.e. "process split"). These schemes include advection, convection, boundary layer mixing and chemistry schemes. The individual schemes are described in the following sections. The model meteorology, such as horizontal wind, temperature and surface pressure, are from reanalyses from the European Centre for Medium Range Weather Forecasts (ECMWF) (Hersbach et al., 2020). In this thesis I use ECMWF's ERA5 reanalysis which has a $\sim 0.25° \times 0.25°$ horizontal resolution and 137 model levels up to 1 hPa (Hersbach et al., 2020). For TOMCAT, the ECMWF meteorology is processed onto a coarser horizontal resolution and 6-hourly time resolution due to storage capacity.

3.2.1.1 Model Grid

The TOMCAT horizontal grid is a variable Gaussian grid with regular longitudinal spacing, although the latitudinal spacing can be irregular. There are no restrictions on the latitudinal spacing and a regular or irregular grid can be chosen. In practice, almost all model simulations use the common Gaussian grids associated with spectral resolutions because of spectral models such as ECMWF. The model grids in this study vary between T21 ($\sim 5.6° \times 5.6°$) and T106 ($\sim 1.125° \times 1.125°$). The meteorology from ECMWF is read in every 6 hours as spectral coefficients and converted to grid-point fields by a spectral transform using associated Legendre functions. The vertical grid follows a hybrid σ-p vertical coordinate system, like many general circulation models (GCMs). The model levels near the surface follow the terrain, i.e. σ levels. At higher altitudes, typically above 10 hPa, the model follows pure pressure levels. The pressure, $p_{(k)}$, of a model grid-box interface is given by

$$p_k = A_k p_0 + B_k p_s \tag{3.1}$$

where p_s is the surface pressure and p_0 is a reference pressure. The version of the model used in this study has 60 vertical levels, up to 0.1 hPa.

3.2.1.2 Advection Scheme

CTMs have to parameterise the mass continuity equation (see Chapter 2, Section 2.2.2) in order to reproduce the advection of tracers in the model. The parameterisation should maintain mass conservation, monotonicity and keep numerical diffusion and dispersion to a minimum. However, no advection scheme is able to satisfy all of these properties. There are two advection schemes which can be used in TOMCAT. The first scheme is described by Prather (1986) and the second is a semi-Langrangian scheme based on the method of Williamson and Rasch (1989). Zonal, meridional and vertical directions are represented by X,Y and Z respectively in this section of text. The scheme described by Prather (1986) is predominantly used in TOMCAT and conserves second-order moments (SOM) of the tracer fields. SOM represent the rate of change of the gradient in all possible directions (XX, XY, XZ, YY, YZ, ZZ) within in a grid cell.

The Prather scheme acts separately for the X, Y and Z directions and conserves total tracer mass (zeroth-order moment, ZOM), FOM and SOM. This scheme conserves mass and produces low numerical diffusion but is not monotonic. It also provides an order of magnitude reduction in the diffusion and absolute error with small additional costs in computation than the FOM method (Prather, 1986). Also it was found that the effective doubling of resolution obtained by conservation of the SOM can be achieved at a lower computational cost than by increasing the number of grid boxes (Prather, 1986).

The vertical advection in TOMCAT is determined from the divergence of horizontal mass fluxes. This maintains continuity and removes the need for interpolation onto the model vertical grid. This may lead to differences between the grid box mass calculated by the model and those produced by the reanalyses pressure at each meteorological time step. The tracer mixing ratio is preserved by rescaling the total grid box mass each time the meteorology is read into the model and the tracer mass in each grid box is scaled according to the difference between the tracer mass calculated by divergence and tracer mass calculated from the reanalyses surface pressure.

The model needs to satisfy the Courant-Friedrichs-Lewy (CFL) stability conditions:

$$\Delta t \frac{u_i}{\Delta x_i} \leq 1, \qquad 1 \leq i \leq 3 \tag{3.2}$$

where u_i is the wind speed in the i^{th} dimension, x_i is the grid box length in the i^{th} dimension and Δt is the dynamical time step. The CFL condition requires the model time step to be small enough so that the mass of the modelled constituent does not propagate through the model grid too quickly, ensuring the stability of the model simulation. For example, the advection scheme will not produce realistic results if CFL condition is not satisfied. The model dynamical time step is chosen to satisfy the CFL condition and varies depending on the model grid resolution. This ensures that the numerical model remains stable throughout the simulation. In Chapter 4, the overall TOMCAT time step is 1 hour (divided into subtimesteps for different processes) and 15 minutes in Chapter 5.

The CFL condition is difficult to satisfy towards the poles due to the decreasing size of the model-grid boxes in the east-west direction. For a stable advection at the poles, a very small time step would be required to satisfy the CFL stability conditions. In order to avoid reducing the time step to meet the conditions at high latitudes, multiple adjacent grid boxes are grouped together in the same latitude band only during the east-west advection. The number of grid boxes that are grouped together depends on the latitude, horizontal and temporal resolution, and the maximum wind speed which is set to 220 ms^{-1}. After the east-west advection has taken place, the standard grid boxes are reformed.

3.2.1.3 Convection Scheme

TOMCAT has to parameterise atmospheric convection as a sub-gridscale process. The online moist convection scheme in TOMCAT is described by Stockwell and Chipperfield (1999), which is based on the widely-used scheme developed by Tiedtke (1989). The convection scheme follows Tiedtke (1989) but with two differences. It includes cumulus updrafts in the vertical direction and turbulent and organised entrainment and detrainment. However, the mid-level convection and convective downdrafts are not included in TOMCAT and there is no organised entrainment of environmental air above the cloud base. A drawback with this scheme is that TOMCAT is attempting to diagnose the occurrence of convection from meteorological fields which have already been stabilised by the effects of convection in the ECMWF reanalyses (Feng et al., 2011). Also, TOMCAT is diagnosing the convection at the relatively coarse resolution of the

CTM experiment.

TOMCAT has an alternative convection scheme which uses archived mass fluxes from ECMWF reanalyses. The updraft/downdraft detrainment rate and updraft/downdraft flux are retrieved from ECMWF Meteorological Archival Retrieval System at a $1° \times 1°$ resolution, with 137 vertical levels for ERA5. The archived mass fluxes are stored at a lower resolution than ECMWF to minimise use of local storage. The model updraft/downdraft entrainment/detrainment mass flux is recalculated every six hours to match the meteorological forcing (Feng et al., 2011). These fluxes are used in the model's convective transport scheme instead of those derived in the Tiedtke scheme. This scheme therefore overcomes the problems of the "online" scheme described above. Moreover the transport in the model is more consistent with ECMWF meteorological forcing, although it does require additional forcing data to be available. Feng et al. (2011) found that generally the Tiedtke scheme underestimates the convective mass flux compared to the ECMWF archived files, however the model simulation fails to capture strong convection transport up to 100 hPa as seen in the ECMWF archived mass fluxes. Overall, this is a challenge for CTMs and GCMs and Tost et al. (2010) found that GCMs using different cumulus convective schemes cannot reproduce the strong convective transport. Despite TOMCAT struggling to capture strong convection transport, making the model consistent with the meteorological fields will be beneficial for future versions of TOMCAT, and for developing the nested grid model, as it will be able to take advantage of higher spatial resolution of the meteorological data and archived mass fluxes.

Both convection schemes have been used in this thesis. The TOMCAT convection scheme by Stockwell and Chipperfield (1999) is used in Chapter 4 and the archived mass fluxes are used in Chapter 5.

3.2.1.4 Planetary Boundary Layer Schemes

There are two main planetary boundary layer (PBL) schemes that can be employed in TOMCAT. The non-local scheme developed by Holtslag and Boville (1993) is predominantly used. It takes account of non-local effects and allows for counter gradient transport. Wang et al. (1999b) implemented this scheme in a similar CTM and found there was stronger transport out of the PBL and into the free troposphere, resulting in better comparisons with radon observations. There is also an alternative PBL scheme, developed in this thesis, which uses the pre-calculated

planetary boundary layer height from the ECMWF reanalyses. The model calculates the total tracer mass in the PBL and equally distributes the mass within the PBL. This method, similar to the convective archived mass flux scheme, means that the PBL height is more consistent with the meteorological reanalyses. The scheme is computationally much cheaper, but again needs the ECMWF reanalyses to be available.

3.2.1.5 Chemistry

TOMCAT has two detailed chemistry schemes. The first is the stratospheric scheme described by Chipperfield (1999) and the second is the tropospheric scheme based on the ASAD chemistry package (Carver et al., 1997). These schemes are used in the "full chemistry" version of TOMCAT which includes reactions of multiple chemical species such as O_x, HO_x and NO_x families, along with HNO_3, N_2O_5, HNO_4, H_2O_2, CO, HONO, H_2O, CH_4, HCHO, CH_3OOH, C_2H_6, C_3H_8, CH_3COCH_3, C_2H_5OOH, CH_3CHO, C_2H_5CHO, iCH_3H_7OOH, nC_3H_7OOH, $CH_3CO_3NO_2$ (PAN), $C_2H_5CO_3NO_2$ (PPAN) and CH_3ONO_2.

It is possible to run the model in an idealised mode which replaces the full tropospheric chemistry scheme with a simplified parameterised chemistry scheme. This offline mode means the concentration of sink species, such as OH, are read into the model instead of calculating them online. This greatly increases the speed of the simulations and gives flexibility in selecting the CH_4 loss rates without having to rely on the full chemistry scheme. The simplified chemistry scheme for CH_4 has been successfully used in a number of studies, for example McNorton et al. (2016) and McNorton et al. (2018) and in Chapters 4 and 5.

3.2.2 TOMCAT Inverse Model Description

INVICAT is a variational inverse transport model based on the TOMCAT CTM and includes TOMCAT's corresponding adjoint model, ATOMCAT. INVICAT was first described by Wilson et al. (2014) and uses 4D-Var data assimilation techniques to provide optimised emission estimates of chemical species, such as CH_4. The next section gives a brief introduction to the 4D-Var method and the adjoint model, ATOMCAT. INVICAT has been used in many CH_4 studies to quantify emissions and to provide optimised fluxes in forward model simulations. These studies include Wilson et al. (2021) and Chapter 4 of this thesis.

3.2.2.1 4D-Var Method

The 4D-Var method is a data assimilation technique derived from Bayesian theory, which iteratively reduces the difference between model predictions and observations. To do this it minimises the cost function $J(\mathbf{x})$

$$J(\mathbf{x}) = \frac{1}{2}(\mathbf{x} - \mathbf{x}^b)^T\mathbf{B}^{-1}(\mathbf{x} - \mathbf{x}^b) + \frac{1}{2}(\mathbf{y} - \mathbf{Hx})^T\mathbf{R}^{-1}(\mathbf{y} - \mathbf{Hx}) \tag{3.3}$$

The notation ^{T} stands for the transpose of a matrix and $^{-1}$ is the inverse of a matrix. The state vector is represented by $\mathbf{x}$ and the a priori state vector by $\mathbf{x}^b$. In this case the state vector includes surface fluxes of chemical species with the initial 3-D atmospheric distribution (Wilson et al., 2014). In TOMCAT the surface fluxes have a monthly temporal resolution and the spatial resolution is dependent on the model grid. It is possible to increase the temporal resolution of surface fluxes in TOMCAT, however the model is predominantly simulated using monthly surface fluxes. The a priori estimate of fluxes is generally the previous best estimate of the surfaces fluxes and is the prior estimate of the state vector, which include flux estimates which have not been assimilated.

The forward model simulation is represented by matrix $\mathbf{H}$ which maps from the state vector $\mathbf{x}$ onto the location and time of the observations, $\mathbf{y}$. $\mathbf{B}$ represents the error covariance matrix for the a priori state vector, $\mathbf{x}^b$ and $\mathbf{R}$ represents the error covariance matrix for the observations. The error covariance matrix contains information on the spatial correlation of errors (Singh et al., 2011). All the errors are assumed to be Gaussian for the Bayesian theory to hold (Wilson et al., 2014). The cost function, Equation 3.3, is made up of two parts. The first part finds the difference between the state vector $\mathbf{x}$, which represents the initial fluxes and 3-D atmospheric distribution of the species, and the a priori state vector $\mathbf{x}^b$, weighted by the uncertainty of the fluxes and concentrations. The second part finds the difference between the simulated mixing ratios at the time and location of the observations, which is weighted by the error covariance matrix. The cost function optimises the model performance against the observation, whilst minimising the changes to the prior. It combines an error-weighted sum of the differences between the model and observations and the uncertainty-weighted sum of changes to the a priori flux estimate (Wilson et al., 2021). By minimising the cost function it is finding an optimised state which takes into account the prior state and the observed state.

The cost function is at its minimum when $\nabla J(\mathbf{x})$ is zero, at this point the state vector is optimised with respect to the observations and the prior estimate, see Equation 3.4. The forward model is a set of discrete mathematical operations and conditional statements, not a matrix operator, and as a result $\mathbf{H}^T$ cannot be explicitly calculated using only the forward model. Therefore, this data assimilation method requires an adjoint version of the forward model.

$$\nabla_x J(\mathbf{x}) = \mathbf{B}^{-1}(\mathbf{x} - \mathbf{x}^{\mathrm{b}}) + \mathbf{H}^{\mathrm{T}}[\mathbf{R}^{-1}(\mathbf{y} - \mathbf{H}\mathbf{x})] = 0 \tag{3.4}$$

3.2.2.2 ATOMCAT Adjoint Model

The adjoint model is defined as the transpose of the Jacobian matrix of a linear model. The forward model M can be defined as:

$$c(t_{(i+1)}) = M[c(t_i)] \tag{3.5}$$

For a concentration field c at time t_i, where t_{i+1} represents one model timestep after t_i. The model contains a number of parameterisations of transport and chemical processes which are made up of a finite number of mathematical operations, M_j:

$$M[c(t_i)] = \prod_j M_j[c(t_i)] \tag{3.6}$$

$$\delta c(t_{i+1}) = \prod_j M_j[c(t_i)]\delta c(t_i) = \prod_j \frac{\partial M_j[c(t_i)]}{\partial c}\delta c(t_i) \tag{3.7}$$

In TOMCAT, each operation M_j is linear and differential which means that its Jacobian can be represented by a tangent linear model (TLM, see Equation 3.7). The TLM simulates the propagation of perturbations forward in time and is dependent on the model state at which linearisation takes place. TOMCAT is a linear model which results in the TLM being identical to the forward model. From the TLM, the adjoint model can be developed. The adjoint model propagates variables backwards through time in order to give the sensitivity of a scalar metric of atmospheric concentration field, such as J, to model input parameters such as surface fluxes.

3.2.2.3 INVICAT

ATOMCAT is incorporated into the variational inverse version of TOMCAT, called INVICAT. The variational scheme was based on the system developed by Chevallier et al. (2005) which makes use of a minimisation program (M1QN3) to minimise the cost function, as described by Gilbert and Lemaréchal (1989). INVICAT first runs TOMCAT with a prior flux and the cost function is calculated using observations and the concentrations from the TOMCAT simulation. Then, ATOMCAT is utilised and the cost function gradient is calculated, following this the minimisation program is called. The program is then iterated until either the cost function or gradient has converged to a pre-defined criteria. The a posterior flux is then produced.

In Chapter 4, INVICAT was run at a 5.6°× 5.6° with 60 vertical levels up to 1 hPa and a 30-min time step. Full details of the inverse model set up can be found in Chapter 4.

3.2.3 NAME Model

NAME is a Lagrangian dispersion model described by Jones et al. (2007) and models atmospheric particles such as air pollutants and chemical species such as CH_4. The model has the flexibility to set the output model grid resolution, making it suitable to investigate point sources of CH_4. I have used NAME to simulate a large point source of CH_4 in Chapter 6 because it has a much higher spatial resolution than TOMCAT.

NAME is an offline model driven by the Met Office's Numerical Weather Prediction (NWP) meteorology from the high-resolution UKV model (Davies et al., 2005; Bush et al., 2023). The stored UKV meteorology has a horizontal resolution of approximately 1.5 km × 1.5 km and 70 vertical levels over the UK, with hourly temporal resolution. NAME simulates emissions of an atmospheric constituent by creating a large number of model objects called model particles. Each model particle represents a certain proportion of mass of the released constituent. In this study, I am modelling CH_4 on a sufficiently small time scale (∼hours) that the loss of CH_4 through its sink processes (e.g. chemical reactions with OH and soil uptake) are assumed negligible given the lifetime of atmospheric CH_4 (∼9 years, Prather (1986)).

3.2.3.1 Model Grid and Domain

The output resolution of the model is user-defined enabling a suite of experiments at various resolutions to be conducted. In this study a structured horizontal grid with a regular lattice

is used, which means that the grid box edges are equi-distant between grid points and all grid boxes have equal areas. Similarly, the vertical grid was also selected to be uniform in altitude.

The domain of the model simulation is also user-defined and allows the user to constrain the region in which the particles are followed within the simulation. It is possible to constrain the horizontal, vertical and temporal extent.

3.2.3.2 Source Terms

NAME is able to represent a wide variety of source types so the source type and characteristics need to be specified. In this study, the molecular weight of CH_4 is specified along with its release characteristic. The release characteristic specifies whether it is a instantaneous source, finite-duration release or continuous release. In this study a single point source is released at a specified release location for a finite duration, depending on the simulation. Full details of the NAME simulations performed for this thesis can be found in Chapter 6.

NAME uses a Lagrangian approach and therefore simulates the specified source type as a finite number of discrete particles which are tracked individually. As a result the maximum number of particles released in a simulation needs to be specified. This describes the maximum number of particles which can be stored in a single instance during the simulation. If the number of particles in the model simulation exceeds the maximum number particles specified, the model will stop releasing more particles into the atmosphere. Statistical noise can be an issue in the tails of plumes if the particle number densities are low. This can occur if the spatial resolution of the model is high and the maximum number of particles released in the simulation is too low. In this study our model grid is on the order of meters and as a result we simulate NAME with a maximum of 9×10^7 particles in consultation with Met Office NAME scientists. This reduced the statistical noise at the edges of the plumes in the simulations discussed in 6.

3.2.3.3 Advection and Diffusion

Model particles in NAME are advected by the 3D wind field from the UKV NWP model and unresolved motions such as turbulence are parameterised by a Monte-Carlo random-walk technique. The general form of the equation of motion used in NAME is given by

$$\boldsymbol{x}_{t+\Delta t} = x_t + (\bar{\boldsymbol{u}}(\boldsymbol{x_t}) + \boldsymbol{u'}(\boldsymbol{x}_t)u_m(\boldsymbol{x}_t))\Delta t \tag{3.8}$$

Where the change in the position of particle, $\boldsymbol{x}$, from its position at time t over a time interval Δt is expressed by the sum of three different velocity terms: mean wind $\bar{\boldsymbol{u}}$ at the particle position and turbulent velocities $\boldsymbol{u}'$ and $u_m(\boldsymbol{x}_t)$ representing the individual treatment of turbulence and unresolved mesoscale motions.

3.2.3.4 Model Output

The model outputs the concentrations of atmospheric species, such as CH_4, on the specified model grid. It does this by summing the mass contribution from all particles in each grid box. The final concentration value is determined by the total mass released (restricted by the release rate) and is distributed across the number of particles released.

3.3 Emissions Datasets

To model CH_4 in the atmosphere, surface flux rates from its sources and sinks are input into the model. Chapter 2 provides an overview of the different types of sources of CH_4, however this section will briefly describe the different emissions inventories used when modelling atmospheric methane in TOMCAT.

3.3.1 Anthropogenic Emissions

The main emissions dataset used for anthropogenic emissions of CH_4 (see Chapter 2, Section 2.4) is the Emissions Database for Global Atmospheric Research (EDGAR) (Crippa et al., 2020b; European Commission et al., 2023). This database provides independent estimates of greenhouse gas emissions for each country with a consistent methodology based on Intergovernmental Panel on Climate Change (IPCC) guidelines (Crippa et al., 2020b). EDGAR provide monthly emissions from 1970-2022 on a $0.1^\circ \times 0.1^\circ$ grid and are routinely updated. Emissions are calculated for CH_4 on an annual basis for each sector using country specific activity data (Crippa et al., 2020a). To determine the monthly emissions Crippa et al. (2020b) disaggregate the annual total emissions into monthly data for each sector. The database includes emissions from a wide range of anthropogenic sectors including: agriculture, energy for buildings, fuel exploitation, industrial combustion, industrial processes, power industry, transport and waste. EDGARv8 estimates the 2017 annual total anthropogenic emissions to be ∼370 Tg which is underestimated compared to bottom-up estimates by the Global Methane Budget which esti-

mates 2017 anthropogenic emissions to be 380 Tg (European Commission et al., 2023; Saunois et al., 2020).

In Chapter 4, I use EDGARv5 emissions estimates, excluding rice paddies and biomass burning. Emissions inventories from the Global Fire Emissions Database (GFED) and Patra et al. (2011) provide better estimates for biomass burning and rice emission sectors. In Chapter 5 I use EDGARv8 emission estimates, excluding rice paddies. EDGARv8 does not include a biomass burning sector but in both Chapter 4 and Chapter 5, I use emissions from GFED. To account for rice emissions in Chapter 4 and 5 I use estimates from the TransCom inter-comparison study (Patra et al., 2011).

3.3.2 Wetland Emissions

A number of models have been developed to quantify the emissions of CH_4 from wetlands (see Chapter 2 Section 2.4.1.1). In this study I use WetCHARTS as prior emission estimates for the atmospheric inversion in Chapter 4 and as wetland CH_4 emissions in a forward simulation of TOMCAT in 2020 in Chapter 5. WetCHARTs was developed by Bloom et al. (2017) and provides an ensemble of wetland emissions and its uncertainty. WetCHARTs combines a multi-instrument satellite-derived surface water extent and precipitation reanalyses, eight carbon cycle models, a data-constrained terrestrial carbon cycle analysis and three temperature dependence parameterisations for 2009-2010. This is called the Full Ensemble and uses 3 global scaling factors which amount to 124.5, 166 or 207.5 Tg year^{-1}. For the period 2001-2015 wetland emissions were from the precipitation and data-constrained terrestrial carbon cycle analysis (Bloom et al., 2017) and this is called the Extended Ensemble. The use of satellite-derived surface water extent has its limitations, particularly around densely vegetated areas due to passive microwave sensors being more sensitive to vegetation moisture in these regions (Bloom et al., 2017). This increases the uncertainty on the wetland emission estimates in areas such as the Amazon river basin. Parker et al. (2020) have shown using TOMCAT and GOSAT that WetCHARTs reproduces the observed seasonal cycle for the majority of wetland regions. However, in some regions such as the Sudd, in South Sudan it does not reproduce the observed seasonal cycle. In this study wetland emissions from WetCHARTs are used in TOMCAT.

In Chapter 4, WetCHARTsv1.0 is used. Since then it has been updated to WetCHARTSv1.3.1, which is used in Chapter 5. This version is the same as the Full Ensemble but the model output

now goes from 2001-2019, the model is now forced with ERA5 reanalyses and the Global Lakes and Wetlands Database wetland extent definitions have been adjusted (Bloom et al., 2021).

3.3.3 Biomass Burning

There are a number of different biomass burning inventories which can be used in model simulations. These include the Global Fire Emissions Database (GFEDv4.1s), Global Fire Assimilation System (GFASv1.2), Quick Fire Emissions Dataset (QFEDv2.5rl), Fire Energetics and Emissions Research (FINNv1.5) and Fire Energetics and Emissions Research (FEERv1.0-G1.2), some of which are used in the Global Carbon Project's assessment on biomass burning emissions and have been compared by Liu et al. (2020). Emission estimates of CH_4 from these biomass burning inventories are impacted by land use and land cover classification, particularly around the treatment of peatlands. The CH_4 emission factor for peat fires is high due to incomplete combustion from smouldering files, leading to higher CH_4 emissions. These are common in boreal and tropical peatlands. Both GFEDv4s and GFASv1.2 account for peatlands as a separate land use and are more in line with observations of smoke-generated PM2.5 (Liu et al., 2020) suggesting these provide more realistic estimates of fire emissions. Liu et al.'s (2020) study highlights the importance of land use and land cover classification of peatlands when calculating CH_4 emission estimates from biomass burning. The GFED biomass burning emission estimates of CH_4 have been used in a number of TOMCAT studies (e.g. Wilson et al., 2021; McNorton et al., 2016; McNorton et al., 2018).

In Chapter 4, I use GFEDv4s which provides monthly emission estimates of CH_4 at a resolution of $0.25° \times 0.25°$ between 1995-2016 (Randerson et al., 2017). These emissions are used as a prior estimate of biomass burning emissions in the atmospheric inversion, described in Chapter 4. In Chapter 5, I use an updated version, GFEDv5, for biomass burning estimates of CH_4 in 2020 in the TOMCAT simulation (Chen et al., 2023).

3.3.4 Other Emissions and Sinks

Other emissions from smaller sources such a termites or geological emissions are limited in data. In this study the ocean emissions diffusion and ebullition are taken from Weber et al. (2019) and geological emissions are taken from Etiope et al. (2019). Both the rice and termite emissions were taken from the TransCom intercomparison study, however the termite emissions were scaled to match Saunois et al. (2020). In addition to the main sources of CH_4, these smaller

emission data are included in the model. The OH fields for the troposphere and stratosphere were taken from Spivakovsky et al. (2000) and scaled downwards by 8 % in accordance to Huijnen et al. (2010) to match MCF concentration in the atmosphere (see Chapter 2, Section 2.4.3; Patra et al. (2011)). The stratospheric loss rates for Cl and $O(^1D)$ were taken from a previous full chemistry TOMCAT simulation (Monks et al., 2017). The soil sink was taken from the Soil Methanotrophy Model (MeMo) model (Murguia-Flores et al., 2018).

Full details on the sources and sinks used in each TOMCAT based study can be found in Chapter 4 and Chapter 5.

Chapter 4

Decreasing seasonal cycle amplitude of methane in the northern high latitudes being driven by lower latitude changes in emissions and transport

Emily Dowd[1], Chris Wilson[1,2], Martyn P. Chipperfield[1,2], Emanuel Gloor[3], Alistair Manning[4], Ruth Doherty[5]

[1]School of Earth & Environment, University of Leeds, Leeds, UK
[2]National Centre for Earth Observation, University of Leeds, Leeds, UK
[3]School of Geography, University of Leeds, Leeds, UK
[4]Met Office, Exeter, UK
[5]School of GeoSciences, University of Edinburgh, Edinburgh, UK

Abstract

Atmospheric methane (CH_4) concentrations are rising which is expected to lead to a corresponding increase in its global seasonal cycle amplitude (SCA), the difference between its seasonal maximum and minimum values. The reaction between CH_4 and its main sink, OH, is dependent on the amount of CH_4 and OH in the atmosphere. The concentration of OH varies seasonally

and due to the increasing burden of CH_4 in the atmosphere, it is expected that the SCA of CH_4 will increase due to increased removal of CH_4 through reaction with OH in the atmosphere. Spatially-varying changes in the SCA could indicate long-term persistent variations in the seasonal sources and sinks but such SCA changes have not been investigated. Here we use surface flask measurements and a 3-D chemical transport model (TOMCAT) to diagnose changes in the SCA of atmospheric CH_4 between 1995-2020 and attribute the changes regionally to contributions from different sectors. We find that the observed SCA decreased by 4 ppb (7.6%) in the northern high latitudes (NHL, 60°N-90°N), whilst globally the SCA increased by 2.5 ppb (6.5%) during this time period. TOMCAT reproduces the change in the SCA at observation sites across the globe. Therefore, we use it to attribute regions which are contributing to the changes in the NHL SCA, which shows an unexpected change in the SCA that differs to the rest of the world. We find that well-mixed background CH_4, likely from emissions originating in, and transported from, more southerly latitudes has the largest impact on the decreasing SCA in the NHL (56.5% of total contribution to NHL). In addition to the background CH_4, recent emissions from Canada, the Middle East and Europe contribute 16.9%, 12.1% and 8.4%, respectively, to the total change in the SCA in the NHL. The remaining contributions are due to changes in emissions and transport from other regions. The three largest regional contributions are driven by increases in summer emissions from the Boreal Plains in Canada, decreases in winter emissions across Europe, and a combination of increases in summer emissions and decreases in winter emissions over the Arabian Peninsula and Caspian Sea in the Middle East. These results highlight that changes in the observed seasonal cycle can be an indicator of changing emission regimes in local and non-local regions, particularly in the NHL where the change is counter-intuitive.

4.1 Introduction

Methane (CH_4) is the second most important anthropogenic greenhouse gas in the atmosphere after carbon dioxide (CO_2) and anthropogenic emissions have contributed an extra 23% to the radiative forcing in the troposphere since 1750 (Saunois et al., 2020). Global observations by the National Oceanic and Atmospheric Administration (NOAA) Earth System Research Laboratories (ESRL) show that concentrations of atmospheric CH_4 have risen since the 1980s, with a short hiatus in the growth between 1999 and 2006. Our understanding of the drivers of the

global trends of CH_4 remains incomplete (Nisbet et al., 2016; Nisbet et al., 2019; Dlugokencky et al., 2021). Long-term trends of CH_4 are monitored through surface flask observations by NOAA ESRL and have been studied extensively. Long-term variations in the seasonal cycle of CH_4 have not been analysed in detail since a study by Dlugokencky et al. (1997), although several studies have briefly discussed its seasonal cycle (e.g. Pickett-Heaps et al. (2011), Bergamaschi et al. (2018), Patra et al. (2011), and Parker et al. (2020)).

CH_4 has a mixture of natural and anthropogenic sources and chemical sinks which lead to a strong seasonal cycle in the atmosphere. Figure 4.1 shows the mean seasonal cycle across NOAA observation sites (Table 4.1) in the northern and southern hemispheres, where concentrations are at a minimum in summer and peak in winter or early spring, depending on location. The atmospheric CH_4 seasonal cycle is driven by the seasonal variations of sources such as wetlands, rice paddies and biomass burning, the chemical loss of CH_4 in the atmosphere, and the transport of CH_4. The main sources which drive the CH_4 cycle are dependent on climatological and meteorological conditions. Emissions from wetlands and rice paddies vary seasonally with changes in temperature, precipitation and soil moisture. Biomass burning emissions in the tropics and boreal regions also vary seasonally (Dlugokencky et al., 1997). It is thought that anthropogenic emissions play a smaller role in the seasonal cycle of CH_4 (e.g. Meirink et al. (2008) and Wilson et al. (2021)) but few studies have investigated the long-term influence of anthropogenic emissions on the observed seasonal cycle. For example, anthropogenic emissions might increase in winter due to increased gas extraction (Nisbet et al., 2019). The sinks of CH_4 also play a large role in the seasonal cycle. The main sink of CH_4 is the hydroxyl radical (OH) which is photochemically produced, which results in the local abundance of OH varying seasonally due to the availability of UV radiation. Finally, transport of CH_4 in the atmosphere through advection, convection and global circulation transporting air to the poles also influences the seasonal cycle.

Many studies have assessed how well wetland models and chemical transport models reproduce the observed CH_4 seasonal cycle, the timing of the seasonal maximum and seasonal minimum, or what might be driving the seasonal cycle on a regional scale (Patra et al., 2011; Bergamaschi et al., 2018; Parker et al., 2020). These studies did not explore how the seasonal cycle amplitude (SCA) has changed over time on a global scale. The SCA is defined as the difference between the annual maximum and the annual minimum concentration at a particular location. Changes

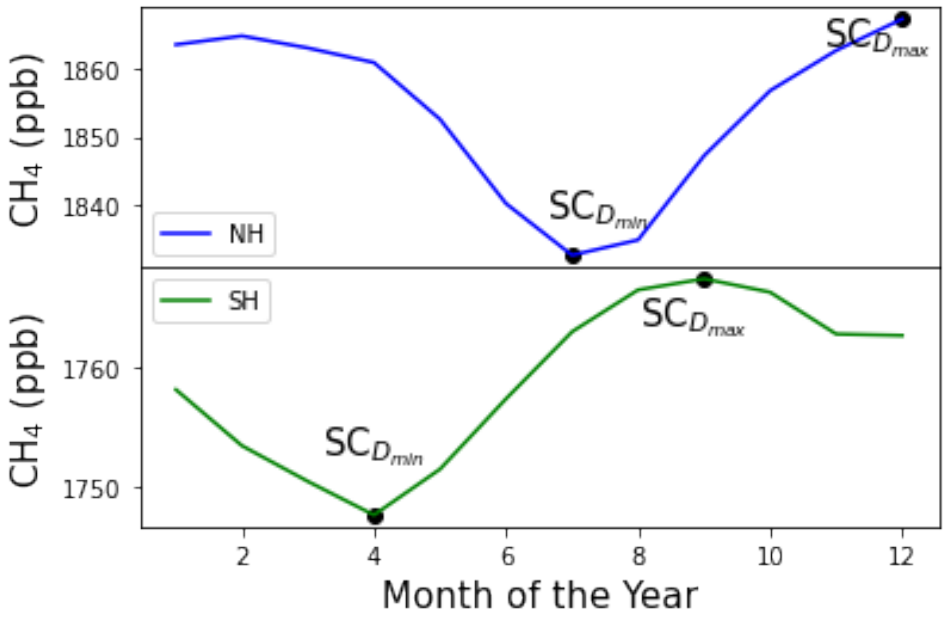

Figure 4.1: The monthly mean CH_4 mixing ratio (ppb) across northern hemisphere (NH) and southern hemisphere (SH) at 22 NOAA surface sites between 1995-2022 (see Table 4.1). $SC_{D_{max}}$ and $SC_{D_{min}}$ represent the seasonal cycle maximum and minimum, respectively.

in the seasonality of emissions will be reflected in the seasonal cycle amplitude of CH_4 and will ultimately impact the annual growth rate. However, changes in loss rates and transport add extra complexity to assessing changes in the seasonal cycle. Studying the SCA could give us a better insight into changes in the CH_4 budget. In this study we regionally attribute the change in SCA of CH_4 between 1995-2020 using the TOMCAT chemical transport model (Chipperfield, 2006) and surface observations from NOAA ESRL (Dlugokencky et al., 2021).

Note that throughout this text we are referring to concentrations when we use "CH_4" alone. In Sect. 4.2 we describe the observations used, the modelling methodology and the SCA analysis. In Sect. 4.3 and Sect. 4.4 we present our results and discuss our findings.

4.2 Methods

4.2.1 Atmospheric Methane Measurements

We assimilate and analyse the long-term surface flask measurements provided by NOAA ESRL. The air samples are collected approximately weekly or biweekly and CH_4 is measured using gas chromatography with flame ionization detection or by cavity ring-down spectroscopy methods (Dlugokencky et al., 2021). The NOAA observation network provides measurements across the globe, but there is a disproportionate number of sites in the northern hemisphere compared

with the southern hemisphere, see Fig. 4.2. There is also a lack of regular observations in some tropical regions, where there are large and uncertain CH_4 emissions.

We assimilate NOAA surface observations in INVICAT, the inverse model of TOMCAT, in order to get optimised estimates of CH_4 fluxes to use in the TOMCAT forward model. We used observations from 80 NOAA surface observation sites and assimilated them at the correct model time step. Full details of the assimilation can be found in Sect. 4.2.3. In the SCA analysis we used a subset of these observations. We calculated the monthly mean CH_4 at 22 NOAA surface sites which were selected if they contained observations for the entire period 1995-2020 and were not strongly influenced by local sources (McNorton et al., 2018). A list of the sites and their site codes are in Table 4.1 and their locations are shown by the blue dots in Fig. 4.2. We also evaluate the model performance using observations from the Center for Global Environmental Research Earth System Division, National Institute for Environmental Studies, Japan (NIES, Tohjima et al. (2002) and Sasakawa et al. (2010)) and the Advanced Global Atmospheric Gases Experiment (AGAGE, Prinn et al., 2018) which have not been assimilated, see Supplement Fig. A.2. The sites from NIES are in Siberia and East Asia and the site from AGAGE is situated in Ireland, their locations are shown as the red dots in Fig. 4.2. The independent observations do not cover the whole study period but we have maximised the time period available from each data set by selecting a period with the most regular observations. The NIES observations in Siberia are from 2009-2015, the remaining NIES observations are from 1997-2015 and the AGAGE observations are from 1996-2020.

4.2.2 Tagged Transport Simulations

TOMCAT is a three-dimensional (3D) atmospheric chemical transport model which has been used in a number of studies to model CH_4 and other chemical species in the atmosphere (e.g. Chipperfield (2006), Parker et al. (2018), and Wilson et al. (2021)). We use TOMCAT to investigate changes in the SCA of CH_4 between 1995 and 2020, including the impact of changes in emissions and transport. The globe was divided into 18 different regions, shown in Fig. 4.2, in order to attribute the changes in the SCA from particular regions. The regions were selected based on the magnitude and type of emission in the distribution used in TOMCAT. The northern oceans, Greenland, Iceland and Svalbard have been grouped together (north oceans and Arctic, NOA), as were the southern oceans and Antarctica (SOA). Northern land regions have been split into Canada (CAN), Europe (EUR) and Russia (RUS) due to their emissions types and

Table 4.1: List of 22 NOAA Sites used in the analysis (Dlugokencky et al., 2021) and the 6 sites used in the independent analysis (Tohjima et al., 2016a; Tohjima et al., 2016b; Sasakawa et al., 2010; Prinn et al., 2018).

Site Name	Latitude (° North)	Longitude (° East)	Site Code	Measurement Network
Alert, Canada	82.45	-62.50	ALT	NOAA
Ny-Ålesund, Svalbard	78.91	11.80	ZEP	NOAA
Barrow, Alaska, USA	71.32	156.60	BRW	NOAA
Stórhöfdaviti, Vestmannaeyjar, Iceland	63.40	-20.28	ICE	NOAA
Mace Head, Republic of Ireland	53.32	-9.90	MHD	NOAA
Ulaan Uul, Mongolia	44.45	111.09	UUM	NOAA
Niwot Ridge, Colorado, USA	40.05	-105.63	NWR	NOAA
Terceira Island, Azores	38.70	-27.35	AZR	NOAA
Mount Waligaun, People's Republic of China	36.27	100.92	WLG	NOAA
Tudor Hill, Bermuda	32.26	-64.87	BMW	NOAA
Izana, Tenerife	28.30	-16.48	IZO	NOAA
Sand Island, Midway	28.22	-177.37	MID	NOAA
Mauna Loa, Hawaii, USA	19.53	-155.58	MLO	NOAA
Cape Kumukahi, Hawaii, USA	19.52	-154.82	KUM	NOAA
Mariana Islands, Guam	13.39	144.65	GMI	NOAA
Ragged Point, Barbados	13.17	-59.43	RPB	NOAA
Mahe Isalnd, Seychelles	-4.68	55.53	SEY	NOAA
Ascension Island, St Helena	-7.97	-14.40	ASC	NOAA
Tutuila, American Samoa	-14.25	-170.56	SMO	NOAA
Palmer Station, Antarctica	-64.92	-64.00	PSA	NOAA
Sywoa Station, Antarctica	-69.00	39.57	SYO	NOAA
South Pole, Antarctica	-89.98	-24.80	SPO	NOAA
Cape Ochi-ishi, Japan	43.16	145.45	COI	NIES
Hateruma, Japan	24.06	123.80	HAT	NIES
Demyanskoe, Russia	59.25	82.42	DEM	NIES
Karasevoe, Russia	58.25	82.42	KRS	NIES
Berezorechka, Russia	56.15	54.33	BRZ	NIES
Mace Head, Republic of Ireland	53.33	-9.90	GC-MD	AGAGE

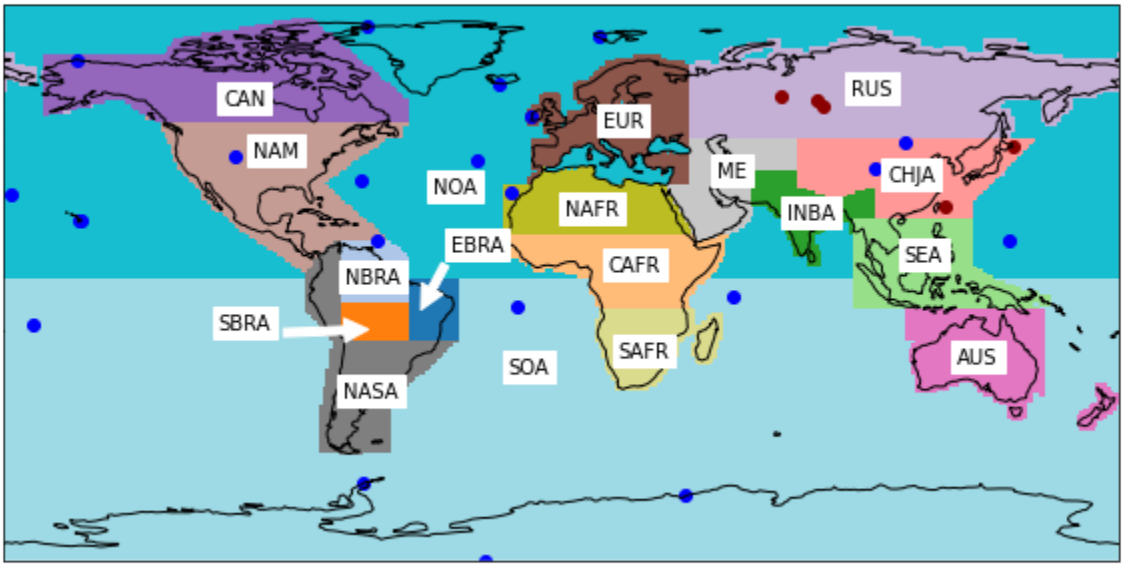

Figure 4.2: A map showing the 18 different regions selected for the tagged tracers, 22 NOAA surface observation site locations (blue) and the independent observations site locations (red). The observation sites shown are the ones used to calculate SCA from 1995-2020.

geographical location. The emissions from these regions include anthropogenic emissions such as those from oil and gas industries, livestock and other agriculture, but also include natural emissions such as those from wetlands and biomass burning. In the northern mid-latitudes regions such as North America (NAM), Middle East (ME) and China & Japan (CHJA) are dominated by large anthropogenic emissions. Africa has been split into three regions because of the influence of central Africa in the CH_4 budget, with recent studies highlighting the large role tropical wetlands play in the recent global growth (Lunt et al., 2021; Feng et al., 2022). Similarly, Brazil has been split into three regions due to the local emission sectors and different responses to seasonal changes in meteorology (Wilson et al., 2021; Basso et al., 2021). The North Brazil (NBRA) emissions are mostly driven by wetlands, whereas East Brazil (EBRA) is more susceptible to biomass burning in the arc of deforestation, a region of regular and intense anthropogenic burning. The South Brazil (SBRA) emissions are driven by a mixture of both wetlands and biomass burning. The rest of South America has been grouped as Non-Amazon South America. Emissions from the South East Asia region (SEA) is from a mixture of rice paddies, biomass burning and other anthropogenic emissions, whilst Australia (AUS) is mostly driven by anthropogenic emissions, such as those from coal mines. The names given to each region are given in Table 4.2.

Emissions from each region were simulated separately in the model and could be summed to

Table 4.2: List of 18 regions and their region code for each tracer.

Region Code	Region Name
AUS	Australasia
CAFR	Central Africa
CAN	Canada
CHJA	China & Japan
EBRA	East Brazil
EUR	Europe
INBA	India & Bangladesh
ME	Middle East
NAFR	North Africa
NAM	North America
NASA	Non-Amazon South America
NBRA	North Brazil
NOA	North Oceans & Arctic
RUS	Russia
SAFR	South Africa
SBRA	South Brazil
SEA	South East Asia
SOA	South Oceans & Antarctica

represent global CH_4. This is possible due to the linearity of the TOMCAT model transport (Wilson et al., 2016) and offline (non-interactive) loss rates. In reality, the loss of CH_4 is not linear because the abundance of CH_4 impacts its rate of loss due to its impact on OH abundance, but this is a small effect relative to the large CH_4 abundance.

TOMCAT was run at a $5.6° \times 5.6°$ horizontal resolution with 60 vertical levels up to 0.1 hPa, between 1983 and 2020 for each regional tagged tracer, a background tracer and a total CH_4 tracer. The background tracer contains CH_4 from the regional tracers once the CH_4 from each region has become well-mixed. Each regional tagged tracer was set to be reallocated into the background tracer using an exponential 9-month decay rate. Typical timescales for horizontal transport in the troposphere from the mid latitudes to the poles is approximately 1-2 months and interhemispheric transport is approximately 1 year (Jacob, 1999). The 9-month decay rate was selected in order to maximise the opportunity for CH_4 to undergo long-range transport from emission locations to surface sites, whilst minimising the effect of well-mixed atmospheric CH_4 on the results. The background tracer allows us to reduce the spin-up time required in the model to reach steady state. Without the background allocation concentrations would continue to increase because it takes approximately 20 years for the CH_4 to reach steady state in the model. The background tracer also allows us to regionally attribute changes in the SCA whilst

accounting for well-mixed CH_4.

The study period begins in 1995 to allow the tracers to become well-mixed in the preceding 12 years. This model simulation is called TOM_regional and uses surface fluxes derived from a TOMCAT-based atmospheric inversion described in Sect. 4.2.3. The meteorology was driven by the European Centre for Medium-Range Weather Forecasts (ECMWF) ERA5 reanalyses (Hersbach et al., 2020) and the OH fields for the troposphere and stratosphere were based on those within the TransCom CH_4 study (Patra et al., 2011). The OH fields were originally taken from Spivakovsky et al. (2000) and scaled downwards by 8% in accordance with Huijnen et al. (2010) in order to match the observed methyl chloroform concentrations in the atmosphere (Patra et al., 2011). The stratospheric loss rates for Cl and $O(^1D)$ varied annually and were taken from a previous full chemistry TOMCAT simulation (Monks et al., 2017). The soil sink was taken from the MeMo model which varied each year between 1990 to 2009, the 1990 values were annually repeated from 1983-1990 and similarly, the 2009 values were repeated annually from 2009-2020 (Murguia-Flores et al., 2018).

We carried out two sensitivity experiments to investigate the impact of the choice of the exponential lifetime used to allocate well-mixed CH_4 into the background tracer, and if it influences the background tracer's contribution to the change in the SCA. Decay rates of 1 and 12 months were selected to show the impact of a short and long decay timescales on the background and regional contributions of the change in the SCA. The simulations are labelled TOM_one for the 1-month decay rate and TOM_twelve for the 12-month rate. The results of the sensitivity experiments can be found in Sect. 4.3.5.

The TOM_regional simulation quantifies the impact regional emissions have on the SCA of CH_4 elsewhere under annually varying transport processes. In order to investigate the role that those transport processes alone play in the change in SCA of CH_4, we also carried out a separate regional tagged tracer simulation using annually-repeating emissions for the same time period. Using annually-repeating values removes the influence of changing emissions, allowing us to investigate changes to the transport undergone by emissions from each region over time. The surface emissions for each month of the year were averaged between 1983-2020. These emissions were repeated annually using the same model set-up as TOM_regional and the same analysis of SCA was repeated for 1995-2020. This constant emissions simulation is labelled TOM_transport. A summary of the TOMCAT simulations can be found in Table 4.3.

Table 4.3: List of the different TOMCAT simulations.

TOMCAT Simulation	Experiment
TOM_regional	Regional tagged tracer simulation
TOM_transport	Investigating changes in transport
TOM_one	Background sensitivity - One month decay rate
TOM_twelve	Background sensitivity - Twelve month decay rate

4.2.3 Fluxes from Atmospheric Inversions

The surface fluxes for the tagged tracer simulations were derived using the TOMCAT-based inverse model, INVICAT (Wilson et al., 2014). INVICAT has been used in a number of studies to constrain emissions of various species, including CH_4 (Gloor et al., 2018; Wilson et al., 2021). It uses a 4D-Var variational method based on that used in Numerical Weather Prediction, with full details on the methods used in INVICAT given in Wilson et al. (2014). The inverse method aims to minimise the value of a cost function, in a least-squares sense. The cost function combines an error-weighted sum of the differences between the model and observations and the uncertainty-weighted sum of changes to the a priori flux estimate (Wilson et al., 2021). The input for INVICAT includes an a priori mean flux value for each grid cell and an error covariance matrix containing the covariances between the flux uncertainties. The output is an a posteriori mean grid cell flux and error covariance matrix. The a priori and a posteriori fluxes will hence be referred to as prior fluxes and posterior fluxes, respectively.

The inverse model simulations were run at a $5.6° \times 5.6°$ horizontal resolution with 60 vertical levels up to 0.1 hPa and a time step of 30 min. The meteorology was taken from ECMWF's ERA5 reanalyses (Hersbach et al., 2020). An inversion was carried out separately for each year and completed 40 minimisation iterations. The 40 iterations were sufficient for the cost function and its gradient norm to be judged as converged, based on both being smaller than 1% of their initial value. The inversion for each year was run for 14 months, until February the following year, in order to better constrain the fluxes in the final months of each year. The final 2 months of each are discarded from the results. Each inversion overlapped with the following one by 2 months to give the transport of fluxes time to reach measurement sites. The overlapping months were initialised using 3-D fields provided from the correct date in the previous year so the total CH_4 burden was conserved across each year.

The 4D-Var-simulated CH_4 mixing ratios were linearly interpolated to the correct longitude,

latitude and altitude of each surface observation used in the inversion at the nearest model time step. The surface observations were given uncorrelated errors of 3 ppb plus a representation error. The representation error was estimated as the mean difference across eight grid cells around the cell which contained the observation. The prior emissions were taken from various inventories. The anthropogenic emissions were taken from EDGARv5 (M et al., 2021), excluding rice paddies and fires. The biomass burning emissions were taken from GFEDv4.1s (Randerson et al., 2017). The WetCHARTS model (Bloom et al., 2017) in a median set-up was used for the wetland fluxes. The median set-up uses the median scaling factor and temperature response from the WetCHARTS suite and the Global Lakes and Wetlands Database distribution of wetlands. The wetland fluxes were then masked to remove emissions which overlap with rice emissions and then scaled back up to 180 Tg to match the top-down mean value from the Global Methane Budget (Saunois et al., 2020). The rice and termite emissions were taken from the Transcom intercomparison project (Patra et al., 2011). The termite emissions were scaled to match the total quoted in Saunois et al. (2020). The geological emissions were from Etiope et al. (2019) and the ocean emissions are taken from Weber et al. (2019). The prior emissions are given cell uncertainties of 250% of the prior flux value but also include 500 km spatial correlations with a Gaussian distribution for all fluxes. Fossil fuel fluxes have temporal correlations based on an exponential distribution with a time scale of 9 months. The tropospheric and stratospheric loss rates are the same as those used in the TOMCAT tagged tracer simulations (Sect. 4.2.2).

4.2.4 Data Processing and Analysis

The monthly mean model output from TOMCAT was interpolated horizontally and vertically to the 22 surface observation sites (Table 4.1) from NOAA's ESRL (Dlugokencky et al., 2021) to check model performance and in order to investigate the regional contribution to the change in SCA at these sites. Following methods used by Lin et al. (2020) for CO_2, the seasonal cycle amplitude (SCA) of CH_4 and the regional contribution to the SCA was analysed.

To calculate the SCA, we isolate the mean annual cycle observed in CH_4 by taking the interpolated model output at each surface observation site and then smooth and detrend the time series using the CCGCRV curve-fitting routine, developed by Thoning et al. (1989). CCGCRV approximates the seasonal cycle and long-term trend variation by fitting a polynomial equation combined with a harmonic function (Pickers and Manning, 2015). The short-term and long-term cut off values can be selected and we chose 80-day and 667-day cut offs, respectively

(Dlugokencky et al., 1994). These parameters have been used in previous studies (Dlugokencky et al., 1994; Parker et al., 2018). The SCA for the observations and the modelled total tracer was calculated by taking the difference between the annual maximum (SC_{Dmax}) and annual minimum (SC_{Dmin}) of the detrended curve:

$$SCA = SC_{Dmax} - SC_{Dmin} \tag{4.1}$$

where D_{max} and D_{min} are the days of the annual CH_4 cycle maximum and minimum. For each tagged regional tracer, i, a pseudo SCA (SCA') was calculated where the pseudo maximum ($SC'_{i,D_{max}}$) or minimum ($SC'_{i,D_{min}}$) is the point of its annual cycle corresponding to D_{max} and D_{min}. The pseudo seasonal cycle amplitude was calculated as:

$$SCA'_i = SC'_{i,D_{max}} - SC'_{i,D_{min}} \tag{4.2}$$

The pseudo SCA was defined to account for the difference in timing of the local D_{max} and D_{min} of the individual tracers and observed CH_4 at the observation sites. The total change in SCA over the study period, ΔSCA (ppb), was derived by calculating the linear trend (k_{SCA}) in the SCA and multiplying it by the number of years in the study (n_{year}, 25 years):

$$\Delta SCA = k_{SCA} \times n_{year} \tag{4.3}$$

Once the SCA and ΔSCA were calculated the surface sites were then grouped into five latitude bands for further analysis. These groups are Northern High Latitudes (NHL, 60°N-90°N), Northern Mid Latitudes (NML, 30°N-60°N), Northern Tropics (NTr, 0°-30°N), Southern Tropics (STr, 0°-30°S) and Southern High Latitudes (SHL 60°S-90°S). There are no surface observations from the Southern Mid Latitudes (SML, 30°S-60°S) so we do not analyse the SCA in this latitude band.

The main sink of CH_4 is through reaction with OH and the rate of removal is dependent on temperature and the amount of CH_4 and OH in the atmosphere (Dlugokencky et al., 1997). The atmospheric burden of CH_4 has been increasing and it is expected that the SCA of CH_4 would increase due to more CH_4 being removed by OH in the atmosphere, assuming that OH

concentrations remain relatively constant during this time. To account for the impact of OH on ΔSCA we calculated the amount of CH_4 lost by OH across the whole atmosphere in each month of the study period:

$$L_{CH_4} = m_{CH_4}(1 - e^{-k[OH]\Delta t}) \tag{4.4}$$

$$k = 2.45 \times 10^{-12} e^{(-1775/T)} \tag{4.5}$$

Where L_{CH_4} is the amount of CH_4 lost (kg) in each model grid box through the reaction with OH in one month and m_{CH_4} is the mass of CH_4 in kg in each grid box. The variable k is the reaction rate constant (in cm^3 $molecules^{-1}s^{-1}$; Equation 4.5 where T is temperature in Kelvin), [OH] is the amount of OH (molecules cm^{-3}) and Δt is number of seconds in one month. L_{CH_4} was converted to ppb and a mean monthly loss was calculated for the northern and southern hemisphere, across all the vertical model levels over the study period. The loss was then smoothed and detrended using the CCGCRV curve fitting routine and ΔSCA was calculated using the same method described above. It is not realistic to account for the contribution to ΔSCA from loss by OH at individual surface sites because this would not capture the seasonal cycle of OH in the mid-troposphere, where the majority of CH_4 loss by OH occurs. This makes it difficult to relate the seasonal changes in CH_4 due to loss by OH at particular sites, hence why we have calculated L_{CH_4} as a mean across the northern and southern hemispheres.

4.3 Results

4.3.1 Observed ΔSCA

The observed ΔSCA was calculated at the 22 observations sites. We find that the global mean SCA at available sites is increasing but there are different regional trends, for example in the NHL the observed ΔSCA decreased at all sites between 1995-2020 (Fig. 4.3). The observed global mean value of ΔSCA was 2.5 ppb, corresponding to an increase of the SCA by 6.5%. The reaction between CH_4 and OH is dependent on the amount of CH_4 available in the atmosphere. The combination of the increasing CH_4 burden in the atmosphere and the photochemically-driven seasonal variation of OH results in more CH_4 being removed from the atmosphere during

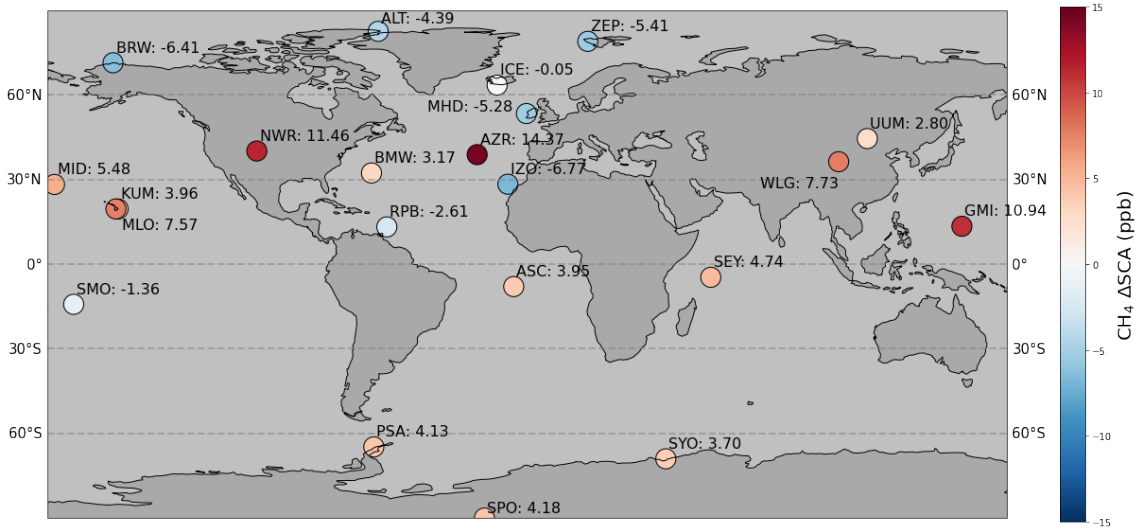

Figure 4.3: Map showing ΔSCA (ppb) at the 22 selected observation sites.

the time of maximum OH. Therefore, an increase in the global mean SCA is expected due to the increasing atmospheric burden of CH_4. However, when we look at the ΔSCA latitudinally, there are large differences in the NHL compared to the rest of the world. The mean observed ΔSCA in the NHL was -4.0 ppb, which represents a 7.6% decrease between 1995 and 2020, and in the Non-NHL region the mean observed value of ΔSCA was 4 ppb, which is an increase of 11.5% for the study period. The reasons for this widespread contrasting behaviour in the NHL compared to the rest of the world is investigated in more detail in the forthcoming sections.

The distribution of ΔSCA at sites in Non-NHL regions is quite variable. For example at NWR, AZR and GMI ΔSCA is large and positive but other sites such as MHD, IZR and SMO have negative ΔSCA values. The sites with the largest positive ΔSCA (e.g. NWR, BMW and AZR, GMI and WLG) are most likely influenced by outflow from the USA and Asia. The sites with large positive ΔSCA and negative ΔSCA in the Non-NHL regions do not have a strong regional or local pattern in ΔSCA, unlike in the NHL. All four sites in the NHL display contrasting behaviour and have a negative ΔSCA compared to the rest of the world therefore; the NHL will be the main focus of our analysis.

BRW, ALT and ZEP have a ΔSCA which ranges from -4 ppb to -5 ppb. The SCA at these sites are variable but have a strong decreasing trend. ICE has a smaller ΔSCA (-0.05 ppb) compared to the other three sites in the NHL. There is a large decrease in the SCA during the first 4 years of the study and then the SCA value steadily fluctuates between ∼30 and ∼40 ppb. This results in no trend in the SCA for the rest of the study period leading resulting in a smaller

negative ΔSCA compared to the other sites (See Supplement Fig. A.3).

The Non-NHL regions had a mean observed ΔSCA of 4 ppb. The three SHL sites sample well-mixed air and are less influenced by local sources. The concentrations at regional sites near to emissions are all affected in different ways, whereas at the sites in Antarctica the effect is smoothed out by the time air reaches the South Pole region. The 3 sites in Antarctica are exposed to well-mixed air and have the same mean increase of 4 ppb, highlighting that the observed ΔSCA in NHL is very different to the global observed ΔSCA. This implies that the Arctic is responding differently to the global increase in CH_4 concentrations than the rest of the world and therefore we focus on investigating the decreasing SCA in the NHL.

4.3.2 Model Evaluation

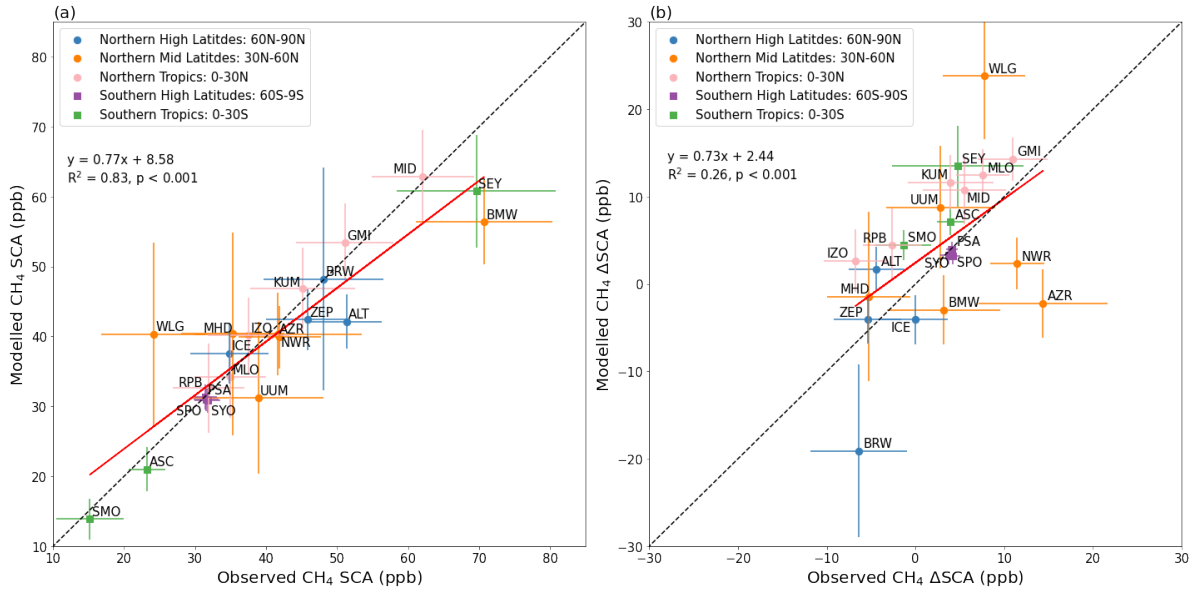

Figure 4.4: Comparison between simulated and observed (a) CH_4 SCA (ppb) and (b) CH_4 ΔSCA (ppb). The SCA shown is the mean SCA between 1995-2020 and ΔSCA is the change in SCA for the same period. The dashed black line represents the 1:1 line and the red line represents the least squares regression line. The error bars denote $\pm 1\sigma$, which represents the interannual variability between 1995-2020.

The observed CH_4 SCA is simulated well by TOMCAT with the surface fluxes from INVICAT in the TOM_regional simulation (Fig. 4.4a). There is a strong linear relationship between the modelled and observed SCA with a mean bias of 0.93 ± 0.09 ppb. However, the model struggles to capture the SCA at Mount Waliguan (WLG) in China. This is likely due to the fact that it has the highest altitude out of all the sites and the reasonably coarse model grid cell will not capture the local topography. The model simulation was also compared with sites that were

not assimilated in INVICAT, although there are limited observations with only 6 sites situated in the Northern Tropics and Northern Mid Latitudes. Due to these sites only having regular observations over a short time period, the comparison only covers the periods 1997-2015 and 2009-2015 (see Supplement). The model captures the SCA well at these independent sites, apart from Cape Ochi-ishi (COI) where the model has a weaker seasonal cycle, particularly during the seasonal cycle minimum. COI is situated near swamps, grazing lands and two cities, so it is possible that the model does not fully capture the complexity of the local sources well. There are large error bars (1σ) for the Siberian sites in both the modelled and observed SCA. This is due to the SCA being quite variable over the short time period available. However, the model still compares well with the observed SCA at these sites, with a mean overestimation of 16 ppb which is well within the 1σ error. Full results of the independent analysis can be found in the Supplement, Fig. A.2. The model captures the mean SCA when compared with NOAA observation sites well but there are larger differences with the independent sites, which is due, in part, to larger variability in the SCA over a shorter time period.

The model also captures ΔSCA well when compared with observations, including the negative ΔSCA and contrasting behaviour in the NHL shown by observations (Fig. 4.4b). As a result, we can use TOMCAT to inform us on what might be driving this significantly different behaviour in the NHL. There is a good correlation (r=0.51) between the model and observations and they almost always match within the 1σ uncertainty of observations, with some outliers. At ALT, TOMCAT shows a ΔSCA of 1.7 ppb and this is due to TOMCAT underestimating the SCA when compared with observations, particularly at the beginning of the study period. At BRW the model has a much stronger negative ΔSCA when compared with the observations and this is due to the model overestimating the SCA at the beginning of the study period. Despite the under- and over-estimations at these two sites (ALT and BRW) in the NHL, the mean value of ΔSCA in TOMCAT is -6.38 ppb in the NHL, which shows a larger negative trend in the SCA than the observed mean ΔSCA value of -4 ppb. This is mostly due to the overestimation of the magnitude of the simulated ΔSCA at BRW. At WLG the model overestimates ΔSCA, again this is likely due to the model representation at this site. The time series of the SCA and its trend at each NOAA site can be found in the Supplement. The model performs better at the NOAA sites partly because these sites are used to provide optimised fluxes in our model and because ΔSCA was calculated over a long time period of 25 years. The independent site at Mace Head (GC-MD) also performs well because ΔSCA is calculated over a period of 18 years.

The independent sites in Siberia do not perform as well compared to GC-MD and the NOAA sites because of the large variability in the SCA over the relatively short time period (6 years) of observations. Despite some differences between the model and observations in the NHL and Non-NHL regions, the model still captures the change in the SCA across the globe, almost all within 1σ uncertainty of the observations. We are confident that the transport in the model is sufficient. Therefore, we can use TOMCAT to regionally attribute the changes in the SCA in the NHL.

4.3.3 The Role of OH

We use the TOM_regional simulation to determine the influence the increasing abundance of CH_4 in the atmosphere has on its removal by OH and the seasonal cycle. In the TOM_regional simulation we use OH fields which vary month to month but do not vary from year to year due to uncertainty in the annual variability. Some studies find a declining trend in OH from 2004 (Rigby et al., 2017; Turner et al., 2017) but Zhao et al. (2019) found an increasing trend in OH between 2000 and 2010. In contrast some studies only find small annual variability in OH (Patra et al., 2021; Naus et al., 2021). These studies contain large uncertainties and do not cover the full period of our study so a year to year variability in OH was not included in our TOMCAT simulations.

We find, using TOMCAT, in the northern hemisphere the ΔSCA due to OH loss is +1.0 ppb, and +1.1 ppb in the southern hemisphere. From this, we would expect the observation sites to show a ΔSCA of $\sim$1 ppb in the absence of any other changes, and any deviations from that are due to changes in transport and/or emissions. These results inform our expectation that the SCA is expected to increase with the increasing atmospheric burden of CH_4 due to more CH_4 being removed by OH.

4.3.4 Regional Contribution to ΔSCA in Northern High Latitudes

We now assess what is driving the decreasing SCA in the NHL by analysing the regional contributions at NHL sites in the TOM_regional simulation. Figure 4.5 shows the contribution of the background and tagged regions as a mean across all sites in each latitude band. The background tracer shows the largest contribution to negative ΔSCA in the NHL (-9.93 ppb, Fig. 4.5a). The background tracer represents CH_4 that is well-mixed in the atmosphere, likely from emissions from distant regions. The largest regional contributors to the negative ΔSCA in

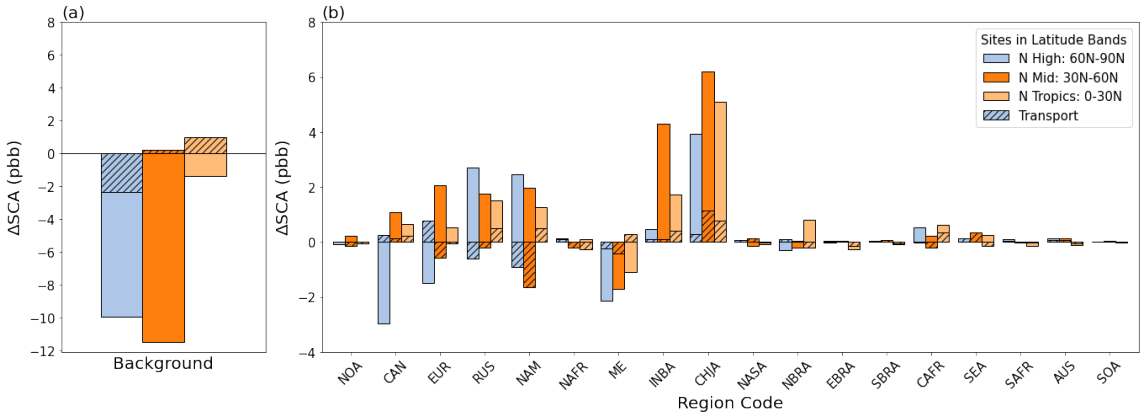

Figure 4.5: The contribution of the (a) background tracer and (b) regional tagged tracers to CH_4 ΔSCA (ppb) for 1995-2020 as a mean across all sites in the latitude band. The blue bars show the NHL and the orange bars are the two Non-NHL latitude bands in the northern hemisphere. The hatched bars show the contribution from transport (TOM_transport) and the solid colour represents the contribution from emissions (TOM_regional). Note, (a) and (b) have different scales.

the NHL include Canada (-2.97 ppb), Middle East (-2.13 ppb) and Europe (-1.48 ppb), shown in Fig. 4.5b. The China & Japan region has the largest positive influence on NHL ΔSCA (3.94 ppb). Despite some positive regional contributions of ΔSCA to the NHL, the ΔSCA in the NHL is still decreasing. This is due to the negative contribution of well-mixed emissions from the background tracer and large regional negative contributions from Canada, Europe and the Middle East.

The TOM_transport simulation represents the contribution of transport to the negative ΔSCA in the NHL and this simulation shows a different regional contribution compared to the TOM_regional simulation (Fig. 4.5, TOM_transport simulation is represented by the hatched bars). From this simulation we find that 33% of the negative ΔSCA in the NHL is due to changes to transport and this can be split into contributions from the background and regional tracers. The largest contribution from transport as a fraction of the total contribution of the tracer is from the background tracer which accounts for 23% (-2.32 ppb). Changes in the transport of emissions from North America and Russia have also contributed to the decrease in the SCA between 1995-2020 in the NHL, however the changes in emissions from these regions contribute to an increase in the SCA. The change in SCA due to emissions is larger in magnitude than the contribution from transport, resulting in an overall increase in the SCA in the NHL from these regions. The TOM_transport contribution to ΔSCA in NHL from Canada and Europe is 0.24 ppb and 0.77 ppb, respectively, resulting in an increase in the SCA in the NHL due to changes

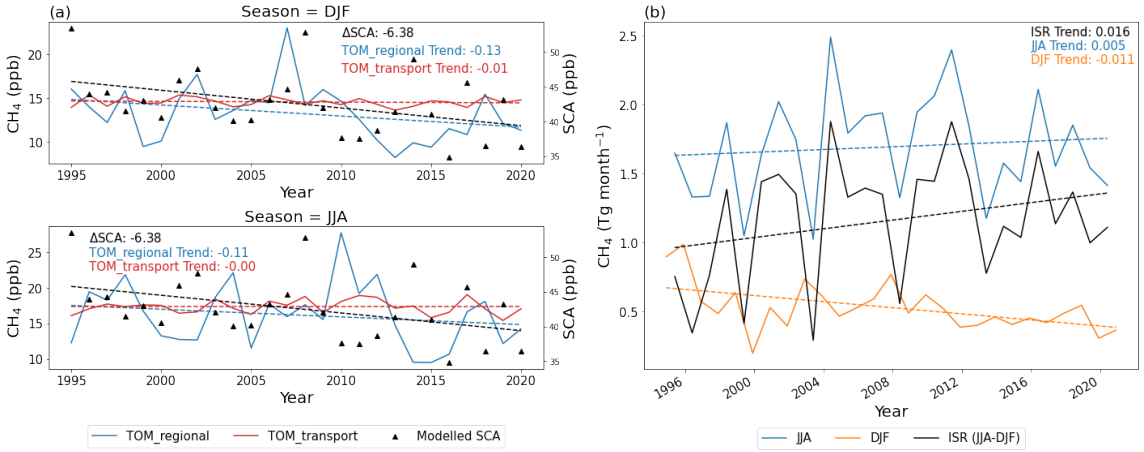

Figure 4.6: (a) Canada's seasonal mean CH_4 (ppb) contribution to the NHL sites (60N-90N) for TOM_regional (blue) and the TOMCAT_transport simulation (red) for 1995-2020. (b) Canada's seasonal mean emissions (Tg month^{-1}) from the inversion for JJA (blue), DJF (orange) and the interseasonal range (ISR, black) for 1995-2020.

in transport. However, changes in emissions result in an overall decrease in the SCA from these regions. This is due to the magnitude of the decrease in SCA being larger than the contribution from transport. This implies that their contributions to the negative ΔSCA in NHL are due to changes in emissions. We also assess the effect that the size of the regional tracers has on our results by normalising the regional contribution by area size. We find the largest contributors to the decreasing SCA in the NHL are still due to changes in emissions from Canada, Middle East and Europe (see Supplement Fig. A.4).

The TOMCAT simulations (TOM_regional and TOM_transport) show the largest contributions to the decrease in ΔSCA in the NHL are mostly due to changes in emissions from Canada, Middle East and Europe. To further investigate the changes in emissions that are driving the negative ΔSCA in the NHL we look at the trends of the regional CH_4 concentration (ppb) contributions from the TOM_regional and TOM_transport simulation as a mean across all sites in the NHL. We refer to these regional CH_4 concentration contributions as the tracer contribution. We also assess the trends of the seasonal emissions from each region. Often the trends in both the CH_4 contributions and the regional emissions are not statistically significant due to their large variability over time. However, we are interested in the direction of these trends in order to determine how emissions and transport from each region are changing over time and their impact on the seasonal cycle in the NHL. We compare the seasonal trends of regional tracer contributions (ppb) to the NHL from the TOMCAT_regional and TOMCAT_transport to further assess the contribution of emissions and transport from individual tracers. If the trend

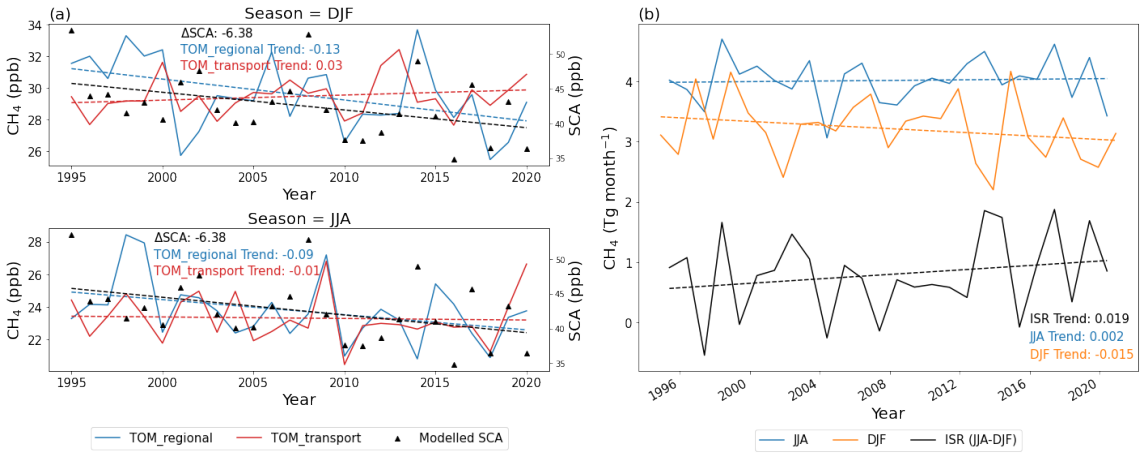

Figure 4.7: (a) Europe's mean CH_4 (ppb) contribution to the NHL sites (60N-90N) for the TOMCAT_regional (blue) and the TOMCAT_transport simulation (red) for 1995-2020. (b) Europe's mean emissions (Tg month^{-1}) from the inversion for JJA (blue), DJF (orange) and the interseasonal range (ISR, black) for 1995-2020.

in the TOMCAT_transport simulation is comparable to the trend in the TOMCAT_regional simulation we can attribute the change to transport and not emissions. To assess the change in the seasonal emissions we calculated the inter-seasonal range (ISR, Tg month^{-1}) which represents the difference between June, July, August (JJA) and December, January, February (DJF) seasonal mean emissions. It is important to note that the emission seasonal cycle is out of phase with the concentration seasonal cycle at northern mid- and high latitudes, so a positive ISR in emissions leads to a decreasing SCA. This is because the CH_4 seasonal cycle minimum is during the summertime in the NHL, so increasing emissions during this time would raise the minimum value, thereby shrinking the seasonal cycle. Similarly, shrinking wintertime emissions would bring down the seasonal maximum which occurs at the same time. This effect is mostly likely in regions near to sites in the NHL. We focus on the three largest regional contributors to the negative ΔSCA in the NHL: Canada, Europe and the Middle East. We also focus on the largest regional positive contributor of ΔSCA in the NHL, China & Japan, to assess its impact on the decreasing SCA at NHL sites.

When we look at the regional tracer contributions in the NHL from Canada and Europe we find stronger trends in the TOM_regional simulation, compared with no trends shown in the TOM_transport simulation during DJF and JJA seasons (Fig. 4.6a) and Fig. 4.7a). This shows that changes in emissions in these regions are driving the decrease in the NHL. This is also shown by a positive ISR in emissions from Canada and Europe (Fig. 4.6b and Fig. 4.7b). The Middle East's tracer contribution in the NHL shows no trends in the TOM_transport simulation

which means that changes in transport from this region has very little impact on the SCA in the NHL (Fig. 4.8a). As a result, changes in emissions in the Middle East are mostly driving the decrease in the SCA in the NHL. This is also shown by a positive ISR in emissions from the Middle East (Fig. 4.8b). Changes in emissions are the main contributor to the decrease in the SCA in the NHL from Canada, the Middle East and Europe. China & Japan contributes the most to increasing the SCA in the NHL, however the overall changes in emissions and transport from the background tracer and other regions still results in a decreasing SCA. We find that a cominbation of changes in emissions and changes in transport from China & Japan are causing an increase in the SCA in the NHL from this region (Fig. 4.9). By comparing the TOM_regional and TOM_transport simulations and the seasonal changes in emissions in these regions, we find that changes in emissions are the largest driver in changes in the SCA in the NHL.

Changes in emissions from Canada are mostly driven by increasing JJA emissions and decreasing DJF emissions. The changes in seasonal emissions lead to a positive ISR (0.02 Tg month^{-1} year^{-1}, pvalue=0.17, Fig. 4.6b). The trend of the DJF tracer contribution in the TOM_regional is decreasing at a faster rate (-0.13 ppb month^{-1}, pvalue = 0.13) than the JJA (-0.11 ppb month^{-1}, pvalue = 0.36), which results in a decrease in the SCA. There is some uncertainty in the trends of both the emissions and tracer contributions due to their large variability during the study period. The combination of weak trends in TOM_transport simulation and the positive ISR indicates that changes in DJF and JJA emissions from Canada is the main contributor to the decreasing SCA in this region.

The emissions from Europe during JJA are increasing slightly but there is a stronger decrease in the DJF emissions. The decrease in winter emissions result in a positive ISR (0.02 Tg month^{-1} year^{-1}, pvalue=0.3, Fig. 4.7b). The mean CH_4 tracer contribution from Europe to the NHL sites in the TOM_transport simulation shows a small positive trend in DJF and a very small decreasing trend in JJA (Fig. 4.7a). This shows that changes in winter transport are contributing to an increase in the SCA in the NHL. However large variability in the TOM_transport concentrations leads to some uncertainty on how much transport is having an impact from this region. The changes in emissions in the TOM_regional simulation contribute more to a decrease in the SCA. The TOM_regional DJF tracer contributions (-0.13 ppb month^{-1}, pvalue=0.02) from Europe are decreasing at a faster rate than the JJA tracer contributions (-0.09 ppb month^{-1}, pvalue=0.06), resulting in an decrease in the SCA. The positive ISR is supported by trends in

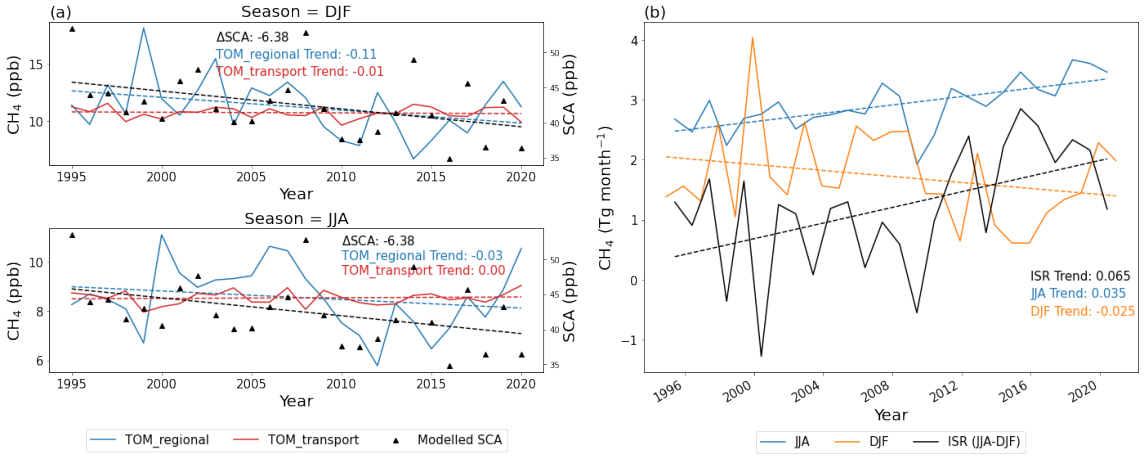

Figure 4.8: (a) The Middle East's mean CH_4 (pbb) contribution to the NHL sites (60N-90N) for the TOM_regional simulation (blue) and the TOM_transport simulation (red) for 1995-2020. (b) The Middle East's mean emissions (Tg month^{-1}) from the inversion for JJA (blue), DJF (orange) and the interseasonal range (ISR, black) for 1995-2020.

the tracer contributions being statistically significant which shows that changes in emissions from this region are driving the decrease in NHL.

The emissions from the Middle East are increasing in JJA and decreasing in DJF, which results in a positive ISR (0.07 Tg month^{-1} year^{-1}, pvalue=0.01, Fig. 4.8b). The mean CH_4 tracer contribution from the Middle East to the NHL sites is decreasing in both JJA (-0.04 ppb month^{-1}, pvalue=0.3) and DJF (-0.11 ppb month^{-1}, pvalue=0.07) in the TOM_regional simulation (Fig. 4.8a). The trend in DJF is decreasing faster than the trend in JJA, resulting in a decrease in the SCA. The combination of the positive trend in the ISR being statistically significant and the fast decreasing winter concentrations indicates that changes in emissions from this region are the main contributor to the decrease in the SCA in the NHL.

The emissions from China & Japan are decreasing slightly in JJA and increasing in DJF, resulting in a negative ISR (-0.07 Tg month^{-1} year^{-1}, pvalue=0.05, Fig. 4.9b). The mean CH_4 tracer contribution from this region to the NHL is increasing in DJF and JJA in the TOM_regional simulation (Fig. 4.9a). The DJF contribution is increasing at a faster rate (0.15 ppb month^{-1}, pvalue=0.03) than the JJA contribution (0.07 ppb month^{-1}, pvalue=0.21), resulting in an increase in the SCA. The TOM_transport simulation shows a small trend in DJF (0.015 ppb month^{-1}, pvalue=0.32) in the tracer contribution from this region and no trend in the JJA contribution, showing that transport is also contributing to an increase in the SCA in NHL. However there is some uncertainty in how much transport is having an impact due to the large variability in the trends in tracer contribution in the TOM_transport simulation. The

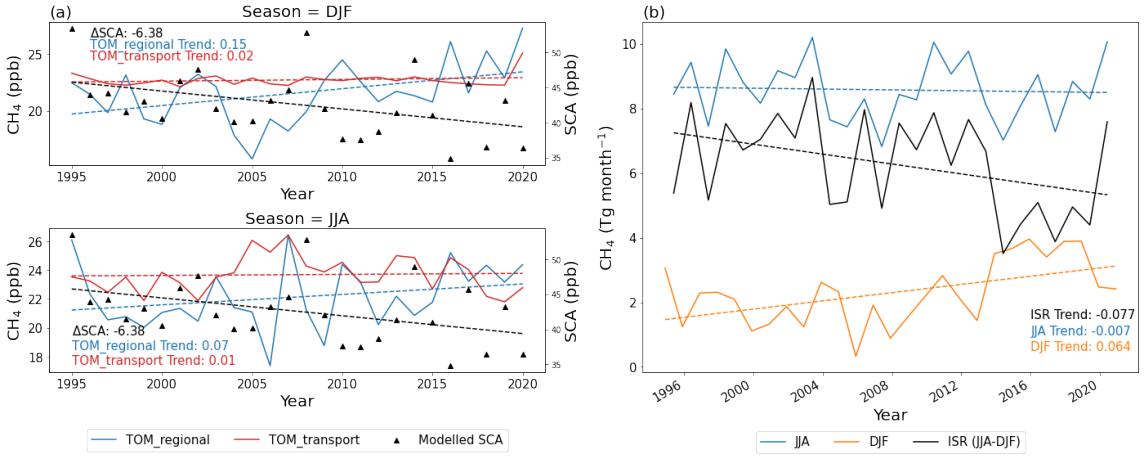

Figure 4.9: (a) shows China & Japan's mean CH_4 (pbb) contribution to the NHL sites (60N-90N) for the TOMCAT_regional (blue) and the TOMCAT_transport simulation (red) for 1995-2020. (b) shows China & Japan's mean emissions (Tg month^{-1}) from the inversion for JJA (blue), DJF (orange) and the interseasonal range (ISR, black) for 1995-2020.

TOMCAT simulations and emission trends show that changes in emissions and DJF transport from China & Japan contributes to an increase in the SCA in the NHL. However, the overall contribution from the background tracer and other regional tracers still results in a decrease in the SCA in the NHL.

4.3.5 Sensitivity Experiments

We carried out two sensitivity experiments to examine the impact of shorter and longer decay rates of regional tracers into the background tracer. These simulations are described in Sect. 4.2.2. The TOM_twelve simulation showed that changing the exponential decay rate from 9 months to 12 months did not change the largest contributors to the ΔSCA. This implies that after 9 months, CH_4 emissions has undergone long-range transport and no longer has a distinguishable emission origin, so has become well-mixed. Reducing the exponential decay rate to 1 month did, however, have an impact on the final results. The TOM_one simulation showed larger regional contributions in the NHL from Canada than the background tracer. The contribution from the background tracer in the TOM_one simulation contains emissions from southern regions because emissions from these regions will have been moved into the background tracer before they had the chance to reach the NHL. For regions close to the NHL sites, such as Canada and Russia, we can see the effect of those emissions before they become well-mixed. The recent local emissions from Canada are having an impact on the decreasing SCA but the effects of mixing and changes in transport will reduce this impact. These sensitivity experiments

show that the 9-month decay rate into the background is a good compromise for quantifying well-mixed emissions. It allows us to look at the effect from relatively recent emissions and also allows enough time for far-away emissions to be transported to the NHL in order to quantify their effect on the ΔSCA. More details on the sensitivity study can be found in Appendix A.3.

4.4 Discussion

Using the NOAA surface observations we have shown that globally the SCA of CH_4 is increasing but in the NHL it is decreasing. As the atmospheric burden of CH_4 is increasing it would be expected that the SCA would show a corresponding increase due to greater removal of CH_4 by OH in the atmosphere. Therefore, the change in the SCA in the NHL is counter-intuitive and we explore through TOMCAT simulations what is driving this decreasing SCA. A persistent change in the SCA indicates a long-term change in the sources, sinks and/or transport of CH_4 and the decreasing SCA in the NHL indicates a different response to the increasing atmospheric CH_4 burden compared to the rest of the world.

We use a TOMCAT-based atmospheric inversion which assimilates NOAA surface observations across the globe. There is a much greater number of sites situated in the northern hemisphere, compared with the southern hemisphere. There are large and variable sources of CH_4 in central Africa and Brazil but the model is not well constrained over these regions due to the lack of observations. The large contribution of emissions to the global CH_4 budget from central Africa and Brazil has been highlighted in a number of recent studies (Lunt et al., 2021; Wilson et al., 2021; Feng et al., 2022) so the surface emissions in our study might not fully capture the magnitude and distribution of emissions from these regions due to the lack of observations.

The TOMCAT tagged tracer simulations perform well when compared with observations (Fig. 4.4). However, from Fig. 4.4b it is noted that BRW, which is situated in the NHL, is an outlier in the model, compared with other sites. The model does capture the change in the SCA within the observation uncertainties, but these are large for this site. To test the influence of BRW on our results we removed it from our analysis. We find that Canada is no longer the largest regional contributor to the decrease in the SCA in the NHL and, in fact, contributes to an increase in the SCA at the other sites (ALT, ICE & ZEP). However, Europe and the Middle East remain the largest contributors to the decrease in the SCA at ALT, ICE and ZEP (See Supplement Fig. A.5). The removal of BRW from our analysis shows that local emissions

are having the largest impact at this site. This is likely due to a strong decrease in emissions in DJF and an increase in emissions in JJA in Alaska and western Canada during the study period (See Supplement Fig. A.7b). The seasonal changes in emissions over eastern Canada are different to Alaska and western Canada and it is likely that a different mechanism is having an effect on the other sites in the NHL. This test shows that the boundaries of the tagged tracer regions and the proximity of Canada and Europe to the NHL does have an impact on the results. For example, if Alaska was grouped into the North America (NAM) region, then NAM could be a large contributor to the decrease in the SCA due to the changes in emissions over Alaska. However, we include Alaska and Canada as one region due to their similar biomes and meteorology. Despite some differences between the model and observations (e.g. at ALT and BRW), TOMCAT does capture the significantly different behaviour in the NHL compared to the rest of the globe. The change in SCA in the NHL is consistently lower compared to the rest of the globe, implying that increasing emissions, both local and non-local, are impacting the NHL differently.

The main focus of our analysis was in the NHL, however observations Mace Head (MHD) also show a decreasing SCA, similar to what is observed in the NHL. When we included MHD in our analysis by extending the NHL (NHL_ext, 52N-60N), we found that its proximity to emission regions had an effect on the regional contribution to ΔSCA in the NHL_ext. Changes in emissions from Canada and the Middle East, and changes in transport from North America and the Middle East contribute the most to the decrease in the NHL_ext SCA. Europe contributes to an increase in the SCA in the NHL_ext (see Supplement Fig A.6). This is because MHD is strongly influenced by local trends in emissions in western Europe (see Supplement Fig. A.9b). The seasonal changes in eastern Europe are quite different to western Europe, which are likely to affect the sites north of 60N differently to MHD.

We can use the model to regionally attribute the change in the SCA because it performs well when compared with observations. However, it is difficult to disaggregate the contribution of different emission types within these regions. When possible, we have estimated emission types by looking at emission maps of each of the largest regional contributors and referring to literature. In addition to regional contributions, the regional tracers were allocated to a background tracer using an exponential 9-month decay rate to represent well-mixed methane that no longer has a distinguishable emission origin. It is not possible to tell from our simulations

what regions are contributing the most to the background tracer.

We have shown through TOMCAT simulations that well-mixed (background) CH_4, likely from emissions from regions far from the NHL, along with regions in the lower northern latitudes, are having a large influence on the SCA in the NHL. Whilst transport from the background tracer is a contributing factor to the decrease in the SCA in the NHL, 83% of all tracer contributions are due to emissions. Here we discuss the emissions sectors that might be driving these seasonal changes from the largest regional contributors to the change in the SCA in NHL. These include Canada, Europe, Middle East and China & Japan.

Canada has the largest negative contribution to the ΔSCA NHL due to emissions (-2.97 ppb), however we have shown that this region predominantly affects BRW. An increase in JJA and a decrease in DJF emissions have impacted the CH_4 contribution in the NHL, leading to a decrease in the SCA. There are a number of different sources which could contribute to the changes in emissions in Canada. Anthropgenic sources of CH_4 in Canada include oil and gas, livestock and landfills and natural sources include wetlands and biomass burning (Scarpelli et al., 2021). Studies investigating the seasonality of the Hudson Bay Lowlands, the second largest boreal wetland in the world, found the wetland emissions peak in July/August and decreases significantly in September-to-November (Pickett-Heaps et al., 2011; Fujita et al., 2018). Fujita et al. (2018) also found that biogenic sources are the most dominant for the seasonal cycle in this region and that the boreal wetlands are the main source. They found that fossil fuels and biomass burning are minor contributors to the CH_4 concentration seasonal cycle. Fossil fuels are often classed as a nonseasonal source but Fujita et al. (2018) find that they contribute significantly to the mole fraction of CH_4 in early winter at the Churchill observation site situated on Hudson Bay's coast. This implies that fossil fuel emissions have some seasonality in this region, peaking in winter. Lu et al. (2021) report that top-down estimates from satellite data show a decreasing trend in anthropgenic emissions for 2010-2017. The emissions used in our model show a decrease annually in September, indicating the wetlands are a large factor in this region's season cycle. The mean seasonal emissions for the study period peak in JJA over western Canada which is an area prone to wildfires and emissions are also large around the Boreal Plains (Environment and Climate Change Canada, 2016). Also the GFED fire emissions database (Werf et al., 2017) shows that annual emissions of CH_4 from biomass burning have been increasing from 1997-2020 (0.03 Tg year^{-1}, pvalue=0.01, see Supplement Fig. A.11).

Despite the emission trends in our results having high p-values, the direction of the trends follow changes reported by literature. It is likely that wetland and biomass burning emissions are increasing during the summer in Canada, contributing to the negative ΔSCA contribution to the NHL, predominantly at BRW, with some influence of decreasing anthropogenic emissions in the winter. The positive trends in emissions are often over wetland and biomass burning regions during summer and the winter decrease in emissions is strongest in western Canada where there are a few main cities (See Supplement, Fig. A.9b).

The Middle East region has the second largest contribution to the decreasing SCA in the NHL (-2.13 ppb). The trend in the ISR of emissions from the Middle East has a pvalue of 0.01 which further implies that emissions are responsible for the contribution to the negative ΔSCA in NHL. Emissions in this region are dominated by anthropogenic emissions such as oil and gas, agriculture and waste. A recent study has shown that the Middle East is one of the largest contributors to the rise in CH_4 emissions between 2000 and 2017 (Stavert et al., 2022). Our emission maps show the largest emissions in JJA, particularly over the Caspian Sea and the Persian Gulf, which is a region of significant oil and gas extraction. The seasonality of emissions from this region is not well documented so it is not possible to be certain of the change in emissions in this region that is contributing to the decreasing SCA in the NHL. The emissions used in the model indicate the largest increases in emissions in JJA and decreases in DJF emissions are in areas known for oil and gas extraction (Supplement, Fig. A.8b). From this, it is likely that anthropogenic emissions are driving the changes in contribution to the decrease in SCA in the NHL from this region.

Europe is the third largest contributor to the decrease in the SCA in the NHL (-1.48 ppb). The TOM_regional JJA and DJF trends in the concentration contributions to the NHL from this region are 0.06 ppb year^{-1} and 0.02 ppb year^{-1}, respectively. This highlights that it is mostly emissions contributing to the decrease in the SCA in this region. Emissions in Europe include natural sources such as wetlands, peatlands and wet soils, and anthropogenic emissions such as agriculture, waste and fossil fuels (Bergamaschi et al., 2018). It is often assumed that wetlands have the strongest seasonality and Bergamaschi et al. (2018) explained that precipitation is important for southern European wetlands but temperate and boreal wetlands are driven by temperature variations. Southern European wetlands could be impacted by a decreasing trend in precipitation shown by Christidis and Stott (2022), which could result in a decrease in wetland

emissions. It is hard to say what emission types are driving the decrease in winter emissions over Europe due to lack of studies of the seasonality of sources in this region; it is possible that sources other than wetlands are having an impact. For example, improvements in the efficiency of fossil fuel use, domestic and/or extraction could result in lower CH_4 emissions in winter.

China & Japan is the region which contributes the most to an increase in the SCA in the NHL. The DJF concentration contribution has a p-value of 0.02 so it is likely that this season is driving this positive contribution. Emissions in China & Japan are mostly driven by agriculture and waste and fossil fuels (Stavert et al., 2022). Stavert et al. (2022) found that fossil fuel emissions have increased by 114% in bottom-up estimates and 78% in top-down estimates between 2000 and 2017. The differences arise due to the emission inventories diverging towards the end of their study period. However, this does show that fossil emissions from China have increased significantly over the last two decades. Approximately 40% of China's anthropogenic emissions are from fossil fuels and the remainder is split equally between livestock, rice paddies and waste (Stavert et al., 2022). Our emissions show the largest emissions are situated in south east China (Supplement, Fig. A.10) where rice paddies, oil and gas, and waste are the main sources of CH_4 (Peng et al., 2016). Despite the fact that emissions are generally increasing in China and causing a large positive contribution to ΔSCA in the NHL, the SCA in the NHL is still decreasing.

We find that Russia does not contribute to the decrease in the SCA in the NHL, despite it being a region that has large natural and anthropogenic emissions of CH_4. The Russian emissions used in the forward simulation are not locally constrained before 2011 but transport from Russia to the NHL sites is short ($\sim$2 weeks) because it is largely zonal (Jacob, 1999). The inversion and forward simulations represent transport of emissions well which means that the four sites in NHL will be impacted by Russian emissions throughout the study period, even when the inversion has few sites to constrain the model in this region. Our results show that changes in transport from Russia contribute to a small decrease in the SCA with a ΔSCA of -0.6 ppb (See Fig. 4.5b). This is a small contribution to the decrease in the SCA in the NHL, which is why we decided to focus on Canada, the Middle East and Europe as they have the largest contributions to decrease in the SCA in the NHL.

There is some uncertainty in the seasonality of CH_4 emissions and how they change over time in Canada, the Middle East, Europe and China & Japan. The emissions used in TOMCAT were

discussed in Section 4.2.3. Our inversion uses prior information from various emission inventories. The prior emissions that predominantly drive the seasonal cycle are wetland emissions from WetCHARTS model and biomass burning emissions from GFEDv4.1s. These emission estimates have been evaluated in previous CH_4 studies (e.g. Parker et al. (2020) and Liu et al. (2020)). These prior emissions are optimised, including their seasonality, when the surface observations are assimilated in our inversion. This means that our emissions used in TOMCAT are optimised seasonally, however it is difficult to disaggregate the emission sectors driving the total emissions' seasonal cycle in each region.

The three main regions that contribute the most to the decreasing SCA in the NHL (Canada, Europe and Middle East) have common trends in emissions and tracer contributions to the NHL sites. The trends in regional tracer contributions across the whole of the NHL at the surface show similar results (See Supplement). In each region the winter emissions are generally decreasing and summer emissions are increasing over the study period. Similarly the regional DJF tracer contribution to the NHL generally decreases at a faster rate than the JJA tracer contribution, resulting in a decrease in the SCA, despite the fact that emissions from the region are increasing in JJA. This is likely due to a redistribution of emissions over time from each region, causing it to be transported differently to the NHL. We have shown that changes in well-mixed emissions and changes in emissions from Canada, Europe and the Middle East are the main contributors to the decreasing SCA in the NHL. The results show that the CH_4 SCA is changing and this should act as motivation to investigate the seasonality of emissions as it highlights changes in the CH_4 budget.

4.5 Conclusions

We have used a 3-D chemical transport model, TOMCAT, with emissions derived from surface observations, to investigate changes in the SCA of CH_4. Using TOMCAT we find that the global mean SCA increased by 1 ppb between 1995-2020 due to the increase in atmospheric CH_4 but this is offset by changes in emissions and transport. The NOAA surface observations show that globally the SCA has increased by a mean value of 2.5 ppb (6.5%) but decreased by 4 ppb (7.6%) in the NHL. The decreasing SCA in the NHL therefore does not follow the global trend and indicates that the seasonal cycle is responding differently to the global increase in atmospheric CH_4.

Our study focused on what was driving the decrease in the SCA in the NHLs and found that well-mixed methane, allocated to a modelled background tracer, was the largest contributor. Around 33% of the background tracer's contribution to the NHL could be attributed to changes in transport whilst the remaining contribution is from emissions. The background tracer contains CH_4 that has become well-mixed and no longer has a distinguishable emission origin. Emissions from distant regions are likely to be main contributors to the background tracer as it is transported to the NHL. The largest regional contributions to the negative ΔSCA in the NHL are from Canada, Europe and the Middle East. Increases in summer emissions from the Boreal Plains in Canada, decreases in winter emissions across Europe, and a combination of increases in summer emissions and decreases in winter emissions over the Arabian Peninsula and Capsian Sea in the Middle East are the other main contributors to the decrease in the SCA in the NHL.

The lack of studies that investigate the seasonality of emissions makes it hard to determine the source sector that is driving the change in emissions in these regions. The changes in the SCA in the NHL and globally indicate a long-term change in sources of CH_4 and highlight the seasonal response to the increasing CH_4 burden. More work is needed to investigate the seasonality of the sources that are having an impact on the decreasing SCA in the NHL.

References

Basso, L. S., Marani, L., Gatti, L. V., Miller, J. B., Gloor, M., Melack, J., Cassol, H. L. G., Tejada, G., Domingues, L. G., Arai, E., Sanchez, A. H., Corrêa, S. M., Anderson, L., Aragão, L. E. O. C., Correia, C. S. C., Crispim, S. P., and Neves, R. A. L. (Nov. 2021). "Amazon methane budget derived from multi-year airborne observations highlights regional variations in emissions". en. In: *Communications Earth & Environment* 2.1. ISSN: 2662-4435. DOI: 10.1038/s43247-021-00314-4.

Bergamaschi, P. et al. (2018). "Inverse modelling of European CH_4 emissions during 2006–2012 using different inverse models and reassessed atmospheric observations". en. In: *Atmospheric Chemistry and Physics* 18.2, pp. 901–920. ISSN: 1680-7324. DOI: 10.5194/acp-18-901-2018.

Bloom, A. A., Bowman, K. W., Lee, M., Turner, A. J., Schroeder, R., Worden, J. R., Weidner, R., McDonald, K. C., and Jacob, D. J. (2017). "A global wetland methane emissions and uncertainty dataset for atmospheric chemical transport models (WetCHARTs version 1.0)". In: *Geoscientific Model Development* 10.6, pp. 2141–2156. DOI: 10.5194/gmd-10-2141-2017.

Chipperfield, M. P. (2006). "New version of the TOMCAT/SLIMCAT off-line chemical transport model: Intercomparison of stratospheric tracer experiments". In: *Quarterly Journal of the Royal Meteorological Society* 132.617, pp. 1179–1203. DOI: https://doi.org/10.1256/qj.05.51.

Christidis, N. and Stott, P. A. (Aug. 2022). "Human Influence on Seasonal Precipitation in Europe". EN. In: *Journal of Climate* 35.15, pp. 5215–5231. ISSN: 0894-8755, 1520-0442. DOI: 10.1175/JCLI-D-21-0637.1.

Dlugokencky, E. J., Masarie, K. A., Tans, P. P., Conway, T. J., and Xiong, X. (1997). "Is the amplitude of the methane seasonal cycle changing?" en. In: *Atmospheric Environment* 31.1, pp. 21–26. ISSN: 1352-2310. DOI: 10.1016/S1352-2310(96)00174-4.

Dlugokencky, E. J., Steele, L. P., Lang, P. M., and Masarie, K. A. (1994). "The growth rate and distribution of atmospheric methane". In: *Journal of Geophysical Research: Atmospheres* 99.D8, pp. 17021–17043. DOI: https://doi.org/10.1029/94JD01245.

Dlugokencky, E., Crotwell, A., Mund, J., Crotwell, M., and Thoning, K. (2021). *Atmospheric Methane Dry Air Mole Fractions from the NOAA GML Carbon Cycle Cooperative Global Air Sampling Network, 1983-2020, Version: 2021-07-30.*

Environment and Climate Change Canada (2016). *Canadian Environmental Sustainability Indicators: Extent of Canada's Wetlands.* Accessed 25/10/2022.

Etiope, G., Ciotoli, G., Schwietzke, S., and Schoell, M. (2019). "Gridded maps of geological methane emissions and their isotopic signature". In: *Earth System Science Data* 11.1, pp. 1–22. DOI: 10.5194/essd-11-1-2019.

Feng, L., Palmer, P. I., Zhu, S., Parker, R. J., and Liu, Y. (Mar. 2022). "Tropical methane emissions explain large fraction of recent changes in global atmospheric methane growth rate". en. In: *Nature Communications* 13.1, p. 1378. ISSN: 2041-1723. DOI: 10.1038/s41467-022-28989-z.

Fujita, R., Morimoto, S., Umezawa, T., Ishijima, K., Patra, P. K., Worthy, D. E. J., Goto, D., Aoki, S., and Nakazawa, T. (2018). "Temporal Variations of the Mole Fraction, Carbon, and Hydrogen Isotope Ratios of Atmospheric Methane in the Hudson Bay Lowlands, Canada". In: *Journal of Geophysical Research: Atmospheres* 123.9, pp. 4695–4711. DOI: 10.1002/2017JD027972.

Gloor, E., Wilson, C., Chipperfield, M. P., Chevallier, F., Buermann, W., Boesch, H., Parker, R., Somkuti, P., Gatti, L. V., Correia, C., Domingues, L. G., Peters, W., Miller, J., Deeter, M. N., and Sullivan, M. J. P. (2018). "Tropical land carbon cycle responses to 2015/16 El Nino as recorded by atmospheric greenhouse gas and remote sensing data". In: *Philosophical Transactions of the Royal Society B: Biological Sciences* 373.1760, p. 20170302. DOI: 10.1098/rstb.2017.0302.

Hersbach, H. et al. (2020). "The ERA5 global reanalysis". In: *Quarterly Journal of the Royal Meteorological Society* 146.730, pp. 1999–2049. DOI: https://doi.org/10.1002/qj.3803.

Huijnen, V., Williams, J., Weele, M. van, Noije, T. van, Krol, M., Dentener, F., Segers, A., Houweling, S., Peters, W., Laat, J. de, Boersma, F., Bergamaschi, P., Velthoven, P. van, Le Sager, P., Eskes, H., Alkemade, F., Scheele, R., Nédélec, P., and Pätz, H.-W. (2010). "The global chemistry transport model TM5: description and evaluation of the tropospheric chemistry version 3.0". In: *Geoscientific Model Development* 3.2, pp. 445–473. DOI: 10.5194/gmd-3-445-2010.

Jacob, D. J. (Dec. 1999). *Introduction to Atmospheric Chemistry*. en. Princeton University Press. ISBN: 978-1-4008-4154-7.

Lin, X., Rogers, B. M., Sweeney, C., Chevallier, F., Arshinov, M., Dlugokencky, E., Machida, T., Sasakawa, M., Tans, P., and Keppel-Aleks, G. (2020). "Siberian and temperate ecosystems shape Northern Hemisphere atmospheric CO2 seasonal amplification". In: *Proceedings of the National Academy of Sciences* 117.35, pp. 21079–21087. ISSN: 0027-8424. DOI: 10.1073/pnas.1914135117.

Liu, T., Mickley, L. J., Marlier, M. E., DeFries, R. S., Khan, M. F., Latif, M. T., and Karambelas, A. (2020). "Diagnosing spatial biases and uncertainties in global fire emissions inventories: Indonesia as regional case study". In: *Remote Sensing of Environment* 237, p. 111557.

Lu, X., Jacob, D. J., Zhang, Y., Maasakkers, J. D., Sulprizio, M. P., Shen, L., Qu, Z., Scarpelli, T. R., Nesser, H., Yantosca, R. M., Sheng, J., Andrews, A., Parker, R. J., Boesch, H., Bloom, A. A., and Ma, S. (Mar. 2021). "Global methane budget and trend, 2010–2017: complementarity of inverse analyses using in situ (GLOBALVIEWplus CH_4 ObsPack) and satellite (GOSAT) observations". English. In: *Atmospheric Chemistry and Physics* 21.6. Publisher: Copernicus GmbH, pp. 4637–4657. ISSN: 1680-7316. DOI: 10.5194/acp-21-4637-2021.

Lunt, M. F., Palmer, P. I., Lorente, A., Borsdorff, T., Landgraf, J., Parker, R. J., and Boesch, H. (2021). "Rain-fed pulses of methane from East Africa during 2018–2019 contributed to atmospheric growth rate". In: *Environmental Research Letters* 16.2. Publisher: IOP Publishing. ISSN: 1748-9326. DOI: 10.1088/1748-9326/abd8fa.

M, C., D, G., M, M., and E, S. (2021). *EDGAR v5.0 Global Air Pollutant Emissions*.

McNorton, J., Wilson, C., Gloor, M., Parker, R. J., Boesch, H., Feng, W., Hossaini, R., and Chipperfield, M. P. (2018). "Attribution of recent increases in atmospheric methane through 3-D inverse modelling". In: *Atmospheric Chemistry and Physics* 18.24, pp. 18149–18168. DOI: 10.5194/acp-18-18149-2018.

Meirink, J. F., Bergamaschi, P., and Krol, M. C. (2008). "Four-dimensional variational data assimilation for inverse modelling of atmospheric methane emissions: method and comparison with synthesis inversion". In: *Atmospheric Chemistry and Physics* 8.21, pp. 6341–6353. DOI: 10.5194/acp-8-6341-2008.

Monks, S. A., Arnold, S. R., Hollaway, M. J., Pope, R. J., Wilson, C., Feng, W., Emmerson, K. M., Kerridge, B. J., Latter, B. L., Miles, G. M., Siddans, R., and Chipperfield, M. P. (2017). "The TOMCAT global chemical transport model v1.6: description of chemical mechanism and model evaluation". In: *Geoscientific Model Development* 10.8, pp. 3025–3057. DOI: 10.5194/gmd-10-3025-2017.

Murguia-Flores, F., Arndt, S., Ganesan, A. L., Murray-Tortarolo, G., and Hornibrook, E. R. C. (2018). "Soil Methanotrophy Model (MeMo v1.0): a process-based model to quantify global uptake of atmospheric methane by soil". In: *Geoscientific Model Development* 11.6, pp. 2009–2032. DOI: 10.5194/gmd-11-2009-2018.

Naus, S., Montzka, S. A., Patra, P. K., and Krol, M. C. (Mar. 2021). "A three-dimensional-model inversion of methyl chloroform to constrain the atmospheric oxidative capacity". English. In: *Atmospheric Chemistry and Physics* 21.6, pp. 4809–4824. ISSN: 1680-7316. DOI: 10.5194/acp-21-4809-2021.

Nisbet, E. G. et al. (2016). "Rising atmospheric methane: 2007–2014 growth and isotopic shift". In: *Global Biogeochemical Cycles* 30.9, pp. 1356–1370. DOI: https://doi.org/10.1002/2016GB005406.

Nisbet, E. G. et al. (2019). "Very Strong Atmospheric Methane Growth in the 4 Years 2014–2017: Implications for the Paris Agreement". In: *Global Biogeochemical Cycles* 33.3, pp. 318–342. DOI: https://doi.org/10.1029/2018GB006009.

Parker, R. J., Boesch, H., McNorton, J., Comyn-Platt, E., Gloor, M., Wilson, C., Chipperfield, M. P., Hayman, G. D., and Bloom, A. A. (2018). "Evaluating year-to-year anomalies in tropical wetland methane emissions using satellite CH4 observations". In: *Remote Sensing of Environment* 211, pp. 261–275. ISSN: 0034-4257. DOI: https://doi.org/10.1016/j.rse.2018.02.011.

Parker, R. J., Wilson, C., Bloom, A. A., Comyn-Platt, E., Hayman, G., McNorton, J., Boesch, H., and Chipperfield, M. P. (2020). "Exploring constraints on a wetland methane emission ensemble (WetCHARTs) using GOSAT observations". In: *Biogeosciences* 17.22. Publisher: Copernicus GmbH. ISSN: 1726-4170. DOI: 10.5194/bg-17-5669-2020.

Patra, P. K., Krol, M. C., Prinn, R. G., Takigawa, M., Mühle, J., Montzka, S. A., Lal, S., Yamashita, Y., Naus, S., Chandra, N., Weiss, R. F., Krummel, P. B., Fraser, P. J., O'Doherty, S., and Elkins, J. W. (2021). "Methyl Chloroform Continues to Constrain the Hydroxyl (OH) Variability in the Troposphere". In: *Journal of Geophysical Research: Atmospheres* 126.4, e2020JD033862. ISSN: 2169-8996. DOI: 10.1029/2020JD033862.

Patra, P. K. et al. (2011). "TransCom model simulations of CH_4 and related species: linking transport, surface flux and chemical loss with CH_4 variability in the troposphere and lower stratosphere". In: *Atmospheric Chemistry and Physics* 11.24, pp. 12813–12837. DOI: 10.5194/acp-11-12813-2011.

Peng, S., Piao, S., Bousquet, P., Ciais, P., Li, B., Lin, X., Tao, S., Wang, Z., Zhang, Y., and Zhou, F. (Nov. 2016). "Inventory of anthropogenic methane emissions in mainland China from 1980 to 2010". In: *Atmospheric Chemistry and Physics* 16.22. ISSN: 1680-7324. DOI: 10.5194/acp-16-14545-2016.

Pickers, P. A. and Manning, A. C. (2015). "Investigating bias in the application of curve fitting programs to atmospheric time series". In: *Atmospheric Measurement Techniques* 8.3, pp. 1469–1489. DOI: 10.5194/amt-8-1469-2015.

Pickett-Heaps, C. A., Jacob, D. J., Wecht, K. J., Kort, E. A., Wofsy, S. C., Diskin, G. S., Worthy, D. E. J., Kaplan, J. O., Bey, I., and Drevet, J. (2011). "Magnitude and seasonality of wetland methane emissions from the Hudson Bay Lowlands (Canada)". In: *Atmospheric Chemistry and Physics* 11.8, pp. 3773–3779. ISSN: 1680-7324. DOI: 10.5194/acp-11-3773-2011.

Prinn, R. G. et al. (2018). "History of chemically and radiatively important atmospheric gases from the Advanced Global Atmospheric Gases Experiment (AGAGE)". In: *Earth System Science Data* 10.2, pp. 985–1018. DOI: 10.5194/essd-10-985-2018.

Randerson, J., Van Der Werf, G., Giglio, L., Collatz, G., and Kasibhatla, P. (2017). *Global Fire Emissions Database, Version 4.1 (GFEDv4)*. en. DOI: 10.3334/ORNLDAAC/1293.

Rigby, M., Montzka, S. A., Prinn, R. G., White, J. W. C., Young, D., O'Doherty, S., Lunt, M. F., Ganesan, A. L., Manning, A. J., Simmonds, P. G., Salameh, P. K., Harth, C. M., Mühle, J., Weiss, R. F., Fraser, P. J., Steele, L. P., Krummel, P. B., McCulloch, A., and Park, S. (2017). "Role of atmospheric oxidation in recent methane growth". In: *Proceedings of the National Academy of Sciences* 114.21, pp. 5373–5377. ISSN: 0027-8424. DOI: 10.1073/pnas.1616426114.

Sasakawa, M., Shimoyama, K., Machida, T., Tsuda, N., Suto, H., Arshinov, M., Davydov, D., Fofonov, A., Krasnov, O., Saeki, T., Koyama, Y., and Maksyutov, S. (2010). *Continuous measurements of methane from a tower network over Siberia*. Reference Date: 2022/10/20. DOI: 10.17595/20160901.004.

Saunois, M. et al. (2020). "The Global Methane Budget 2000–2017". In: *Earth System Science Data* 12.3, pp. 1561–1623. DOI: 10.5194/essd-12-1561-2020.

Scarpelli, T. R., Jacob, D. J., Moran, M., Reuland, F., and Gordon, D. (Dec. 2021). "A gridded inventory of Canada's anthropogenic methane emissions". In: *Environmental Research Letters* 17.1, p. 014007. ISSN: 1748-9326. DOI: 10.1088/1748-9326/ac40b1.

Spivakovsky, C. M., Logan, J. A., Montzka, S. A., Balkanski, Y. J., Foreman-Fowler, M., Jones, D. B. A., Horowitz, L. W., Fusco, A. C., Brenninkmeijer, C. A. M., Prather, M. J., Wofsy,

S. C., and McElroy, M. B. (2000). "Three-dimensional climatological distribution of tropospheric OH: Update and evaluation". In: *Journal of Geophysical Research: Atmospheres* 105.D7, pp. 8931–8980. DOI: https://doi.org/10.1029/1999JD901006.

Stavert, A. R. et al. (2022). "Regional trends and drivers of the global methane budget". In: *Global Change Biology* 28.1. ISSN: 1365-2486. DOI: 10.1111/gcb.15901.

Thoning, K. W., Tans, P. P., and Komhyr, W. D. (1989). "Atmospheric carbon dioxide at Mauna Loa Observatory: 2. Analysis of the NOAA GMCC data, 1974–1985". In: *Journal of Geophysical Research: Atmospheres* 94.D6, pp. 8549–8565. DOI: https://doi.org/10.1029/JD094iD06p08549.

Tohjima, Y. et al. (2016a). *Continuous observational data of atmospheric CH4 mixing ratios on Cape Ochi-ishi, Ver. 1.0*. Reference Date: 2022/06/30. DOI: 10.17595/20160901.003..

– (2016b). *Continuous observational data of atmospheric CH4 mixing ratios on Hateruma Island, Ver. 1.2)*. Reference Date: 2022/06/30. DOI: 10.17595/20160901.003..

Tohjima, Y., Machida, T., Utiyama, M., Katsumoto, M., Fujinuma, Y., and Maksyutov, S. (2002). "Analysis and presentation of in situ atmospheric methane measurements from Cape Ochi-ishi and Hateruma Island". In: *Journal of Geophysical Research: Atmospheres* 107.D12, ACH 8-1-ACH 8–11. DOI: https://doi.org/10.1029/2001JD001003.

Turner, A. J., Frankenberg, C., Wennberg, P. O., and Jacob, D. J. (2017). "Ambiguity in the causes for decadal trends in atmospheric methane and hydroxyl". In: *Proceedings of the National Academy of Sciences* 114.21, pp. 5367–5372. ISSN: 0027-8424. DOI: 10.1073/pnas.1616020114.

Weber, T., Wiseman, N. A., and Kock, A. (2019). "Global ocean methane emissions dominated by shallow coastal waters". In: *Nature communications* 10.1, pp. 1–10.

Werf, G. R. van der, Randerson, J. T., Giglio, L., Leeuwen, T. T. van, Chen, Y., Rogers, B. M., Mu, M., Marle, M. J. E. van, Morton, D. C., Collatz, G. J., Yokelson, R. J., and Kasibhatla, P. S. (2017). "Global fire emissions estimates during 1997–2016". In: *Earth System Science Data* 9.2, pp. 697–720. DOI: 10.5194/essd-9-697-2017.

Wilson, C., Chipperfield, M. P., Gloor, M., and Chevallier, F. (2014). "Development of a variational flux inversion system (INVICAT v1.0) using the TOMCAT chemical transport model". In: *Geoscientific Model Development* 7.5, pp. 2485–2500. DOI: 10.5194/gmd-7-2485-2014.

Wilson, C., Chipperfield, M. P., Gloor, M., Parker, R. J., Boesch, H., McNorton, J., Gatti, L. V., Miller, J. B., Basso, L. S., and Monks, S. A. (2021). "Large and increasing methane emissions from eastern Amazonia derived from satellite data, 2010–2018". In: *Atmospheric Chemistry and Physics* 21.13, pp. 10643–10669. DOI: 10.5194/acp-21-10643-2021.

Wilson, C., Gloor, M., Gatti, L. V., Miller, J. B., Monks, S. A., McNorton, J., Bloom, A. A., Basso, L. S., and Chipperfield, M. P. (2016). "Contribution of regional sources to atmospheric methane over the Amazon Basin in 2010 and 2011". In: *Global Biogeochemical Cycles* 30.3, pp. 400–420. DOI: https://doi.org/10.1002/2015GB005300.

Zhao, Y. et al. (2019). "Inter-model comparison of global hydroxyl radical (OH) distributions and their impact on atmospheric methane over the 2000-2016 period". In: *Atmospheric Chemistry and Physics* 19.21, pp. 13701–13723. DOI: 10.5194/acp-19-13701-2019.

Chapter 5

Development of a nested grid version of the TOMCAT chemical transport model (ZOOMCAT v1.0)

Emily Dowd[1], Chris Wilson[1,2], Martyn P. Chipperfield[1,2], Emanuel Gloor[3], Alistair Manning[4], Ruth Doherty[5]

[1]School of Earth & Environment, University of Leeds, Leeds, UK
[2]National Centre for Earth Observation, University of Leeds, Leeds, UK
[3]School of Geography, University of Leeds, Leeds, UK
[4]Met Office, Exeter, UK
[5]School of GeoSciences, University of Edinburgh, Edinburgh, UK

Abstract

This paper summarises development of a new one-way nested grid model, ZOOMCAT, based on the global chemical transport model TOMCAT. TOMCAT is used in a range of global studies of atmospheric constituents but is currently too computationally expensive to run at high resolution globally for long periods of time. The nested grid model is able to simulate a region of interest at high resolution, with boundary conditions provided by the global coarse model. With the increase in spatial resolution of observations, it is important to be able to simulate atmospheric constituents on the same scale to better represent observed changes.

We carry out two case studies using CH_4 measurements from tall tower sites and satellite

retrievals over Europe to demonstrate the performance of ZOOMCAT and the increase in spatial resolution. One case study simulated CH_4 using coarse resolution meteorology. The other case study simulated the Nord Stream gas leak to demonstrate model transport with high-resolution meteorology. These case studies combined show the importance of meteorology in ZOOMCAT simulations. We find that ZOOMCAT does not perform better than TOMCAT when compared with observations and recommend using high resolution meteorology to improve the model simulations. However, further work is needed to identify why the increase in spatial resolution in ZOOMCAT does not improve simulated concentrations when compared with TOMCAT.

5.1 Introduction

Chemical transport models (CTMs) are useful tools for investigating changes in atmospheric constituents and are widely used in a number of studies to address a range of scientific problems. A Eulerian CTM is a numerical computer model which simulates atmospheric constituents in a fixed frame of reference represented as a 3D grid and has a fixed coordinate system (Jacob, 1999). The spatial resolution of observations of atmospheric constituents has been increasing and currently global CTMs are often too computationally expensive to run for long periods of time at the same spatial resolution of these new observations. This is because the atmosphere is split into a finite number of grid boxes to simulate transport of mass across these grid boxes. A higher spatial resolution increases the number of grid boxes and therefore the computational expense. To address this problem, a high-resolution grid can be developed for CTMs and applied over a smaller region - "nested" within the global grid. In a nested grid model, atmospheric constituents are therefore simulated globally at a coarse spatial resolution, providing the boundary conditions for a regional simulation at a higher spatial resolution. When the flow of information is directed only from the coarse grid to the finer one, this is called a one-way nested grid approach. The nested grid approach means that areas of interest can be modelled at high spatial resolution without the computational expense of running the model at high resolution globally.

The concentrations of atmospheric constituents can be influenced by a number of factors. For example, methane (CH_4) is influenced by local sources, long-range transport, vertical exchange with the stratosphere and chemical removal (which occurs predominantly in the tropics). As a result, it is important to consider the entire Earth's atmosphere when simulating regional

atmospheric composition. Therefore, a nested grid model is a suitable approach for high-resolution regional modelling. CTMs such as TM5 and GEOS-Chem have nested grid models and it has been shown that the higher spatial resolution represents chemical species better when compared with surface and aircraft observations, respectively (e.g. Wang et al. (2004) and Krol et al. (2005)). There are several methods available to measure atmospheric constituents, including surface observations, tall tower observations, surface-based mobile surveys, aircraft campaigns and satellite observations. These different methods are representative across varying spatial and temporal scales.

In recent years the spatial and temporal resolution of satellite observations in particular have increased. For example, the Tropospheric Monitoring Instrument (TROPOMI) onboard Sentinel-5P, launched in 2017, has a spatial resolution of 5.5 km $\times$ 7 km with near-global coverage every day (Lorente et al., 2021). It measures atmospheric constituents such as CH_4, carbon monoxide (CO), ozone (O_3) and nitrogen dioxide (NO_2). TROPOMI's spatial resolution improves on instruments such as the Infrared Atmospheric Sounding Interferometer (IASI) on MetOp and Ozone Monitoring Instrument (OMI) on NASA's EOS-Aura satellite, which already have relatively high resolution. IASI has a pixel size of $\sim$12 km in diameter and provides global coverage twice per day and OMI has a spatial resolution of 24 km $\times$ 13 km with daily global coverage (Boersma et al., 2007; Siddans et al., 2017). For CH_4, the Greenhouse Gases Observing Satellite (GOSAT) is predominately used due to its vertical sensitivity close to the surface. GOSAT has a pixel size of 10 km in diameter and global coverage every 3 days, resulting in sparse coverage for chemical transport modelling studies (Parker et al., 2011). The highest spatial resolution global CTMs are generally simulated at is $\sim 1^\circ \times 1^\circ$, which is approximately 100 km at the equator, which is too coarse to compare with satellite data. The increase in spatial resolution of observations provides more information on the spatial distribution of sources and how these atmospheric constituents are changing, emphasising the importance of being able to simulate them at the same spatial scales in models.

Nested grid modelling has been used in a number of atmospheric composition studies with comparisons to different observation types. The combination of satellite observations and nested grid modelling has improved our understanding of the interannual variability of carbon monoxide (CO) over the Amazon, by being able to compare the nested model derived emission estimates with bottom-up estimates over specific Brazilian states and land-use types (Naus et al., 2022).

Similarly, nested grid modelling combined with surface observations have also shown that anthropogenic emission estimates by the Emissions Database for Global Atmospheric Research (EDGAR v6.0) are not able to reproduce the observed trend in atmospheric CH_4 concentrations over Europe from 2012-2020 (Mannisenaho et al., 2023).

In this paper, we present a new one-way nested grid model, ZOOMCAT, based on the TOMCAT CTM. TOMCAT is a Eulerian three-dimensional CTM, first described by Chipperfield et al. (1993). It was was created in the early 1990s to study the polar stratosphere. TOMCAT was originally two separate models known as TOMCAT and SLIMCAT, which were used for modelling the troposphere and stratosphere respectively, but were later combined into one model and named TOMCAT (Chipperfield, 2006). Currently, the maximum practical spatial resolution of TOMCAT is $\sim 1.125° \times 1.125°$, which is approximately 100 km at the equator. The spatial resolution of TOMCAT is too coarse to simulate atmospheric species with the same detail as satellite observations such as those from TROPOMI. TOMCAT has been successfully used in a number of studies, including Wilson et al. (2021), Pimlott et al. (2022), and Arosio et al. (2024). A nested grid model for TOMCAT will allow us to model selected regions at a higher spatial resolution and increase our understanding of changes in atmospheric composition, as demonstrated by Naus et al. (2022) and Mannisenaho et al. (2023). In 2014, a variational inverse transport model, INVICAT, based on the TOMCAT CTM was developed providing optimised emission estimates of atmospheric constituents (Wilson et al., 2014). In future, it would be beneficial to combine ZOOMCAT and INVICAT to produce optimised high resolution emissions to be used in ZOOMCAT.

We focus here on simulating atmospheric CH_4 in both ZOOMCAT and TOMCAT to demonstrate improvements in spatial resolution and compare our results to tall tower observations from the Integrated Carbon Observations System (ICOS) and satellite retrievals from TROPOMI. We selected CH_4 as our case study so we could assess ZOOMCAT's spatial representation of CH_4 against the high resolution retrievals from TROPOMI and simulate CH_4 from the Nord Stream gas leaks to demonstrate ZOOMCAT's high-resolution transport of plumes. Atmospheric CH_4 is the second most important anthropogenic greenhouse gas in our atmosphere after carbon dioxide (CO_2). Global variations of CH_4 are not fully understood (Nisbet et al., 2019). The combination of high-resolution satellite data and high-resolution models will provide further insight into what might be driving these variations on a regional scale because the spatial rep-

resentation of transport and distribution of emissions in the model will be improved. We have selected Europe as our nested region for this study because it emits a mixture of natural and anthropogenic sources - for example wetlands, landfills and oil and gas emissions. Europe is also influenced by well-mixed CH_4 from the North Atlantic and has a dense network of CH_4 observations suitable for validating ZOOMCAT.

The structure of this paper is as follows. In Section 5.2 we describe the TOMCAT model, while in Section 5.3 we describe ZOOMCAT, the nested grid approach to TOMCAT. In Section 5.5 we describe the observations used to validate the model. In Section 5.4 we describe the atmospheric CH_4 simulation using ZOOMCAT over Europe and in Section 5.6 we describe the performance of ZOOMCAT when compared with observations and TOMCAT.

5.2 TOMCAT Chemical Transport Model

TOMCAT is an offline Eulerian CTM described in Chipperfield et al. (1993), Chipperfield (1999), Chipperfield (2006) and Monks et al. (2017). The horizontal grid in TOMCAT is a variable Gaussian grid with regular longitudinal spacing and irregular latitudinal spacing. The vertical grid follows σ-p coordinates. The model is typically run at a spatial resolution of 2.8°× 2.8° with 60 vertical levels up to 0.1 hPa for full chemistry simulations. The model has the capability to be run at a horizontal resolution of ∼1.125°× 1.125°, although in this study we perform simulations at 2.8°× 2.8° to reduce computational requirements. The model meteorology is driven by the European Centre for Medium-Range Weather Forecasts (ECMWF) ERA5 reanalyses (Hersbach et al., 2020a). The meteorology is read into the model every 6 hours and transformed onto the TOMCAT model grid. The model uses a process split method, where separate processes which affect tracers are represented in different routines in the model and are executed in sequence. The main transport processes in the model include advection, convection and boundary layer mixing. The advection scheme is based on Prather (1986) and conserves second-order moments of the tracer distribution. The advection scheme is split in to three subroutines which execute tracer transport zonally, meridionally and vertically. The convection scheme uses archived mass fluxes of updraft/downdraft detrainment rate and updraft/downdraft fluxes from ECMWF ERA5 reanalyses. The ERA5 instantaneous updraft/downdraft entrainment/detrainments mass flux is recalculated every six hours to match the large-scale meteorological forcing provided by ECMWF (Feng et al., 2011). These values are used here

in the model's convective transport scheme instead of the previous "online" scheme based on Tiedtke (1989). The archived mass fluxes are used so that the convection is more consistent with the ECMWF meteorological forcing. Feng et al. (2011) shows in a simulation with a radon tracer that the use of the archived mass fluxes in the TOMCAT convection scheme provides some improvements to the model relative to the previous scheme, when compared with observations. Similarly, a new boundary layer mixing scheme, developed in this study, takes pre-calculated boundary layer height (BLH) from the ECMWF reanalyses. The model calculates the total tracer mass in the planetary boundary layer (PBL) and equally distributes the tracer mass across the PBL. This method, similar to the convective archived mass flux scheme, means that the PBL height is now also consistent with the forcing meteorological reanalyses. The model contains the option of a full tropospheric chemistry scheme, described in Monks et al. (2017), simulating 79 chemical species with 220 chemical reactions. There is also an option to replace the full chemistry scheme with a simplified offline version in which previously calculated fields of either 4D mixing ratios of sink species or 4D loss rates are read in to the model instead of being calculated online, increasing the computational speed and giving flexibility in selecting the CH_4 loss rates without having to rely on the full chemistry scheme. Previous studies of atmospheric composition using TOMCAT include Wilson et al. (2021), Pimlott et al. (2022), and Arosio et al. (2024)

5.3 ZOOMCAT Description

ZOOMCAT is the nested grid model based on the TOMCAT CTM. As in TOMCAT, the transport emissions and chemistry of tracers are solved by the process split method (described in Section 5.2). Both TOMCAT and ZOOMCAT are driven by meteorological data from ECMWF and we require mass conservation and positive concentrations. Negative concentrations are not permitted in the model because they cause problems in mathematical routines which solve equations of chemical interactions between species (Krol et al., 2005). The nested grid modelling technique is to simulate an area of interest at a higher spatial resolution to the global model. The coarse region represents the global domain, named Level 1 (L1), and provides the boundary conditions for the higher resolution nested region, named Level 2 (L2). At present the L2 grid does not transfer information back to the L1 grid and as a result ZOOMCAT is currently a one-way nested grid. The L1 grid is therefore simulated independently from the L2 grid; it is

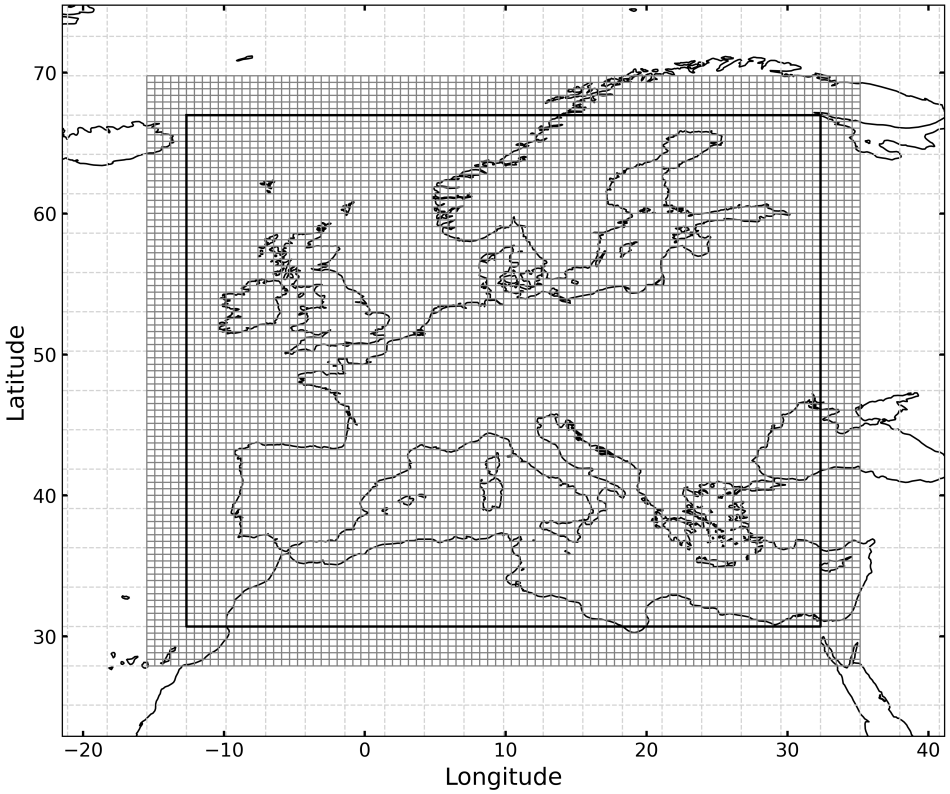

Figure 5.1: Example schematic representation of ZOOMCAT. The thick black line is the boundary of the nested model. The small grid boxes outside the black box in the fine-resolution domain represent the buffer zone for boundary conditions. In this example the coarse grid is at a resolution of $\sim$2.8°$\times$ 2.8° and the nested grid is at a resolution of $\sim$0.5°$\times$ 0.5°.

planned to implement the L2 to L1 feedback in the future.

The L2 grid location and horizontal resolution is initialised by specifying several criteria which are based on the L1 grid. The western-most boundary of the L2 grid is determined by specifying the number of L1 grid boxes to offset from the prime meridian in the eastwards direction. The northern-most boundary of the L2 grid is determined by specifying the number of L1 grid boxes to offset from L1's northern-most grid box in the southwards direction. The extent of the L2 domain is dependent on the number of latitude and longitude grid boxes specified in the L2 grid and the resolution is dependent on the number of L2 grid boxes for each L1 grid box. The L1 grid box can be divided up by different number of L2 grid boxes in the latitudinal and longitudinal directions. The ability to specify these criteria means that ZOOMCAT's location, domain size and spatial resolution is fully flexible and can be adjusted to the users requirements. The limitations of the spatial resolution will be discussed in Section 5.7. Figure 5.1 shows an example of a L2 grid, overlaid on the L1 grid. The vertical grid in ZOOMCAT follows the same σ-p coordinates as TOMCAT, in the simulations presented here, with 60 vertical levels up to 0.1

hPa. The model vertical grid is fully flexible, therefore it is possible to use a different vertical grid for L2.

Once the L2 horizontal grid has been initialised, the tracer mixing ratio and some meteorological model parameters are linearly interpolated to the L2 grid. At the start of each 6-hour cycle, the winds and convection fields are linearly interpolated onto both the L1 and L2 grids. The model is then integrated over the time steps within each 6 hour cycle, interpolating the meteorology to each model time step. The meteorological data can be supplied to the model at any spectral resolution as it is then linearly interpolated online to the correct L1 or L2 resolution. In order to optimise the L2 grid, it is preferable to supply the meteorological data at the highest available resolution which is currently at $\sim$1.125°$\times$ 1.125°. The meteorological data is stored locally at the same spatial resolution as TOMCAT to minimise the use of local storage. At the start of each model time step the meteorological parameters are linearly interpolated from the $\sim$1.125°$\times$ 1.125° onto the L2 grid. A buffer region of high-resolution grid boxes is implemented so that the L1 grid provides boundary conditions for the L2 grid at every model time step. The outermost grid boxes in the L2 that fit into one L1 grid box are selected as the buffer zone (see Figure 5.1). The L1 tracer mixing ratios in this buffer region are linearly interpolated onto the L2 grid, converted to tracer mass and used as the boundary conditions. The grid box mass is calculated from the surface area of the grid box and its pressure at the vertical boundaries. By applying the boundary conditions at the start of each model iteration, the L1 tracer mixing ratio has undergone all the transport and chemical processes during the previous iteration. This assumes that all the transport and chemistry happens at the same time, which can be justified since the model time step is relatively short.

Once the boundary conditions have been applied, the advection scheme is then implemented in the L2 grid. It uses the same scheme as TOMCAT, based on Prather (1986), and conserves second-order moments. The L2 convection scheme and PBL mixing scheme follows the same methods as TOMCAT, described in Section 5.2. The chemistry scheme is the final process to be called in the model time step iteration. The chemistry scheme is the same as described in Section 5.2 but the 4D mixing ratios of sink species and 4D loss rates are linearly interpolated from the L1 grid. The emissions are read into the model in the chemistry scheme and are transformed onto L1 and L2 horizontal grid by applying an area-weighted summation. Emissions are typically read in at 1°$\times$ 1° resolution but we have added the option to read in emissions at 0.5°$\times$ 0.5°

resolution. The differences between the emissions once transformed onto the L1 and L2 model grid are described in Section 5.4. The full chemistry scheme is not included in this work as it is not necessary for the CH_4 test cases presented; it will be added as an option in a future version of ZOOMCAT.

5.4 ZOOMCAT Simulations of CH_4

We conduct three ZOOMCAT simulations to test the performance of nested grid approach against observations from the ICOS tall tower network and TROPOMI satellite retrievals. All three simulations are conducted over Europe and the domain and extent of the L2 grid, overlaid on the L1 grid, is shown in Figure 5.1. The domain of the L2 grid, including the boundary region, is from 15.47°W to 35.34°E and 27.91°N to 69.78°N and the nested grid region is from 12.66°W to 32.34°E and 30.70°N to 67.0°N. In this example, the domain of the L2 grid includes the majority of mainland Europe, the UK and a small portion of the North Atlantic. The resolution of the L2 grid is ∼0.5°× 0.5° and is overlaid on the coarser L1 grid which has a resolution of ∼2.8°× 2.8°. For each L1 grid box there are five L2 grid boxes in the longitudinal direction and six L2 grid boxes in the latitudinal direction. The vertical grid in L1 and L2 follow the same σ-p coordinates with 60 vertical levels up to 0.1 hPa. The initial conditions for each simulation were provided from a previous TOMCAT simulation (Wilson et al., 2021). The meteorology was provided by ECMWF ERA5 and read into the model every 6 hours and the model time step was 15 minutes. To satisfy the Courant-Friedrichs-Lewy (CFL) condition ($\Delta t(u_i/\Delta x_i) <= 1$) for advection in ZOOMCAT (∼ 50 km at equator) with a model time step of 15 minutes, the maximum wind speed in the model has to be 55 ms^{-1}. The longitudinal distance of 0.5° decreases towards the poles. For example at approximately 55°N, the longitudinal distance of the grid box is ∼ 31 km and therefor the maximum wind speed needs to be 34 ms^{-1} to satisfy the CFL condition.

The first simulation, named ZOOM1, was from January to May 2020 using the standard emissions files for TOMCAT, which are read into the model at a resolution of 1°× 1°. The purpose of this simulation was to demonstrate ZOOMCAT using ECMWF meteorology on the TOMCAT resolution of 2.8°× 2.8° in both L1 and L2 grids. In the second simulation, named ZOOM05, we increased the resolution of the emission files to be 0.5°× 0.5° for the L2 grid. This simulation was run from January to December 2020 and the meteorology remained at the coarse resolu-

tion of 2.8°× 2.8° due to data availability. This simulation was carried out to demonstrate the differences in ZOOMCAT when given higher resolution emission data and to analyse how the model performs during a year-long simulation.

The emissions datasets used to simulate CH_4 in these simulations come from a variety of emissions inventories. We use monthly anthropogenic emissions from EDGARv8 (excluding agriculture). We use annual emissions from EDGARv8 for enteric fermentation and manure management because monthly emissions are not available for these individual sectors. We use separate estimates for agricultural rice emissions. EDGARv8 fluxes are provided at a spatial resolution of 0.1°× 0.1° (European Commission et al., 2023). For biomass burning we use the Global Fire Emissions Database (GFEDv5) monthly emission estimates which are provided at a resolution of 0.25°× 0.25° (Chen et al., 2023). The wetland emissions come from the updated ensemble from WetCHARTSv1.3.1 which has a resolution of 0.5°× 0.5° (Bloom et al., 2021). WetCHARTS emissions do not extend to 2020 so we compute a climatology of the ensemble members which have a global scaling factor of 207.5 Tg CH_4 yr^{-1}. Rice emissions come from the TransCom inter-comparison study; termites also come from TransCom but are scaled to match emissions reported by the Global CH_4 Budget (Patra et al., 2011; Saunois et al., 2020) and are provided on a 1°× 1° grid. Geological emissions come from Etiope et al. (2019) on a 1°× 1° grid and ocean emissions from diffusion and ebullition on a 0.25°× 0.25° grid are taken from Weber et al. (2019). The emission estimates are read into ZOOMCAT at 1°× 1° or 0.5°× 0.5° resolution. The combined emissions estimate total global emissions for 2020 to be 653 Tg and 47 Tg over the L2 region. The main sink of CH_4 is the hydroxyl radical (OH) and fields of this species for the troposphere and stratosphere were taken from Spivakovsky et al. (2000) and scaled downwards by 8 % in accordance to Huijnen et al. (2010) to match methyl chloroform (MCF) concentrations in the atmosphere (Patra et al., 2011). The stratospheric loss rates for reaction with chlorine (Cl) and excited oxygen atom $O(^1D)$ were taken from a previous full chemistry TOMCAT simulation (Monks et al., 2017). The soil sink was taken from the Soil Methanotrophy Model (MeMo) model (Murguia-Flores et al., 2018). The soil sink data are only available until 2009 so a climatology is used for the soil sink. These OH fields and loss rates have been shown to perform well in previous studies (e.g McNorton et al., 2018; Wilson et al., 2021). Figure 5.2 shows the emissions redistributed on to the L1 and L2 grids by applying an area-weighted mean. On the L1 grid, 1°× 1° emissions show the largest emissions of total CH_4 over central Europe, for example over Belgium, northern Italy and Romania. The emissions on

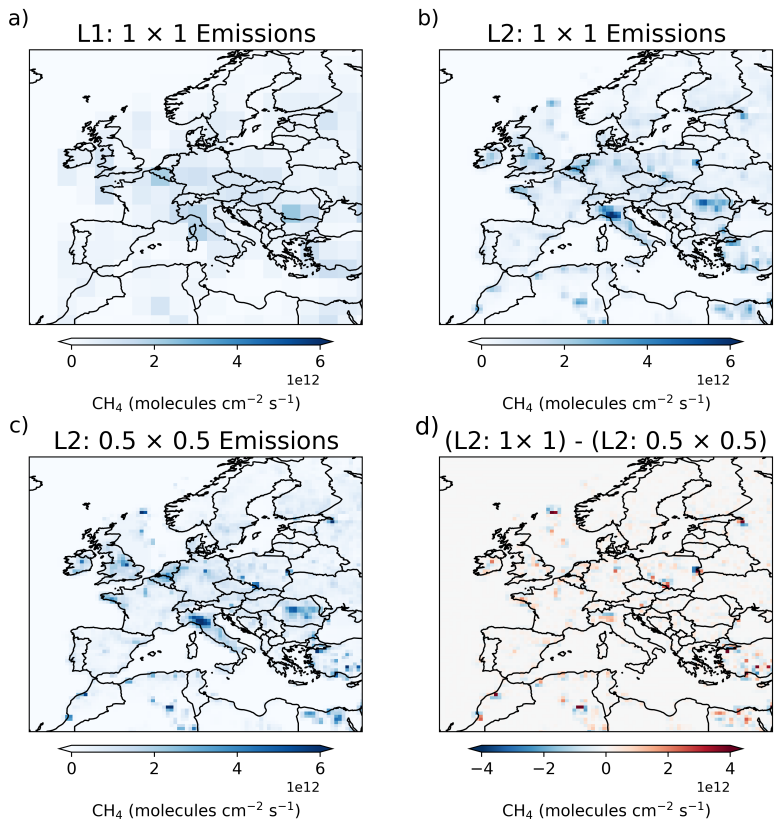

Figure 5.2: ZOOMCAT 1°× 1° CH_4 emissions redistributed onto a) the L1 model grid and b) the L2 model grid. Panel c) shows the 0.5°× 0.5° emissions redistributed onto the L2 grid. Panel d) shows the difference between the 1°× 1° and 0.5°× 0.5° on the L2 grid.

the L2 grid are distributed with better spatial detail, where larger emissions from point sources are more distinctive (see Figure 5.2b). Larger emissions can now be seen over central England, the North Sea, Po Valley (an industrial area in Italy) and coal mining regions in Poland. When the L2 grid is given 0.5°× 0.5° resolution emissions (Figure 5.2c), the areas of high emissions shown in Figure 5.2b) are more defined and distributed over a smaller area.

The final simulation, named ZOOM_nord, models a CH_4 plume from the Nord Stream pipeline gas leak in September 2022. Nord Stream is a submerged pipeline network which carries natural gas from Russia to Western Europe. It was estimated to have released 215-390 Gg of CH_4 into the atmosphere on the first two days of the leak, between 26th September and 28th September 2022 (Wilson et al., 2023). The pipeline stopped leaking on 2nd October 2022. The pipeline leaked from three locations: 15.41°E, 54.88°N; 15.60°E, 55.54°N, and 15.79°E, 55.56°N (Wilson et al., 2023). We simulated CH_4 emissions that were not related to the gas leak using the emissions described above. The emissions from the gas leak were released at the closest model grid box to the three leak locations. The point source emission was instantaneously spread across

Table 5.1: List of ZOOMCAT simulations.

ZOOMCAT Simulation	Simulation Length	Emission Resolution	Meteorology Resolution
ZOOM1	5 Months	1°× 1°	2.8°× 2.8°
ZOOM05	1 Year	0.5°× 0.5°	2.8°× 2.8°
ZOOM_nord	3 Days	0.5°× 0.5° + point source	∼1.125°× 1.125°

the surface model grid cell at a rate of 4.17 Gg hr^{-1}, approximately 100 Gg a day (4,170 tonnes hr^{-1}, Wilson et al. (2023)), with a model timestep of 15 minutes. The model was run from midnight on 26th September to midnight on 29th September 2022. We used ECMWF operational reanalyses data, read into the model at a resolution of ∼1.125°× 1.125° and regridded to the same vertical and horizontal resolution as the model. Due to data availability September 2020 ECMWF BLH was used. We chose to simulate the Nord Stream gas leak to demonstrate the transport in ZOOMCAT is working as expected through modelling the plume and demonstrate any improvements to the model using higher-resolution ECMWF meteorology. Table 5.1 gives a summary of the different simulations carried out in this study.

5.5 Observations for Validation

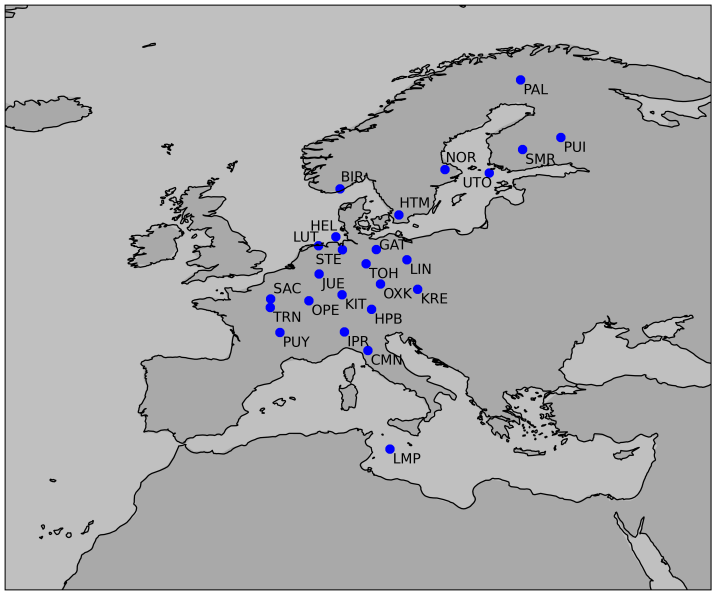

Figure 5.3: Map of ICOS site locations used to compare with ZOOMCAT.

We use two types of observations to validate ZOOMCAT. We use observations from the ICOS tall tower network across Europe and satellite retrievals from TROPMI. There are more than 140 tall tower sites in the ICOS network which measure CH_4 using cavity ring down spectroscopy (CRDS; Levin et al. (2020)). In this study we use 25 sites spread across Europe to test the model

performance in the first two simulations (see Figure 5.3; ICOS RI et al. (2024)). We selected the lowest measurement a.g.l (above ground level) and highest measurement a.g.l available at each site to capture local and regional changes in concentrations. The heights vary from 2.5 m a.g.l. to 341 m a.g.l. Table 5.2 shows the name, location and height of each measurement used in this study. The ICOS sites measure CH_4 with a mean bias of 0.2 $\pm$0.8 ppb and as a result are a reliable source to test the model performance (Levin et al., 2020). We interpolate the model to the location and altitude of the ICOS site and calculated daily mean values from the model and the observations for ZOOM1 and ZOOM05 comparisons. We also used four sites, out of the 25 selected, to test the model performance when simulating the Nord Stream gas leak. These are Birkenes, Norway (BIR); Hyltemossa, Sweden (HTM); Norunda, Sweden (NOR); and Utö, Finland (UTO). In the ZOOM_nord simulation we compare the hourly observation data with the hourly model output.

The ICOS observations only capture changes in atmospheric CH_4 at a certain location over time. To assess the spatial distribution of the model, we compare ZOOMCAT and TOMCAT with CH_4 retrievals from TROPOMI on board Sentinel-5P. TROPOMI is a push-broom sprectrometer with two modules, where the first uses ultraviolet (UV), visible and NIR spectral bands and the second contains SWIR spectral bands around 2.3μm. The instrument provides near-global coverage of CH_4 every day with a spatial resolution of 5.5 km $\times$ 7 km. In this study we use CH_4 retrievals from the University of Bremen Weighting Function Modified Differential Optical Absorption Spectroscopy (WFM-DOAS) v1.8 algorithm. To compare the model simulation with the satellite retrievals we sample the model at the observation time and then interpolate the model to each observation location before applying the averaging kernels (AK) to the model. After the AKs have been applied the model is regridded back onto a 0.5°$\times$ 0.5° grid. We also grid the TROPOMI retrievals by taking a mean across a 0.5°$\times$ 0.5° grid. We then compare monthly mean column average mixing ratios from TROPOMI and TOMCAT/ZOOMCAT, see Section 5.6.1. Studies have shown that TROPOMI has biases retrieving CH_4 over high and low albedo regions (Lorente et al., 2023; Balasus et al., 2023). We find a large mean bias over Africa of 29 ppb between ZOOMCAT and the satellite. As a result, we mask the TROPOMI and model output to only consider mainland Europe. This removes northern Africa from our analysis, where the albedo and dust impact the retrieval.

5.6 ZOOMCAT Model Output

5.6.1 ZOOM1 and ZOOM05

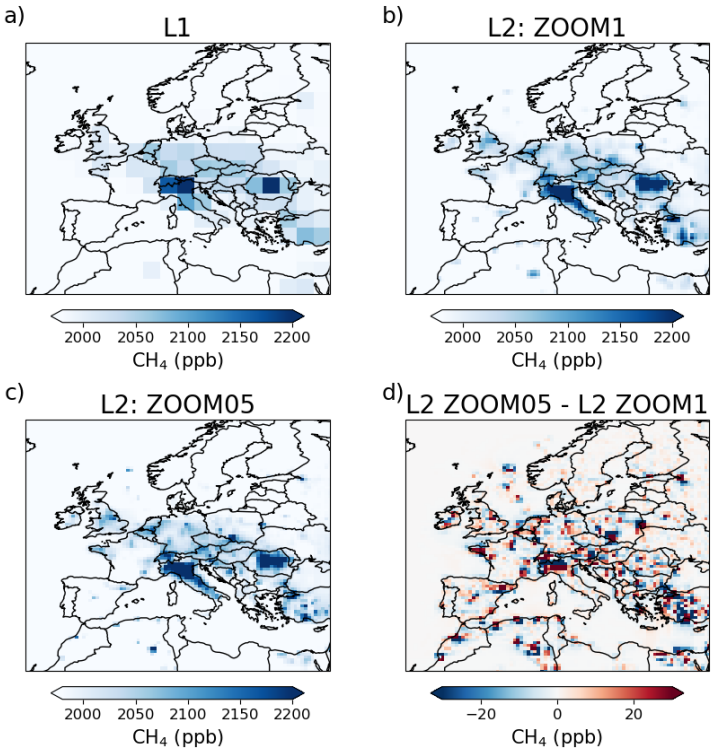

Figure 5.4: Figure showing the seasonal mean CH_4 concentrations at the surface during March, April and May (MAM) for a) L1 model grid, b) L2 model grid (ZOOM1) and c) L2 model grid (ZOOM05). Panel d) shows difference between the L2 grids with different emission inputs.

We first aim to demonstrate the improvement in the spatial resolution of ZOOMCAT through our model simulations of CH_4 concentration. Figure 5.4 shows the March, April, May (MAM) seasonal mean mixing ratio from TOMCAT and the two ZOOMCAT simulations. Figure 5.4 b) shows the ZOOM1 simulation using the standard TOMCAT set up, with $1^\circ \times 1^\circ$ emissions. The figure demonstrates an improvement in the spatial distribution of concentrations near larger point sources in ZOOMCAT when compared with TOMCAT, particularly around large cities in Germany, the Po Valley in Italy and the coal mining regions in Poland. These sources are further defined in Figure 5.4c) when the $0.5^\circ \times 0.5^\circ$ emissions are used in the model. The impact of the spatial distribution of the sources, using different resolution emissions, can be seen in Figure 5.4 d). The differences, as expected are predominantly due to the change in distribution of emissions between the $1^\circ \times 1^\circ$ emissions to $0.5^\circ \times 0.5^\circ$ emissions estimates. For example, large point sources over the North Sea are more evident in Figure 5.4 c) than in Figure 5.4 b).

Figure 5.5 shows the zonal monthly mean latitude-height cross section of the L1 grid, L2 grid

Table 5.2: List of 25 ICOS Sites used in the analysis.

Site Name	Latitude (° North)	Longitude (° East)	Site Code	Altitude (m a.s.l)	Minimum Height (m a.g.l.)	Maximum Height (m a.g.l.)
Steinkimmen, Germany	53.04	8.45	STE	29	32	252
Torfhaus, Germany	51.81	10.54	TOH	801	10	147
Trainou, France	47.96	2.11	TRN	131	50	180
Utö - Baltic Sea, Finland	59.78	21.37	UTO	8	57	-
Birkenes, Norway	58.39	8.25	BIR	219	10	75
Monte Cimone, Italy	44.19	10.70	CMN	2165	8	-
Gartow, Germany	53.06	11.44	GAT	70	30	341
Helgoland, Germany	54.18	7.88	HEL	43	110	-
Hohenpeissenberg, Germany	47.80	11.02	HPB	934	50	93
Hyltemossa, Sweden	56.09	13.4	HTM	115	30	150
Ispra, Italy	45.81	8.63	IPR	210	40	100
Jülich, Germany	50.19	6.41	JUE	98	50	120
Karlsruhe, Germany	49.09	8.42	KIT	110	30	200
Křešín u Pacova, Czech Republic	49.57	15.08	KRE	534	50	250
Lindenberg, Germany	52.16	14.12	LIN	73	2.5	98
Lutjewad, Netherlands	53.40	6.35	LUT	1	60	-
Norunda, Sweden	60.08	17.47	NOR	46	32	100
Observatoire Pérenne de l'Environnement, France	48.56	5.50	OPE	390	10	120
Ochsenkopf, Germany	50.03	11.81	OXK	1022	90	163
Pallas, Finland	67.97	24..11	PAL	565	12	-
Puy de Dôme, France	45.77	2.97	PUY	1465	10	-
Puijo, Finland	62.91	27.65	PUI	232	47	84
Saclay, France	48.72	2.14	SAC	160	15	100
Hyytiälä, Finland	61.84	24.29	SMR	181	16.8	125

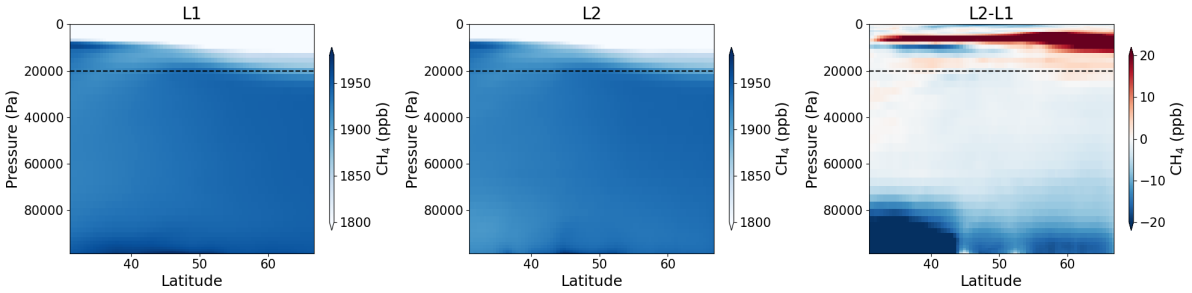

Figure 5.5: Monthly zonal mean CH_4 concentrations June from the ZOOM05 simulations, for a) L1 model grid (interpolated onto the L2 grid), b) L2 model grid and c) the difference between L2 and L1. The dashed line shows the tropopause at 200 hPa.

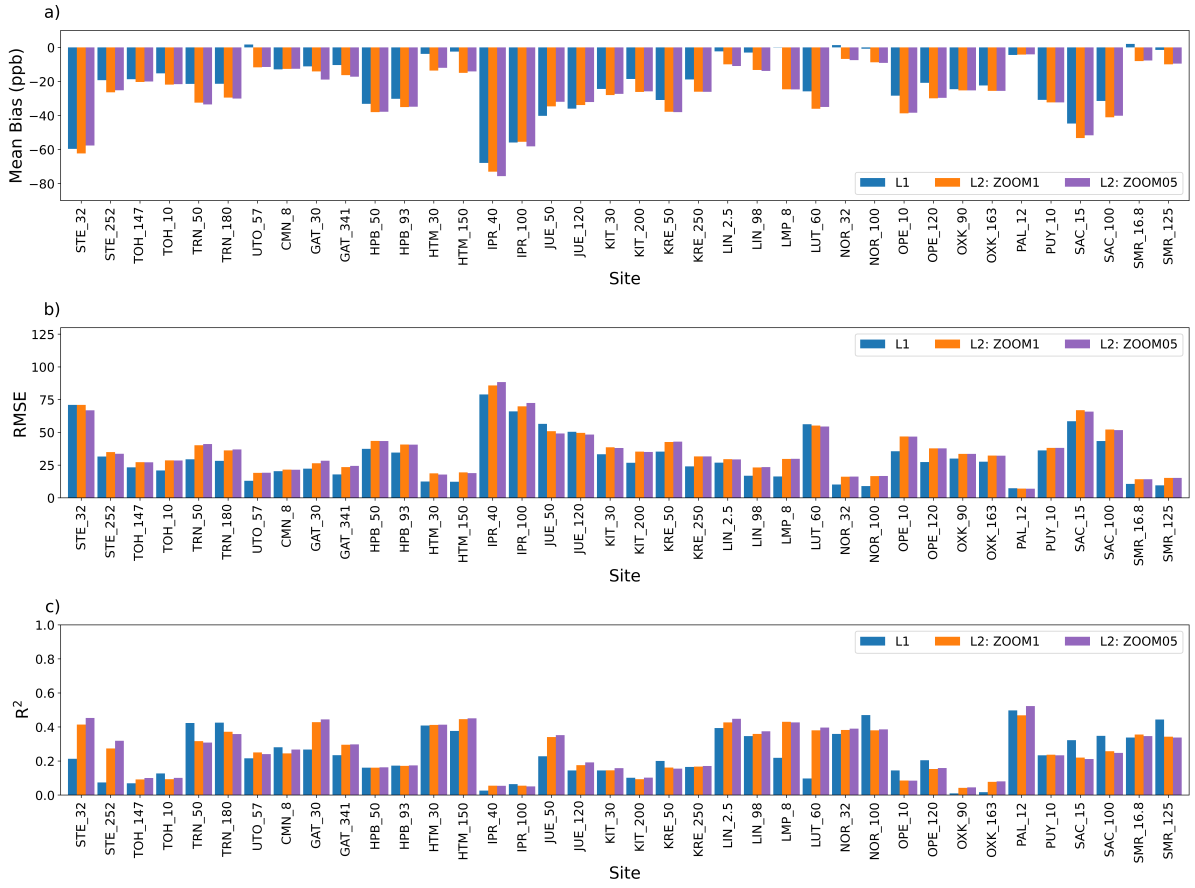

Figure 5.6: Comparison of statistics of L1 (blue) and L2 grids for the ZOOM1 (orange) and ZOOM05 (purple) CH_4 simulations compared against ICOS sites between March and May 2020. Panel a) shows the mean bias, b) shows the root mean square error (RMSE) and c) shows R^2. Each site is labelled on the x axis as "Site Code"_"Sampling Height".

and their differences in June 2020. This example shows that the L2 grid has smaller concentrations near the surface than L1 in southerly latitudes of the nested grid region but there is good agreement in the mid-troposphere between both grids. The L2 grid simulates higher concentrations than the L1 grid in the stratosphere, but note that the figure is using a linear pressure scale on the y axis. The CTM calculates vertical motion by using the divergence of the specified horizontal winds. As this integration is performed in a model column from the top level downwards, the higher resolution grid has the potential to increase the variability in this vertical transport. In regions of strong vertical gradients in CH_4, such as the stratosphere, this can impact the local mixing ratios.

To test ZOOMCAT's performance and demonstrate improvements compared to the original TOMCAT model, we compared daily mean concentrations from the ZOOM1 and ZOOM05 simulation with daily mean ICOS observations between March and May 2020. Figure 5.6 shows the mean bias, root mean square error (RMSE) and R^2 values for the model simulations, at

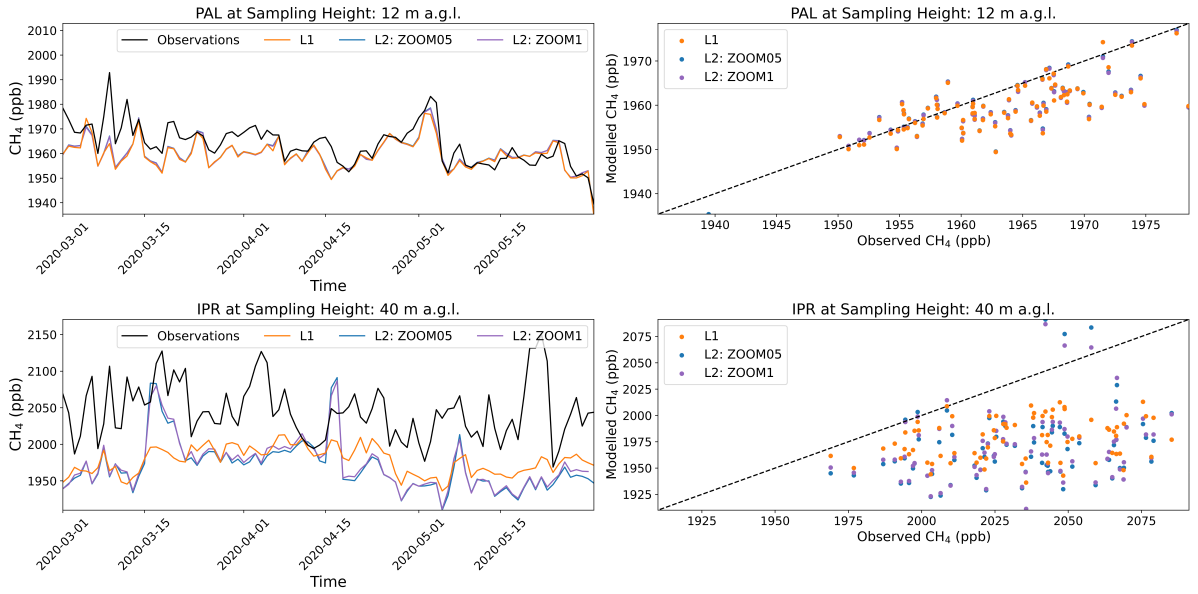

Figure 5.7: The comparison of simulated concentrations from the L1 grid (orange) and the L2 grid from ZOOM1 (blue) and ZOOM05 (purple) against observations (black) at Pallas (PAL) and Ispra (IPR) between March and May 2020.

each observation site's highest and lowest inlet. The L2 grid mean bias and RMSE for both simulations are generally larger than the L1 grid and the R^2 is generally higher, showing very small improvements in the high resolution simulation. However, some improvements are shown at some sites. The L2 grid in the ZOOM1 simulation had a smaller RMSE at 10% of observation locations (4 out of 36 locations) when compared to the L1 grid. The L2 grid in the ZOOM1 simulation has larger R^2 value at 57% of observation sites (22 out 38 observation locations) when compared to the L1 grid, where 4 of these sites also had smaller RMSE than the L1 grid. The L2 grid in the ZOOM05 had a smaller RMSE at 60% of location (22 out of 38 sites) when compared with the L2 grid in the ZOOM1 simulation. The L2 also has a larger R^2 values at 65% of locations (25 out of 38 locations) when compared with the L2 grid in the ZOOM1 simulation, where 19 of these sites also have a smaller RMSE. This shows that the higher resolution emissions read into the L2 grid generally perform better when compared with observations than the L2 grid with coarse emissions.

From these results, we selected one site which showed the largest improvements in the L2 grid from the ZOOM05 simulation compared to the L2 grid from ZOOM1 simulation (e.g smallest RMSE and largest R^2). We also selected the site that had the worst performance when compared to the L1 grid (e.g largest RMSE and smallest R^2). We did this to show the temporal variability of ZOOMCAT and compare the differences with observation. We find the best performing site

to be Pallas (PAL) in Finland and the worst performing site to be Ispra (IPR) in Italy. Figure 5.7 shows the comparison of the L1, L2 (ZOOM1) and L2 (ZOOM05) concentrations against observations at these two selected sites. There is very little difference between concentrations from the ZOOM1 and ZOOM05 simulations on the L2 grid. At PAL the L1 and L2 (ZOOM1) grids capture the variation of observed concentrations well with a RMSE of 7.3 ppb and 7.7 ppb and an R^2 of 0.50 and 0.47, respectively. The L2 (ZOOM05) also captures the variation well with a RMSE of 6.9 ppb and an R^2 of 0.52, showing a slight improvement on L2 ZOOM1 simulation. Figure 5.7 shows at IPR that the L1 and L2 (ZOOM1) grids does not capture the variation of the observed concentrations well with a RMSE of 78.9 ppb and 85.8 ppb and an R^2 of 0.02 and 0.05, respectively. The L2 (ZOOM05) also performs poorly a RMSE of 88.3 ppb and an R^2 of 0.05. The L2 grid also underestimates CH_4 concentrations more than the L1 at IPR. Although comparisons are over a small time period they demonstrate that the L2 grid performs better with higher resolution emissions but it does not improve upon the L1 grid. The reasons for this will be discussed in detail in Section 5.7.

We also compared the ZOOM05 simulation with ICOS sites over 12 months in 2020 to assess how the model performs over a longer time period. We find that the L2 grid captures the variation of concentrations better, with a higher R^2 value than the L1 grid, at 15 out of 38 observation locations. However, the L2 RMSE is often larger than the L1 (see Figure 5.8). We selected two sites which showed the best improvements in the L2 grid from the ZOOM05 simulation compared to the L1 grid (e.g smallest RMSE or largest R^2). We find in the ZOOM05 simulation, over one year, that the L2 grid performs well at the PAL observation site. Figure 5.9 shows the time series comparison at PAL highlighting that the L1 and L2 grids capture the variation in concentration well until July 2020. After July 2020, ZOOMCAT does not capture the summer increase but follows a similar variation to observations by winter. L2 also performs well compared with observations at KIT with an R^2 value of 0.7 but it has a large RMSE of 56.8 ppb due it overestimating large peak concentrations in January, November and December. We also selected the site which had the worst performance when compared to the L1 grid (e.g largest RMSE and smallest R^2). Figure 5.9 shows that ZOOMCAT does not perform well at IPR over a whole year; both L1 and L2 grids underestimate concentrations but the L2 overestimates large peaks in January and December.

We also compared the ZOOM05 simulation to column average CH_4 concentrations observed by

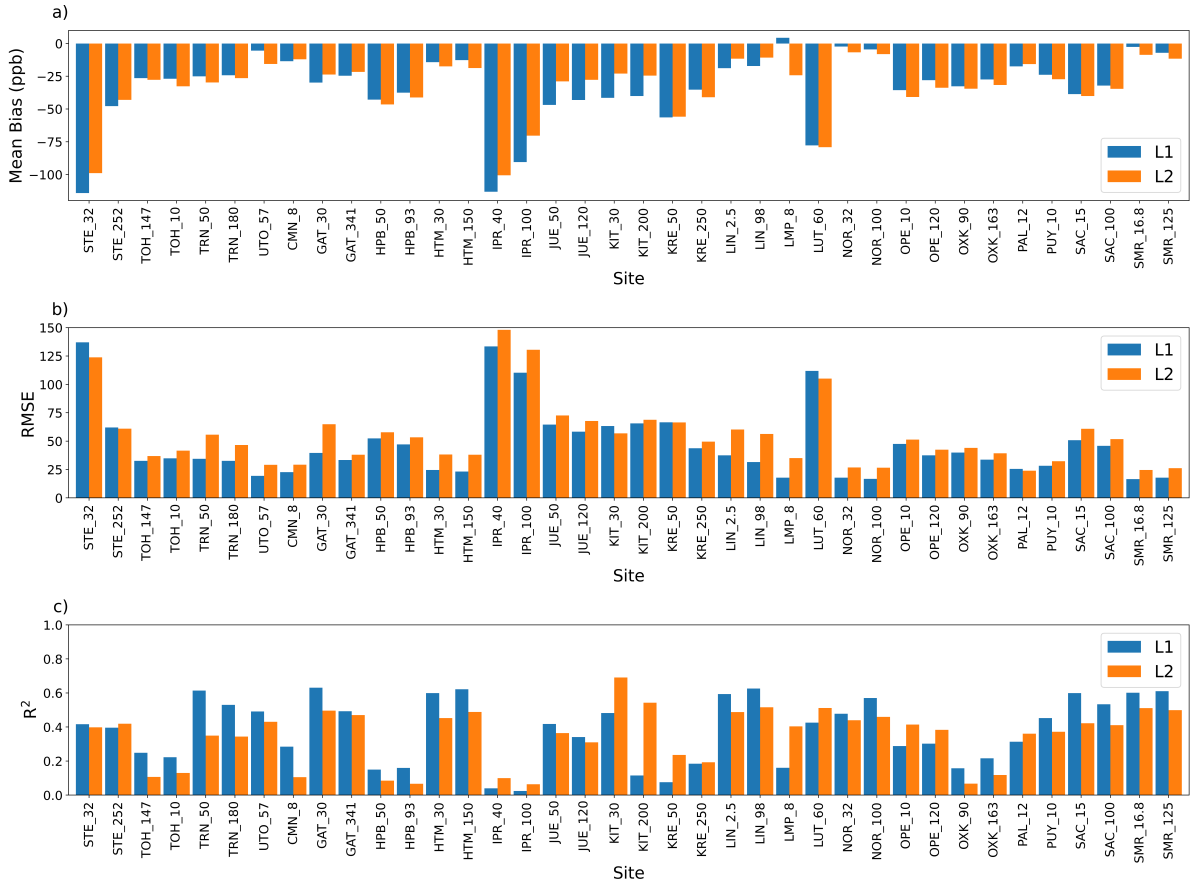

Figure 5.8: The comparison of statistics of L1 (blue) and L2 grids (orange) concentrations compared against ICOS observation sites between January and December 2020. The site is shown as the site code followed by its sampling height. Panel a) shows the mean bias, b) shows the root mean square error (RMSE) and c) shows R^2.

TROPOMI to test the simulated spatial distribution. The modelled column average concentrations were substantially higher than those observed by TROPOMI so we applied a spatially homogeneous monthly mean bias correction of the modelled data for the nested domain. The mean bias corrections for L1 and L2 were 40 ppb. Figure 5.10 shows comparison between L2 grid and the satellite, and the differences between L1 and L2 grids with the TROPOMI averaging kernels applied for April, August and November 2020.

The TROPOMI observations shown in Figure 5.10 a) show very little spatial variation of column average concentrations over mainland Europe for April and August. Some lower concentrations are observed over Portugal, Spain and northern Scandinavia in April and larger concentrations are observed over northern Italy. CH_4 mixing ratios in August exhibit a similar spatial pattern to those in April with larger concentrations over Portugal and Spain. In November, observed concentrations increase particularly over northern Spain, south-western France and Poland. However, these higher CH_4 concentrations are associated with larger uncertainties in

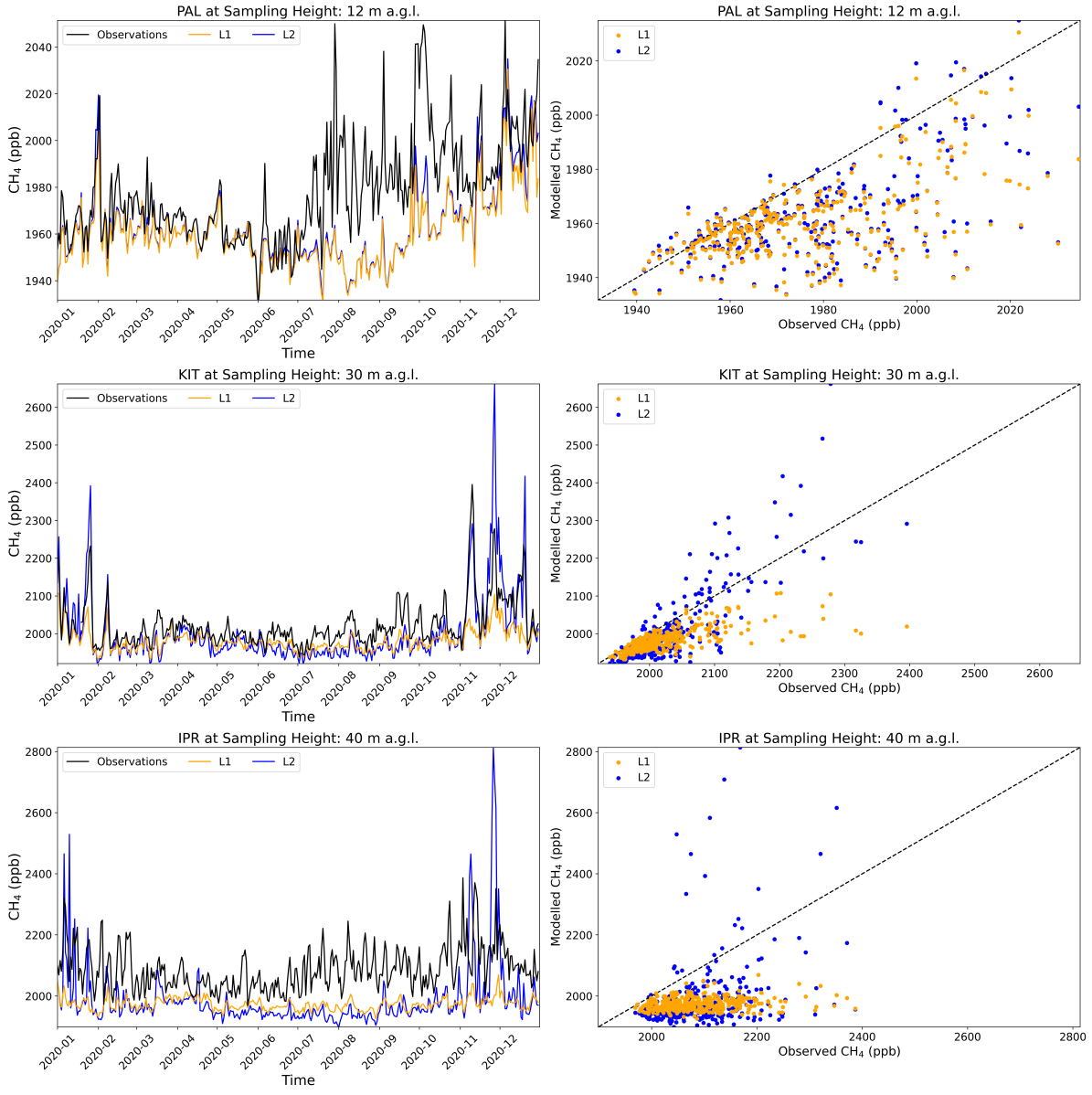

Figure 5.9: The comparison of simulated concentrations from the L1 grid (orange) and the L2 grid from ZOOM05 (blue) against observations (black) at Pallas (PAL), Karlsruhe (KIT) and Ispra (IPR) between March and May 2020.

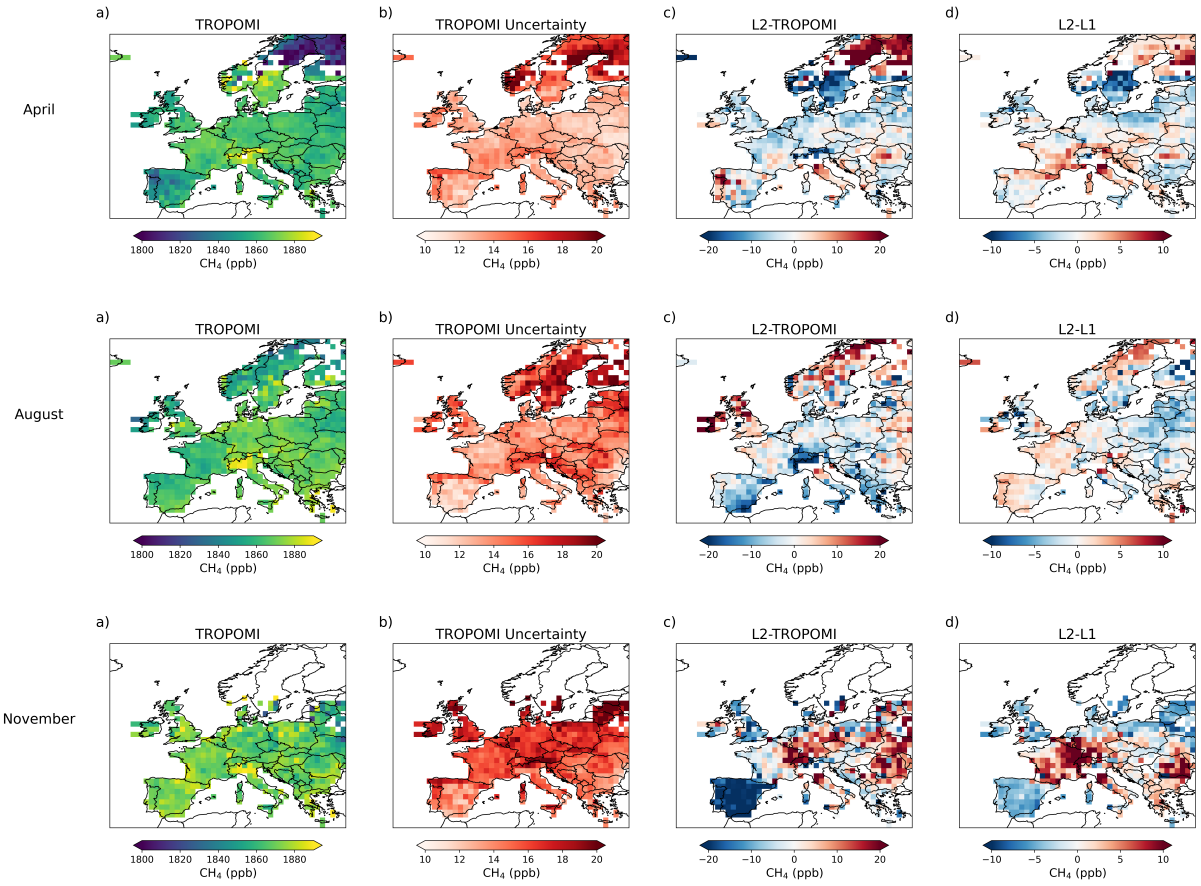

Figure 5.10: Comparison of TROPOMI CH_4 and ZOOMCAT. Column a) shows the TROPOMI monthly mean column average mixing ratio (ppb), column b) is the monthly mean uncertainty on the TROPOMI retrieval, column c) is the difference between the L2 grid and TROPOMI and d) shows the difference between the L2 and L1 grids (both with TROPOMI averaging kernels applied) for April, August and November.

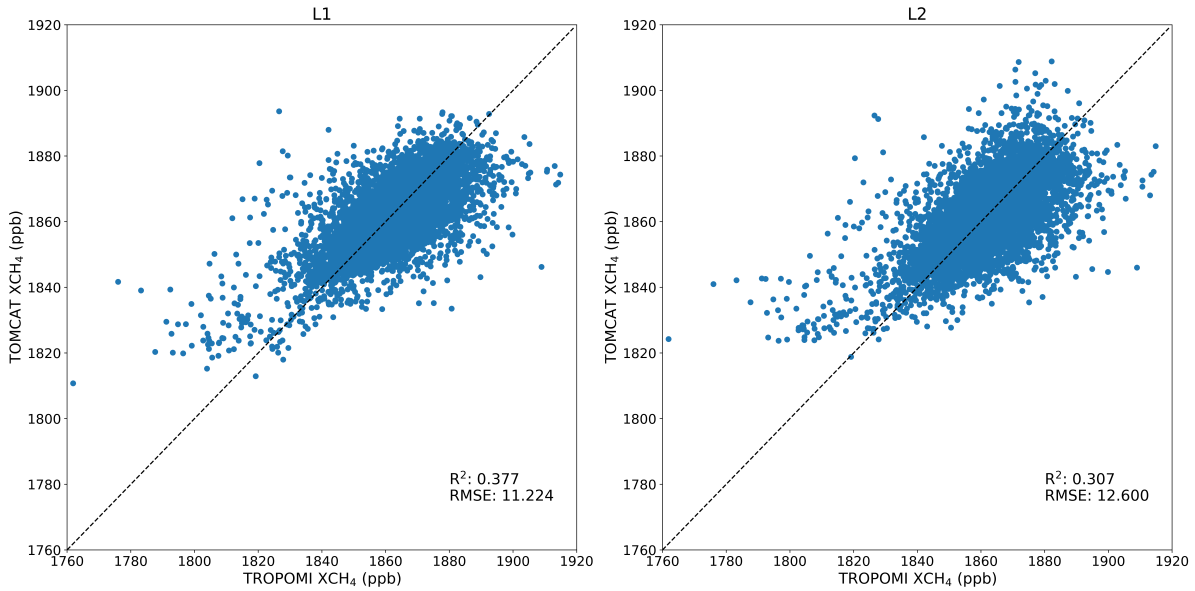

Figure 5.11: Modelled and observed column average mixing ratios (ppb) of CH_4 from January to December 2020 for the L1 (left) and L2 (right) grids.

the retrieval, (Figure 5.10 b) April-November). The retrievals are more uncertain at higher latitudes, for example over northern Scotland and Scandinavia. In November the observations have much higher uncertainties than the previous months, likely due to the availabiliy of light at higher latitudes during winter.

We find that the L2 grid generally underestimates concentrations compared with TROPOMI in April, apart from over Portugal, Italy and Romania. In August the L2 grid also underestimates concentrations when compared with TROPOMI but overestimates in regions with high uncertainty on the retrieval (e.g. over Scotland and Scandinavia). In November, the L2 grid has very large differences when compared with TROPOMI, where the model overestimates concentrations in central Europe but underestimates over Spain and Portugal. Retrievals across Europe during November are more uncertain than April and August. Despite there being large differences between the L2 grid and TROPOMI, Figure 5.10 d) shows that the L2 grid provides more spatial variation in the concentrations than L1 grid, for example southern France, Italy and Romania.

Figure 5.11 shows the comparison of TROPOMI and the model simulations from the ZOOM05 simulations for one year. The L1 and L2 grids compare well over 1 year with RMSE of 11.2 ppb and 12.6 ppb but have a low R^2 value of 0.38 and 0.31 respectively. The L2 grid over and underestimates CH_4 more than the L1 grid when compared with TROPOMI at higher concentrations, which is likely why the RMSE is higher than the L1 grid. The mean uncertainty

on the retrievals for 2020 over the nested area is 15.1 ppb, therefore ZOOMCAT is within the mean uncertainty of the retrievals. These values demonstrate no improvements in the L2 grid column average CH_4 estimates compared to TROPOMI and the L1 grid.

5.6.2 ZOOM_nord

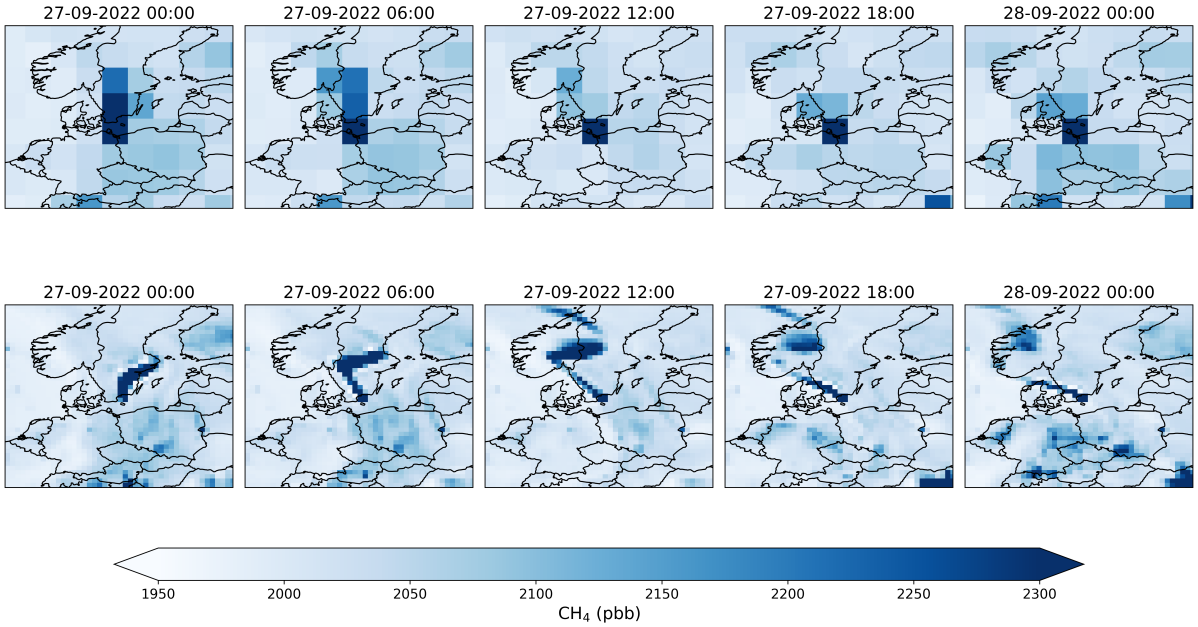

Figure 5.12: The evolution of the Nord Stream CH_4 plume between 27th September and 29th September 2022 in TOMCAT (top row) and ZOOMCAT (bottom row).

We simulated the Nord Stream pipeline leak in 2022 to demonstrate the atmospheric transport of a CH_4 plume in the model but also to demonstrate improvements to the model simulation using higher resolution meteorology. Figure 5.12 shows the evolution of the Nord Stream plume, every 6 hours at the surface in the L1 (upper row) and L2 grids (bottom row). The L1 grid shows the plume is transported north over southern Sweden and then west towards Norway. The L2 grid provides more spatial detail in the plume transport, showing that the plume is transported north over southern Sweden and then pushed eastwards, towards Stockholm by midnight on 27th September. By 12:00 noon on 27th September the plume has moved west towards southern Norway. The transport of the plume is similar to that in the simulated column average shown in Wilson et al. (2023) but there are some differences likely due to differences in the BLH scheme used and differences in vertical transport due to higher spatial resolution, as mentioned in Section 5.6.1.

We also compare the hourly model output against ICOS hourly observations at BIR, HTM,

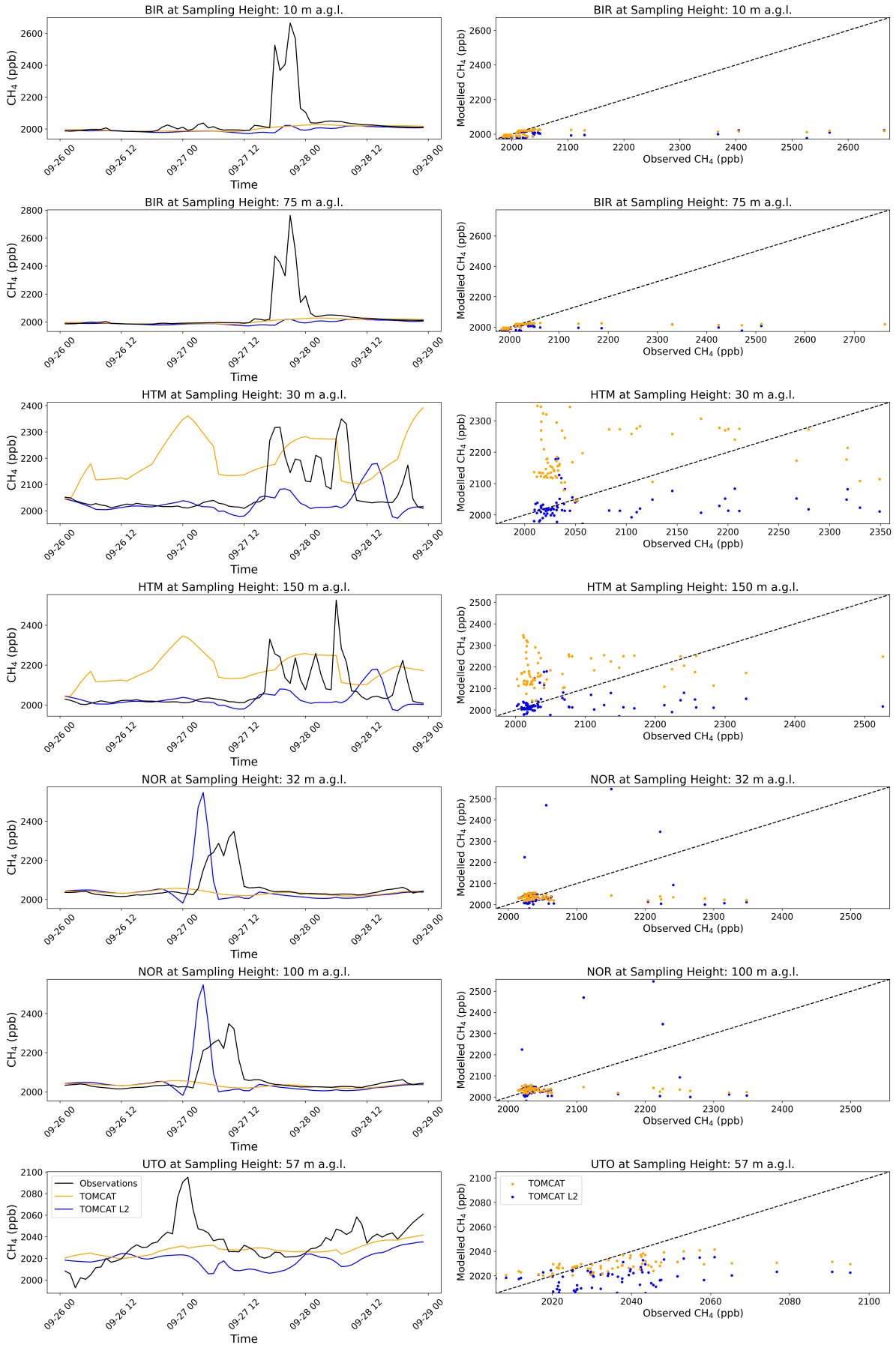

Figure 5.13: Hourly mean TOMCAT (L1, yellow) and ZOOMCAT (L2, blue) mixing ratios (ppb) along with ICOS hourly mean observations (black) at Birkenes (BIR), Hyltemossa (HTM), Norunda (NOR); and Utö (UTO).

NOR and UTO. Figure 5.13 shows the time series comparison of the model and observations between 26th and 29th September 2022. Generally concentrations from L2 grid are lower than the L1 grid, and lower than the observations. This underestimation matches with the previous L2 simulations described in Section 5.6.1. At BIR the models do not capture the large peak in CH_4 concentrations on the evening of 27th September shown by the observations. The L2 grid has a very small peak in concentrations at 6pm on 27th September, showing that the plume has been transported in the correct direction but the concentrations are too low. Similarly, at UTO neither model grids capture the peak in concentrations at midnight on 27th September. The spatial maps show that the plume is not transported far enough east to reach UTO. However, in Wilson et al. (2021), simulated peaks are captured at NOR, BIR and UTO. Differences in ZOOMCAT are likely due to the different BLH scheme or vertical transport described above.

At HTM, the L1 concentrations are much larger than the L2 concentrations, and are also larger than the observations. HTM is situated in southern Sweden and the closest site to the leak location. This site demonstrates that the increase in spatial resolution in the L2 captures the variation in concentration better than coarser L1 resolution. The variation in L2 concentrations at HTM show an increase in concentrations in the afternoon of 27th September which is earlier than the increase shown in the observations. The L2 grid also does not capture the peaks shown by observations on 27th and 28th of September, apart from one peak on the afternoon of 28th. However, it is difficult to infer if the timing of this modelled peak is related to the earlier or later peak shown in the observations. The L2 grid also performs better than L1 grid at the NOR site. The L1 concentrations shows no peak in CH_4 concentrations during the simulation but L2 concentrations show a large peak in the early hours on 27th September. The L2 peak is earlier and larger than the peak shown in observation. Despite the timing and magnitude of the peaks in the L2 concentrations, this site also demonstrates that the increase in the spatial resolution, combined with high resolution meteorology in the L2 grid captures the variation of CH_4 better at this site.

5.7 Discussion

We have shown through our simulations that we are able to perform a "nested" simulation, through the development of the ZOOMCAT regional model. The simulations show that the model is able to simulate CH_4 concentrations at a higher spatial resolution when given $1° \times 1°$

resolution or 0.5°× 0.5° resolution emissions. As a result, we are able to represent the transport and variation of large point sources of CH_4 better than TOMCAT as shown by the ZOOM_nord simulation.

To test the model performance we compared ZOOMCAT to the ICOS observation sites. We found that both grids underestimate concentrations and this is likely due to underestimated emissions. The L2 grid does not represent the observed concentrations better than the L1 grid. However, we did see improvements in the model when using the L2 grid with 0.5°× 0.5° resolution emissions when compared to the ICOS sites. The nested grid performed best at the PAL site in both ZOOM1 and ZOOM05 simulations. The PAL site is based in northern Finland and observes background concentrations of CH_4. The site is also situated in the boundary region of the nested grid. This highlights that the emissions used in the model simulation are captured well on both the L1 and L2 grids. It also shows that model transport in boundary region between the L1 and L2 grids is working as expected. If we remove PAL from our analysis the the best performing site is NOR, which predominantly observes background concentrations. These results highlight that ZOOMCAT performs better in regions that are not influenced by large sources of CH_4.

In ZOOM1 and ZOOM05 we simulate CH_4 with ∼2.8°× 2.8° resolution meteorology due to data availability. Therefore, the transport of emissions will be the same on average for all the L2 grid boxes which lie within a L1 grid box. This could mean that some emissions which are better represented by the higher spatial resolution are not being transported correctly, resulting in a poor comparisons with the ICOS sites. To test this theory we used the operational meteorology we had available in our ZOOM_nord simulation. The operational meteorology was read into the model at a resolution of ∼1.125°× 1.125°, although this is still coarser than the L2 grid resolution. Figure 5.13 shows that the L2 grid better represents the Nord Stream plume at ICOS observations sites compared to the L1 grid. The L2 concentrations follow a similar temporal variation to the observed concentrations but the timing of the main peaks from the Nord Stream plume differ from that observed. This simulation provides a good example of the improvement of the L2 grid compared to the L1 grid. It is possible that the timing of the peaks will improve if we simulated CH_4 in the model using the ECMWF reanalyses fields instead of the operational meteorology. Currently, it is not possible to do this due to local data availability. The ZOOM_nord simulation also demonstrates the model transport in the L2 grid

well and highlights the improvement of the spatial resolution compared with the L1 grid.

We also compared monthly mean ZOOMCAT output with monthly mean satellite retrievals from TROPOMI. We find the agreement between the observations and the model simulation to be mixed across different times of the year. In April and August we are able to show that the L2 model provides better spatial distribution of column average CH_4 concentrations than the L1 grid. The differences between the L1 and L2 column average concentrations are likely due to distribution of BLH data used in the simulation. We used the ECMWF-calculated BLH which is read into the model at $1° \times 1°$ resolution and then redistributed on to the two model grids via an area weighted mean. This causes differences in the distribution of BLH between the L1 and L2 grids, which will result in a different column average concentrations between the different resolution grids due to the vertical sensitivity of the satellite.

There are several factors which could contribute to differences between ZOOMCAT and the satellite data, some of which are related to the satellite retrieval or related to the model inputs. Hachmeister et al. (2022) and Schneising et al. (2023) have shown biases relating to surface albedo and the elevation model used in the TROPOMI retrieval. Schneising et al. (2023) show that the WFM-DOAS retrieval is less susceptible to spectral albedo features than the operational algorithm for TROPOMI CH_4 retrievals. However, it is likely that some albedo features still impact the retrieval. For example, over the Sahara desert we found large mean differences of 29 ppb between the ZOOMCAT and TROPOMI and removed the region from our analysis. Hachmeister et al. (2022) found anomalies of up to 100 ppb in observed column average CH_4 which were correlated to differences in the digital elevation model (DEM) used in the retrieval when compared with a more recent DEM dataset. In v1.8 retrieval (used in this study) the DEM was updated to the Copernicus GLO-90 DEM which is based on radar satellite data and has an accuracy of 2.17 m with a confidence interval of 90% (Schneising et al., 2023). However, this DEM is more uncertain over boreal, tundra and forests due to the penetration depths of the radar and lidar over this regions (Schneising et al., 2023). As a result, biases related to topography are reduced with the largest differences (increases of $\sim$ 5- 10 ppb) occurring over Scandinavia with the new DEM, when only considering the nested region used in this study.

In addition to the biases seen in TROPOMI retrievals, inputs into ZOOMCAT such as emissions or BLH may also contribute to differences between the model and the observations. It is possible that the emissions in the model do not reproduce the observed variation in CH_4. For example, at

KIT the temporal variation of concentrations compare well with observations but the magnitude is too low (see Figure 5.9). Another factor which could influence the column average value in ZOOMCAT is the pre-calculated BLH from ECMWF as noted above. In the model, we distribute the tracer over the troposphere with a constant mixing ratio up to the BLH. As mentioned above, we also use $\sim 2.8^\circ \times 2.8^\circ$ resolution meteorology which impacts how emissions are transported in the L2 grid. Further simulations should be carried out in ZOOMCAT with higher resolution meteorology in order to improve comparisons with observations.

Despite the L2 grid not producing an improved comparison to surface observations when compared with the L1 grid, we reduce the computational cost when simulating a region at high resolution. We generally simulate TOMCAT using 16 processors and have the computation time for these simulations. We currently do not have simulation lengths available for different TOMCAT simulations at different resolutions using one processor, therefore we assume that it takes 16 times longer (in this case) to simulate TOMCAT at those resolutions. When we simulate one global CH_4 tracer in TOMCAT with a spatial resolution of $\sim 2.8^\circ \times 2.8^\circ$ for one year using 16 processors on University of Leeds ARC4 high performance computer, it takes approximate 52 minutes for the model to run. For the equivalent simulation using one processor it takes approximately 832 minutes (almost 14 hours). Similarly, when we simulate one CH_4 tracer in TOMCAT with a spatial resolution of $\sim 1.125^\circ \times 1.125^\circ$ for one year, using 16 processors it takes approximately 191 minutes ($\sim$3.2 hours) for the model to run, or approximately 3056 minutes ($\sim$34.3 hours) with one processor. It is possible that the simulation time is faster than our assumption. In ZOOMCAT, it takes approximately 1744 minutes (29 hours) to simulate one tracer for one year with the L1 grid at a coarse resolution of $\sim 2.8^\circ \times 2.8^\circ$ and the L2 grid at a resolution of $\sim 0.5^\circ \times 0.5^\circ$. This is faster than simulating TOMCAT at a resolution of $\sim 1.125^\circ \times 1.125^\circ$ for one year, demonstrating the lower computational cost of ZOOMCAT for regional high-resolution modelling.

The increase in computational speed is advantageous when simulating atmospheric constituents at a high spatial resolution. In our case studies we simulate ZOOMCAT with a global resolution (L1) of $\sim 2.8^\circ \times 2.8^\circ$ and a nested resolution (L2) of $\sim 0.5^\circ \times 0.5^\circ$. In Section 5.3, we described the flexibility of the horizontal resolution. It is possible to increase the L1 resolution to approximately $\sim 1.125^\circ \times 1.125^\circ$ which can provide higher resolution boundary conditions for the L2 grid. This will be beneficial when the L2 resolution is increased further. There are limitations

on the resolution of the L2 grid due to reasons discussed above. For example, the resolution of the emissions datasets are limited. In the case of CH_4 emissions from wetlands, the largest natural source, the inventory used in our simulations has a resolution $0.5° \times 0.5°$. We also have shown that the resolution of the meteorology used in ZOOMCAT is important. Due to data availability we use meteorology which has a resolution of $\sim 1.125° \times 1.125°$ but the resolution of ERA5 can go up to $0.25° \times 0.25°$ (Hersbach et al., 2020b). We selected a L2 grid resolution of $0.5° \times 0.5°$ because we found no additional improvement was gained when simulating at higher resolutions in the ZOOM1 simulation. By improving the spatial resolution of emissions and meteorology read into ZOOMCAT, it could be possible to simulate ZOOMCAT L2 grid at a higher resolution than shown here. Simulating a higher resolution would increase the computational time and the model time step would need to decrease to satisfy the CFL condition.

In this study we are able to simulate CH_4 at a higher spatial resolution over Europe with a relatively low computational cost. We find that the L1 grid does not compare well with the ICOS sites, with a mean RSME of 30 ppb and a mean R^2 of 0.24 (from ZOOM05 simulation). Our results also show that the L2 grid does not perform well with a mean RMSE of 36 ppb and mean R^2 of 0.26 when compared with observations (from ZOOM05 simulation). This is likely due to the resolution of the meteorology (see Section 5.6). As a result we recommend using high resolution meteorology, when available, in future simulations. Future simulations have the potential to simulate inert species such as radon or sulfur hexafluoride (SF_6) to assess transport processes because these species do not have any sinks.

5.8 Summary

This paper provides a description of the new, one-way nested grid model for TOMCAT, called ZOOMCAT, where a region of interest can be simulated at a higher spatial resolution within a global low resolution model. This is achieved at a lower computational cost than simulating the full globe at a high resolution.

As TOMCAT is an offline CTM, ZOOMCAT could be developed in a simple way which adds an additional high resolution grid (L2) onto the existing global low resolution grid (L1). The offline meteorology is interpolated directly onto either grid, which ensures that the L2 grid makes full use of any available higher resolution forcing winds. As part of the work, TOMCAT was developed so that a boundary layer mixing scheme also used specified ECMWF fields (along

with the convection) to ensure consistency between the meteorology at the two resolutions. Communication from the L1 grid to the L2 grid is achieved by transferring the L1 tracer mixing ratios at the edge of the L2 region as boundary conditions. ZOOMCAT has the flexibility to vary the size and resolution of the nested region and to move it to any location in the world. ZOOMCAT has the potential for many applications within the science topics addressed with TOMCAT simulations. In particular, the nested model can save considerable time in full chemistry simulations by reducing the number of grid boxes in which chemistry is calculated. Here, the potential of ZOOMCAT has been demonstrated through simulations of a CH_4 tracer.

Our simulations show that the increase in spatial resolution afforded by ZOOMCAT shows a better spatial distribution of CH_4 emissions and concentrations. However, comparison of our ZOOM1 and ZOOM05 simulations with ICOS observations shows that the L2 grid does not show any improvement over the L1 grid. This is likely due to either the coarse resolution (T42, $2.8^\circ \times 2.8^\circ$) meteorology or the emissions used in the simulation. We show in our ZOOM_nord simulation that using high resolution operational meteorology improves the comparison between the L2 grid and observations by capturing the variation in emissions better than the L1 grid.

With the increasing availability of high spatial resolution observations, it is important to be able to efficiently simulate atmospheric constituents at similar resolutions to produce comparable outputs and to diagnose the causes of any observed changes. ZOOMCAT can be used to investigate regional changes in atmospheric composition but requires high resolution meteorology to produce the most accurate simulations. A suitable database of high resolution meteorology, likely covering many years, will need to be made available locally for use in the TOMCAT model for ZOOMCAT to realise this potential. The meteorology will also allow further testing of the model, for example the performance of the boundary layer mixing. This work has demonstrated the successful development of the nested 3-D model and offers great potential to aid studies which use the TOMCAT CTM.

References

Arosio, C., Chipperfield, M. P., Rozanov, A., Weber, M., Dhomse, S., Feng, W., Jaross, G., Zhou, X., and Burrows, J. P. (2024). "Investigating Zonal Asymmetries in Stratospheric Ozone Trends From Satellite Limb Observations and a Chemical Transport Model". In: *Journal of Geophysical Research: Atmospheres* 129.8, e2023JD040353. DOI: https://doi.org/10.1029/2023JD040353.

Balasus, N., Jacob, D. J., Lorente, A., Maasakkers, J. D., Parker, R. J., Boesch, H., Chen, Z., Kelp, M. M., Nesser, H., and Varon, D. J. (2023). "A blended TROPOMI+GOSAT satellite data product for atmospheric methane using machine learning to correct retrieval biases". In: *Atmospheric Measurement Techniques* 16.16, pp. 3787–3807. DOI: 10.5194/amt-16-3787-2023.

Bloom, A., Bowman, K., Lee, M., Turner, A., Schroeder, R., Worden, J., Weidner, R., McDonald, K., and Jacob, D. (2021). *CMS: Global 0.5-deg Wetland Methane Emissions and Uncertainty (WetCHARTs v1.3.1)*. en. DOI: 10.3334/ORNLDAAC/1915.

Boersma, K. F., Eskes, H. J., Veefkind, J. P., Brinksma, E. J., A, R. J. van der, Sneep, M., Oord, G. H. J. van den, Levelt, P. F., Stammes, P., Gleason, J. F., and Bucsela, E. J. (Apr. 2007). "Near-real time retrieval of tropospheric NO_2 from OMI". In: *Atmospheric Chemistry and Physics* 7.8. Publisher: Copernicus GmbH, pp. 2103–2118. ISSN: 1680-7316. DOI: 10.5194/acp-7-2103-2007.

Chen, Y., Hall, J., Wees, D. van, Andela, N., Hantson, S., Giglio, L., Werf, G. R. van der, Morton, D. C., and Randerson, J. T. (Mar. 2023). *Global Fire Emissions Database (GFED5) Burned Area*. Version 0.1. Zenodo. DOI: 10.5281/zenodo.7668424.

Chipperfield, M. P. (1999). "Multiannual simulations with a three-dimensional chemical transport model". In: *Journal of Geophysical Research: Atmospheres* 104.D1, pp. 1781–1805. DOI: https://doi.org/10.1029/98JD02597.

– (2006). "New version of the TOMCAT/SLIMCAT off-line chemical transport model: Intercomparison of stratospheric tracer experiments". In: *Quarterly Journal of the Royal Meteorological Society* 132.617, pp. 1179–1203. DOI: https://doi.org/10.1256/qj.05.51.

Chipperfield, M. P., Cariolle, D., Simon, P., Ramaroson, R., and Lary, D. J. (1993). "A three-dimensional modeling study of trace species in the Arctic lower stratosphere during winter 1989–1990". In: *Journal of Geophysical Research: Atmospheres* 98.D4, pp. 7199–7218. DOI: https://doi.org/10.1029/92JD02977.

Etiope, G., Ciotoli, G., Schwietzke, S., and Schoell, M. (2019). "Gridded maps of geological methane emissions and their isotopic signature". In: *Earth System Science Data* 11.1, pp. 1–22. DOI: 10.5194/essd-11-1-2019.

European Commission, Centre, J. R., Crippa, M., Guizzardi, D., Schaaf, E., Monforti-Ferrario, F., Quadrelli, R., Risquez Martin, A., Rossi, S., Vignati, E., Muntean, M., Brandao De Melo, J., Oom, D., Pagani, F., Banja, M., Taghavi-Moharamli, P., Köykkä, J., Grassi, G., Branco, A., and San-Miguel, J. (2023). *GHG emissions of all world countries – 2023*. Last Accessed:05/06/2024. Publications Office of the European Union. DOI: doi/10.2760/953322.

Feng, W., Chipperfield, M. P., Dhomse, S., Monge-Sanz, B. M., Yang, X., Zhang, K., and Ramonet, M. (June 2011). "Evaluation of cloud convection and tracer transport in a three-dimensional chemical transport model". English. In: *Atmospheric Chemistry and Physics* 11.12. Publisher: Copernicus GmbH, pp. 5783–5803. ISSN: 1680-7316. DOI: 10.5194/acp-11-5783-2011.

Hachmeister, J., Schneising, O., Buchwitz, M., Lorente, A., Borsdorff, T., Burrows, J. P., Notholt, J., and Buschmann, M. (2022). "On the influence of underlying elevation data on Sentinel-5 Precursor TROPOMI satellite methane retrievals over Greenland". In: *Atmospheric Measurement Techniques* 15.13, pp. 4063–4074. DOI: 10.5194/amt-15-4063-2022.

Hersbach, H. et al. (2020a). "The ERA5 global reanalysis". en. In: *Quarterly Journal of the Royal Meteorological Society* 146.730. _eprint: https://onlinelibrary.wiley.com/doi/pdf/10.1002/qj.3803, pp. 1999–2049. ISSN: 1477-870X. DOI: 10.1002/qj.3803.

– (2020b). "The ERA5 global reanalysis". In: *Quarterly Journal of the Royal Meteorological Society* 146.730, pp. 1999–2049. DOI: https://doi.org/10.1002/qj.3803.

Huijnen, V., Williams, J., Weele, M. van, Noije, T. van, Krol, M., Dentener, F., Segers, A., Houweling, S., Peters, W., Laat, J. de, Boersma, F., Bergamaschi, P., Velthoven, P. van, Le Sager, P., Eskes, H., Alkemade, F., Scheele, R., Nédélec, P., and Pätz, H.-W. (2010). "The global chemistry transport model TM5: description and evaluation of the tropospheric chemistry version 3.0". In: *Geoscientific Model Development* 3.2, pp. 445–473. DOI: 10.5194/gmd-3-445-2010.

ICOS RI et al. (2024). *ICOS Atmosphere Release 2024-1 of Level 2 Greenhouse Gas Mole Fractions of CO2, CH4, N2O, CO, meteorology and 14CO2, and flask samples analysed for CO2, CH4, N2O, CO, H2 and SF6*. DOI: 10.18160/0F1E-DKXT.

Jacob, D. J. (Dec. 1999). *Introduction to Atmospheric Chemistry*. en. Princeton University Press. ISBN: 978-1-4008-4154-7.

Krol, M., Houweling, S., Bregman, B., Broek, M. van den, Segers, A., Velthoven, P. van, Peters, W., Dentener, F., and Bergamaschi, P. (2005). "The two-way nested global chemistry-transport zoom model TM5: algorithm and applications". In: *Atmospheric Chemistry and Physics* 5.2, pp. 417–432. DOI: 10.5194/acp-5-417-2005.

Levin, I., Karstens, U., Eritt, M., Maier, F., Arnold, S., Rzesanke, D., Hammer, S., Ramonet, M., Vítková, G., Conil, S., Heliasz, M., Kubistin, D., and Lindauer, M. (2020). "A dedicated flask sampling strategy developed for Integrated Carbon Observation System (ICOS) stations based on CO_2 and CO measurements and Stochastic Time-Inverted Lagrangian Transport (STILT) footprint modelling". In: *Atmospheric Chemistry and Physics* 20.18, pp. 11161–11180. DOI: 10.5194/acp-20-11161-2020.

Lorente, A., Borsdorff, T., Butz, A., Hasekamp, O., Brugh, J. aan de, Schneider, A., Wu, L., Hase, F., Kivi, R., Wunch, D., Pollard, D. F., Shiomi, K., Deutscher, N. M., Velazco, V. A., Roehl, C. M., Wennberg, P. O., Warneke, T., and Landgraf, J. (2021). "Methane

retrieved from TROPOMI: improvement of the data product and validation of the first 2 years of measurements". In: *Atmospheric Measurement Techniques* 14.1, pp. 665–684. DOI: 10.5194/amt-14-665-2021.

Lorente, A., Borsdorff, T., Martinez-Velarte, M. C., and Landgraf, J. (2023). "Accounting for surface reflectance spectral features in TROPOMI methane retrievals". In: *Atmospheric Measurement Techniques* 16.6, pp. 1597–1608. DOI: 10.5194/amt-16-1597-2023.

Mannisenaho, V., Tsuruta, A., Backman, L., Houweling, S., Segers, A., Krol, M., Saunois, M., Poulter, B., Zhang, Z., Lan, X., Dlugokencky, E. J., Michel, S., White, J. W. C., and Aalto, T. (2023). "Global Atmospheric δ13CH4 and CH4 Trends for 2000–2020 from the Atmospheric Transport Model TM5 Using CH4 from Carbon Tracker Europe–CH4 Inversions". In: *Atmosphere* 14.7. ISSN: 2073-4433. DOI: 10.3390/atmos14071121.

McNorton, J., Wilson, C., Gloor, M., Parker, R. J., Boesch, H., Feng, W., Hossaini, R., and Chipperfield, M. P. (2018). "Attribution of recent increases in atmospheric methane through 3-D inverse modelling". In: *Atmospheric Chemistry and Physics* 18.24, pp. 18149–18168. DOI: 10.5194/acp-18-18149-2018.

Monks, S. A., Arnold, S. R., Hollaway, M. J., Pope, R. J., Wilson, C., Feng, W., Emmerson, K. M., Kerridge, B. J., Latter, B. L., Miles, G. M., Siddans, R., and Chipperfield, M. P. (2017). "The TOMCAT global chemical transport model v1.6: description of chemical mechanism and model evaluation". In: *Geoscientific Model Development* 10.8, pp. 3025–3057. DOI: 10.5194/gmd-10-3025-2017.

Murguia-Flores, F., Arndt, S., Ganesan, A. L., Murray-Tortarolo, G., and Hornibrook, E. R. C. (2018). "Soil Methanotrophy Model (MeMo v1.0): a process-based model to quantify global uptake of atmospheric methane by soil". In: *Geoscientific Model Development* 11.6, pp. 2009–2032. DOI: 10.5194/gmd-11-2009-2018.

Naus, S., Domingues, L. G., Krol, M., Luijkx, I. T., Gatti, L. V., Miller, J. B., Gloor, E., Basu, S., Correia, C., Koren, G., Worden, H. M., Flemming, J., Pétron, G., and Peters, W. (2022). "Sixteen years of MOPITT satellite data strongly constrain Amazon CO fire emissions". In: *Atmospheric Chemistry and Physics* 22.22, pp. 14735–14750. DOI: 10.5194/acp-22-14735-2022.

Nisbet, E. G. et al. (2019). "Very Strong Atmospheric Methane Growth in the 4 Years 2014–2017: Implications for the Paris Agreement". In: *Global Biogeochemical Cycles* 33.3, pp. 318–342. DOI: https://doi.org/10.1029/2018GB006009.

Parker, R., Boesch, H., Cogan, A., Fraser, A., Feng, L., Palmer, P. I., Messerschmidt, J., Deutscher, N., Griffith, D. W. T., Notholt, J., Wennberg, P. O., and Wunch, D. (2011). "Methane observations from the Greenhouse Gases Observing SATellite: Comparison to ground-based TCCON data and model calculations". en. In: *Geophysical Research Letters* 38.15. ISSN: 1944-8007. DOI: 10.1029/2011GL047871.

Patra, P. K. et al. (2011). "TransCom model simulations of CH_4 and related species: linking transport, surface flux and chemical loss with CH_4 variability in the troposphere and lower stratosphere". In: *Atmospheric Chemistry and Physics* 11.24, pp. 12813–12837. DOI: 10.5194/acp-11-12813-2011.

Pimlott, M. A., Pope, R. J., Kerridge, B. J., Latter, B. G., Knappett, D. S., Heard, D. E., Ventress, L. J., Siddans, R., Feng, W., and Chipperfield, M. P. (Aug. 2022). "Investigating

the global OH radical distribution using steady-state approximations and satellite data". In: *Atmospheric Chemistry and Physics* 22.16. Publisher: Copernicus GmbH, pp. 10467–10488. ISSN: 1680-7316. DOI: 10.5194/acp-22-10467-2022.

Prather, M. J. (1986). "Numerical advection by conservation of second-order moments". In: *Journal of Geophysical Research: Atmospheres* 91.D6, pp. 6671–6681. DOI: https://doi.org/10.1029/JD091iD06p06671.

Saunois, M. et al. (2020). "The Global Methane Budget 2000–2017". In: *Earth System Science Data* 12.3, pp. 1561–1623. DOI: 10.5194/essd-12-1561-2020.

Schneising, O., Buchwitz, M., Hachmeister, J., Vanselow, S., Reuter, M., Buschmann, M., Bovensmann, H., and Burrows, J. P. (2023). "Advances in retrieving XCH_4 and XCO from Sentinel-5 Precursor: improvements in the scientific TROPOMI/WFMD algorithm". In: *Atmospheric Measurement Techniques* 16.3, pp. 669–694. DOI: 10.5194/amt-16-669-2023.

Siddans, R., Knappett, D., Kerridge, B., Waterfall, A., Hurley, J., Latter, B., Boesch, H., and Parker, R. (Nov. 2017). "Global height-resolved methane retrievals from the Infrared Atmospheric Sounding Interferometer (IASI) on MetOp". In: *Atmospheric Measurement Techniques* 10.11. Publisher: Copernicus GmbH, pp. 4135–4164. ISSN: 1867-1381. DOI: 10.5194/amt-10-4135-2017.

Spivakovsky, C. M., Logan, J. A., Montzka, S. A., Balkanski, Y. J., Foreman-Fowler, M., Jones, D. B. A., Horowitz, L. W., Fusco, A. C., Brenninkmeijer, C. A. M., Prather, M. J., Wofsy, S. C., and McElroy, M. B. (2000). "Three-dimensional climatological distribution of tropospheric OH: Update and evaluation". In: *Journal of Geophysical Research: Atmospheres* 105.D7, pp. 8931–8980. DOI: https://doi.org/10.1029/1999JD901006.

Tiedtke, M. (Aug. 1989). "A Comprehensive Mass Flux Scheme for Cumulus Parameterization in Large-Scale Models". EN. In: *Monthly Weather Review* 117.8. Publisher: American Meteorological Society Section: Monthly Weather Review, pp. 1779–1800. ISSN: 1520-0493, 0027-0644. DOI: 10.1175/1520-0493(1989)117<1779:ACMFSF>2.0.CO;2.

Wang, Y. X., McElroy, M. B., Jacob, D. J., and Yantosca, R. M. (2004). "A nested grid formulation for chemical transport over Asia: Applications to CO". In: *Journal of Geophysical Research: Atmospheres* 109.D22. DOI: https://doi.org/10.1029/2004JD005237.

Weber, T., Wiseman, N. A., and Kock, A. (2019). "Global ocean methane emissions dominated by shallow coastal waters". In: *Nature communications* 10.1, pp. 1–10.

Wilson, C., Chipperfield, M. P., Gloor, M., and Chevallier, F. (2014). "Development of a variational flux inversion system (INVICAT v1.0) using the TOMCAT chemical transport model". In: *Geoscientific Model Development* 7.5, pp. 2485–2500. DOI: 10.5194/gmd-7-2485-2014.

Wilson, C., Chipperfield, M. P., Gloor, M., Parker, R. J., Boesch, H., McNorton, J., Gatti, L. V., Miller, J. B., Basso, L. S., and Monks, S. A. (2021). "Large and increasing methane emissions from eastern Amazonia derived from satellite data, 2010–2018". In: *Atmospheric Chemistry and Physics* 21.13, pp. 10643–10669. DOI: 10.5194/acp-21-10643-2021.

Wilson, C., Kerridge, B. J., Siddans, R., Moore, D. P., Ventress, L. J., Dowd, E., Feng, W., Chipperfield, M. P., and Remedios, J. J. (2023). "Quantifying large methane emissions from the Nord Stream pipeline gas leak of September 2022 using IASI satellite observations and inverse modelling". In: *EGUsphere* 2023, pp. 1–26. DOI: 10.5194/egusphere-2023-1652.

Chapter 6

First validation of high-resolution satellite-derived methane emissions from an active gas leak in the UK

Emily Dowd[1,2], Alistair Manning[3], Bryn Orth-Lashley[4], Marianne Girard[4], James France[5,6], Rebecca E. Fisher[5], Dave Lowry[5], Mathias Lanoisellé[5], Joseph R. Pitt[7], Kieran M. Stanley[7], Simon O'Doherty[7], Dickon Young[7], Glen Thistlethwaite[8], Martyn P. Chipperfield[1,2], Emanuel Gloor[9], and Chris Wilson[1,2]

[1]School of Earth and Environment, University of Leeds, Leeds, UK
[2]National Centre for Earth Observation, University of Leeds, Leeds, UK
[3]Met Office Hadley Centre, Exeter, UK
[4]GHGSat Inc., Montréal, Canada
[5]Department of Earth Sciences, Royal Holloway, University of London, Egham, UK
[6]Environmental Defense Fund, 41 Eastcheap, London, UK
[7]School of Chemistry, University of Bristol, Bristol, UK
[8]UK National Atmospheric Emissions Inventory, Ricardo Energy & Environment, Harwell, Oxfordshire, UK
[9]School of Geography, University of Leeds, Leeds, UK

Abstract

Atmospheric methane (CH_4) is the second most important anthropogenic greenhouse gas and has a 20-year global warming potential 82 times greater than carbon dioxide (CO_2). Anthropogenic sources account for ∼60% of global CH_4 emissions, of which 20% come from oil and gas exploration, production and distribution. High-resolution satellite-based imaging spectrometers are becoming important tools for detecting and monitoring CH_4 point source emissions, aiding

mitigation. However, validation of these satellite measurements, such as those from the commercial GHGSat satellite constellation, has so far not been documented for active leaks. Here we present the monitoring and quantification, by GHGSat's satellites, of the CH_4 emissions from an active gas leak from a downstream natural gas distribution pipeline near Cheltenham, UK in Spring/Summer 2023, and provide the first validation of the satellite-derived emission estimates using surface-based mobile greenhouse gas surveys. We also use a Lagrangian transport model, NAME, to estimate the flux from both satellite and ground-based observation methods and assess the leak's contribution to observed concentrations at a local tall tower site (30 km away). We find GHGSat's emission estimates to be in broad agreement with those made from the in-situ measurements. During the study period (March-June 2023) GHGSat's emission estimates are 236-1357 kg CH_4 hr^{-1} whereas the mobile surface measurements are 634-846 kg CH_4 hr^{-1}. The large variability is likely down to variations in flow through the pipe and engineering works across the 11-week period. Modelled flux estimates in NAME are 181-1243 kg CH_4 hr^{-1}, which are lower than the satellite- and mobile survey-derived fluxes but are within the uncertainty. After detecting the leak in March 2023, the local utility company was contacted, and the leak was fixed by mid-June 2023. Our results demonstrate that GHGSat's observations can produce flux estimates that broadly agree with surface-based mobile measurements. Validating the accuracy of the information provided by targeted, high-resolution satellite monitoring shows how it can play an important role in identifying emission sources, including unplanned fugitive releases that are inherently challenging to identify, track and estimate their impact and duration. Rapid, widespread access to such data to inform local action to address fugitive emission sources across the oil and gas supply chain could play a significant role in reducing anthropogenic contributions to climate change.

6.1 Introduction

Atmospheric methane (CH_4) has a 20-year global warming potential 82 times greater than carbon dioxide (CO_2) and the increase in atmospheric CH_4 concentrations since 1750 has contributed an extra 23% to the radiative forcing in the troposphere (Forster et al., 2023; Saunois et al., 2020). CH_4 has a mixture of natural and anthropogenic sources. Anthropogenic sources account for ∼60% of global CH_4 emissions, of which 20% come from oil & gas exploitation and transportation (Saunois et al., 2020). The United Kingdom (UK) contributes 0.48% (European

Commission, 2022) to global anthropogenic CH_4 emissions and 9% of UK anthropogenic emissions are from fugitive emissions from fuels (NAEI, 2022). Fugitive emissions of CH_4 from oil and gas distribution in the UK were estimated to be 187.3 kilotonnes of CH_4 in 2020 (NAEI, 2022). Natural gas is mostly composed of CH_4 (Bains et al., 2016) and fugitive emissions are unintentional releases of substances, such as natural gas, making them difficult to estimate. In the UK, fugitive emissions of natural gas from low-pressure distribution, medium pressure gas mains and above-ground installations are currently estimated by individual utility companies using an industry wide Shrinkage and Leakage model (SLM). The model combines parameters including pipeline length, annual leakage rate and average system pressure correction to estimate fugitive emissions, which are then aggregated to give a UK estimate (Marshall, 2023). The leakage rates are determined by sampling pipes during National Leakage Tests commissioned by the UK Gas Distribution Networks (GDN, Governance (2020)). However, regular monitoring of pipes and detection of leaks through other methods such as emission identification and source rate quantification from high-resolution satellite observations and in-situ monitoring could be incorporated into leakage estimates to improve frequency of quantification and validate estimates.

The UK currently does not have a system to regularly monitor fugitive emissions of CH_4 but the United Nations Environment Programme (UNEP) International Methane Emissions Observatory (IMEO) has a Methane Alert and Response System (MARS) (UNEP, 2023) to inform governments and organisations of large emissions. MARS uses TROPOMI on board Sentinel-5P to identify very large methane plumes ($>$ 25,000 kg h^{-1}, Lauvaux et al. (2022)) and other very large methane hot spots, and combines other satellite instruments such as ASI PRISMA to attribute the plume to a specific source. TROPOMI has a pixel size of 5.5 km $\times$ 7 km with a detection threshold of 25,000 kg h^{-1} (Lauvaux et al., 2022) and ASI PRISMA 30 m $\times$ 30 m with a detection threshold of 500-2,000 kg h^{-1} (Guanter et al., 2021). MARS is an example of how high-resolution satellite-based imaging spectrometers, such as TROPOMI and ASI PRISMA, are becoming important tools for detecting and monitoring CH_4 point source emissions, aiding mitigation globally.

GHGSat was the first satellite constellation launched specifically for CH_4 point-source emission identification, quantification, and attribution, and was the first system to provide high-resolution data to IMEO, although these data are not incorporated into MARS. GHGSat's constellation

provides global monitoring of sites that are emitting above 100 kg h^{-1} and also targets locations based on detected emissions using Sentinel-5P or Sentinel-2 (Schuit et al., 2023). Not all leaks can be detected by global monitoring satellites, such as Sentinel-5P or Sentinel-2, due to their high detection threshold and lower resolution and so GHGSat's ability to detect smaller sources is important for observing leaks that might otherwise go undetected and unreported. However, there is a trade-off between global monitoring satellites and GHGSat because GHGSat requires a target to observe. GHGSat has previously detected and quantified CH_4 emissions from a variety of sources including landfill sites, coal mining and natural gas pipelines (GHGSat, 2023b; ESA, 2021; GHGSat, 2023a). Validation of GHGSat's technology has been performed on controlled releases and blind validation tests (McKeever and Jervis, 2022; Sherwin et al., 2023). There are a number of different methods that can be used to estimate emissions from point sources using measurements from satellite data, e.g. Gaussian Plume Model, Local Mass Balance for near-source pixels, Gauss Theorem, Cross-Sectional Flux (CSF) and Integrated Mass Enhancement (IME) (Jacob et al., 2016).

Validation of the emission estimates from the GHGSat satellite constellation, using the IME method, has so far not been documented for active leaks. Here we present the detection, monitoring and quantification, by GHGSat's satellites, of CH_4 emissions from an active gas leak near Cheltenham, UK in Spring/Summer 2023, and provide the first study using surface-based mobile greenhouse gas surveys to validate GHGSat's estimates. There are two main methods for estimating the emission flux from surface-based mobile surveys; the Gaussian Plume Model and the Other Test Method 33A (OTM 33A).

In this study we provide estimates of the Cheltenham gas leak using three different methods: i) GHGSat-derived fluxes using the Integrated Mass Enhancement Method (IME); ii) Fluxes derived from ground-based observations using a Gaussian Plume model; and iii) Estimates from plumes simulated by the UK Met Office's Numerical Atmospheric-dispersion Modelling Environment (NAME, Jones et al. (2007)) scaled to match the satellite and mobile survey observations. We also estimate mole fractions from the leak at a local tall tower monitoring site using NAME. We compare the modelled mole fractions from the gas leak with the observed above-background concentrations and discuss the implications of the leak in terms of the UK National Atmospheric Emissions Inventory (NAEI) and the success in monitoring and mitigating it. Note that, throughout this text, were refer to kg CH_4 h^{-1} as kg h^{-1}.

6.2 Methods

6.2.1 Gas Leak Location

The University of Leeds requested, through the Third Party Missions Programme with the European Space Agency (ESA), that GHGSat monitor a landfill site near the town of Cheltenham, UK and provide Level 4 emission estimate data. By chance, the monitored area included the location of a large (> 100 kg h^{-1}) gas leak (within 1 km of the landfill) allowing it to be detected by the satellite constellation. The landfill site was found to be below the satellite's detection threshold. The gas leak was first detected by GHGSat during its first cloud-free overpass on 27 March 2023 and the location of the leak from the satellite was estimated to be 51.95097 °N, 2.09956 °W at approximately 33 m above sea level (m.a.s.l). A GHGSat operator determines the source location by the shape of the observed plume (plume tail direction) and the area most concentrated at the beginning of the plume tail. When the plume shape and concentration gradient in the plume does not show a traditional directional plume-shape, the wind direction from Goddard Earth Observing System Forward Processing (GEOS-FP; NASA (2024)) is used to determine which side of the emission will most likely correspond to the source location. When GHGSat detect an emission from a site which is not in their database, other datasets such as visible satellite imagery and infrastructure maps are used to determine the source. In this case, GHGSat confirmed the source by contacting the utility company. The leak was from a low-pressure gas distribution pipeline situated in a field next to a railway line, approximately 5 km north of Cheltenham. The UK gas pipeline network is currently being upgraded from old metal pipes to new plastic ones and it is likely that the gas leak came from an older pipe (Wales & West Utilities, 2023). The GHGSat satellite constellation monitored the site over approximately 11 weeks (6 successful observations, one with no emissions detected) until the leaking pipe was repaired. The area surrounding the leak is a mixture of pastoral and arable agricultural land with one farm ∼70 m to the east of the site, two waste management sites less than half a kilometre to the south and a small residential area less than 200 m to the east and southeast of the leak location. The farm closest to the site rears cattle so they are also a likely source of CH_4 to the atmosphere along with manure produced by other animals, although these sources are much more diffuse. There is one single carriageway road to the south of the leak location, which passes within ∼30 m of the estimated location of the gas leak. The leak location estimated here is an approximate location for the surface emission and is not necessarily the

precise location of the pipeline break. In our analysis, we use a mean location for the leak, 51.95088°N, 2.09962°W, estimated by the satellite. The individual estimated locations for each satellite observation can be found in the Supplement. The estimated locations were in close agreement with each other, within ±25 m, apart from one outlier.

6.2.2 Atmospheric Methane Measurements

6.2.2.1 GHGSat Measurements

GHGSat is a constellation of 9 SmallSats (∼15 kg) orbiting in low Earth orbit at altitudes ranging from 500 – 550 km which retrieve vertical column density of CH_4 and detect concentration enhancements above background from targeted industrial facilities globally. The satellite retrievals are collected using a Wide-Angle Fabry-Perot (WAF-P) imaging spectrometer, which is a hyperspectral spectrometer operating in the short-wave infrared (SWIR) at 1630 - 1675 nm, where methane absorption lines can be resolved for each pixel in the 12 km × 12 km sensor field-of-view (Jervis et al., 2021). This sensor system achieves both high spatial and spectral resolution, enabling precise geolocation and low noise measurements. For the 8 commercially operating satellites (GHGSAT-C1 to C8), the system achieves a spatial resolution of 25 m and spectral resolution of 0.3 nm (Jacob et al., 2022), having the capability of a 1-2 day revisit time. This allows for precise attribution of CH_4 emission enhancements to sources with emission rates above 100 kg h^{-1} (50% probability of detection at wind speeds of 3 m s^{-1}). The performance of the system has been independently verified through controlled releases of CH_4 at known rates that were measured using the GHGSat system (Sherwin et al., 2023).

The raw images collected by the satellites are processed through GHGSat's proprietary toolchain and reviewed by experts at GHGSat. The surface reflectance and column-averaged concentration of CH_4 in parts per billion (ppb) are retrieved for each pixel by fitting a model of the instrument and atmosphere. These data are georeferenced using the satellite's GPS outputs and Landsat-8 imagery with sub-pixel accuracy, achieving a geolocation accuracy of ∼25 m for the source location.

6.2.2.2 Mobile Greenhouse Gas Observations

Royal Holloway, University of London's (RHUL) mobile greenhouse gas laboratory was used for ground-based verification of the leak location, source type and emission rate. The mobile labo-

ratory includes a suite of cavity enhanced laser absorption spectrometers for the measurement of CH_4, CO_2 and ethane (C_2H_6) mole fractions and methane isotopes (δ13C-CH_4): Picarro G2311-f (10 Hz CH_4 and CO_2), Licor-7810 (1 Hz CH_4 and CO_2), LGR UMEA - ultraportable methane ethane analyser (1 Hz CH_4 and C_2H_6) and Picarro G2210-i (1 Hz CH_4, CO_2, C_2H_6 and δ13C-CH_4). The instruments are powered using a 6 kW portable lithium power station (Goal Zero Yeti 6000). Air is pumped to the instruments from inlets on the roof of a hybrid car, 1.8 m above ground level. A sonic anemometer (Campbell CSAT3B 3-D) and GPS receiver are also installed on the roof of the vehicle. Another air inlet is connected to a diaphragm pump for filling 3 litre multilayer foil bags with air, for subsequent high precision methane δ13C analysis by isotope ratio mass spectrometry (Fisher et al., 2006) and methane mole fraction analysis using the Licor-7810. The air bags were filled when the car was parked both in and outside of the emissions plume. Instruments are harmonised to international scales for CH_4 and CO_2 at RHUL using cylinders of ambient air calibrated by NOAA (National Oceanic and Atmospheric Administration).

Mobile surveys were carried out during daytime on 26 May, 12 June and 22 June 2023. These dates were chosen because the wind direction was from between NW and ENE, allowing the emissions plume to be measured on the nearest road, which was to the south of where GHGSat had identified the source. During each survey, the car was driven at 20-30 mph (32-48 km h^{-1}) on a public road downwind of the emissions site with at least 12 passes. The public road included a road bridge over a railway, close to satellite-derived leak location.

6.2.2.3 Greenhouse Gas Tall Tower Measurements

The UK Deriving Emissions linked to Climate Change (UK DECC) network currently consists of four tall tower sites within the UK (in addition to the baseline station at Mace Head, Ireland). The UK DECC network has been collecting measurements since 2012 and measures various atmospheric constituents including CH_4 (Stanley et al., 2018). CH_4 is measured by a cavity ring-down spectrometer (CRDS) at multiple inlet heights. The CRDS is calibrated using both a standard of approximately ambient mole fraction and a set of calibration standards which range above and below ambient mole fractions (Stanley et al., 2018). Calibrant and standard gases are used in the CRDS at all sites and are of natural composition. The standard gas is measured once a day to assess linear instrumental drift and the calibration gases are measured once a month to assess for instrument nonlinearity. The repeatability of the daily standard measurements is

< 0.3 nmol mol^{-1} (Stanley et al., 2018). The two key stations from the UK DECC network in this study are Mace Head (MHD) on the west coast of Ireland and Ridge Hill (RGL) in central western England. MHD is at 53.32667°N, 9.90456°W and close to the shoreline. The surrounding area is sparsely populated, resulting in low local anthropogenic emissions at the site. Prevailing winds from the west and south-west bring well-mixed Atlantic air to MHD. As a result, the majority of measurements obtained at MHD at 10 m above ground level (a.g.l.) are representative of northern hemisphere, mid-latitude background concentrations (Stanley et al., 2018). RGL is a rural site situated at 51.99747°N, 2.53992°W which is approximately 30 km east of the border between England and Wales. RGL is surrounded by land primarily used for agriculture. It is also 16 km south-east from Hereford and 30 km south west of Worcester, both large towns, and there are a number of wastewater treatment plants within a 40 km radius of the site (Stanley et al., 2018). RGL measures CH_4 at 45 and 90 m a.g.l. and in this study, we use measurements from the 90 m a.g.l. inlet because it has a larger footprint of influence. The different source sectors surrounding RGL have an impact on the observed concentrations, but the main waste sites in the area are not upwind of the leak, which is 30 km east of RGL.

We use the concentrations representative of well-mixed mid-latitude northern hemisphere air measured at MHD to produce a time-varying background concentration at RGL, as described in Manning et al. (2021). The background concentrations are subtracted from the observed concentrations to obtain an above-background concentration at RGL.

6.2.3 Flux Estimation Methods

6.2.3.1 GHGSat Flux Estimation

The satellite-derived fluxes are estimated using the Integrated Mass Enhancement (IME) method (Varon et al., 2018). First, the emission signal is identified and masked by isolating methane enhancements that are not instrument artefacts or signal from albedo features. The IME method relates the emission source rate to the emission mass downwind of the source (defined by the masked methane concentration and the source location) based on the expected transport of methane in the wind (defined by the GEOS-FP model wind data). The IME of the observed plume is:

$$IME = \sum_{j=1}^{N} \Delta\Omega_j A_j, (j = 1...N) \tag{6.1}$$

where N is the number of pixels, $\Delta\Omega_j$ is the mean source pixel enhancement and A_j is area of each pixel. The IME of the observed plume and the source rate Q is related by the residence time of methane in the plume, τ, where τ can be expressed in terms of the effective wind speed U_{eff} (m s-1) and plume size L (m):

$$Q = \frac{IME}{\tau} = \frac{U_{eff}}{L} IME = \frac{U_{eff}}{L} \sum_{j=1}^{N} \Delta\Omega_j A_j \tag{6.2}$$

where U_{eff} is a function of the 10m wind speed from GEOS-FP, see Varon et al. (2018) for full description of IME method. The uncertainty on the source rate is the 1σ standard deviation based on the uncertainties on the wind speed, measurement uncertainties, and the IME model parameters, where the wind speed is the dominant source of uncertainty. Details of how the wind speed uncertainty is calculated can be found in the Supplement of Varon et al. (2019).

There are a number of different methods to estimate the flux using satellite data, as listed in Section 6.1. The Gaussian Plume Model is the simplest way to simulate a CH_4 plume and is described in Section 6.2.3.2. Due to atmospheric conditions, CH_4 plumes can be turbulent and sometimes discontinuous which means that it can be unrealistic to model satellite-observed plumes as Gaussian (Jongaramrungruang et al., 2019). The Local Mass Balance method for near-source pixels estimates the flux by only considering the column enhancement over the point source pixel, neglecting information of the plume downwind (Varon et al., 2018). This method can be effective when the pixel size is coarse and contains most of the information of the plume. However, it is not suitable for high-resolution retrievals, such as those from GHGSat, because it does not use information of the plume downwind, where there may be strong variability in the wind from small-scale turbulence and the source pixel transport may be by turbulent horizontal diffusion rather than advection by the mean wind (Varon et al., 2018). The Gauss Theorem method is the outward flux summed along a contour surrounding the point source and does not account for the contribution of turbulent diffusion to the outward flux (Jacob et al., 2022). This method is often used for in situ aircraft observations which circle the source and measures wind and methane at the same time (Jacob et al., 2022).

The Cross-sectional Flux (CSF) and IME methods are both used to estimate fluxes of point sources from satellite retrievals because they provide consistent results (Varon et al., 2019). The CSF method estimates the flux from the product of the methane enhancement and the wind speed integrated across the plume width. Varon et al. (2018) found that the IME method performs best for GHGSat data and is the selected method for our analysis.

6.2.3.2 Gaussian Plume Inversion Method

The flux estimates from the mobile greenhouse gas measurements were calculated using a Gaussian plume model to determine the mole fraction of a gas as a function of distance downwind of a point source (Seinfeld and Pandis, 2006). We use this model, developed by Pasquill and Smith (1983), to estimate the emission rate of the source using the concentrations observed downwind of the plume to scale an idealised Gaussian plume model. In the idealised model, the mole fraction at a point in the plume is a function of flux of the source (Q, kg h^{-1}), advective horizontal wind speed (u, m s^{-1}), the rate of dispersion and the distance from the source, see Eq. 6.3. The plume measured during each transect during the mobile survey was manually identified in the dataset and distance and angle to the emission source calculated. We used a mean of the source locations provided by the satellite retrievals as the source location in the model. We then took the observed concentration data and wind speed data to create the initial model plume using Eq. 6.3. On 26 May we used a mean wind speed observed by the vehicle's 10Hz sonic anemometer for each transect, whereas on the 12 June we used wind speed data, averaged to the nearest hour, from the Met Office's UKV model due to the unavailability of the anemometer.

$$C(x,y,z) = \frac{Q}{\pi\sigma_y\sigma_z u} exp\left(-\frac{y^2}{2\sigma_y^2}\right)\left[exp\left(-\frac{(z-h)^2}{2\sigma_z^2}\right) + exp\left(-\frac{(z+h)^2}{2\sigma_z^2}\right)\right] \tag{6.3}$$

where C (μg m^{-3}) is the atmospheric concentration of methane at (x, y, z), x is the distance downwind from the source (m), y is the distance crosswind (m), z is the height above ground level (m), Q is the source strength (kg h^{-1}), σ_y and σ_z are the diffusion coefficients in the crosswind and vertical directions respectively, u represents the horizontal time-averaged wind speed (m s^{-1}) and h is the height of the release (m). The dispersion coefficients of the plume (σ_y and σ_z) are approximated using Brigg's assumptions in the Pasquill-Gifford atmospheric stability classification. σ_y and σ_z are given as functions of downwind distance x (m) and stability class.

Equation 6.4 shows the general form of parameterisation of plume width parameters according to Briggs (1973).

$$\sigma_y = \frac{ax}{\sqrt{1+\beta x}} \quad \text{and} \quad \sigma_x = ax(1+\beta x)^y \tag{6.4}$$

The observations are measured in parts per billion (ppb) and are scaled to μg m^{-3} at standard temperature and pressure (STP) conditions. To scale from the idealised plume to the measurements, the flux through a control surface of 1m height and the width of the plume is determined using the measurement data (Eq. 6.5).

$$\sum(c_i[CH_4] \cdot \Delta x_i \cdot \Delta z) \tag{6.5}$$

where c_i is the concentration at point i, Δx_i is the distance driven by the car at this point, and Δz=1 m is the vertical extent of the control surface. The height of the control surface is allowed to vary between 2 and 7 m a.g.l to best match the height of the vehicle inlet above ground level when accounting for the effect of the bridge structure. The corresponding control surface flux is then calculated for the modelled plume and the ratio between the measured control surface flux and modelled control surface flux used to scale the model to the measured plume. There are several assumptions made when using the Gaussian plume model. We assume that the source is emitting at a constant rate, the CH_4 mass is conserved and there are no additional sources or sinks during transport. We also assume that the wind speed and vertical eddy diffusivity are constant, the diffusion in the x direction and horizontal wind shear is negligible and the molecular diffusion is negligible compared to turbulent diffusion. Local baseline CH_4 is taken as the second-percentile measurement over a 5-minute moving average window as per other mobile campaigns. However, only measurements more than 1 ppm above baseline concentrations were used in the calculation of gas leak flux to conservatively ensure that the total is not enhanced by any small emissions from surrounding sources such as the farm or waste sites. The baseline was calculated using the methods described in Fernandez et al. (2022).

We performed a Monte-Carlo simulation to determine the CH_4 emission estimates and the associated uncertainty for each surface-based mobile survey. The leak location is randomly assigned to any point within an approximate 10 m $\times$ 10 m box around the mean location of the leak

(derived by the satellite observations). The box is bounded by the coordinates: 51.9506799°N, 2.099682°W; 51.9506635°N, 2.0997039°W; 51.9506682°N, 2.0997021°W; 51.9506718°N, 2.0997023°W. The wind speed for each individual plume is determined using the mean wind speed during the traverse. The wind speed for each plume also has a random uncertainty assigned with a mean of 1 ms^{-1} and was allowed to vary according to a Gaussian distribution. The vehicle height varied during the traverse of the plume due to the presence of a road bridge over a railway line. To account for the difference between the ground height and inlet height, we allowed the simulation to vary randomly between 2.5 m - 6.5 m, with 1 m intervals. We also selected the most appropriate atmospheric stability classification based on the averaged wind speed per each Monte-Carlo run. The sky conditions did not vary significantly during the period of measurement on each day, resulting in the selection being based on wind speed only (see Supplement, Table B.2 for the stability classes and meteorological conditions). The Monte-Carlo simulation was run 1,000 times for each suite of transects.

There are two main methods for estimating the flux using a ground-based mobile survey, as described in Section 6.1. The OTM 33A requires measurements to be taken downwind of the source, perpendicular to the wind direction in order to detect the plume centre line. Once the centre line has been found, the CH_4 concentrations and meteorological conditions are measured continuously for 20 minutes. The emissions are then quantified using a Gaussian Plume model with three assumptions; the measurement inlet is at the height of release, measurements are taken directly downwind of the source and reflection from the ground is negligible from the source (Ražnjević et al., 2022). However in this study it was not feasible to carry out the OTM 33A because we took observations on a public road and could not be static in the plume for the required time.

6.2.3.3 NAME Dispersion Modelling

We simulated the dispersion of the gas leak through a suite of experiments using the UK Met Office's Numerical Atmospheric-dispersion Modelling Environment (NAME, Jones et al. (2007)). We use NAME to estimate the flux of the leak using the observed concentrations from both GHGSat and the mobile survey to provide some continuity between the two observation and flux estimation techniques. We also modelled the leak's mole fractions of CH_4 at Ridge Hill (RGL) tall tower site (30 km away) and compared them to the observed above-background concentrations at RGL.

NAME is a Lagrangian dispersion model which simulates the transport and dispersion of chemical species through the atmosphere (Jones et al., 2007). The model is offline and for this study is driven by the Met Office's Numerical Weather Prediction (NWP) meteorology from the high-resolution UKV model (Davies et al., 2005; Bush et al., 2023). The UKV meteorology has a horizontal resolution of 1.5 km × 1.5 km and 70 vertical levels over the UK with hourly temporal resolution. NAME follows individual theoretical particles during the simulation and the number of particles within the user-defined grid determines the total mass output per grid cell for each time step. Model particles are advected by three-dimensional wind fields provided by the NWP model and are dispersed using random walk techniques which account for turbulent velocity structures in the atmosphere (Jones et al., 2007). NAME includes additional parametrizations for atmospheric processes which are unresolved in the NWP model, which influence the transport of pollutants, including deep convection, horizontal mesoscale motions, and turbulence (Meneguz and Thomson, 2014; Webster et al., 2018). The output resolution of NAME is user-defined, allowing a suite of experiments to be performed at various resolutions. In our simulations we assume the chemical sinks of CH_4 to be negligible due to the short transport time to both the road near the leak site (∼minutes, depending on wind direction) and to RGL (∼7-10 hours, depending on wind direction) compared to the long atmospheric lifetime of CH_4 (∼9 years, Prather et al. (2012)).

In the first experiment, we set up a high-resolution grid in NAME to estimate the magnitude of the flux from the concentrations observed by the satellite and mobile survey. We did this to provide a flux estimation for both observation methods, using the same model and meteorology to provide some continuity between the satellite and mobile survey-derived estimates. To estimate the flux using the satellite retrievals we simulated the gas leak with a unit release (1 g s^{-1}), starting 1 hour before the time of observation and simulated the release for three hours. The simulation was output with a horizontal resolution of 25 m × 25 m with a 500 m vertical resolution up to 1000 m a.g.l. and a 1-hourly time step. We selected the model time step closest to the observation time to do our analysis. We produced a pressure-weighted mean total column value from the two layers, where concentrations in the layer above 500 m were approximately 0 ppb. The modelled and observed plumes did not overlap well so we defined certain criteria in the modelled plume to capture the modelled dispersion of CH_4 in a way that is comparable with the GHGSat plume. We defined the plume by removing concentrations less than 1% of the maximum value and limited the length of the modelled plume to match the observed length

of GHGSat's plume. This method assumes that the CH_4 emitted in NAME has travelled at the same distance and speed as detected by GHGSat. We integrated the CH_4 over the total column concentrations in both the GHGSat plume and the defined area of the NAME plume to obtain a scaling factor for the NAME flux. We then used this scaling factor to estimate the flux of the gas leak using NAME. To test the robustness of our modelled flux estimate we also calculated fluxes using two other plume definitions: (1) We removed values less than 1% of the maximum value; and (2) less than 5% of the maximum value, ignoring the plume length criteria in both cases. We then scaled the model using the integrated mass from these defined plumes to test the robustness of the flux estimation method. Apart from the release location and length of the plume, no other constraints from the observed satellite plume are applied to the modelled plume. The three different plume definitions are analogous to the threshold value used by GHGSat to filter noise around the detected plume.

We applied a similar mass integration method to estimate the flux in NAME using the observations from the mobile survey. We simulated the gas leak with a unit release (1 g s^{-1}), starting 1 hour before the peak observation time and simulated the release for three hours. The model was output at a horizontal resolution of 10 m $\times$ 10 m with a single 4 m layer to capture the volume observed by the mobile survey. We selected three values centred on the maximum concentration in the model and mobile survey concentrations along the road that the survey was completed. In the model the selected values include the maximum value of the plume along the road and the two grid boxes either side of the maximum value. From the observations we used the median concentrations calculated from the different observed transects during the mobile survey (see Supplement Section B.3), then selected the maximum value and the observations taken immediately before and after the maximum value. These values are approximately 10 m apart. We integrated across the three peak values for the model and mobile survey in order to scale the model and deriv a modelled flux. We then calculated flux estimation uncertainties by taking the three grid boxes to the left and three grid boxes to the right of the peak value on the road and use the mass of these grid boxes to scale the model to the observed peak concentrations. Flow-charts showing the calculation processes of the three different flux estimation methods can be found in the Supplement, Section B.3.

The second experiment involved estimating the leak's contribution to the observed above-background concentrations at the nearby tall tower (RGL) and assessing the likelihood of the

leak contributing to most of the observed above-background concentration. We ran NAME with an output resolution of 2.5 km × 2.5 km with 40 m vertical resolution up to 120 m a.g.l. to capture the height of the observations at RGL. We used the five observed emission rates provided by GHGSat. We simulated the leak as a point source in NAME at 51.95088°N, 2.09962°W from 27 March to 13 June, with the emission rate being held constant at each derived emission rate from the date that the observation was made until the date of the next available observation (see Fig 6.3a). We also simulated the upper and lower uncertainty emission rates from the satellite-derived fluxes (see Fig 6.3a). The model produced a one-hourly time series output at the RGL tall tower location at 80-120 m a.g.l. which we compared to the above-background observations. This simulation is called 'NAME_spring'. Note, the prevailing wind at the leak site is from the west/southwest but a north easterly wind is needed for the emissions from the leak to be transported to RGL.

In the third experiment, we simulated the leak with the same model set up as NAME_spring but with two alternative constant flux rates and simulated an extra year before the date that the leak was discovered, giving a simulation time of approximately 1 year and 5 months (1 March 2022 to 13 June 2023). We simulated both the maximum flux derived by GHGSat and the maximum flux derived from the mobile survey separately. This simulation is called 'NAME_long'. We selected this time period to cover a full year previous to the leak discovery, to assess the frequency of large contributions at RGL from a theoretical leak over a longer time period, including different seasons. It should be noted that the UK DECC network was set up to monitor long-term greenhouse gas concentrations across the UK and is not specifically designed to detect fugitive emissions, like this gas leak. However, due to the location of the tall tower site relative to the gas leak in this case (within 30 km), it is reasonable to consider whether it might have been possible to use statistical analysis and inverse modelling techniques to recognise that the leak was ongoing without the use of GHGSat.

6.3 Results

6.3.1 Observations and Flux Comparisons

We first observed an enhancement over a field, which was later confirmed to be a gas leak, on 27 March 2023 via satellite when targeting the nearby landfill site. The satellite was centred on 51.9402°N, 2.0998°W with a 12 km × 12 km field-of-view. After detecting the leak, GHGSat

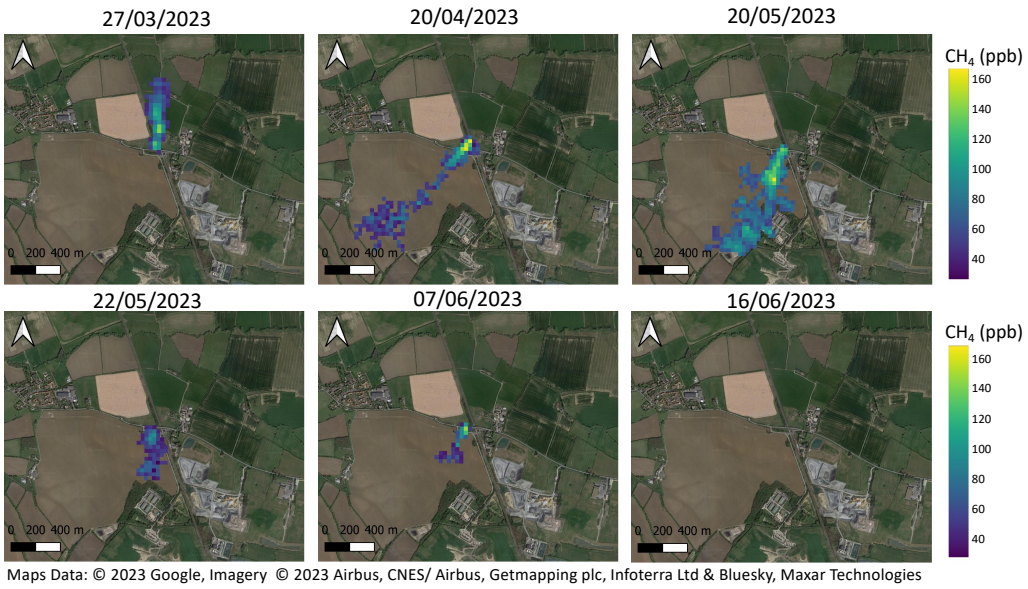

Figure 6.1: Total column CH_4 (ppb) observations from the GHGSat satellite showing the variation in strength and size of the plume from the gas leak on six dates between March and June 2023 (©Google Maps 2023). The geographical area shown is not the full field-of-view of the satellite and contains only the area where enhanced CH4 concentrations were identified.

continued to monitor the site with the same field-of-view to quantify how much CH_4 was being released. Figure 6.1 shows the CH_4 plumes measured by the satellite between 27 March and 16 June 2023. The initial observation on 27 March produced a flux estimate from the leak of 236 $\pm$ 157 kg h^{-1} and the peak observed leak rate occurred on 20 May with an estimated flux rate of 1375 $\pm$ 481 kg h^{-1}. The observations taken after 20 May show that the size and strength of the plume was decreasing, with the last observed emission on 7 June with an estimated flux rate of 290 $\pm$ 130 kg h^{-1}. The satellite-derived fluxes were estimated using the IME method. The next successful observation on 16th June shows no emissions above the 100 kg h^{-1} detection threshold.

During the satellite observation period, we conducted mobile greenhouse gas surveys of the leak to validate the satellite measurements. On 26 May and 12 June, observed CH_4 mole fractions were large enough to be above the dynamic range (20 ppm but capable up to 60 ppm) of the Picarro G2311-f when driving through the plume. The Licor-7810 data were therefore used for

the Gaussian plume modelling. The maximum CH_4 mole fractions recorded in each pass were 77 - 588 ppm (77,000 - 588,000 ppb) on 26 May and 120 - 839 ppm (120,000 - 839,000 ppb) on 12 June. Gaussian plume estimates of the flux were estimated to be 846 ± 453 kg h^{-1} on 26 May and 634 ± 299 kg h^{-1} on 12 June. The ethane/methane ratio in the plume was 0.05 and the δ13C isotopic signature was -36.7 ± 2.1 ‰. These values are characteristic of the thermogenic gas in the UK gas network (Zazzeri et al., 2015; Lowry et al., 2020), and confirm that the leak was from a gas pipeline. On 22 June there were no significant enhanced concentrations recorded downwind of the leak site.

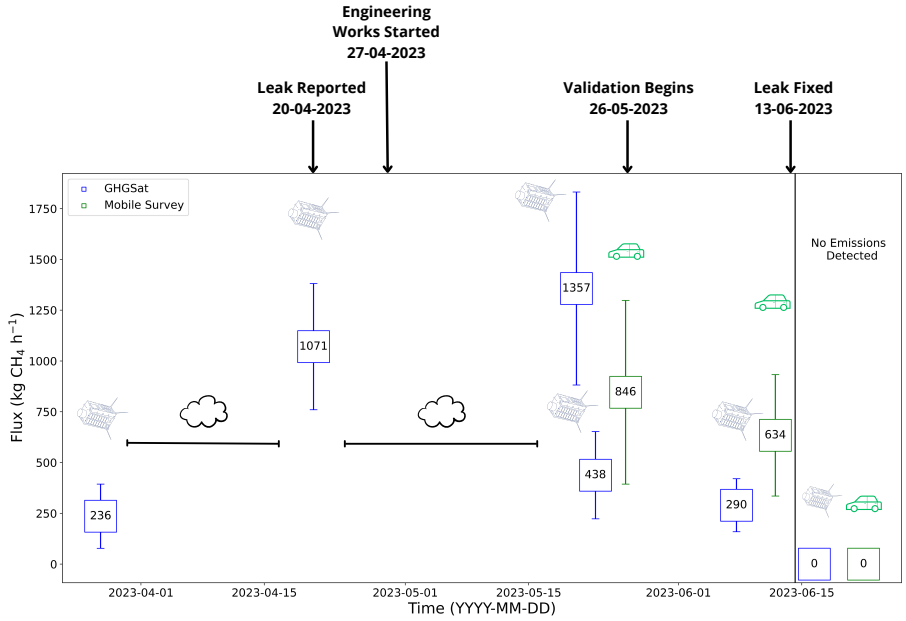

Figure 6.2: Timeline of events during the observation period of the gas leak and the flux estimates (kg CH_4 h^{-1}) from the different instruments. The satellite-derived fluxes are in blue and the mobile survey-derived fluxes are in green. The error bars represent the uncertainty on the flux estimates, as described in Section 6.2.3.1 and Section 6.2.3.2.

Figure 6.2 shows the timeline of events, including estimated fluxes (with their uncertainty), from both estimation methods. Also shown are the dates that the leak was reported to the utility company by GHGSat, when work started on the leak, when the leak was resolved according to the utility company and when there were no further emissions detected by satellite or mobile survey. Once the persistence of the leak was confirmed on 20th April, GHGSat contacted the utility company. A member of public had also reported the smell of gas to the utility company prior to the notification from GHGSat and the utility company started work on assessing and repairing the leak on 27 April. GHGSat continued to monitor the leak and validation of the

Table 6.1: The comparison between the mobile survey and GHGSat-derived fluxes (kg h^{-1}) and the equivalent fluxes derived in NAME (kg h^{-1}). The bounds of NAME-derived fluxes are shown in brackets.

Date	Mobile Survey Flux (kg $^{-1}$)	NAME-Derived Flux from MS Concentrations (kg $^{-1}$)	GHGSat Flux (kg h^{-1})	NAME-Derived Flux from GHGSat Concentrations (kg h^{-1})
27/03/2023	-	-	236 ± 157	181 [135, 329]
20/04/2023	-	-	1071 ± 310	745 [539, 1376]
20/05/2023	-	-	1375 ± 481	1243 [931, 2322]
22/05/2023	-	-	438 ± 215	408 [169, 286]
26/05/2023	846 ± 453	406 [366, 680]	-	-
07/06/2023	-	-	290 ± 131	204 [77, 241]
12/06/2023	634 ± 299	512 [498, 681]	-	-

satellite retrievals by mobile survey began on 22nd May. We directly compare the flux estimates derived from the satellite and mobile surveys. Cloud obstructed the view of the satellite on the mobile survey days, so we compare the mobile survey-derived fluxes with the most recent satellite-derived flux to validate the satellite fluxes. We compare the mobile survey-derived flux on 26 May (846 ± 452 kg h^{-1}) and 12 June (634 ± 299 kg h^{-1}) with the satellite-derived flux on 22 May (438 ± 215 kg h^{-1}) and 7 June (290 ± 131 kg h^{-1}), respectively, finding that the mobile survey-derived fluxes are larger than the satellite derived fluxes on these dates. Both sets of fluxes have relatively large uncertainties, predominantly due to wind speed estimates used in the flux estimation, and the uncertainties overlap for the fluxes derived from the two observation methods, see Fig. 6.2. Differences between the satellite and ground survey fluxes will be discussed in detail in Sect. 6.4.

6.3.1.1 Flux Estimations from NAME Plume Modelling

We also use NAME to obtain a modelled estimate of the gas leak on each observation date for GHGSat and mobile survey observations to allow continuity between different observation and flux estimation methods. We simulated the gas leak with a unit release (1 g s^{-1}) and then used the observed concentrations to scale NAME to estimate the flux as described in Sect. 6.2.3.3. Table 6.1 shows the flux estimations from GHGSat and the mobile survey and their corresponding NAME-derived flux estimation, with the bounds of the estimation quoted in brackets from NAME. The NAME-derived flux estimations are smaller than the GHGSat-derived fluxes, but are always within the GHGSat uncertainty (Table 6.1). The smallest flux observed by GHGSat on 27th March was estimated to be 236 ± 157 kg h^{-1} and we estimate a flux of 181 [135, 329] kg h^{-1}, with a difference of 23% (55 kg h^{-1}) compared with the central estimate of the GHGSat-derived flux. The bounds of the NAME-derived flux estimations described in

Sect. 6.2.3.3 are shown in brackets. The largest flux observed by GHGSat on 20th May was estimated to be 1375 ± 481 kg h^{-1} and we estimate a flux of 1243 [931, 2322] kg h^{-1}, with a difference of 10% (132 kg h^{-1}) compared with the central estimate of the GHGSat-derived flux. The estimation uncertainties for the NAME-derived fluxes are much larger than the GHGSat-derived fluxes on 20 April and 20 May and this is likely due to higher wind speeds used in the model compared with the wind speeds used in GHGSat's IME method (see Supplement, Table B.4).

We also simulated the gas leak in NAME to derive a flux from the mobile survey observations. The NAME-derived fluxes are lower than the mobile survey-derived fluxes but they lie within the mobile survey estimation uncertainty (Table 6.1). The peak concentrations measured during the mobile survey were larger on 12 June than the concentrations measured on 26 May. However, the Gaussian Plume Model estimates a large flux on 26 May (846 ± 453 kg h^{-1}) due to differences in wind speeds on the observation days. The NAME-derived flux is larger on 12 June (512 [498,681] kg h^{-1}) than the NAME-derived flux on 26 May (406 [366,680] kg h^{-1}). The NAME-derived fluxes use the same wind speeds as the Gaussian Plume Model on 12 June so differences between the model and the mobile survey fluxes are likely due to differences in the peak location along the road and the model resolution.

6.3.1.2 Modelled Concentrations at Tall Tower Site

We carried out two simulations in NAME to assess the likelihood of the leak contributing to most of the observed above-background concentrations at RGL, described in Section 6.2.3.3. The occasions when the gas leak concentrations contribute to most of the above-background concentrations at RGL are defined as simulated concentrations that are at least two standard deviations (2σ, 14 ppb) larger than the observed background concentrations and contributing a significant percentage (>=90%) of the above-background concentrations - we call this a 'leak pollution event' (LPE). We investigated the number of LPEs at RGL over the period of the leak to assess whether statistical analysis and inverse modelling techniques might have been used to recognise the gas leak. Figure 6.3b shows that the observed above-background concentrations at RGL are almost always much larger than the contributions from the gas leak during the NAME_spring simulation. We calculated the number of times the gas leak concentrations at RGL met two different criteria. We first calculated the number of times the gas leak concentration was at least 2σ larger than the background concentration at RGL, i.e. when the leak's

contribution was above the noise of the background concentrations. We also calculated number of times the gas leak contributed to a LPE ($> 2\sigma$ and $> 90\%$ above-background) at RGL. Table 2 shows the results of these criteria during the NAME_spring simulation with hourly output. In the NAME_spring simulation, concentrations were above 2σ of the background concentrations 21 times and a LPE only occurred once. The enhancements due to the gas leak were larger than the noise of the background for at least one hour on 8 of the 79 simulated days. The single pollution event from the NAME_spring simulation shows that although CH_4 from the gas leak can make up a large portion of the above-background concentrations at RGL, this does not happen frequently and therefore it is not sufficient for statistical analysis or inverse modelling to identify the leak due to the significant contributions from other local sources.

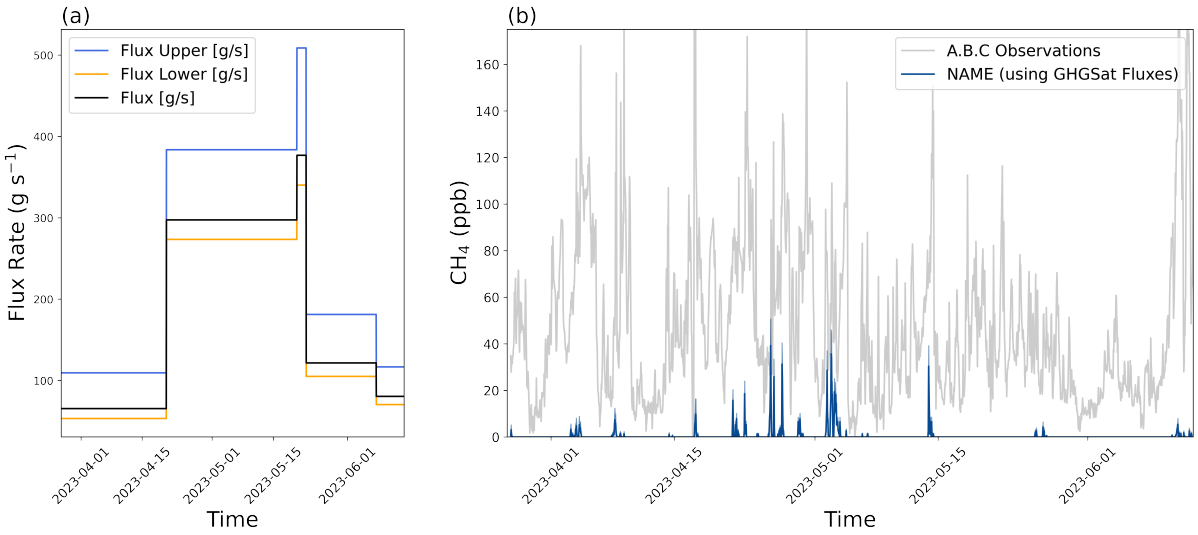

Figure 6.3: a) Varying flux rates (g s^{-1}) used in the NAME model simulation 'NAME_spring'. (b) Modelled CH4 concentrations (ppb) at the Ridge Hill (RGL) tall tower site from GHGSat-derived flux rates in the NAME-spring simulation (blue) and observed above-background concentrations (A.B.C) at RGL (grey).

The results from the NAME_spring simulation show that the frequency of LPEs at RGL was low during Spring 2023, therefore we investigated the gas leak contribution at RGL over a longer period (NAME_long). The NAME_long simulation is a hypothetical situation in which the gas leak is emitting at its highest estimated rate (from both observation methods) for much longer than we actually observed the leak. Similar to the NAME_spring, the above-background concentrations at RGL during the NAME_long simulation period were much larger than the concentrations modelled from the gas leak at RGL, making it difficult to determine LPEs (see Supplement, Fig. B.8). We applied the same criteria as the NAME_spring and found that during the NAME_long simulation the leak concentrations at RGL were 2σ above the

Table 6.2: The comparison between the mobile survey and GHGSat-derived fluxes (kg h^{-1}) and the equivalent fluxes derived in NAME (kg h^{-1}). The bounds of NAME-derived fluxes are shown in brackets.

Criteria	NAME Simulation	GHGSat Lower	GHGSat Central	GHGSat Upper	MS Lower	MS Central	MS Upper
Flux (kg h^{-1})	NAME_spring	Variable	Variable	Variable	-	-	-
No. of times > 2σ B.C.	NAME_spring	20	21	25	-	-	-
No. of times > 2σ B.C. and > 90% of A.B.C.	NAME_spring	1	1	2			
Flux (kg h^{-1})	NAME_long	893	1367	1841	621	998	1375
No. of times > 2σ B.C.	NAME_long	115	226	285	47	140	229
No. of times > 2σ and > 90% of A.B.C.	NAME_long	10	18	39	3	13	19

background concentrations 226 times when using the GHGSat flux, and 140 times when using the mobile survey flux. The gas leak was above the noise of the background concentrations for at least one hour on 80 of 470 simulated days when using the satellite-derived flux. When we simulate the gas leak using the mobile survey-derived flux we find the gas leak to be above the noise of background concentrations on 63 days for at least one hour. The gas leak also meets the LPE criteria 18 times for the GHGSat flux and 13 times for the mobile survey flux. LPEs from the gas leak occurred on 12 of 470 simulation days for at least one hour when simulating the satellite-derived flux and on 7 days when simulating the mobile survey-derived flux. The majority of the LPEs occurred during April 2023. Based on these figures, the frequency of LPEs from the gas leak during the NAME_long simulation is very low even when we assume that the gas leak is constantly emitted at the highest estimated flux rates. This means that it is difficult to recognise the gas leak above the noise of the background concentrations and to determine the flux of the gas leak using inverse modelling techniques and observations at RGL. Both the NAME_spring and NAME_long simulations show there is a low number of LPEs from the gas leak at RGL, which makes it difficult to recognise whether the above-background concentrations are from the leak or from other local sources.

6.4 Discussion

In this study we detected, monitored and validated fluxes of a large gas leak from a low-pressure gas distribution pipe near Cheltenham, UK. The global monitoring satellite Sentinel-5P was not able to detect this leak during its overpass times because it was obstructed by clouds and the emission rate was lower than its theoretical detection threshold (25,000 kg h^{-1}, Lauvaux et al. (2022)). The GHGSat detection threshold has a linear relationship with wind speed and is 100 kg h^{-1} at 3 m s-1 and 200 kg h^{-1} at 6 m s-1 (see McKeever and Jervis (2022)). GHGSat has demonstrated it can detect down to 42 kg h^{-1} (McKeever and Jervis, 2022) and up to 79,000

kg h^{-1} (GHGSat, 2023b). As a result, the Cheltenham gas leak is well within the detection threshold of GHGSat. The high spectral resolution of GHGSat means that it is not affected by surface type as strongly as other satellites such as Sentinel 2 or Landsat. GHGSat has been tested across a mixture of surface types and found to have a column precision of ∼2% (MacLean et al., 2024; Jacob et al., 2022).The GHGSat retrievals are predominantly during a northerly (N) or north easterly (NE) wind, which means that the enhancement detected by the satellite will almost entirely be from the leak due to few CH_4 sources upwind of the leak. The N/NE wind is useful for comparisons with the mobile survey and our tall tower model simulations because RGL is situated to the west of the gas leak. However, the first satellite retrieval on 27th March is during southerly wind. No emissions from the landfill were detected by GHGSat which implies that emissions from the landfill are below 100 kg h^{-1}, possibly lower than 42 kg h^{-1}. Also, by the time the landfill emissions reach the gas leak location, the CH_4 concentrations would be more diffuse resulting in very small percentage of the mole fraction in the retrieved pixel of the plume, so the effect of the landfill upwind of the gas leak on this day is considered negligible.

We also confirmed and assessed the leak by completing a mobile survey on 26 May and 22 June along the roads closest to the satellite-derived leak location. The mobile survey also sampled CH_4 concentrations on the roads closest to the nearby landfill sites but did not detect any CH_4 enhancements. The measured concentrations of the gas leak on 22 June were higher and the associated flux was lower than the equivalent concentrations and fluxes on 26 May, likely due to higher estimated wind speeds on 26 May. The Gaussian Plume Model has large uncertainties due to a number of factors: e.g. the variability in the measured plume from changes in wind speed and direction, the lack of granularity in the Pasquill classification (Fredenslund et al., 2019) and the lack of certainty over the exact position of the leak itself.

The satellite-derived flux estimates and flux estimates based on the ground-based measurements display some differences. These could be due to actual differences in the leak rate on different days from changes in pipeline pressure or biases between the two measurement and flux estimation methods. There are significant uncertainties associated with both flux estimation methods which overlap for the satellite and mobile survey estimates on 22 and 26 May, respectively. The second mobile survey resulted in similar fluxes to the first survey and both were much larger than those estimated by GHGSat during the same week. Unfortunately, we were unable to

obtain satellite retrievals on the same days as the mobile measurements due to obstruction by clouds. Since we were monitoring a live leak, it is likely that changes in flow through the pipe and engineering works will have caused variations in the flux, contributing to the differences between the satellite and mobile survey estimates. During the second mobile survey, on 12 June, repairs on the pipe were being carried out, so it is likely this estimate included more diffuse emissions from a wider area of excavated soil (see Supplement, Fig. B.1). More diffuse emissions could result in a wider CH_4 plume with lower concentrations which may not be above the threshold for enhanced CH_4 in the satellite retrievals. In addition to the effects of actual leak rate variations at the site, the satellite and mobile survey used different methods to estimate the fluxes, based on different meteorology. However, despite the mobile measurement fluxes being measured on different days, they agree well with the April and May satellite estimations. Based on the available observations, it is difficult to be certain whether the leak rate did drop in late May, as suggested by the GHGSat data, or continued at high rates as suggested by the mobile survey.

The mobile survey allowed us to validate the gas leak by confirming the CH_4 detected by the satellite was present and through isotope measurements also confirmed that the source was natural gas. While there are differences between the satellite-derived fluxes and the mobile survey-derived fluxes, they are of the same magnitude, and differences could be due to the active nature of the leak.

The GHGSat Level 4 data, provided through the ESA TPM programme, give flux estimates for a source using GEOS-FP wind data as standard. GHGSat would not normally have access to the higher resolution UKV wind data. In order to provide some continuity between the different observation and flux estimation types we calculated the flux of the gas leak using NAME based on the observed concentrations from the satellite retrievals and the mobile survey. We find that the NAME-derived fluxes follow the same temporal flux pattern but are slightly lower than the GHGSat flux estimations. The difference between the GHGSat-derived fluxes and the NAME-derived fluxes could be due to a number of reasons. The modelled and satellite-observed plumes did not overlap well, making it difficult to define a plume shape that fully captured the dispersion of the modelled plume. We employed a 25 m $\times$ 25 m horizontal resolution with 1.5 km resolution meteorology in NAME, which means the model might not capture local wind effects on the plume, leading to differences in the plume direction. The model simulations used

a unit release making it difficult to define the plume shape using the threshold value GHGSat applies to their retrievals (Jervis et al., 2021) or to apply any concentration thresholds based on the GHGSat retrievals because the modelled concentrations are were not on the same scale. As a result, the criteria applied to the modelled plume, described in Section 6.2.3.3, is mostly independent from the satellite-derived plume apart from the length limit. The NAME-derived fluxes using the GHGSat concentrations are dependent on the plume selection criteria (see Table 6.1), particularly for larger fluxes, during 20 April and 20 May, where the bounds of the estimation are much larger. This could be due to different wind speeds used in the model and the IME method used by GHGSat when deriving the fluxes; the wind speed in NAME is generally higher than GEOS-FP (see Supplement, Table B.4) and wind speeds are the largest uncertainty in the GHGSat IME flux estimation method (Jervis et al., 2021). On 22 May the main flux estimate is larger than the estimation bounds (408 [169, 286] kg h^{-1}) and this is due to the plume selection criteria on this day. When we remove values less than 5% of the maximum value, the modelled plume length remains larger than the observed plume and as a result the scaling factor is smaller and the estimated flux is smaller than the main estimate. This is not the case for the other NAME-derived fluxes which use satellite observations. This further emphasises that the NAME-derived flux estimate is dependent on the plume selection criteria. We also applied a similar method to estimate the fluxes in NAME using the observations from the mobile survey. We find that the peak mixing ratios of the simulated plume do not align well with the peak mixing ratios from the mobile survey. This is likely due to the model meteorology not capturing local wind effects in this area. The road where the survey was conducted was approximately 30 m away from the estimated source location at its closest point, but at this location the car is either ascending or descending the railway bridge which is not fully accounted for in the model. We find that the NAME-derived fluxes using the mobile survey observations are smaller than the Gaussian Plume Model estimates, despite using the same wind speeds on 12 June. Differences between flux estimates could be due to different parameterisations in the NAME model compared with the Gaussian plume, for example the Gaussian Plume Model assumes a neutral boundary layer and uses different dispersion assumptions. We are also sampling a very small section of the plume in the model, which might not fully represent the main peak of the plume but was chosen to be similar in distance between the estimated source location and mobile survey observations. Also, during the mobile survey, instantaneously-measured concentrations from the gas leak fluctuated significantly whilst driving through the

plume, showing predominately perturbations in atmospheric mixing. These effects are averaged out slightly when the emission is calculated because it incorporates multiple transects over a 30-minute period, but some of these perturbations will still remain and the NAME model averages them out in the 1-hourly model time step.

The NAME-derived fluxes do provide some continuity between the different flux estimation methods because they show a similar temporal pattern. The NAME-derived fluxes still peak on 20 April and fluctuate in a similar pattern to the other estimation methods in May and June. This implies that there were fluctuations in the leaking gas, likely due to repairs on the pipe were being carried out in May and June. The variation between the NAME-derived fluxes from both observation methods is smaller than the differences between the satellite-derived fluxes using the IME method and the mobile-survey derived fluxes using the Gaussian Plume method. This implies that the flux estimation methodologies are responsible for some differences between the satellite and mobile survey-derived fluxes. In all three flux estimation methods the resolution of the wind data is much coarser than the size of the observed plume. Atmospheric transport at the surface through small-scale turbulence and influence of the local terrain may not be well represented, contributing to the uncertainty in the flux estimate. Also any systematic biases in the measurements or flux estimation methods are likely to be negligible in comparison to the uncertainties from wind speed and model uncertainties described in Section 6.2. Another uncertainty in modelling the flux in NAME from both the satellite and the mobile survey observations is the location of the leak. Four out of five locations were clustered together and these were used to calculate the mean location for the NAME modelling and for the Gaussian plume modelling. One estimated location was positioned on the other side of the road to the actual leak and was considered an outlier. The mean location derived from the satellite data is approximately 30 - 40 m away from the engineering works (see Supplement, Figure B.1). The location of the gas leaking into the atmosphere is not necessarily the location of the pipeline break. WWU confirmed they replaced the whole pipe at once so could not confirm the precise location of the leak. We cannot give an independent location due to lack of access to the area and no noticeable infrastructure to provide an estimate, resulting in the Gaussian Plume Model and NAME estimates being guided by the satellite-derived location. During the second ground-based mobile surveys we discovered an area of dead vegetation close to the satellite-derived location which could be due to plants being suffocated by the amount of CH_4 (see Supplement Figure B.2), however this is circumstantial.

To assess the impact of the source location on the NAME flux estimates we perturbed the leak location in the model by 10 m north (N), south (S), east (E) and west (W). We selected 10 m location perturbation to match the resolution of the NAME simulations using the surface-based observations. We kept the perturbations the same for the NAME simulations which use the satellite observations. Perturbing the source location shows that the mean location for the previous NAME simulations give the lowest flux values. We also find that the flux estimations are lower than the satellite-derived fluxes, apart from on 20 May (see Supplement, Table B.3). The NAME fluxes, including the bounds of the estimation, derived on 20 May in the N/S/E/W directions are all higher than the satellite-derived flux and the NAME-derived flux at the mean location. The wind speed remains the same as the original simulation for each perturbed location and as a result, the maximum value of the plume was influenced most by the particles being advected by unresolved motions, such as turbulence, which are simulated by a random-walk technique. This contributes to the uncertainty in the NAME-derived fluxes and shows that the flux estimation is dependent on the precise location of the leak when comparing with the IME and Gaussian Plume Model-derived fluxes. Large uncertainties occur when the fluxes are large (e.g. 20 April and 20 May) or when estimated over a very small area (e.g. scaling the model using grid boxes along the road where the mobile-survey measurements were taken).

In the NAME experiments, the maximum number of particles in the simulation can be adjusted so that the model does not stop producing particles during the simulation. We conducted all NAME runs with a maximum of 9×10^7 particles. This value was selected in consultation with Met Office NAME scientists and was determined to be the optimal number for our high-resolution simulations. The final flux value is not sensitive to the number of particles because the total mass released (determined by the release rate) is distributed across the number of particles released. Although the ground-based mobile survey-derived fluxes and NAME-derived fluxes used independent observations and/or methodologies for the flux estimation, the assumed leak location was taken from the mean of GHGSat-derived location estimates. Despite using independent observations and models from the satellite data, it is noted that the flux estimates are not fully independent because we were unable to determine an independent estimate for the leak location.

We ran simulations in NAME to assess the frequency of the gas leak's contribution to the

observed CH_4 at the nearby tall tower site, RGL. This method assumes that the meteorology and transport of CH_4 from the gas leak in the model is correct, however it is likely that local meteorological effects and the surrounding terrain (e.g. the nearby railway bridge) will have had some influence on the transport of CH_4 from the gas leak to RGL. We assessed the frequency of pollution events during both our NAME_spring and NAME_long simulations and found a low number of LPEs. The results show that it is possible for the gas leak to contribute to a LPE at RGL. However, the low number of events means that it is difficult to estimate the location and magnitude of the flux using inverse modelling techniques. There are a number of different sources surrounding RGL which contribute to above-background concentrations such as agriculture, waste and fossil fuels from nearby towns and cities. When the wind is coming from the gas leak to RGL, the main sources near to the gas leak site are from pastoral and arable agriculture, household waste landfills and food waste recycling. The addition of these other CH_4 sources being transported to RGL also adds further complexity to the above-background signal at RGL. The coverage of the tall tower network in the UK is sparse and not specifically designed for monitoring time-limited fugitive emissions like this gas leak and these simulations show that it is unlikely that the RGL observations can be used to alert us to a gas leak of this size, location and duration. This highlights the importance of validating other observations methods, such as the GHGSat satellite constellation. In this case, it was fortuitous that the gas leak was close to a tall tower site at all - due to the sparse coverage of the UK DECC network most gas leaks would likely not be near an observation site. Regular high-resolution satellite monitoring will allow us to detect emission locations, before monitoring them further through ground-based and drone-based surveys. GHGSat needs to be directed to observe the correct area in order to observe an emission and they carry out daily 'intelligence-led' targeting using information such as weather forecasts, past plume detection and locations of facilities likely to emit. However, a more robust 'early-warning' system to tell GHGSat would be useful in determining locations for the satellite to target. For example, Schuit et al. (2023) have developed a machine learning model to detect emission plumes in Sentinel-5P measurements which allows GHGSat to identify and quantify emissions at a higher resolution. However, in this case the gas leak would not have been detected by Sentinel-5P, so other methods should be developed to detect smaller emissions. A disadvantage of monitoring methane emissions via satellite in the UK is that the country is often covered in cloud. However, GHGSat has a frequent revisit time of 1-2 days and with more satellites coming online there is an increased chance of a successful observation. A hybrid

monitoring system combining satellite retrievals and mobile surveys could enable the operational detection of fugitive emissions and enhance countries capabilities to reduce CH_4 emissions.

We investigated whether emission estimates from this gas leak would be reported in the UK's National Atmospheric Emissions Inventory (NAEI), which is funded by the UK Government's Department for Sustainability and Net Zero (DESNZ) and the Department for Environment, Food and Rural Affairs (Defra). The NAEI estimates emissions to the atmosphere from all anthropogenic sources, including CH_4, from gas leakage across the UK's National Transmission Network (operated by National Grid) and the downstream gas networks that are operated by Wales and West Utilities (WWU) and other GDN operators (such as Cadent, Northern Gas Networks, and SGN). The NAEI receives annual submissions from each of the GDNs to provide annual estimates of gas leakage from their distribution networks, using an industry-wide SLM. The SLM enables GDNs to apply consistent methods to generate emission estimates from several different source types across the gas network, with specific methods developed and agreed across the sector for: above ground installations (leakage, venting), low pressure pipe leakage, medium pressure pipe leakage, own gas use, theft and third party damage. The annual gas leakage estimates are also reported by each of the GDNs to Ofgem (UK's independent energy regulator) as part of the network price control and performance mechanisms (Ofgem, 2023). For the gas leak detected by GHGSat, WWU would estimate the leakage of gas as described in Marshall (2023), which would be included in the annual estimate reported to NAEI. The annual submissions to the NAEI do not provide incident-specific estimates because the annual leakage estimates are aggregated prior to reporting to the NAEI. Therefore, the transparency and completeness of those reported emission estimates, including from third party damage incidents, such as this gas leak, is uncertain. In addition to detecting and monitoring the leak, GHGSat contacted the relevant utility company who took steps to fix the leak. The utility company confirmed that the leak was fixed on 13 June. This is a good example of how satellite data can be used to detect fugitive emissions and inform facility operators of their emissions, encouraging them to take action to fix leaks. We estimate over 11 weeks with a mean emission rate of 754 kg h^{-1}, the pipeline would have leaked a total of 1,393,392 kg of CH_4. Using the United States Environmental Protection Agency's Greenhouse Gas Equivalencies calculator (EPA, 2023), we estimate the mass of CH_4 lost to be 39,015 tonnes of CO_2 equivalent, which is equivalent to the emissions from the average annual electricity consumption of 7,500 homes.

6.5 Conclusion

In this study, we detected and monitored a gas leak from a low-pressure distribution pipeline near Cheltenham, UK using GHGSat's high-resolution satellite constellation. We also validated the satellite-derived fluxes by completing two ground based mobile greenhouse gas surveys and found differences with the satellite-derived fluxes, likely due to observations taking place on different days. During the observation period, the satellite-derived fluxes varied from 236-1357 kg h^{-1} and the mobile measurement derived fluxes were between 634-846 kg h^{-1}. The mobile survey measurements agree better with earlier satellite estimates on 20th April and 20th May than the retrievals taken in late May and June covering the same weeks as the mobile survey, although they were not made concurrently with the satellite observations. We also estimated the gas leak flux using the NAME model to provide some continuity between the different flux estimation methods. We find that the fluxes in NAME are smaller than both the satellite- and mobile survey-derived fluxes but are within the uncertainty of both and more consistent with each other. We also assessed the gas leak's contribution at the nearby tall tower site, RGL, although the UK DECC network is sparse and was not specifically designed to detect fugitive emissions. Our simulations show that for a gas leak 30 km from RGL we cannot provide a confident estimate of the flux rate using the RGL observations and inverse modelling techniques and it was not likely that any significantly large above-background concentrations would have stood out in the observations.

Steps taken by GHGSat to inform the utility company also led to mitigation, which is a good example of how satellites can be used to aid companies and government bodies in reducing their emissions. This study shows that GHGSat has the capability to detect and monitor fugitive emissions over 100 kg h^{-1} within the UK. The UK has access to mobile measurement laboratories, which can aid in monitoring CH_4 whilst the views from satellites are obscured by cloud. This gas leak was coincidentally discovered whilst trying to measure emissions from a nearby landfill. The discovery of this very large fugitive emission (by UK standards) raises the question of how many other large gas leaks are happening in the UK that are going undetected or unresolved. Although there are no current plans to carry this out operationally, combining satellite observations and mobile surveys means that the UK can access the technology to regularly monitor for fugitive emissions and take steps to significantly reduce their CH_4 emissions. It would seem prudent for the UK to explore how multiscale measurement methods currently

used, primarily for academic research, can be moved into operational modes to assist with leak detection and repair programmes for the GDN. Currently, the focus on methane intensity and emissions reduction is on the upstream sector, but events such as these suggest that significant challenges face the distribution networks too. This study highlights the capability of GHGSat and ground-based mobile surveys in monitoring fugitive emissions. Despite some differences in the emission estimates likely due to issues inherent in monitoring an active and variable leak, it is an excellent case study in validating satellite technology and collaborating with industry to reduce the human impact on climate

References

Bains, M., Hill, L., and Rossington, P. (2016). *Material comparators for end-of-waste decisions. Fuels: Natural Gas.*

Briggs, G. A. (1973). *Diffusion estimation for small emissions, Air Resources Atmosphereic Turbulence and Diffusion Laboratory, NOAA*. DOI: https://doi.org/10.2172/5118833.

Bush, M., Boutle, I., Edwards, J., Finnenkoetter, A., Franklin, C., Hanley, K., Jayakumar, A., Lewis, H., Lock, A., Mittermaier, M., Mohandas, S., North, R., Porson, A., Roux, B., Webster, S., and Weeks, M. (Mar. 2023). "The second Met Office Unified Model–JULES Regional Atmosphere and Land configuration, RAL2". In: *Geoscientific Model Development* 16.6. Publisher: Copernicus GmbH, pp. 1713–1734. ISSN: 1991-959X. DOI: 10.5194/gmd-16-1713-2023.

Davies, T., Cullen, M. J. P., Malcolm, A. J., Mawson, M. H., Staniforth, A., White, A. A., and Wood, N. (2005). "A new dynamical core for the Met Office's global and regional modelling of the atmosphere". In: *Quarterly Journal of the Royal Meteorological Society* 131.608, pp. 1759–1782. ISSN: 1477-870X. DOI: 10.1256/qj.04.101.

EPA (2023). *Greenhouse Gas Equivalencies Calculator*. Last Accessed: 22/09/2023.

ESA (Oct. 2021). *Satellites detect large methane emissions from Madrid landfills.*

European Commission (2022). *EDGAR (Emissions Database for Global Atmospheric Research) Community GHG Database (a collaboration between the Eu- ropean Commission, Joint Research Centre (JRC), the Inter- national Energy Agency (IEA), and comprising IEA-EDGAR CO2, EDGAR CH4, EDGAR N2O, EDGAR F-GASES version 7.0,* Last Accessed: 27/02/2024.

Fernandez, J., Maazallahi, H., France, J., Menoud, M., Corbu, M., Ardelean, M., Calcan, A., Townsend-Small, A., van der Veen, C., Fisher, R., Lowry, D., Nisbet, E., and Röckmann, T. (2022). "Street-level methane emissions of Bucharest, Romania and the dominance of urban wastewater." In: *Atmospheric Environment: X* 13, p. 100153. ISSN: 2590-1621. DOI: https://doi.org/10.1016/j.aeaoa.2022.100153.

Fisher, R., Lowry, D., Wilkin, O., Sriskantharajah, S., and Nisbet, E. G. (2006). "High-precision, automated stable isotope analysis of atmospheric methane and carbon dioxide using continuous-flow isotope-ratio mass spectrometry". In: *Rapid Communications in Mass Spectrometry* 20.2, pp. 200–208. DOI: https://doi.org/10.1002/rcm.2300.

Forster, P., Storelvmo, K., Armour, W., and Collins, W. J. (2023). *The Earth's Energy Budget, Climate Feedbacks and Climate Sensitivity*. Cambridge University Press, pp. 923–1054. DOI: https://doi.org/10.1017/9781009157896.009.

Fredenslund, A. M., Mønster, J., Kjeldsen, P., and Scheutz, C. (2019). "Development and implementation of a screening method to categorise the greenhouse gas mitigation potential of 91 landfills". In: *Waste Management* 87, pp. 915–923. ISSN: 0956-053X. DOI: https://doi.org/10.1016/j.wasman.2018.03.005.

GHGSat (2023a). *Coal Mining Methane Emissions — Case Study - GHGSat.*

– (2023b). *GHGSat measures its largest emission from Nord Stream 2 leak - GHGSat.*

Governance, G. (2020). *Shrinkage and Leakage Model Review 2020.* Last Accessed: 27/02/2024.

Guanter, L., Irakulis-Loitxate, I., Gorroño, J., Sánchez-García, E., Cusworth, D. H., Varon, D. J., Cogliati, S., and Colombo, R. (2021). "Mapping methane point emissions with the PRISMA spaceborne imaging spectrometer". In: *Remote Sensing of Environment* 265, p. 112671. ISSN: 0034-4257. DOI: https://doi.org/10.1016/j.rse.2021.112671.

Jacob, D. J., Turner, A. J., Maasakkers, J. D., Sheng, J., Sun, K., Liu, X., Chance, K., Aben, I., McKeever, J., and Frankenberg, C. (2016). "Satellite observations of atmospheric methane and their value for quantifying methane emissions". In: *Atmospheric Chemistry and Physics* 16.22, pp. 14371–14396. DOI: 10.5194/acp-16-14371-2016.

Jacob, D. J., Varon, D. J., Cusworth, D. H., Dennison, P. E., Frankenberg, C., Gautam, R., Guanter, L., Kelley, J., McKeever, J., Ott, L. E., Poulter, B., Qu, Z., Thorpe, A. K., Worden, J. R., and Duren, R. M. (2022). "Quantifying methane emissions from the global scale down to point sources using satellite observations of atmospheric methane". In: *Atmospheric Chemistry and Physics* 22.14. Publisher: Copernicus GmbH, pp. 9617–9646. ISSN: 1680-7316. DOI: 10.5194/acp-22-9617-2022.

Jervis, D., McKeever, J., Durak, B. O. A., Sloan, J. J., Gains, D., Varon, D. J., Ramier, A., Strupler, M., and Tarrant, E. (2021). "The GHGSat-D imaging spectrometer". In: *Atmospheric Measurement Techniques* 14.3. Publisher: Copernicus GmbH, pp. 2127–2140. ISSN: 1867-1381. DOI: 10.5194/amt-14-2127-2021.

Jones, A., Thomson, D., Hort, M., and Devenish, B. (2007). "The U.K. Met Office's Next-Generation Atmospheric Dispersion Model, NAME III". en. In: *Air Pollution Modeling and Its Application XVII.* Ed. by C. Borrego and A.-L. Norman. Springer US, pp. 580–589. ISBN: 978-0-387-68854-1. DOI: 10.1007/978-0-387-68854-1_62.

Jongaramrungruang, S., Frankenberg, C., Matheou, G., Thorpe, A. K., Thompson, D. R., Kuai, L., and Duren, R. M. (2019). "Towards accurate methane point-source quantification from high-resolution 2-D plume imagery". In: *Atmospheric Measurement Techniques* 12.12, pp. 6667–6681. DOI: 10.5194/amt-12-6667-2019.

Lauvaux, T., Giron, C., Mazzolini, M., d'Aspremont, A., Duren, R., Cusworth, D., Shindell, D., and Ciais, P. (Feb. 2022). "Global assessment of oil and gas methane ultra-emitters". eng. In: *Science (New York, N.Y.)* 375.6580, pp. 557–561. ISSN: 1095-9203. DOI: 10.1126/science.abj4351.

Lowry, D., Fisher, R. E., France, J. L., Coleman, M., Lanoisellé, M., Zazzeri, G., Nisbet, E. G., Shaw, J. T., Allen, G., Pitt, J., and Ward, R. S. (2020). "Environmental baseline monitoring for shale gas development in the UK: Identification and geochemical characterisation of local source emissions of methane to atmosphere". In: *Science of The Total Environment* 708, p. 134600. ISSN: 0048-9697. DOI: https://doi.org/10.1016/j.scitotenv.2019.134600.

MacLean, J.-P. W., Girard, M., Jervis, D., Marshall, D., McKeever, J., Ramier, A., Strupler, M., Tarrant, E., and Young, D. (2024). "Offshore methane detection and quantification from space using sun glint measurements with the GHGSat constellation". In: *Atmospheric Measurement Techniques* 17.2, pp. 863–874. DOI: 10.5194/amt-17-863-2024.

Manning, A. J. et al. (2021). "Evidence of a recent decline in UK emissions of hydrofluorocarbons determined by the InTEM inverse model and atmospheric measurements". In: *Atmospheric Chemistry and Physics* 21.16, pp. 12739–12755. DOI: 10.5194/acp-21-12739-2021.

Marshall, M. (2023). *Material comparators for end-of-waste decisions. Fuels: Natural Gas*. Last Accessed: 27/02/2024.

McKeever, J. and Jervis, D. (2022). *Validation and Metrics for Emissions Detection by Satellite*. Last Accessed: 27/02/2024.

Meneguz, E. and Thomson, D. J. (2014). "Towards a new scheme for parametrisation of deep convection in NAME III". In: *International Journal of Environment and Pollution* 54.2-4, pp. 128–136. DOI: 10.1504/IJEP.2014.065113.

NAEI (2022). *Pollutant Information: Methane, NAEI*. Last Accessed: 1/08/2023.

NASA (2024). *Global Modelling and Assimilation Office: Research Site, NASA GMAO*. Last Accessed: 30/08/2023.

Ofgem (2023). *Network price controls 2021–2028 (RIIO-2)*. Last Accessed: 19/09/2023.

Pasquill, F. and Smith, F. B. (1983). "Atmospheric Diffusion, 3rd edn." In: *Ellis Horwood, Chichester UK*.

Prather, M. J., Holmes, C. D., and Hsu, J. (2012). "Reactive greenhouse gas scenarios: Systematic exploration of uncertainties and the role of atmospheric chemistry". In: *Geophysical Research Letters* 39.9. DOI: https://doi.org/10.1029/2012GL051440.

Ražnjević, A., Heerwaarden, C. van, and Krol, M. (2022). "Evaluation of two common source estimation measurement strategies using large-eddy simulation of plume dispersion under neutral atmospheric conditions". In: *Atmospheric Measurement Techniques* 15.11, pp. 3611–3628. DOI: 10.5194/amt-15-3611-2022.

Saunois, M. et al. (2020). "The Global Methane Budget 2000–2017". In: *Earth System Science Data* 12.3, pp. 1561–1623. DOI: 10.5194/essd-12-1561-2020.

Schuit, B. J., Maasakkers, J. D., Bijl, P., Mahapatra, G., Berg, A.-W. van den, Pandey, S., Lorente, A., Borsdorff, T., Houweling, S., Varon, D. J., McKeever, J., Jervis, D., Girard, M., Irakulis-Loitxate, I., Gorroño, J., Guanter, L., Cusworth, D. H., and Aben, I. (2023). "Automated detection and monitoring of methane super-emitters using satellite data". In: *Atmospheric Chemistry and Physics* 23.16, pp. 9071–9098. DOI: 10.5194/acp-23-9071-2023.

Seinfeld, J. H. and Pandis, S. N. (2006). "Atmospheric chemistry and physics: from air pollution to climate change". In: *John Wiley & Sons*.

Sherwin, E. D., Rutherford, J. S., Chen, Y., Aminfard, S., Kort, E. A., Jackson, R. B., and Brandt, A. R. (Mar. 2023). "Single-blind validation of space-based point-source detection and quantification of onshore methane emissions". en. In: *Scientific Reports* 13.1. Publisher: Nature Publishing Group, p. 3836. ISSN: 2045-2322. DOI: 10.1038/s41598-023-30761-2.

Stanley, K. M., Grant, A., O'Doherty, S., Young, D., Manning, A. J., Stavert, A. R., Spain, T. G., Salameh, P. K., Harth, C. M., Simmonds, P. G., Sturges, W. T., Oram, D. E., and Derwent, R. G. (2018). "Greenhouse gas measurements from a UK network of tall towers: technical description and first results". In: *Atmospheric Measurement Techniques* 11.3, pp. 1437–1458. ISSN: 1867-1381. DOI: 10.5194/amt-11-1437-2018.

UNEP (2023). *What is the Methane Alert and Response System (MARS)?* Last Accessed: 1/08/2023.

Varon, D. J., Jacob, D. J., McKeever, J., Jervis, D., Durak, B. O. A., Xia, Y., and Huang, Y. (2018). "Quantifying methane point sources from fine-scale satellite observations of atmospheric methane plumes". In: *Atmospheric Measurement Techniques* 11.10, pp. 5673–5686. DOI: 10.5194/amt-11-5673-2018.

Varon, D. J., McKeever, J., Jervis, D., Maasakkers, J. D., Pandey, S., Houweling, S., Aben, I., Scarpelli, T., and Jacob, D. J. (2019). "Satellite Discovery of Anomalously Large Methane Point Sources From Oil/Gas Production". en. In: *Geophysical Research Letters* 46.22. ISSN: 1944-8007. DOI: 10.1029/2019GL083798.

Wales & West Utilities (2023). *Gas Pipe Upgrades*. Last Accessed: 30/08/2023.

Webster, H. N., Whitehead, T., and Thomson, D. J. (2018). "Parameterizing Unresolved Mesoscale Motions in Atmospheric Dispersion Models". In: *Journal of Applied Meteorology and Climatology* 57.3, pp. 645–657. DOI: 10.1175/JAMC-D-17-0075.1.

Zazzeri, G., Lowry, D., Fisher, R., France, J., Lanoisellé, M., and Nisbet, E. (2015). "Plume mapping and isotopic characterisation of anthropogenic methane sources". In: *Atmospheric Environment* 110, pp. 151–162. ISSN: 1352-2310. DOI: https://doi.org/10.1016/j.atmosenv.2015.03.029.

Chapter 7

Summary

The work in this thesis was divided into three papers which aimed to investigate changes in atmospheric CH_4 across different spatial and temporal scales. In all three papers, I take advantage of different observations and atmospheric models to fill gaps in our knowledge of atmospheric CH_4. The papers focused on changes in global, regional and point sources of CH_4, respectively. Monitoring and modelling at each of these scales is important for improving our understanding of global variations of atmospheric CH_4.

Paper 1 focused on investigating the seasonal cycle of atmospheric CH_4 between 1995-2020, using NOAA's long term-observing network and the global chemical transport model TOMCAT. The key aims of this work were to:

- Determine whether the seasonal cycle amplitude (SCA) of atmospheric CH_4 is changing.
- Identify regional contributors to the changes in the SCA in areas where it is changing.
- Identify possible changes in sources and sinks which could be driving the change in the SCA.

Paper 2 focused on developing a nested grid model for TOMCAT to represent atmospheric CH_4 on similar spatial scales to new high-resolution satellite observations. The key aims of this study were:

- Develop a nested grid model for the TOMCAT CTM.
- Demonstrate the nested grid's performance against surface-based observations and spatial distribution with satellite retrievals.

- Investigate atmospheric CH_4 over Europe during 2020.

Paper 3 originally aimed to assess top-down and bottom-up estimates of large point sources in the UK using high-resolution satellite data and the UK's tall tower network. However, during the satellite retrieval phase of the study we detected a gas leak and the focus of the study shifted. The key aims of the study became:

- Quantify the emission rate of a gas leak using satellite observations.
- Validate the satellite-derived emission estimates using a surface-based mobile survey.
- Determine whether the current UK observing network can detect fugitive emissions of CH_4 through modelling the satellite-derived emissions estimates.

The motivation and key results from each paper will be discussed below.

7.1 Paper 1

Atmospheric CH_4 exhibits a seasonal cycle due to the seasonality of its sources and sinks. There is currently an imbalance of the sources and sinks of CH_4, leading to year-on-year increases of global CH_4 concentrations. Any long-term changes in the sources or sinks of CH_4 will have an impact on global CH_4 concentrations. Investigating changes in the seasonal cycle contributes to our understanding of the global variations of CH_4. Many studies have discussed the seasonal cycle of CH_4 but long-term variations of the seasonal cycle have not been studied in detail since Dlugokencky et al. (1997). A study by Lin et al. (2020) attributed changes in the SCA of CO_2 regionally and I followed a similar method to investigate whether there were changes in the CH_4 SCA.

The key findings of this work were:

1. The SCA of CH_4 is decreasing in the northern high latitudes (NHL) between 1995 to 2020 despite the SCA increasing globally.
2. The changes in the SCA of CH_4 in the NHL are being driven by changes in emissions and transport from lower latitudes.
3. The main contributor to the decrease in the SCA in the NHL is from well-mixed CH_4 as diagnosed by a background tracer, whilst the largest regional contributors are from Canada, Europe and the Middle East.

4. The main drivers of the regional contributions are increases in summer emissions from the Boreal Plains in Canada, decreases in winter emissions across Europe, and a combination of increases in summer emissions and decreases in winter emissions over the Arabian Peninsula and Caspian Sea in the Middle East.

The results from this paper raise further questions about the seasonal cycle of CH_4 and the impact transport has on observed seasonal variation. The lack of data on the seasonality of emissions makes it difficult to attribute which sources within each region are driving the changes. Therefore, further research would be beneficial to understand the seasonal variability of emissions in Canada, Europe and the Middle East. Similarly, it would be interesting to investigate the seasonality of anthropogenic emissions from sources such as oil and gas, agriculture and landfills, as this is poorly understood. When simulating these fluxes they are often either held constant during each year or assumed to be linearly increasing each year (Wilson et al., 2021). It would also be beneficial to investigate the changes in the SCA amplitude using emission estimates derived from an inversion that assimilates GOSAT data to determine if there are similar trends in the SCA during 2010 to 2020. GOSAT has the advantage of better spatial coverage than the NOAA observation network and an observation period of $\sim$15 years.

In terms of modelling, it would be advantageous to simulate the 20 year spin up beforehand and remove the need for a background tracer. Finally, a recent study by East et al. (2024) has recommended the Lund-Potsdam-Jena Wald Schnee und Landschaft (LPJ-wsl) with Modern-Era Retrospective Analysis v2 (MERRA-2) wetlands model should be used as a prior estimate for wetlands emissions when investigating the seasonal cycle of CH_4 using atmospheric inversions. It would be beneficial to investigate whether the LPJ-wsl with MERRA-2 wetlands model reproduces the same seasonal cycle in TOMCAT and what impact this may have on the modelled SCA of CH_4.

7.2 Paper 2

New high resolution satellite observations of atmospheric CH_4 have become available in recent years. Currently, the horizontal grids of many global chemical transport models are too coarse to simulate atmospheric constituents at this spatial scale for a long time period. Nested grid models are able simulate areas of interest at a higher spatial resolution and at a lower computational cost than running the global model. Motivated by the high spatial resolution of TROPOMI,

I developed a nested grid model for the TOMCAT CTM. This paper describes a new nested grid model, ZOOMCAT, based on TOMCAT. It also assesses the performance of ZOOMCAT against observations from the ICOS European tall tower network and provides comparisons against TROPOMI retrievals to assess the spatial distribution of the model.

The key findings of this model development paper are:

1. ZOOMCAT is able to simulate CH_4 at a higher spatial resolution than TOMCAT.
2. The high-resolution L2 grid (nested in a coarser grid) does not improve upon the coarse L1 grid when compared with observations.
3. High-resolution meteorology is important when simulating constituents in the L2 grid.

Due to the performance of ZOOMCAT when compared with observations using the $2.8° \times 2.8°$ resolution meteorology, it was not worthwhile to investigate changes in atmospheric CH_4 over Europe during 2020. Further improvements are needed in ZOOMCAT before it can be used in scientific studies, such as checking the performance of the ECMWF pre-calculated boundary layer height against the more commonly used Holtslag and Boville (1993) scheme. Secondly, higher resolution meteorology will be needed to improve the accuracy of the model, as shown in Chapter 5. Once the model has been tested further, it would be suitable for conducting high-resolution studies. For example over South Sudan where large enhancements of CH_4 have observed, or over the the northern high latitudes to further investigate the changes in the seasonal cycle.

7.3 Paper 3

New high-resolution imaging spectrometers can detect CH_4 at a spatial scale of 25 m and as a result have the capability to determine emissions from specific facilities. The study originally aimed at assessing top-down and bottom-up estimates of large point sources in the UK using GHGSat's high-resolution satellite-derived emission estimates, the Met Office's NAME model and the UK's tall tower network. The comparison of the two estimation methods provides insight into how well the UK's emission inventory accounts for large point sources in the UK. When targeting GHGSat at large point sources of CH_4 in the UK, we came across a gas leak from a gas distribution pipeline and the motivation of the study shifted to assessing the gas leak. This study presented the detection, monitoring and quantification of CH_4 emissions of

an active gas leak near Cheltenham, UK in the spring and summer of 2023. This study also provided the first validation of satellite-derived emission estimates of CH_4 using a surface-based mobile survey. Validating satellite-derived emission estimates is important to ensure national and global anthropogenic emission estimates are correct.

The main findings of this study were:

1. GHGSat-derived emissions of the gas leak range between 236–1357 kg CH_4 h^{-1} which broadly agree with the surface-based mobile survey derived emissions estimates which range from 634–846 kg CH_4 h^{-1}.

2. The NAME-derived emission estimates are smaller in magnitude than emissions derived from observations using the Integrated Mass Enhancement Method and the Gaussian Plume model, but are within the uncertainty of observation derived estimates and show similar temporal patterns.

3. Modelling the CH_4 emissions of the gas leak in NAME has shown that the UK's tall tower network was in this case too sparse to reliably flag up and quantify fugitive emissions on this scale, although they are not design for this purpose.

This study has demonstrated the need for multi-scale and multi-instrument observations to detect fugitive emissions of CH_4 and raises the question regarding the scale and frequency of gas leaks that are undetected. As a result, more observations of CH_4 are needed to detect and mitigate fugitive emissions because it is not possible to automatically detect emissions on this scale with satellite monitoring from GHGSat alone. The flux estimation method in NAME from this study could also be improved for future use over the UK. This could be done by implementing more robust plume criteria in the model (i.e not rely on the maximum value in the modelled plume), or by increasing the concentrations in the plume iteratively to match observed concentrations. In addition to the methods available, a standardised method should be developed to derive emission estimates from satellite observations of point sources so that they can be incorporated into emission inventories. For example, a integrated mass enhancement method using the same meteorological dataset for consistent estimates. This will be important as more satellite instruments are launched to measure CH_4 (see Section 7.5). Finally, it would be useful to complete the original aim of this study and assess top-down and bottom-up estimates of large point sources. However, it is important to note that mainland Europe has a larger

network of observations and may be a more suitable region to detect large emissions using GHGSat than the UK. We did not detect any emissions at the locations selected over the UK until the gas leak was detected.

7.4 Critical Discussion

This Section will provide a critical discussion on the uncertainties and limitations of observing and modelling atmospheric CH_4 across difference spatial and temporal scales.

7.4.1 Modelling Uncertainties

This work takes advantage of chemical transport models and dispersion models in Chapters 4-6 to investigate causes of changes in CH_4 globally, regionally and locally. Uncertainties in modelling CH_4 can arise from several factors ranging from the input data used to those associated with model parameterisations. Input data used in the models include emissions, meteorology, the sink species (e.g. OH) mixing ratios and loss rates. The spatial resolution of the model is too coarse to accurately resolve atmospheric processes such as boundary layer mixing and convection so these processes are parameterised.

The uncertainties associated with modelling CH_4 across difference spatial and temporal scales will be discussed below.

7.4.1.1 Emissions

Emissions used in models come from a range of different emission inventories, all which vary in spatial scale. The EDGAR emissions inventory is predominantly used to represent anthropogenic emissions of CH_4. The emissions are provided on a spatial scale of $0.1^\circ \times 0.1^\circ$ with annual or monthly temporal resolution. The temporal variation of EDGAR emissions is derived by distributing the annual total to monthly emissions using temporal disaggregation, increasing the uncertainty in the estimates. (Crippa et al., 2020b). Monthly wetland emissions provided by WetCHARTs are provided on a spatial scale of $0.5^\circ \times 0.5^\circ$ but v1.0 (used in Chapter 4) only spans from 2001-2015 and v1.3.1 (used in Chapter 5) only spans from 2001-2019 (Bloom et al., 2017; Bloom et al., 2021). These emissions estimates do not cover the period of record breaking global increases in atmospheric CH_4 which means a climatology value is used in these years. This adds to the uncertainty in the model simulations of CH_4 because wetlands make up the

largest natural source. Monthly fire emissions are from GFED where v4 (used in Chapter 4 covers 1997-2016 and v5 (used in Chapter 5) spans 1997-2020. The spatial resolution is 1°× 1° between 1997-2000. The spatial resolution is increased to 0.25°× 0.25° from 2000 onwards where the total burned area is derived from the Moderate Resolution Imaging Spectroradiometer (MODIS) instrument on the Terra and Aqua satellites (Chen et al., 2023). The remaining emissions are climatological values for rice, termites, geological and ocean emissions provided at a 1°× 1° resolution. The varying spatial and temporal scales of emission inventories adds to the uncertainty of simulated CH_4 concentrations and some inventories need to be updated to account for recent observed variations of atmospheric CH_4.

Global emission estimates of CH_4 simulated in models often do not reproduce the observed trend in concentrations. To address this, studies use atmospheric inversions which combine the emission inventories and observations to provide optimised emission estimates. This helps to reduce the uncertainty in simulating CH_4 mixing ratios. However uncertainties still remain in regions with sparse observations; e.g. in Amazonia and central Africa, where there are large and varying CH_4 emissions. Emission estimates in these regions from the atmospheric inversion are highly dependent on the prior emission estimates described above and model transport.

In addition to global emission estimates, the flux estimations of point source emitters are becoming possible due to the increase in spatial resolution of satellites. The biggest uncertainty in the flux estimation is the wind speed. In the case of GHGSat, they use an Integrated Mass Enhancement (IME) method to estimate the emission rate of a point source with winds from GEOS-FP analyses which has a much coarser spatial resolution than the observation. As a result local wind effects may not be accounted for properly, increasing the uncertainty in the emission estimate.

7.4.1.2 Sink Species

The main sink of CH_4 is OH, and the scale of the inter-annual variation of OH is uncertain due to it being difficult to measure directly. Often models use a climatology for OH mixing ratios due to conflicting conclusions on how OH is varying over time. As a result it is difficult to quantify the impact of OH on various species in modelling studies. New approaches like Pimlott et al. (2022)'s satellite-derived steady state approximation for OH should be tested in CH_4 studies to quantify the impact of OH on variations of atmospheric CH_4.

7.4.1.3 Model Transport

The meteorology used to drive model simulations is important in representing CH_4 in the atmosphere. It is expected that increasing the resolution of meteorology fields will reduce the errors in transport of modelled concentrations when compared with observations. In Chapter 5, I have shown that the spatial resolution of the meteorology is important when simulating CH_4 at higher spatial resolutions in regional modelling.

Similarly, estimates of wind speed from reanalyses data are important for quantifying emissions from point sources. Meteorological reanalyses are too coarse ($\sim$ km) to match the resolution of GHGSat observations ($\sim$ m), and as a result may not capture local influences. This adds to the uncertainty in the satellite-derived emission estimates. As the spatial resolution of observations increases, there will be an increase in the need for higher regional meteorology as we start to analyse CH_4 at higher spatial scales regionally.

In Chapter 6, the NAME model is used to simulate the gas leak. The modelled plume distribution did not compare well with the satellite observed plume. This is likely due to the parameterisation of turbulent motions in the model. This further added to the uncertainty when estimating fluxes in transport models.

7.4.2 Satellite Observations Uncertainties

CH_4 retrievals from TROPOMI have been shown to have biases due to spectral albedo and surface elevation data used in the retrieval (discussed in full in Chapter 6.2, Section 3.1.2). In Chapter 5, I have shown that across 2020, the uncertainty on retrievals is quite variable and more uncertain at higher latitudes. There are now three different products for TROPOMI CH_4 retrievals. There is the operational product by SRON, the WFM-DOAS product by the University of Bremen and now there is a new blended TROPOMI+GOSAT product by Balasus et al. (2023) at Harvard. The blended product uses machine learning and GOSAT to correct for spectral features (such as albedo and aerosol scattering) in TROPOMI and retains the spatial resolution. In future studies it would be useful to compare all three products to reduce the uncertainty in the total column observation from TROPOMI.

7.5 Future of Monitoring CH_4 Across Different Scales

Global concentrations of atmospheric CH_4 continue to grow and its variations are not fully understood (Lan et al., 2024; Nisbet et al., 2019). CH_4 has a mixture of natural and anthropogenic sources, all of which vary in spatial scale. There are large-scale sources, such as wetlands and biomass burning, and point source emitters such as landfills and gas leaks. These emissions also exhibit temporal variability some of which are short-lived or have a seasonal variability. By investigating CH_4 across different spatial and temporal scales this research improves our understanding of how short- to long-term emissions might contribute to changes global concentrations of CH_4.

In recent years the resolution of satellite data has increased and observing CH_4 by satellite has become more prevalent. The spatial resolution of TROPOMI means that it is possible to detect variations in both natural and anthropogenic sources. Detecting and mitigating anthropogenic emissions, such as gas leaks and emissions from landfills, will help to reduce the human impact on climate change (see Chapter 6). Despite it being possible to detect very large point sources with TROPOMI, its spatial resolution is too coarse to determine sources at the facility scale. Therefore, TROPOMI can be used to tip-and-cue high resolution imaging spectrometers such as GHGSat ($\sim$25 m resolution) to determine the exact source. GHGSat's data is not open access and a result researchers only have free access to their data through proposals made to the ESA Third Party Mission programme (TPM) in Europe or through Satellite Applications Catapult in the UK.

More private companies and non-profit organisations have been developing sensors to detect CH_4, particularly targeting anthropogenic emissions. For example, the non-profit organisation Carbon Mapper have developed a sensor to detect CH_4 at a spatial resolution of 30 m $\times$ 30 m, with a detection limit of approximately 100 kg h^{-1}. Its first two instruments are expected to launch in 2024 (Jacob et al., 2022; Carbon Mapper, 2024). The aim of Carbon Mapper is to monitor and quantify emissions of CH_4 and CO_2 using satellite and aircraft data (Carbon Mapper, 2024). Their data is open access which means it can be used more widely than GHGSat data. On 4th March 2024, Environmental Defense Fund's satellite, MethaneSAT, was launched (MethaneSAT, 2024). MethaneSAT focuses on detecting anthropogenic emissions of CH_4 but it has the capability to detect area and point source emissions with a spatial resolution of 100 m $\times$ 400 m with a detection limit of approximately 500 kg h^{-1} (MethaneSAT, 2024). This

satellite bridges the gap between TROPOMI and point source imaging sensors such as GHGSat and Carbon Mapper. With all these instruments orbiting, the ability to detect and quantify large anthropogenic emissions of CH_4 and take steps to mitigate them will be more achievable. As a result this has the potential to reduce the human impact on climate change on a relatively short time scale, at the same time reducing our CO_2 emissions.

In addition to monitoring anthropogenic emissions, variations in natural sources such as wetlands should continue to be monitored. We do not fully understand how wetland emissions respond to changes in climate variables such a temperature and precipitation. During 2020 and 2021, studies have shown that CH_4 from tropical regions largely contributed to the record-breaking increase in global CH_4 concentrations. Therefore, it is important to also investigate and monitor changes in natural emissions on a regional and global scales, taking advantage of models and observations available (see Chapter 1, Figure 1.1). This will improve our understanding of changes of natural emissions of CH_4 and how they might respond to a changing climate. Observing and modelling atmospheric CH_4 across difference spatial and temporal scales has the potential to improve our understanding of both changes in natural and anthropogenic sources of CH_4, and global variations in CH_4 concentrations.

Chapter 8

Conclusions

Global concentrations of atmospheric CH_4 have been rising rapidly in recent years and are poorly understood. Atmospheric CH_4 is the result of a range of sources and sinks. The sources vary in spatial distribution from more diffuse long-term sources to rapidly-varying point sources. Therefore it is important to analyse CH_4 across different spatial and temporal scales as doing so gives an insight into how different natural and anthropogenic sources are changing. In 2020 and 2021, record-breaking global annual increases of atmospheric CH_4 were observed, emphasising the importance in resolving the methane budget to determine what is driving these global trends (Lan et al., 2024).

The aim of this thesis was to analyse CH_4 across different spatial and temporal scales to improve our understanding of the drivers of variations in global CH_4 concentrations. CH_4 has a mixture of natural and anthropogenic sources, all of which emit across different spatial scales and vary temporally (e.g. seasonally or temporarily). This study explores changes in the seasonal cycle on a global scale, demonstrates the capability of regional modelling through comparisons with high-resolution satellite data, and at the point-scale quantifies and validates satellite derived emissions from a natural gas leak.

Long-term changes in the seasonal cycle of CH_4 can indicate long-term changes in its sources or sinks, which in turn impact the annual increase in concentrations. Chapter 4 found that the observed SCA decreased by 4 ppb (7.6%) in the northern high latitudes (NHLs; 60°N-90°N) but increased everywhere else. By regionally attributing these changes, the study showed that changes in emissions and transport from lower altitude regions impact the SCA in the NHLs.

This thesis also demonstrated an example of regional modelling with a new nested grid model called ZOOMCAT in Chapter 5. It provided a comparison of CH_4 simulations with high resolution TROPOMI satellite retrievals. However, more work is needed to improve the model before it can be used in scientific studies.

The final research Chapter 6 detected and quantified emissions from a gas leak near Cheltenham, UK and provided the first validation of the GHGSat satellite derived emission estimates using a surface-based mobile survey. It was also the first gas leak in the UK to be detected by satellite and mitigated, highlighting the importance of satellite data in reducing the human impact on climate change. The results of this study showed that the satellite derived emission estimates were in broad agreement with those derived from the mobile survey, highlighting that GHGSat can detect CH_4 with comparable capability to ground based methods. In this Chapter the results demonstrate the benefit of satellite data to reduce CH_4 emissions and the need for multi-scale, multi-instrument monitoring of CH_4 to detect fugitive emissions. The impact of this study is still being discussed in scientific media in the context of targeted reduction of CH_4 emissions a year on from initial publication (O'Callaghan, 2024).

This thesis highlighted the vital importance of using observations and models across different spatial and temporal scales, to improve our understanding of the variation of global CH_4 concentrations. With the increase in spatial resolution of observations, it is becoming more important to be able to represent CH_4 on the same spatial scales in model simulations. This gives the models the ability to investigate changes in large scale anthropogenic emissions down to point source emitters observed by satellites and surface measurements. By detecting changes in anthropogenic emissions, such as fugitive emissions from oil and gas or landfills, steps can be taken to mitigate them, reducing the human impact on climate change. Additionally observing and modelling natural sources such as wetlands could improve our understanding on how they respond to changes in temperature and precipitation in a warming climate. By considering these aspects together, we will gain a better understanding of variations of atmospheric CH_4, which has 20-year global GWP 82 times greater than carbon dioxide (CO_2).

References

Abe, T., Bignell, D. E., Higashi, M., Higashi, T., and Abe, Y. (2000). *Termites: evolution, sociality, symbioses, ecology*. Springer Science & Business Media.

Allan, W., Struthers, H., and Lowe, D. C. (2007). "Methane carbon isotope effects caused by atomic chlorine in the marine boundary layer: Global model results compared with Southern Hemisphere measurements". In: *Journal of Geophysical Research: Atmospheres* 112.D4. DOI: https://doi.org/10.1029/2006JD007369.

Allen, G. (Apr. 2023). "How to quantify anthropogenic methane emissions with aircraft surveys". en. In: *Communications Earth & Environment* 4.1. Publisher: Nature Publishing Group, pp. 1–3. ISSN: 2662-4435. DOI: 10.1038/s43247-023-00794-6.

Andrews, A., Miles, N., Kofler, J., Trudeau, M., Bakwin, P., Fischer, M., Sweeney, C., Desai, C., Viner, B. J., Parker, M. J., Jaffe, D. A., Miller, C. E., Wekker, S. F. J. de, and Miller, J. B. (2023). *NOAA Global Monitoring Laboratory. Version: 2023-08-23*. DOI: http://dx.doi.org/10.7289/V57W69F2.

Bakkaloglu, S., Lowry, D., Fisher, R. E., France, J. L., Brunner, D., Chen, H., and Nisbet, E. G. (2021). "Quantification of methane emissions from UK biogas plants". In: *Waste Management* 124, pp. 82–93. ISSN: 0956-053X. DOI: https://doi.org/10.1016/j.wasman.2021.01.011.

Balasus, N., Jacob, D. J., Lorente, A., Maasakkers, J. D., Parker, R. J., Boesch, H., Chen, Z., Kelp, M. M., Nesser, H., and Varon, D. J. (2023). "A blended TROPOMI+GOSAT satellite data product for atmospheric methane using machine learning to correct retrieval biases". In: *Atmospheric Measurement Techniques* 16.16, pp. 3787–3807. DOI: 10.5194/amt-16-3787-2023.

Barker, P. A., Allen, G., Pitt, J. R., Bauguitte, S. J.-B., Pasternak, D., Cliff, S., France, J. L., Fisher, R. E., Lee, J. D., Bower, K. N., and Nisbet, E. G. (Dec. 2021). "Airborne quantification of net methane and carbon dioxide fluxes from European Arctic wetlands in Summer 2019". In: *Philosophical Transactions of the Royal Society A: Mathematical, Physical and Engineering Sciences* 380.2215. Publisher: Royal Society, p. 20210192. DOI: 10.1098/rsta.2021.0192.

Berden, G., Peeters, R., and Meijer, G. (Oct. 2000). "Cavity ring-down spectroscopy: Experimental schemes and applications". In: *International Reviews in Physical Chemistry* 19.4. Publisher: Taylor & Francis, pp. 565–607. ISSN: 0144-235X. DOI: 10.1080/014423500750040627.

Bey, I., Jacob, D. J., Yantosca, R. M., Logan, J. A., Field, B. D., Fiore, A. M., Li, Q., Liu, H. Y., Mickley, L. J., and Schultz, M. G. (2001). "Global modeling of tropospheric chemistry with assimilated meteorology: Model description and evaluation". In: *Journal of Geophysical Research: Atmospheres* 106.D19, pp. 23073–23095. DOI: https://doi.org/10.1029/2001JD000807.

Bloom, A. A., Bowman, K. W., Lee, M., Turner, A. J., Schroeder, R., Worden, J. R., Weidner, R., McDonald, K. C., and Jacob, D. J. (2017). "A global wetland methane emissions and uncertainty dataset for atmospheric chemical transport models (WetCHARTs version 1.0)". In: *Geoscientific Model Development* 10.6, pp. 2141–2156. DOI: 10.5194/gmd-10-2141-2017.

Bloom, A., Bowman, K., Lee, M., Turner, A., Schroeder, R., Worden, J., Weidner, R., McDonald, K., and Jacob, D. (2021). *CMS: Global 0.5-deg Wetland Methane Emissions and Uncertainty (WetCHARTs v1.3.1)*. en. DOI: 10.3334/ORNLDAAC/1915.

Bönisch, H., Engel, A., Birner, T., Hoor, P., Tarasick, D. W., and Ray, E. A. (2011). "On the structural changes in the Brewer-Dobson circulation after 2000". In: *Atmospheric Chemistry and Physics* 11.8, pp. 3937–3948. DOI: 10.5194/acp-11-3937-2011.

Bousquet, P., Ringeval, B., Pison, I., Dlugokencky, E. J., Brunke, E.-G., Carouge, C., Chevallier, F., Fortems-Cheiney, A., Frankenberg, C., Hauglustaine, D. A., Krummel, P. B., Langenfelds, R. L., Ramonet, M., Schmidt, M., Steele, L. P., Szopa, S., Yver, C., Viovy, N., and Ciais, P. (Apr. 2011). "Source attribution of the changes in atmospheric methane for 2006–2008". In: *Atmospheric Chemistry and Physics* 11.8. Publisher: Copernicus GmbH, pp. 3689–3700. ISSN: 1680-7316. DOI: 10.5194/acp-11-3689-2011.

Buchwitz, M., Beek, R. de, Noël, S., Burrows, J. P., Bovensmann, H., Schneising, O., Khlystova, I., Bruns, M., Bremer, H., Bergamaschi, P., Körner, S., and Heimann, M. (July 6, 2006). "Atmospheric carbon gases retrieved from SCIAMACHY by WFM-DOAS: version 0.5 CO and CH_4 and impact of calibration improvements on CO_2 retrieval". In: *Atmospheric Chemistry and Physics* 6.9. Publisher: Copernicus GmbH, pp. 2727–2751. ISSN: 1680-7316. DOI: 10.5194/acp-6-2727-2006.

Bush, M., Boutle, I., Edwards, J., Finnenkoetter, A., Franklin, C., Hanley, K., Jayakumar, A., Lewis, H., Lock, A., Mittermaier, M., Mohandas, S., North, R., Porson, A., Roux, B., Webster, S., and Weeks, M. (Mar. 2023). "The second Met Office Unified Model–JULES Regional Atmosphere and Land configuration, RAL2". In: *Geoscientific Model Development* 16.6. Publisher: Copernicus GmbH, pp. 1713–1734. ISSN: 1991-959X. DOI: 10.5194/gmd-16-1713-2023.

Butchart, N. (2014). "The Brewer-Dobson circulation". In: *Reviews of Geophysics* 52.2, pp. 157–184. DOI: https://doi.org/10.1002/2013RG000448.

Carbon Mapper (2024). Last Accessed: 23/07/2024.

Carver, G. D., Brown, P. D., and Wild, O. (Oct. 1997). "The ASAD atmospheric chemistry integration package and chemical reaction database". en. In: *Computer Physics Communications* 105.2, pp. 197–215. ISSN: 0010-4655. DOI: 10.1016/S0010-4655(97)00056-8.

Caulton, D. R., Li, Q., Bou-Zeid, E., Fitts, J. P., Golston, L. M., Pan, D., Lu, J., Lane, H. M., Buchholz, B., Guo, X., McSpiritt, J., Wendt, L., and Zondlo, M. A. (2018). "Quantifying uncertainties from mobile-laboratory-derived emissions of well pads using inverse Gaussian methods". In: *Atmospheric Chemistry and Physics* 18.20, pp. 15145–15168. DOI: 10.5194/acp-18-15145-2018.

Chang, J., Peng, S., Ciais, P., Saunois, M., Dangal, S. R., Herrero, M., Havlík, P., Tian, H., and Bousquet, P. (2019). "Revisiting enteric methane emissions from domestic ruminants and their δ 13 C CH4 source signature". In: *Nature communications* 10.1, pp. 1–14.

Chen, H., Zhu, Q., Peng, C., Wu, N., Wang, Y., Fang, X., Jiang, H., Xiang, W., Chang, J., Deng, X., et al. (2013). "Methane emissions from rice paddies natural wetlands, lakes in China: synthesis new estimate". In: *Global change biology* 19.1, pp. 19–32.

Chen, Y., Hall, J., Wees, D. van, Andela, N., Hantson, S., Giglio, L., Werf, G. R. van der, Morton, D. C., and Randerson, J. T. (Mar. 2023). *Global Fire Emissions Database (GFED5) Burned Area*. Version 0.1. Zenodo. DOI: 10.5281/zenodo.7668424.

Chevallier, F., Fisher, M., Peylin, P., Serrar, S., Bousquet, P., Bréon, F.-M., Chédin, A., and Ciais, P. (2005). "Inferring CO2 sources and sinks from satellite observations: Method and application to TOVS data". In: *Journal of Geophysical Research: Atmospheres* 110.D24. DOI: https://doi.org/10.1029/2005JD006390.

Chipperfield, M. P. (1999). "Multiannual simulations with a three-dimensional chemical transport model". In: *Journal of Geophysical Research: Atmospheres* 104.D1, pp. 1781–1805. DOI: https://doi.org/10.1029/98JD02597.

– (2006). "New version of the TOMCAT/SLIMCAT off-line chemical transport model: Intercomparison of stratospheric tracer experiments". In: *Quarterly Journal of the Royal Meteorological Society* 132.617, pp. 1179–1203. DOI: https://doi.org/10.1256/qj.05.51.

Chipperfield, M. P., Cariolle, D., Simon, P., Ramaroson, R., and Lary, D. J. (1993). "A three-dimensional modeling study of trace species in the Arctic lower stratosphere during winter 1989–1990". In: *Journal of Geophysical Research: Atmospheres* 98.D4, pp. 7199–7218. DOI: https://doi.org/10.1029/92JD02977.

Couret, C. and Schmidt, M. (2023). *ICOS ATC NRT CO2 growing time series, Zugspitze (3.0 m), 2022-03-01–2023-03-22*.

Covey, K. R. and Megonigal, J. P. (2019). "Methane production and emissions in trees and forests". In: *New Phytologist* 222.1, pp. 35–51. DOI: https://doi.org/10.1111/nph.15624.

Crippa, M., Solazzo, E., Huang, G., Guizzardi, D., Koffi, E., Muntean, M., Schieberle, C., Friedrich, R., and Janssens-Maenhout, G. (Apr. 2020a). "High resolution temporal profiles in the Emissions Database for Global Atmospheric Research". en. In: *Scientific Data* 7.1. ISSN: 2052-4463. DOI: 10.1038/s41597-020-0462-2.

Crippa, M., Solazzo, E., Huang, G., Guizzardi, D., Koffi, E., Muntean, M., Schieberle, C., Friedrich, R., and Janssens-Maenhout, G. (Apr. 2020b). "High resolution temporal profiles in the Emissions Database for Global Atmospheric Research". en. In: *Scientific Data* 7.1. Publisher: Nature Publishing Group, p. 121. ISSN: 2052-4463. DOI: 10.1038/s41597-020-0462-2.

Cusworth, D. H., Jacob, D. J., Varon, D. J., Chan Miller, C., Liu, X., Chance, K., Thorpe, A. K., Duren, R. M., Miller, C. E., Thompson, D. R., Frankenberg, C., Guanter, L., and Randles, C. A. (Oct. 2019). "Potential of next-generation imaging spectrometers to detect and quantify methane point sources from space". English. In: *Atmospheric Measurement Techniques* 12.10. Publisher: Copernicus GmbH, pp. 5655–5668. ISSN: 1867-1381. DOI: 10.5194/amt-12-5655-2019.

Davies, T., Cullen, M. J. P., Malcolm, A. J., Mawson, M. H., Staniforth, A., White, A. A., and Wood, N. (2005). "A new dynamical core for the Met Office's global and regional modelling of the atmosphere". In: *Quarterly Journal of the Royal Meteorological Society* 131.608, pp. 1759–1782. ISSN: 1477-870X. DOI: 10.1256/qj.04.101.

Dlugokencky, E. J., Houweling, S., Bruhwiler, L., Masarie, K. A., Lang, P. M., Miller, J. B., and Tans, P. P. (2003). "Atmospheric methane levels off: Temporary pause or a new steady-state". In: *Geophysical Research Letters* 30.19.

Dlugokencky, E. J., Masarie, K. A., Tans, P. P., Conway, T. J., and Xiong, X. (1997). "Is the amplitude of the methane seasonal cycle changing?" en. In: *Atmospheric Environment* 31.1, pp. 21–26. ISSN: 1352-2310. DOI: 10.1016/S1352-2310(96)00174-4.

Dlugokencky, E., Crotwell, A., Mund, J., Crotwell, M., and Thoning, K. (2019). *Atmospheric Methane Dry Air Mole Fractions from the NOAA ESRL Carbon Cycle Cooperative Global Air Sampling Network, 1983-2018, Version: 2019-07.*

– (2021). *Atmospheric Methane Dry Air Mole Fractions from the NOAA GML Carbon Cycle Cooperative Global Air Sampling Network, 1983-2020, Version: 2021-07-30.*

Dlugokencky, E. J., Nisbet, E. G., Fisher, R., and Lowry, D. (2011). "Global atmospheric methane: budget, changes and dangers". In: *Philosophical Transactions of the Royal So-*

ciety A: Mathematical, Physical and Engineering Sciences 369.1943, pp. 2058–2072. DOI: 10.1098/rsta.2010.0341.

Dutaur, L. and Verchot, L. V. (2007). "A global inventory of the soil CH4 sink". In: *Global biogeochemical cycles* 21.4.

East, J. D., Jacob, D. J., Balasus, N., Bloom, A. A., Bruhwiler, L., Chen, Z., Kaplan, J. O., Mickley, L. J., Mooring, T. A., Penn, E., Poulter, B., Sulprizio, M. P., Worden, J. R., Yantosca, R. M., and Zhang, Z. (2024). "Interpreting the Seasonality of Atmospheric Methane". In: *Geophysical Research Letters* 51.10, e2024GL108494. DOI: https://doi.org/10.1029/2024GL108494.

Ehret, T., De Truchis, A., Mazzolini, M., Morel, J.-M., d'Aspremont, A., Lauvaux, T., Duren, R., Cusworth, D., and Facciolo, G. (July 2022). "Global Tracking and Quantification of Oil and Gas Methane Emissions from Recurrent Sentinel-2 Imagery". In: *Environmental Science & Technology* 56.14. Publisher: American Chemical Society, pp. 10517–10529. ISSN: 0013-936X. DOI: 10.1021/acs.est.1c08575.

EPA (2022). *EPA's Supplemental Proposal to Reduce Climate- and Health- Harming Pollution from Oil and Natural Gas Operations: Fact Sheet for Communities*. Last Accessed:19/05/2024.

ESA (Oct. 2021). *Satellites detect large methane emissions from Madrid landfills*.

Etiope, G., Ciotoli, G., Schwietzke, S., and Schoell, M. (2019). "Gridded maps of geological methane emissions and their isotopic signature". In: *Earth System Science Data* 11.1, pp. 1–22. DOI: 10.5194/essd-11-1-2019.

European Commission, Centre, J. R., Crippa, M., Guizzardi, D., Schaaf, E., Monforti-Ferrario, F., Quadrelli, R., Risquez Martin, A., Rossi, S., Vignati, E., Muntean, M., Brandao De Melo, J., Oom, D., Pagani, F., Banja, M., Taghavi-Moharamli, P., Köykkä, J., Grassi, G., Branco, A., and San-Miguel, J. (2023). *GHG emissions of all world countries – 2023*. Last Accessed:05/06/2024. Publications Office of the European Union. DOI: doi/10.2760/953322.

Feng, L., Palmer, P. I., Parker, R. J., Lunt, M. F., and Bösch, H. (2023). "Methane emissions are predominantly responsible for record-breaking atmospheric methane growth rates in 2020

and 2021". In: *Atmospheric Chemistry and Physics* 23.8, pp. 4863–4880. DOI: 10.5194/acp-23-4863-2023.

Feng, L., Palmer, P. I., Zhu, S., Parker, R. J., and Liu, Y. (Mar. 2022). "Tropical methane emissions explain large fraction of recent changes in global atmospheric methane growth rate". en. In: *Nature Communications* 13.1, p. 1378. ISSN: 2041-1723. DOI: 10.1038/s41467-022-28989-z.

Feng, W., Chipperfield, M. P., Dhomse, S., Monge-Sanz, B. M., Yang, X., Zhang, K., and Ramonet, M. (June 2011). "Evaluation of cloud convection and tracer transport in a three-dimensional chemical transport model". English. In: *Atmospheric Chemistry and Physics* 11.12. Publisher: Copernicus GmbH, pp. 5783–5803. ISSN: 1680-7316. DOI: 10.5194/acp-11-5783-2011.

Fisher, R., Lowry, D., Wilkin, O., Sriskantharajah, S., and Nisbet, E. G. (2006). "High-precision, automated stable isotope analysis of atmospheric methane and carbon dioxide using continuous-flow isotope-ratio mass spectrometry". In: *Rapid Communications in Mass Spectrometry* 20.2, pp. 200–208. DOI: https://doi.org/10.1002/rcm.2300.

Forster, P., Storelvmo, K., Armour, W., and Collins, W. J. (2023). *The Earth's Energy Budget, Climate Feedbacks and Climate Sensitivity*. Cambridge University Press, pp. 923–1054. DOI: https://doi.org/10.1017/9781009157896.009.

Frankenberg, C., Aben, I., Bergamaschi, P., Dlugokencky, E. J., Hees, R. van, Houweling, S., Meer, P. van der, Snel, R., and Tol, P. (2011). "Global column-averaged methane mixing ratios from 2003 to 2009 as derived from SCIAMACHY: Trends and variability". In: *Journal of Geophysical Research: Atmospheres* 116.D4. ISSN: 2156-2202. DOI: 10.1029/2010JD014849.

Frankenberg, C., Platt, U., and Wagner, T. (Jan. 2005). "Iterative maximum a posteriori (IMAP)-DOAS for retrieval of strongly absorbing trace gases: Model studies for CH_4 and CO_2 retrieval from near infrared spectra of SCIAMACHY onboard ENVISAT". English. In: *Atmospheric Chemistry and Physics* 5.1. Publisher: Copernicus GmbH, pp. 9–22. ISSN: 1680-7316. DOI: 10.5194/acp-5-9-2005.

Frankenberg, C., Bergamaschi, P., Butz, A., Houweling, S., Meirink, J. F., Notholt, J., Petersen, A. K., Schrijver, H., Warneke, T., and Aben, I. (2008). "Tropical methane emissions: A revised view from SCIAMACHY onboard ENVISAT". In: *Geophysical Research Letters* 35.15. DOI: https://doi.org/10.1029/2008GL034300.

Gerbig, C., Dolman, A. J., and Heimann, M. (2009). "On observational and modelling strategies targeted at regional carbon exchange over continents". In: *Biogeosciences* 6.10, pp. 1949–1959. DOI: 10.5194/bg-6-1949-2009.

GHGSat (2023a). *Coal Mining Methane Emissions — Case Study - GHGSat.*

– (2023b). *GHGSat measures its largest emission from Nord Stream 2 leak - GHGSat.*

Gilbert, J. C. and Lemaréchal, C. (Aug. 1989). "Some numerical experiments with variable-storage quasi-Newton algorithms". en. In: *Mathematical Programming* 45.1, pp. 407–435. ISSN: 1436-4646. DOI: 10.1007/BF01589113.

Gromov, S., Brenninkmeijer, C. A. M., and Jöckel, P. (2018). "A very limited role of tropospheric chlorine as a sink of the greenhouse gas methane". In: *Atmospheric Chemistry and Physics* 18.13, pp. 9831–9843. DOI: 10.5194/acp-18-9831-2018.

Guanter, L., Irakulis-Loitxate, I., Gorroño, J., Sánchez-García, E., Cusworth, D. H., Varon, D. J., Cogliati, S., and Colombo, R. (2021). "Mapping methane point emissions with the PRISMA spaceborne imaging spectrometer". In: *Remote Sensing of Environment* 265, p. 112671. ISSN: 0034-4257. DOI: https://doi.org/10.1016/j.rse.2021.112671.

Hachmeister, J., Schneising, O., Buchwitz, M., Lorente, A., Borsdorff, T., Burrows, J. P., Notholt, J., and Buschmann, M. (2022). "On the influence of underlying elevation data on Sentinel-5 Precursor TROPOMI satellite methane retrievals over Greenland". In: *Atmospheric Measurement Techniques* 15.13, pp. 4063–4074. DOI: 10.5194/amt-15-4063-2022.

Heard, I. P. C., Manning, A. J., Haywood, J. M., Witham, C., Redington, A., Jones, A., Clarisse, L., and Bourassa, A. (2012). "A comparison of atmospheric dispersion model predictions with observations of SO2 and sulphate aerosol from volcanic eruptions". In: *Journal of Geophysical Research: Atmospheres* 117.D20. DOI: https://doi.org/10.1029/2011JD016791.

Hersbach, H. et al. (2020). "The ERA5 global reanalysis". In: *Quarterly Journal of the Royal Meteorological Society* 146.730, pp. 1999–2049. DOI: https://doi.org/10.1002/qj.3803.

Holtslag, A. a. M. and Boville, B. A. (Oct. 1993). "Local Versus Nonlocal Boundary-Layer Diffusion in a Global Climate Model". EN. In: *Journal of Climate* 6.10. Publisher: American Meteorological Society Section: Journal of Climate, pp. 1825–1842. ISSN: 0894-8755, 1520-0442. DOI: 10.1175/1520-0442(1993)006<1825:LVNBLD>2.0.CO;2.

Houweling, S., Bergamaschi, P., Chevallier, F., Heimann, M., Kaminski, T., Krol, M., Michalak, A. M., and Patra, P. (Jan. 2017). "Global inverse modeling of CH_4 sources and sinks: an overview of methods". English. In: *Atmospheric Chemistry and Physics* 17.1. Publisher: Copernicus GmbH, pp. 235–256. ISSN: 1680-7316. DOI: 10.5194/acp-17-235-2017.

Hu, H., Landgraf, J., Detmers, R., Borsdorff, T., Aan de Brugh, J., Aben, I., Butz, A., and Hasekamp, O. (2018). "Toward Global Mapping of Methane With TROPOMI: First Results and Intersatellite Comparison to GOSAT". In: *Geophysical Research Letters* 45.8, pp. 3682–3689. DOI: https://doi.org/10.1002/2018GL077259.

Huijnen, V., Williams, J., Weele, M. van, Noije, T. van, Krol, M., Dentener, F., Segers, A., Houweling, S., Peters, W., Laat, J. de, Boersma, F., Bergamaschi, P., Velthoven, P. van, Le Sager, P., Eskes, H., Alkemade, F., Scheele, R., Nédélec, P., and Pätz, H.-W. (2010). "The global chemistry transport model TM5: description and evaluation of the tropospheric chemistry version 3.0". In: *Geoscientific Model Development* 3.2, pp. 445–473. DOI: 10.5194/gmd-3-445-2010.

Jacob, D. J., Turner, A. J., Maasakkers, J. D., Sheng, J., Sun, K., Liu, X., Chance, K., Aben, I., McKeever, J., and Frankenberg, C. (2016). "Satellite observations of atmospheric methane and their value for quantifying methane emissions". In: *Atmospheric Chemistry and Physics* 16.22, pp. 14371–14396. DOI: 10.5194/acp-16-14371-2016.

Jacob, D. J. (Dec. 1999). *Introduction to Atmospheric Chemistry*. en. Princeton University Press. ISBN: 978-1-4008-4154-7.

Jacob, D. J., Varon, D. J., Cusworth, D. H., Dennison, P. E., Frankenberg, C., Gautam, R., Guanter, L., Kelley, J., McKeever, J., Ott, L. E., Poulter, B., Qu, Z., Thorpe, A. K., Wor-

den, J. R., and Duren, R. M. (2022). "Quantifying methane emissions from the global scale down to point sources using satellite observations of atmospheric methane". In: *Atmospheric Chemistry and Physics* 22.14. Publisher: Copernicus GmbH, pp. 9617–9646. ISSN: 1680-7316. DOI: 10.5194/acp-22-9617-2022.

Jervis, D., McKeever, J., Durak, B. O. A., Sloan, J. J., Gains, D., Varon, D. J., Ramier, A., Strupler, M., and Tarrant, E. (2021). "The GHGSat-D imaging spectrometer". In: *Atmospheric Measurement Techniques* 14.3. Publisher: Copernicus GmbH, pp. 2127–2140. ISSN: 1867-1381. DOI: 10.5194/amt-14-2127-2021.

Jones, A., Thomson, D., Hort, M., and Devenish, B. (2007). "The U.K. Met Office's Next-Generation Atmospheric Dispersion Model, NAME III". en. In: *Air Pollution Modeling and Its Application XVII*. Ed. by C. Borrego and A.-L. Norman. Springer US, pp. 580–589. ISBN: 978-0-387-68854-1. DOI: 10.1007/978-0-387-68854-1_62.

Joos, F. et al. (2013). "Carbon dioxide and climate impulse response functions for the computation of greenhouse gas metrics: a multi-model analysis". In: *Atmospheric Chemistry and Physics* 13.5, pp. 2793–2825. DOI: 10.5194/acp-13-2793-2013.

Kendall, E., Hort, M., and Witham, C. (2019). *Grenfell Tower fire: modelling smoke plume dispersion and air quality impact using NAME. Forecasting Research Tehcnical Report No. 633*. Tech. rep. Met Office.

Kirschke, S., Bousquet, P., Ciais, P., Saunois, M., Canadell, J. G., Dlugokencky, E. J., Bergamaschi, P., Bergmann, D., Blake, D. R., Bruhwiler, L., et al. (2013). "Three decades of global methane sources and sinks". In: *Nature geoscience* 6.10, pp. 813–823.

Krol, M., Houweling, S., Bregman, B., Broek, M. van den, Segers, A., Velthoven, P. van, Peters, W., Dentener, F., and Bergamaschi, P. (2005). "The two-way nested global chemistry-transport zoom model TM5: algorithm and applications". In: *Atmospheric Chemistry and Physics* 5.2, pp. 417–432. DOI: 10.5194/acp-5-417-2005.

Kumar, P., Broquet, G., Yver-Kwok, C., Laurent, O., Gichuki, S., Caldow, C., Cropley, F., Lauvaux, T., Ramonet, M., Berthe, G., Martin, F., Duclaux, O., Juery, C., Bouchet, C., and Ciais, P. (2021). "Mobile atmospheric measurements and local-scale inverse estimation

of the location and rates of brief CH_4 and CO_2 releases from point sources". In: *Atmospheric Measurement Techniques* 14.9, pp. 5987–6003. DOI: 10.5194/amt-14-5987-2021.

Lan, X., Thoning, K., and Dlugokencky, E. (2024). *Trends in globally-averaged CH4, N2O, and SF6 determined from NOAA Global Monitoring Laboratory measurements. Version 2024-07.* DOI: https://doi.org/10.15138/P8XG-AA10.

Lauvaux, T., Giron, C., Mazzolini, M., d'Aspremont, A., Duren, R., Cusworth, D., Shindell, D., and Ciais, P. (Feb. 2022). "Global assessment of oil and gas methane ultra-emitters". eng. In: *Science (New York, N.Y.)* 375.6580, pp. 557–561. ISSN: 1095-9203. DOI: 10.1126/science.abj4351.

Le Texier, H., Solomon, S., and Garcia, R. (1988). "The role of molecular hydrogen and methane oxidation in the water vapour budget of the stratosphere". In: *Quarterly Journal of the Royal Meteorological Society* 114.480, pp. 281–295.

Lelieveld, J., Gromov, S., Pozzer, A., and Taraborrelli, D. (2016). "Global tropospheric hydroxyl distribution, budget and reactivity". In: *Atmospheric Chemistry and Physics* 16.19, pp. 12477–12493. DOI: 10.5194/acp-16-12477-2016.

Lin, J. and Qian, T. (Nov. 2019). "A New Picture of the Global Impacts of El Nino-Southern Oscillation". In: *Scientific Reports* 9.1. Publisher: Nature Publishing Group, p. 17543. ISSN: 2045-2322. DOI: 10.1038/s41598-019-54090-5.

Lin, X., Rogers, B. M., Sweeney, C., Chevallier, F., Arshinov, M., Dlugokencky, E., Machida, T., Sasakawa, M., Tans, P., and Keppel-Aleks, G. (2020). "Siberian and temperate ecosystems shape Northern Hemisphere atmospheric CO2 seasonal amplification". In: *Proceedings of the National Academy of Sciences* 117.35, pp. 21079–21087. ISSN: 0027-8424. DOI: 10.1073/pnas.1914135117.

Liu, T., Mickley, L. J., Marlier, M. E., DeFries, R. S., Khan, M. F., Latif, M. T., and Karambelas, A. (2020). "Diagnosing spatial biases and uncertainties in global fire emissions inventories: Indonesia as regional case study". In: *Remote Sensing of Environment* 237, p. 111557.

Lorente, A., Borsdorff, T., Butz, A., Hasekamp, O., Brugh, J. aan de, Schneider, A., Wu, L., Hase, F., Kivi, R., Wunch, D., Pollard, D. F., Shiomi, K., Deutscher, N. M., Velazco,

V. A., Roehl, C. M., Wennberg, P. O., Warneke, T., and Landgraf, J. (2021). "Methane retrieved from TROPOMI: improvement of the data product and validation of the first 2 years of measurements". In: *Atmospheric Measurement Techniques* 14.1, pp. 665–684. DOI: 10.5194/amt-14-665-2021.

Lorente, A., Borsdorff, T., Martinez-Velarte, M. C., and Landgraf, J. (2023). "Accounting for surface reflectance spectral features in TROPOMI methane retrievals". In: *Atmospheric Measurement Techniques* 16.6, pp. 1597–1608. DOI: 10.5194/amt-16-1597-2023.

Lorente, A., Borsdorff, T., Martinez-Velarte, M. C., Butz, A., Hasekamp, O. P., Wu, L., and Landgraf, J. (Nov. 2022). "Evaluation of the methane full-physics retrieval applied to TROPOMI ocean sun glint measurements". English. In: *Atmospheric Measurement Techniques* 15.22. Publisher: Copernicus GmbH, pp. 6585–6603. ISSN: 1867-1381. DOI: 10.5194/amt-15-6585-2022.

Lowry, D., Fisher, R. E., France, J. L., Coleman, M., Lanoisellé, M., Zazzeri, G., Nisbet, E. G., Shaw, J. T., Allen, G., Pitt, J., and Ward, R. S. (2020). "Environmental baseline monitoring for shale gas development in the UK: Identification and geochemical characterisation of local source emissions of methane to atmosphere". In: *Science of The Total Environment* 708, p. 134600. ISSN: 0048-9697. DOI: https://doi.org/10.1016/j.scitotenv.2019.134600.

Lunt, M. F., Palmer, P. I., Lorente, A., Borsdorff, T., Landgraf, J., Parker, R. J., and Boesch, H. (2021). "Rain-fed pulses of methane from East Africa during 2018–2019 contributed to atmospheric growth rate". In: *Environmental Research Letters* 16.2. Publisher: IOP Publishing. ISSN: 1748-9326. DOI: 10.1088/1748-9326/abd8fa.

Lutgens, F. and Tarbuck, E. (2001). *The Atmosphere: 8th Edition*. Pearson.

MacLean, J.-P. W., Girard, M., Jervis, D., Marshall, D., McKeever, J., Ramier, A., Strupler, M., Tarrant, E., and Young, D. (2024). "Offshore methane detection and quantification from space using sun glint measurements with the GHGSat constellation". In: *Atmospheric Measurement Techniques* 17.2, pp. 863–874. DOI: 10.5194/amt-17-863-2024.

Manning, A. J. et al. (2021). "Evidence of a recent decline in UK emissions of hydrofluorocarbons determined by the InTEM inverse model and atmospheric measurements". In: *Atmospheric Chemistry and Physics* 21.16, pp. 12739–12755. DOI: 10.5194/acp-21-12739-2021.

Matthews, E. and Fung, I. (1987). "Methane emission from natural wetlands: Global distribution, area, and environmental characteristics of sources". In: *Global Biogeochemical Cycles* 1.1, pp. 61–86. DOI: https://doi.org/10.1029/GB001i001p00061.

McNorton, J., Chipperfield, M. P., Gloor, M., Wilson, C., Feng, W., Hayman, G. D., Rigby, M., Krummel, P. B., O'Doherty, S., Prinn, R. G., Weiss, R. F., Young, D., Dlugokencky, E., and Montzka, S. A. (2016). "Role of OH variability in the stalling of the global atmospheric CH_4 growth rate from 1999 to 2006". In: *Atmospheric Chemistry and Physics* 16.12, pp. 7943–7956. DOI: 10.5194/acp-16-7943-2016.

McNorton, J., Wilson, C., Gloor, M., Parker, R. J., Boesch, H., Feng, W., Hossaini, R., and Chipperfield, M. P. (2018). "Attribution of recent increases in atmospheric methane through 3-D inverse modelling". In: *Atmospheric Chemistry and Physics* 18.24, pp. 18149–18168. DOI: 10.5194/acp-18-18149-2018.

MethaneSAT (2024). Last Accessed: 23/07/2024.

Monks, S. A., Arnold, S. R., Hollaway, M. J., Pope, R. J., Wilson, C., Feng, W., Emmerson, K. M., Kerridge, B. J., Latter, B. L., Miles, G. M., Siddans, R., and Chipperfield, M. P. (2017). "The TOMCAT global chemical transport model v1.6: description of chemical mechanism and model evaluation". In: *Geoscientific Model Development* 10.8, pp. 3025–3057. DOI: 10.5194/gmd-10-3025-2017.

Murguia-Flores, F., Arndt, S., Ganesan, A. L., Murray-Tortarolo, G., and Hornibrook, E. R. C. (2018). "Soil Methanotrophy Model (MeMo v1.0): a process-based model to quantify global uptake of atmospheric methane by soil". In: *Geoscientific Model Development* 11.6, pp. 2009–2032. DOI: 10.5194/gmd-11-2009-2018.

Myhre, G. et al. (2013). "Anthropogenic and Natural Radiative Forcing. In: Climate Change 2013: The Physical Science Basis. Contribution of Working Group I to the Fifth Assessment Report of the Intergovernmental Panel on Climate Change". In.

NAEI (2024). *Gridded Emissions Data*. Last Accessed:10/11/2024.

Nauer, P. A., Hutley, L. B., and Arndt, S. K. (2018). "Termite mounds mitigate half of termite methane emissions". In: *Proceedings of the National Academy of Sciences* 115.52, pp. 13306–13311.

Naus, S., Montzka, S. A., Patra, P. K., and Krol, M. C. (Mar. 2021). "A three-dimensional-model inversion of methyl chloroform to constrain the atmospheric oxidative capacity". English. In: *Atmospheric Chemistry and Physics* 21.6, pp. 4809–4824. ISSN: 1680-7316. DOI: 10.5194/acp-21-4809-2021.

Nisbet, E. G. et al. (2016). "Rising atmospheric methane: 2007–2014 growth and isotopic shift". In: *Global Biogeochemical Cycles* 30.9, pp. 1356–1370. DOI: https://doi.org/10.1002/2016GB005406.

Nisbet, E. G. et al. (2019). "Very Strong Atmospheric Methane Growth in the 4 Years 2014–2017: Implications for the Paris Agreement". In: *Global Biogeochemical Cycles* 33.3, pp. 318–342. DOI: https://doi.org/10.1029/2018GB006009.

NOAA (2024a). *Curve Fitting Methods Applied to Time Series in NOAA GML*. Last Accessed: 12/11/2024.

– (2024b). *Introduction to the Atmosphere*. Last Accessed: 19/07/2024.

– (2024c). *Trends in Atmospheric Methane*. https://www.esrl.noaa.gov/gmd/ccgg/trends_ch4/. Accessed: 23/04/2024.

O'Callaghan, J. O. (2024). *Tracking methane super-emitters from space*. Last Accessed: 14/11/2024. DOI: https://doi.org/10.1038/d41586-024-03594-w.

Pandey, S., Gautam, R., Houweling, S., Gon, H. D. van der, Sadavarte, P., Borsdorff, T., Hasekamp, O., Landgraf, J., Tol, P., Kempen, T. van, Hoogeveen, R., Hees, R. van, Hamburg, S. P., Maasakkers, J. D., and Aben, I. (2019). "Satellite observations reveal extreme methane leakage from a natural gas well blowout". In: *Proceedings of the National Academy of Sciences* 116.52, pp. 26376–26381. ISSN: 0027-8424. DOI: 10.1073/pnas.1908712116.

Pandey, S., Houweling, S., Lorente, A., Borsdorff, T., Tsivlidou, M., Bloom, A. A., Poulter, B., Zhang, Z., and Aben, I. (Jan. 2021). "Using satellite data to identify the methane emission controls of South Sudan's wetlands". English. In: *Biogeosciences* 18.2. ISSN: 1726-4170. DOI: 10.5194/bg-18-557-2021.

Parker, R., Boesch, H., Cogan, A., Fraser, A., Feng, L., Palmer, P. I., Messerschmidt, J., Deutscher, N., Griffith, D. W. T., Notholt, J., Wennberg, P. O., and Wunch, D. (2011). "Methane observations from the Greenhouse Gases Observing SATellite: Comparison to ground-based TCCON data and model calculations". en. In: *Geophysical Research Letters* 38.15. ISSN: 1944-8007. DOI: 10.1029/2011GL047871.

Parker, R. J., Boesch, H., McNorton, J., Comyn-Platt, E., Gloor, M., Wilson, C., Chipperfield, M. P., Hayman, G. D., and Bloom, A. A. (2018). "Evaluating year-to-year anomalies in tropical wetland methane emissions using satellite CH4 observations". In: *Remote Sensing of Environment* 211, pp. 261–275. ISSN: 0034-4257. DOI: https://doi.org/10.1016/j.rse.2018.02.011.

Parker, R. J., Wilson, C., Bloom, A. A., Comyn-Platt, E., Hayman, G., McNorton, J., Boesch, H., and Chipperfield, M. P. (2020). "Exploring constraints on a wetland methane emission ensemble (WetCHARTs) using GOSAT observations". In: *Biogeosciences* 17.22. Publisher: Copernicus GmbH. ISSN: 1726-4170. DOI: 10.5194/bg-17-5669-2020.

Patra, P. K., Krol, M. C., Prinn, R. G., Takigawa, M., Mühle, J., Montzka, S. A., Lal, S., Yamashita, Y., Naus, S., Chandra, N., Weiss, R. F., Krummel, P. B., Fraser, P. J., O'Doherty, S., and Elkins, J. W. (2021). "Methyl Chloroform Continues to Constrain the Hydroxyl (OH) Variability in the Troposphere". In: *Journal of Geophysical Research: Atmospheres* 126.4. e2020JD033862 2020JD033862, e2020JD033862. DOI: https://doi.org/10.1029/2020JD033862.

Patra, P. K. et al. (2011). "TransCom model simulations of CH_4 and related species: linking transport, surface flux and chemical loss with CH_4 variability in the troposphere and lower stratosphere". In: *Atmospheric Chemistry and Physics* 11.24, pp. 12813–12837. DOI: 10.5194/acp-11-12813-2011.

Peng, S., Lin, X., Thompson, R. L., Xi, Y., Liu, G., Hauglustaine, D., Lan, X., Poulter, B., Ramonet, M., Saunois, M., Yin, Y., Zhang, Z., Zheng, B., and Ciais, P. (Dec. 2022). "Wetland emission and atmospheric sink changes explain methane growth in 2020". In: *Nature* 612.7940. Publisher: Nature Publishing Group, pp. 477–482. ISSN: 1476-4687. DOI: 10.1038/s41586-022-05447-w.

Pérez-Barbería, F. J. (Feb. 2017). "Scaling methane emissions in ruminants and global estimates in wild populations". en. In: *Science of The Total Environment* 579, pp. 1572–1580. ISSN: 0048-9697. DOI: 10.1016/j.scitotenv.2016.11.175.

Peters, W., Krol, M. C., Dlugokencky, E. J., Dentener, F. J., Bergamaschi, P., Dutton, G., Velthoven, P. v., Miller, J. B., Bruhwiler, L., and Tans, P. P. (2004). "Toward regional-scale modeling using the two-way nested global model TM5: Characterization of transport using SF6". In: *Journal of Geophysical Research: Atmospheres* 109.D19. DOI: https://doi.org/10.1029/2004JD005020.

Philip, S., Martin, R. V., and Keller, C. A. (May 2016). "Sensitivity of chemistry-transport model simulations to the duration of chemical and transport operators: a case study with GEOS-Chem v10-01". English. In: *Geoscientific Model Development* 9.5. Publisher: Copernicus GmbH, pp. 1683–1695. ISSN: 1991-959X. DOI: 10.5194/gmd-9-1683-2016.

Pimlott, M. A., Pope, R. J., Kerridge, B. J., Latter, B. G., Knappett, D. S., Heard, D. E., Ventress, L. J., Siddans, R., Feng, W., and Chipperfield, M. P. (Aug. 2022). "Investigating the global OH radical distribution using steady-state approximations and satellite data". In: *Atmospheric Chemistry and Physics* 22.16. Publisher: Copernicus GmbH, pp. 10467–10488. ISSN: 1680-7316. DOI: 10.5194/acp-22-10467-2022.

Portmann, R., Daniel, J., and Ravishankara, A. (2012). "Stratospheric ozone depletion due to nitrous oxide: influences of other gases". In: *Philosophical Transactions of the Royal Society B: Biological Sciences* 367.1593, pp. 1256–1264.

Poulter, B. et al. (Sept. 2017). "Global wetland contribution to 2000–2012 atmospheric methane growth rate dynamics". en. In: *Environmental Research Letters* 12.9. Publisher: IOP Publishing, p. 094013. ISSN: 1748-9326. DOI: 10.1088/1748-9326/aa8391.

Prather, M. J. (1986). "Numerical advection by conservation of second-order moments". In: *Journal of Geophysical Research: Atmospheres* 91.D6, pp. 6671–6681. DOI: https://doi.org/10.1029/JD091iD06p06671.

Prather, M. J., Holmes, C. D., and Hsu, J. (2012). "Reactive greenhouse gas scenarios: Systematic exploration of uncertainties and the role of atmospheric chemistry". In: *Geophysical Research Letters* 39.9. DOI: https://doi.org/10.1029/2012GL051440.

Prinn, R. G. et al. (2018). "History of chemically and radiatively important atmospheric gases from the Advanced Global Atmospheric Gases Experiment (AGAGE)". In: *Earth System Science Data* 10.2, pp. 985–1018. DOI: 10.5194/essd-10-985-2018.

Randerson, J., Van Der Werf, G., Giglio, L., Collatz, G., and Kasibhatla, P. (2017). *Global Fire Emissions Database, Version 4.1 (GFEDv4)*. en. DOI: 10.3334/ORNLDAAC/1293.

Rigby, M., Montzka, S. A., Prinn, R. G., White, J. W. C., Young, D., O'Doherty, S., Lunt, M. F., Ganesan, A. L., Manning, A. J., Simmonds, P. G., Salameh, P. K., Harth, C. M., Mühle, J., Weiss, R. F., Fraser, P. J., Steele, L. P., Krummel, P. B., McCulloch, A., and Park, S. (2017). "Role of atmospheric oxidation in recent methane growth". In: *Proceedings of the National Academy of Sciences* 114.21, pp. 5373–5377. ISSN: 0027-8424. DOI: 10.1073/pnas.1616426114.

Rowlinson, M. J., Rap, A., Arnold, S. R., Pope, R. J., Chipperfield, M. P., McNorton, J., Forster, P., Gordon, H., Pringle, K. J., Feng, W., Kerridge, B. J., Latter, B. L., and Siddans, R. (2019). "Impact of El Niño–Southern Oscillation on the interannual variability of methane and tropospheric ozone". In: *Atmospheric Chemistry and Physics* 19.13, pp. 8669–8686. DOI: 10.5194/acp-19-8669-2019.

Sánchez-García, E., Gorroño, J., Irakulis-Loitxate, I., Varon, D. J., and Guanter, L. (Mar. 2022). "Mapping methane plumes at very high spatial resolution with the WorldView-3 satellite". In: *Atmospheric Measurement Techniques* 15.6. Publisher: Copernicus GmbH, pp. 1657–1674. ISSN: 1867-1381. DOI: 10.5194/amt-15-1657-2022.

Sasakawa, M., Shimoyama, K., Machida, T., Tsuda, N., Suto, H., Arshinov, M., Davydov, D., Fofonov, A., Krasnov, O., Saeki, T., Koyama, Y., and Maksyutov, S. (2010). *Continuous*

measurements of methane from a tower network over Siberia. Reference Date: 2022/10/20. DOI: 10.17595/20160901.004.

Saunois, M. et al. (2020). "The Global Methane Budget 2000–2017". In: *Earth System Science Data* 12.3, pp. 1561–1623. DOI: 10.5194/essd-12-1561-2020.

Schneising, O., Buchwitz, M., Hachmeister, J., Vanselow, S., Reuter, M., Buschmann, M., Bovensmann, H., and Burrows, J. P. (2023). "Advances in retrieving XCH_4 and XCO from Sentinel-5 Precursor: improvements in the scientific TROPOMI/WFMD algorithm". In: *Atmospheric Measurement Techniques* 16.3, pp. 669–694. DOI: 10.5194/amt-16-669-2023.

Schneising, O. et al. (2019). "A scientific algorithm to simultaneously retrieve carbon monoxide and methane from TROPOMI onboard Sentinel-5 Precursor". English. In: *Atmospheric Measurement Techniques* 12.12. Publisher: Copernicus GmbH. ISSN: 1867-1381. DOI: 10.5194/amt-12-6771-2019.

Schuit, B. J., Maasakkers, J. D., Bijl, P., Mahapatra, G., Berg, A.-W. van den, Pandey, S., Lorente, A., Borsdorff, T., Houweling, S., Varon, D. J., McKeever, J., Jervis, D., Girard, M., Irakulis-Loitxate, I., Gorroño, J., Guanter, L., Cusworth, D. H., and Aben, I. (2023). "Automated detection and monitoring of methane super-emitters using satellite data". In: *Atmospheric Chemistry and Physics* 23.16, pp. 9071–9098. DOI: 10.5194/acp-23-9071-2023.

Shaw, J. T., Shah, A., Yong, H., and Allen, G. (Sept. 2021). "Methods for quantifying methane emissions using unmanned aerial vehicles: a review". In: *Philosophical Transactions of the Royal Society A: Mathematical, Physical and Engineering Sciences* 379.2210. Publisher: Royal Society, p. 20200450. DOI: 10.1098/rsta.2020.0450.

Sherwin, E. D., Rutherford, J. S., Chen, Y., Aminfard, S., Kort, E. A., Jackson, R. B., and Brandt, A. R. (Mar. 2023). "Single-blind validation of space-based point-source detection and quantification of onshore methane emissions". en. In: *Scientific Reports* 13.1. Publisher: Nature Publishing Group, p. 3836. ISSN: 2045-2322. DOI: 10.1038/s41598-023-30761-2.

Singh, K., Jardak, M., Sandu, A., Bowman, K., Lee, M., and Jones, D. (Apr. 2011). "Construction of non-diagonal background error covariance matrices for global chemical data as-

similation". English. In: *Geoscientific Model Development* 4.2. Publisher: Copernicus GmbH, pp. 299–316. ISSN: 1991-959X. DOI: 10.5194/gmd-4-299-2011.

Spivakovsky, C. M., Logan, J. A., Montzka, S. A., Balkanski, Y. J., Foreman-Fowler, M., Jones, D. B. A., Horowitz, L. W., Fusco, A. C., Brenninkmeijer, C. A. M., Prather, M. J., Wofsy, S. C., and McElroy, M. B. (2000). "Three-dimensional climatological distribution of tropospheric OH: Update and evaluation". In: *Journal of Geophysical Research: Atmospheres* 105.D7, pp. 8931–8980. DOI: https://doi.org/10.1029/1999JD901006.

Stanley, K. M., Grant, A., O'Doherty, S., Young, D., Manning, A. J., Stavert, A. R., Spain, T. G., Salameh, P. K., Harth, C. M., Simmonds, P. G., Sturges, W. T., Oram, D. E., and Derwent, R. G. (2018). "Greenhouse gas measurements from a UK network of tall towers: technical description and first results". In: *Atmospheric Measurement Techniques* 11.3, pp. 1437–1458. ISSN: 1867-1381. DOI: 10.5194/amt-11-1437-2018.

Stockwell, D. Z. and Chipperfield, M. P. (1999). "A tropospheric chemical-transport model: Development and validation of the model transport schemes". en. In: *Quarterly Journal of the Royal Meteorological Society* 125.557. _eprint: https://rmets.onlinelibrary.wiley.com/doi/pdf/10.1002/qj.4971 pp. 1747–1783. ISSN: 1477-870X. DOI: https://doi.org/10.1002/qj.49712555714.

Stone, D., Whalley, L. K., and Heard, D. E. (2012). "Tropospheric OH and HO2 radicals: field measurements and model comparisons". In: *Chem. Soc. Rev.* 41 (19), pp. 6348–6404. DOI: 10.1039/C2CS35140D.

TCCON (2023). Last Accessed:24/07/2024.

Tiedtke, M. (Aug. 1989). "A Comprehensive Mass Flux Scheme for Cumulus Parameterization in Large-Scale Models". EN. In: *Monthly Weather Review* 117.8. Publisher: American Meteorological Society Section: Monthly Weather Review, pp. 1779–1800. ISSN: 1520-0493, 0027-0644. DOI: 10.1175/1520-0493(1989)117<1779:ACMFSF>2.0.CO;2.

Tohjima, Y. et al. (2016a). *Continuous observational data of atmospheric CH4 mixing ratios on Cape Ochi-ishi, Ver. 1.0*. Reference Date: 2022/06/30. DOI: 10.17595/20160901.003..

– (2016b). *Continuous observational data of atmospheric CH4 mixing ratios on Hateruma Island, Ver. 1.2)*. Reference Date: 2022/06/30. DOI: 10.17595/20160901.003..

Tol, P. J. J., Kempen, T. A. van, Hees, R. M. van, Krijger, M., Cadot, S., Snel, R., Persijn, S. T., Aben, I., and Hoogeveen, R. W. M. (2018). "Characterization and correction of stray light in TROPOMI-SWIR". In: *Atmospheric Measurement Techniques* 11.7, pp. 4493–4507. DOI: 10.5194/amt-11-4493-2018.

Tost, H., Lawrence, M. G., Brühl, C., Jöckel, P., Team, T. G., and Team, T. S.-O.-D. (2010). "Uncertainties in atmospheric chemistry modelling due to convection parameterisations and subsequent scavenging". In: *Atmospheric Chemistry and Physics* 10.4, pp. 1931–1951. DOI: 10.5194/acp-10-1931-2010.

Turner, A. J., Frankenberg, C., Wennberg, P. O., and Jacob, D. J. (2017). "Ambiguity in the causes for decadal trends in atmospheric methane and hydroxyl". In: *Proceedings of the National Academy of Sciences* 114.21, pp. 5367–5372. ISSN: 0027-8424. DOI: 10.1073/pnas.1616020114.

Varon, D. J., Jacob, D. J., McKeever, J., Jervis, D., Durak, B. O. A., Xia, Y., and Huang, Y. (2018). "Quantifying methane point sources from fine-scale satellite observations of atmospheric methane plumes". In: *Atmospheric Measurement Techniques* 11.10, pp. 5673–5686. DOI: 10.5194/amt-11-5673-2018.

Varon, D. J., Jervis, D., McKeever, J., Spence, I., Gains, D., and Jacob, D. J. (2021). "High-frequency monitoring of anomalous methane point sources with multispectral Sentinel-2 satellite observations". In: *Atmospheric Measurement Techniques* 14.4, pp. 2771–2785. DOI: 10.5194/amt-14-2771-2021.

Wang, H.-J., Zhang, R.-H., Cole, J., and Chavez, F. (Sept. 1999a). "El Niño and the related phenomenon Southern Oscillation (ENSO): The largest signal in interannual climate variation". In: *Proceedings of the National Academy of Sciences* 96.20, pp. 11071–11072. DOI: 10.1073/pnas.96.20.11071.

Wang, K., Pyle, J. A., Sanderson, M. G., and Bridgeman, C. (1999b). "Implementation of a convective atmospheric boundary layer scheme in a tropospheric chemistry transport model". In: *Journal of Geophysical Research: Atmospheres* 104.D19, pp. 23729–23745. DOI: https://doi.org/10.1029/1999JD900383.

Wang, Y., Fang, M., Lou, Z., He, H., Guo, Y., Pi, X., Wang, Y., Yin, K., and Fei, X. (Apr. 2024). "Methane emissions from landfills differentially underestimated worldwide". en. In: *Nature Sustainability* 7.4. Publisher: Nature Publishing Group, pp. 496–507. ISSN: 2398-9629. DOI: 10.1038/s41893-024-01307-9.

Wang, Y. X., McElroy, M. B., Jacob, D. J., and Yantosca, R. M. (2004). "A nested grid formulation for chemical transport over Asia: Applications to CO". In: *Journal of Geophysical Research: Atmospheres* 109.D22. DOI: https://doi.org/10.1029/2004JD005237.

Weber, T., Wiseman, N. A., and Kock, A. (2019). "Global ocean methane emissions dominated by shallow coastal waters". In: *Nature communications* 10.1, pp. 1–10.

Williamson, D. L. and Rasch, P. J. (Jan. 1989). "Two-Dimensional Semi-Lagrangian Transport with Shape-Preserving Interpolation". EN. In: *Monthly Weather Review* 117.1. Publisher: American Meteorological Society Section: Monthly Weather Review, pp. 102–129. ISSN: 1520-0493, 0027-0644.

Wilson, C., Chipperfield, M. P., Gloor, M., and Chevallier, F. (2014). "Development of a variational flux inversion system (INVICAT v1.0) using the TOMCAT chemical transport model". In: *Geoscientific Model Development* 7.5, pp. 2485–2500. DOI: 10.5194/gmd-7-2485-2014.

Wilson, C., Chipperfield, M. P., Gloor, M., Parker, R. J., Boesch, H., McNorton, J., Gatti, L. V., Miller, J. B., Basso, L. S., and Monks, S. A. (2021). "Large and increasing methane emissions from eastern Amazonia derived from satellite data, 2010–2018". In: *Atmospheric Chemistry and Physics* 21.13, pp. 10643–10669. DOI: 10.5194/acp-21-10643-2021.

Worden, J. R., Bloom, A. A., Pandey, S., Jiang, Z., Worden, H. M., Walker, T. W., Houweling, S., and Röckmann, T. (Dec. 2017). "Reduced biomass burning emissions reconcile conflicting estimates of the post-2006 atmospheric methane budget". In: *Nature Communications* 8.1, p. 2227. ISSN: 2041-1723. DOI: 10.1038/s41467-017-02246-0.

Wunch, D., Toon, G. C., Blavier, J.-F. L., Washenfelder, R. A., Notholt, J., Connor, B. J., Griffith, D. W. T., Sherlock, V., and Wennberg, P. O. (May 2011). "The Total Carbon Column Observing Network". In: *Philosophical Transactions of the Royal Society A: Mathematical,*

Physical and Engineering Sciences 369.1943. Publisher: Royal Society, pp. 2087–2112. DOI: 10.1098/rsta.2010.0240.

Yong, H., Allen, G., Mcquilkin, J., Ricketts, H., and Shaw, J. T. (2024). "Lessons learned from a UAV survey and methane emissions calculation at a UK landfill". In: *Waste Management* 180, pp. 47–54. ISSN: 0956-053X. DOI: https://doi.org/10.1016/j.wasman.2024.03.025.

Zavala-Araiza, D., Lyon, D., Alvarez, R. A., Palacios, V., Harriss, R., Lan, X., Talbot, R., and Hamburg, S. P. (2015a). "Toward a Functional Definition of Methane Super-Emitters: Application to Natural Gas Production Sites". In: *Environmental Science & Technology* 49.13, pp. 8167–8174. DOI: 10.1021/acs.est.5b00133.

Zavala-Araiza, D., Lyon, D. R., Alvarez, R. A., Davis, K. J., Harriss, R., Herndon, S. C., Karion, A., Kort, E. A., Lamb, B. K., Lan, X., Marchese, A. J., Pacala, S. W., Robinson, A. L., Shepson, P. B., Sweeney, C., Talbot, R., Townsend-Small, A., Yacovitch, T. I., Zimmerle, D. J., and Hamburg, S. P. (2015b). "Reconciling divergent estimates of oil and gas methane emissions". In: *Proceedings of the National Academy of Sciences* 112.51, pp. 15597–15602. DOI: 10.1073/pnas.1522126112.

Zhang, Z., Zimmermann, N. E., Calle, L., Hurtt, G., Chatterjee, A., and Poulter, B. (2018). "Enhanced response of global wetland methane emissions to the 2015-2016 El Niño-Southern Oscillation event". In: *Environmental Research Letters* 13.7, p. 074009. DOI: 10.1088/1748-9326/aac939.

Zhao, Y. et al. (2019). "Inter–model comparison of global hydroxyl radical (OH) distributions and their impact on atmospheric methane over the 2000–2016 period". In: *Atmospheric Chemistry and Physics* 19.21, pp. 13701–13723. DOI: 10.5194/acp-19-13701-2019.

Appendix A

Supplement: Paper 1

A.1 Seasonal Cycle Time Series

Figure A.1 shows the smoothed and detrended times series of the modelled and observed CH_4 concentrations at each observation site used in the study. The modelled detreneded time series compares well with the observed detrended time series.

A.2 Errors on the SCA

This study computes the seasonal cycle amplitude (SCA) by finding the difference between the annual maximum (SC_{Dmax}) and the annual minimum (SC_{Dmax}) of the smoothed and detrended time series (See Section 4.2.4, Equation 4.1). The 1σ error bars shown in Figure 4.4a) represent the interannual variability of the mean SCA. In Figure 4.4b) the error bars represent the standard error on the estimated slope, multiplied by the number of years.

The uncertainty analysis on the calculated SCA value could be extended further in this work. Following methods by NOAA (2024a), I have calculated the standard deviation on the amplitude (Equation A.1). Table A.1 shows the standard deviation on the SCA at each observation site.

$$\sigma_{amp} = \sqrt{\sigma^2_{cycle(max)} + \sigma^2_{cycle(min)}} \tag{A.1}$$

Despite the uncertainty on the observed SCA, the observations show that the change in the SCA NHL is consistently lower compared to the rest of the world. I have applied a Welch's t-test to

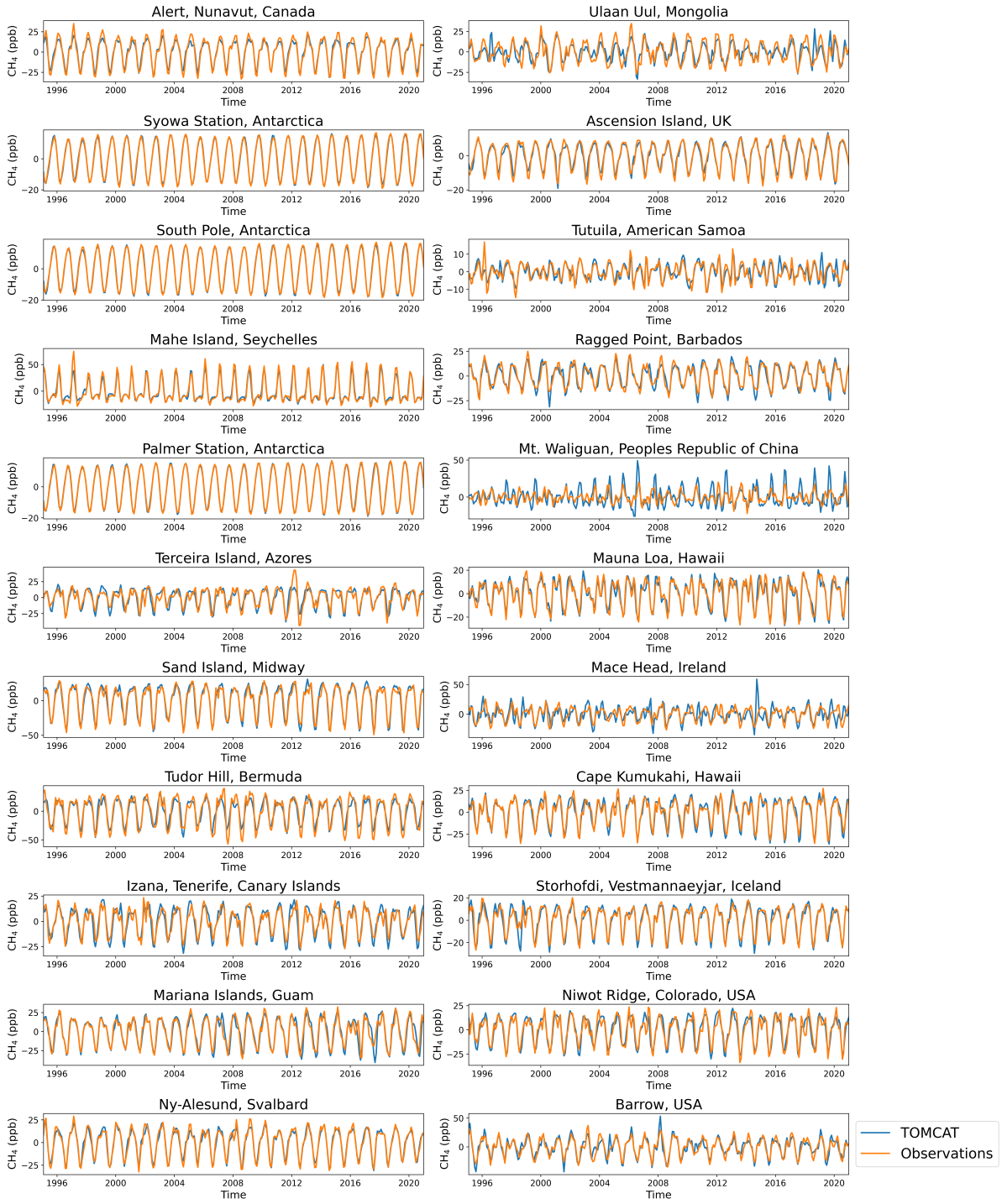

Figure A.1: The modelled (blue) and observed (orange) smoothed and detrended time series of CH_4 (ppb) at each observation site used in the analysis.

the mean values of the ΔSCA in the NHL and non-NHL and found the p-value to equal 0.002. Therefore that we can conclude that the ΔSCA in NHLs is statistically significantly different to ΔSCA in the non-NHLs.

Table A.1: The σ_{amp} (ppb) of 22 NOAA Sites used in the analysis (Dlugokencky et al., 2021).

Site Code	σ_{amp} (ppb)	Site Code	σ_{amp} (ppb)
ALT	4.7	MLO	4.3
UUM	6.9	MID	6.1
SYO	1.5	MHD	5.5
ASC	2.3	BMW	8.7
SPO	1.4	KUM	6.5
SMO	3.9	IZO	4.6
SEY	9.2	ICE	4.7
RPB	5.2	GMI	6.3
PSA	1.3	NWR	5.6
WLG	6.1	ZEP	5.5
AZR	9.5	BRW	6.8

A.3 Sensitivity Testing on Background Tracer

We carried out a sensitivity experiment on the exponential decay of the CH_4 tracer into the background. The results of these model runs showed that changing the e-folding time (lifetime) from 9 months to 12 months did not have a large impact on the results. We also set the lifetime to 1 month, this did have an impact on the final results but 1 month lifetime is too short to represent well-mixed methane. Find the results of the model simulations in Table A.2.

Table A.2: A table comparing the results ΔSCA (ppb) of TOM_regional, TOM_transport, TOM_twelve and TOM_one simulations.

Tagged Tracers	TOM_regional	TOM_transport	TOM_twelve	TOM_one
Total (sum of all tracers)	-6.38	-2.09	-6.38	-6.38
Sum of Regions	3.54	0.23	3.43	-2.61
Background	-9.93	-2.32	-9.81	-3.74
Canada	-2.97	0.24	-2.91	-4.09
Middle East	-2.13	-0.22	-2.14	-0.95
Europe	-1.48	0.76	-1.5	1.43
Russia	2.71	-0.60	2.67	1.56
North America	2.46	-0.91	2.52	0.52

A.4 Model Comparison of Independent Sites

Here we show the comparison between the model and surface observations at the independent observation sites that have not been used in the assimilation. The model captures the SCA amplitude well when compared with surface observations (Fig. A.2). The Siberia sites (DEM, BRZ and KRS) have a very short observation record of 6 years and the SCA is quite variable

within this time period, leading to large error bars.

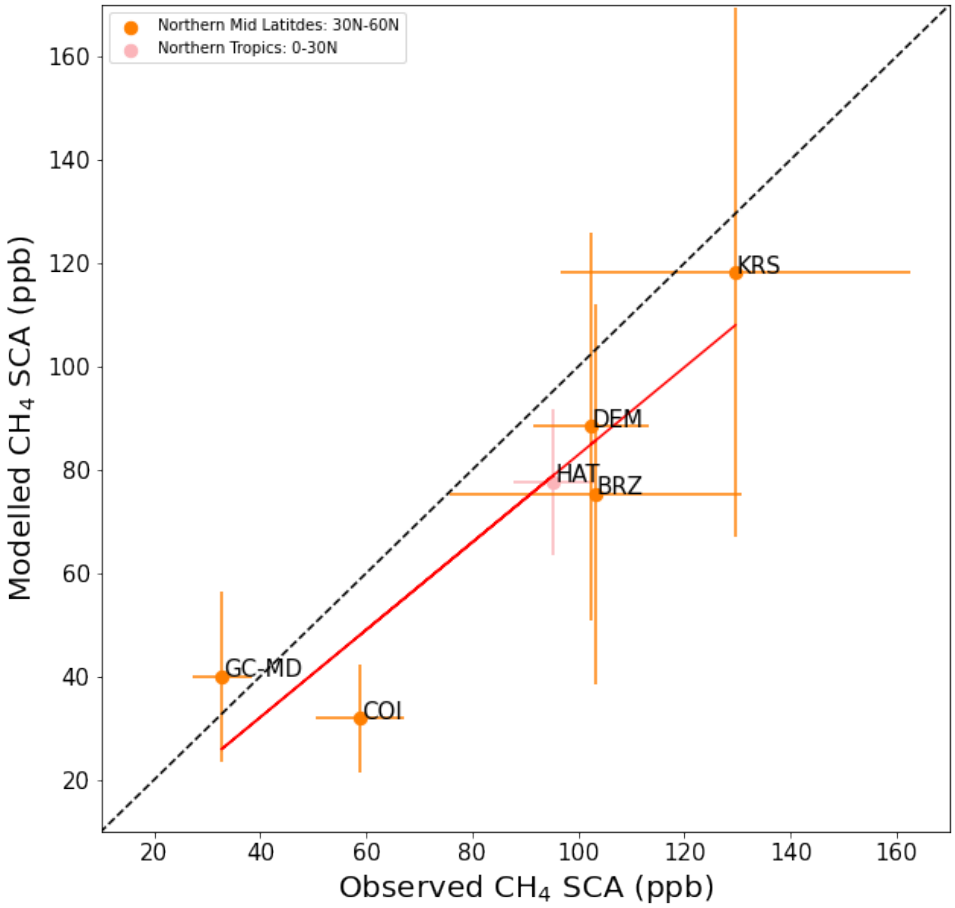

Figure A.2: The comparison between simulated and observed CH_4 SCA at the independent observation sites. The solid line represents the unit line and the red line represents the least squares regression line, respectively. The error bars denote $\pm 1\sigma$.

Table A.3: A table comparing the results ΔSCA (ppb) of TOM_regional, TOM_transport, TOM_twelve and TOM_one simulations.

Site Name	Latitude (°N)	Longitude (°)	Site Code
Cape Ochi-ishi, Japan	43.16	145.45	COI
Hateruma, Japan	24.06	123.80	HAT
Demyanskoe, Russia	59.79	70.87	DEM
Karasevoe, Russia	58.25	82.42	KRS
Berezorechka, Russia	56.15	84.33	BRZ
Mace Head, Republic of Ireland	53.33	0-9.90	GC-MD

A.5 SCA Time Series

This section contains the time series of the modelled and observed SCA and the trend at the NOAA observation sites (Fig. A.3)

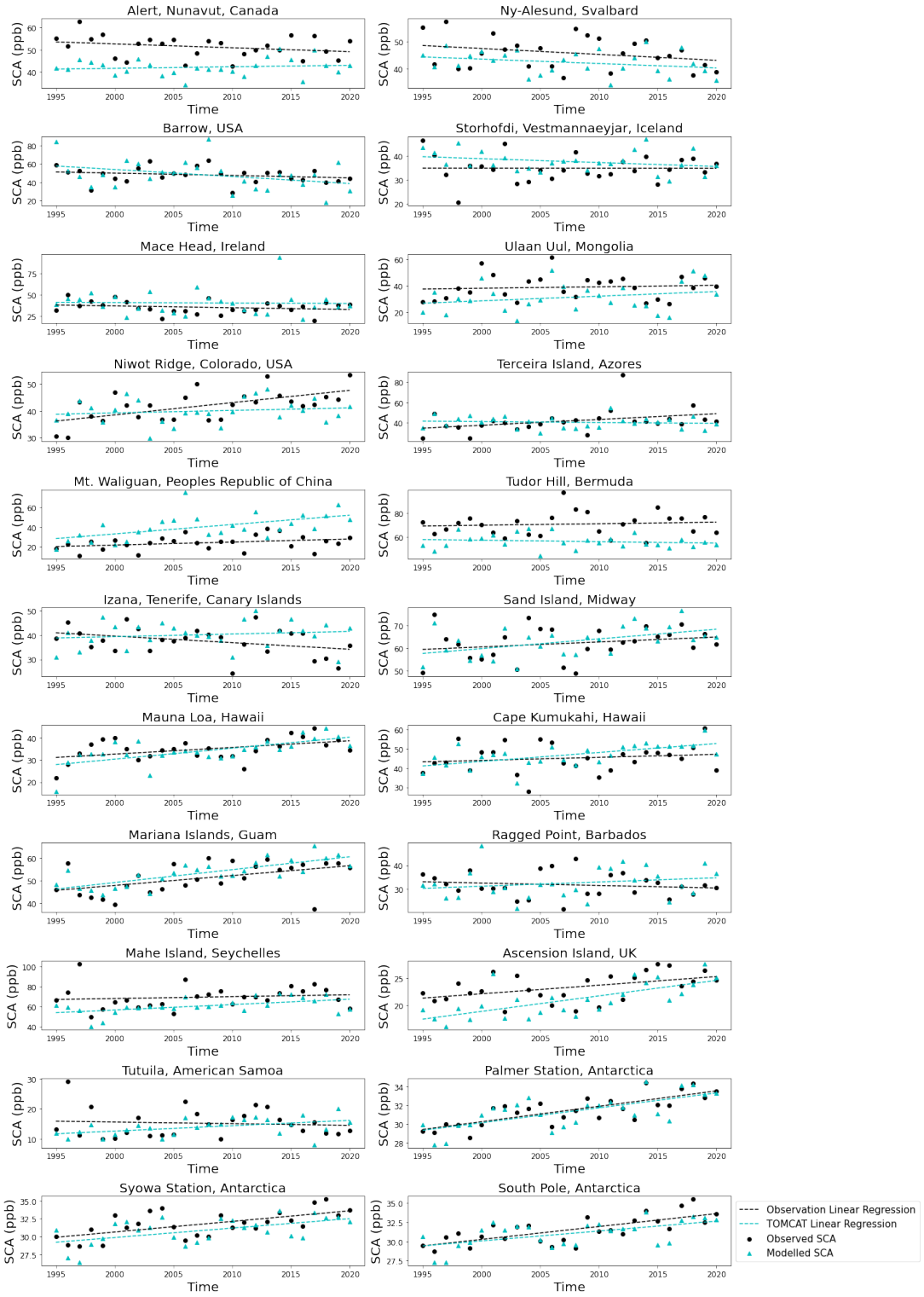

Figure A.3: The time series comparison of modelled and observed SCA and the trend at the NOAA observation sites. The sites are ordered north to south.

A.6 Regional Contribution to the NHL

This section contains the regional contributions under different scenarios. Figure A.4 shows the normalised contributions of the regional tagged tracers to show the impact of the region size

on the results. Figure A.5 shows the contributions of the tagged tracers without BRW in the NHL regions. Figure A.6 shows the contributions of the tagged tracers with MHD in the NHL which is classed as 52N-60N in this case.

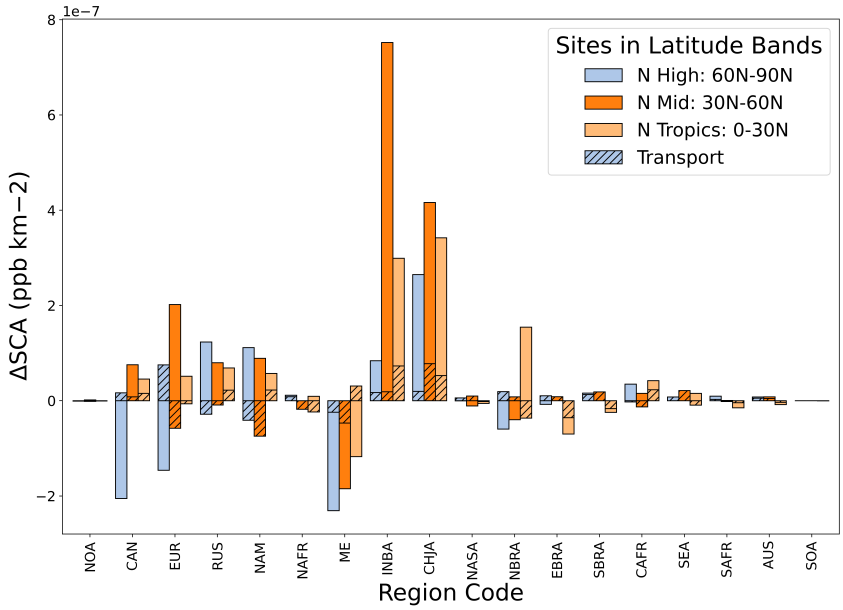

Figure A.4: The normalised contribution of the regional tagged tracers to CH4 ΔSCA (ppb km^{-2}) as a mean across all sites in the latitude band. The hatched bars show the contribution from transport (TOM_transport) and the solid colour represents the contribution from emissions (TOM_regional).

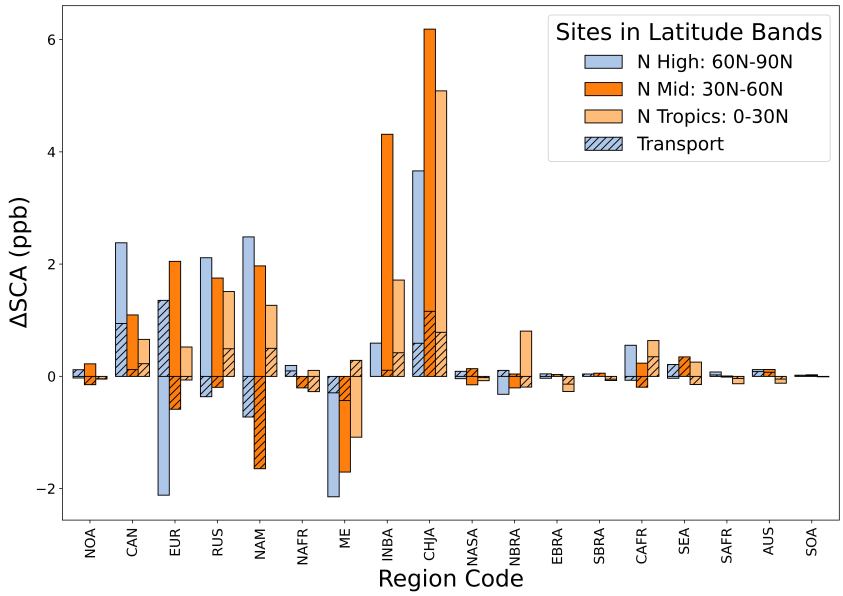

Figure A.5: The contribution of the regional tagged tracers to CH_4 ΔSCA (ppb) as a mean across all sites in the latitude band. The hatched bars show the contribution from transport (TOM_transport) and the solid colour represents the contribution from emissions (TOM_regional). The site at BRW has been removed in the NHL.

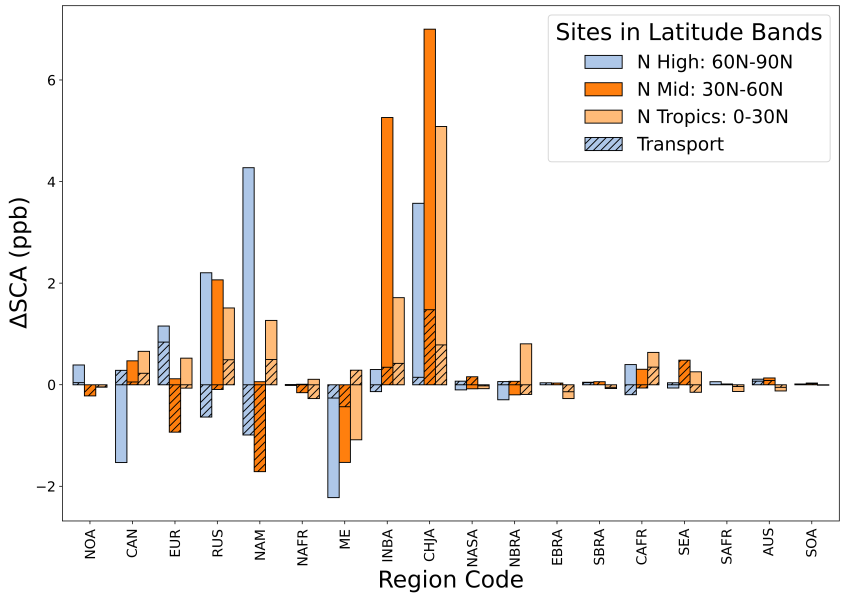

Figure A.6: The contribution of the regional tagged tracers to CH4 ΔSCA (ppb) as a mean across all sites in the latitude band. The hatched bars show the contribution from transport (TOM_transport) and the solid colour represents the contribution from emissions (TOM_regional). MHD has been added to the NHL region (52N-90N).

A.7 Mean Emission Maps and Trends

This section contains the seasonal mean emissions for the regions which contribute the most to the ΔSCA in the NHL. It also contains the seasonal trends of emissions in each of these regions.

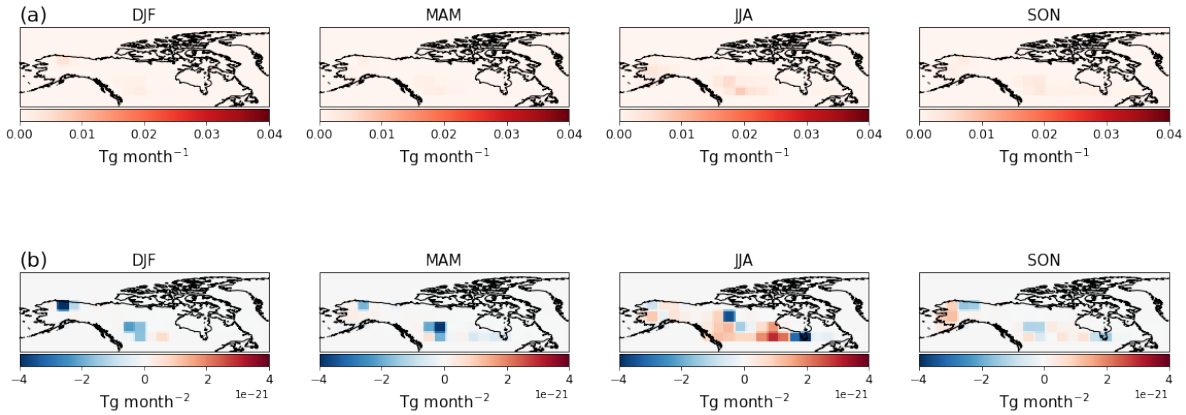

Figure A.7: (a) Seasonal mean emissions (Tg month^{-1}) and (b) seasonal trend in emissions (Tg month^{-2}) over Canada between 1995-2020.

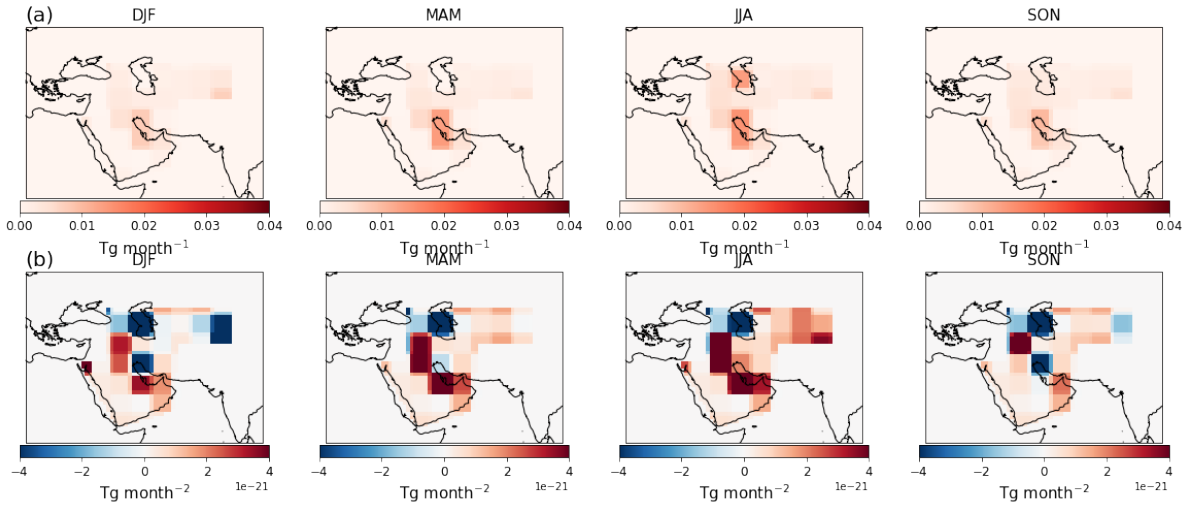

Figure A.8: (a) Seasonal mean emissions (Tg month^{-1}) and (b) seasonal trend in emissions (Tg month^{-2}) over the Middle East between 1995-2020.

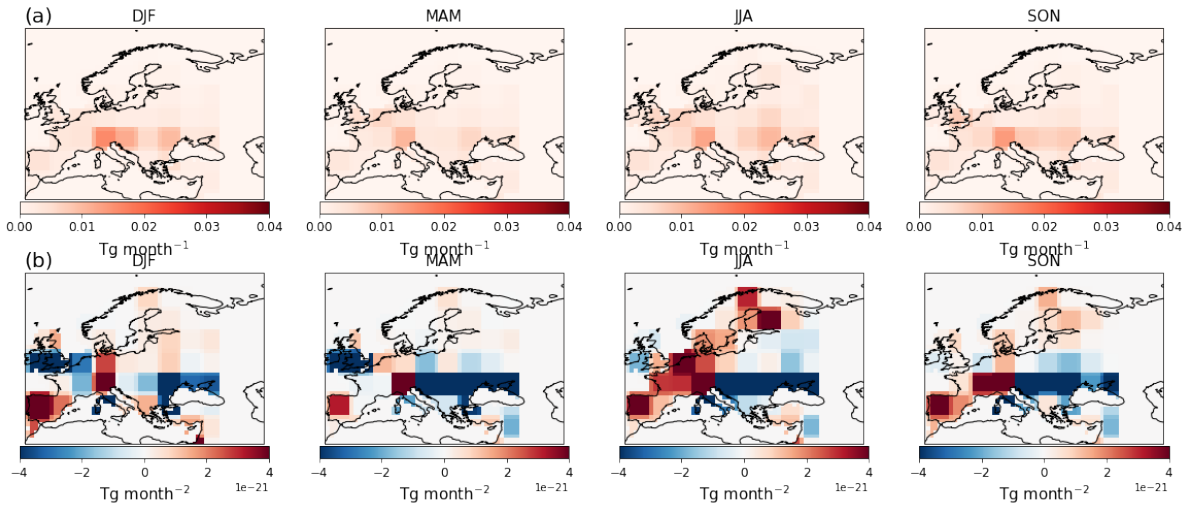

Figure A.9: (a) Seasonal mean emissions (Tg month^{-1}) and (b) seasonal trend in emissions (Tg month^{-2}) over Europe between 1995-2020.

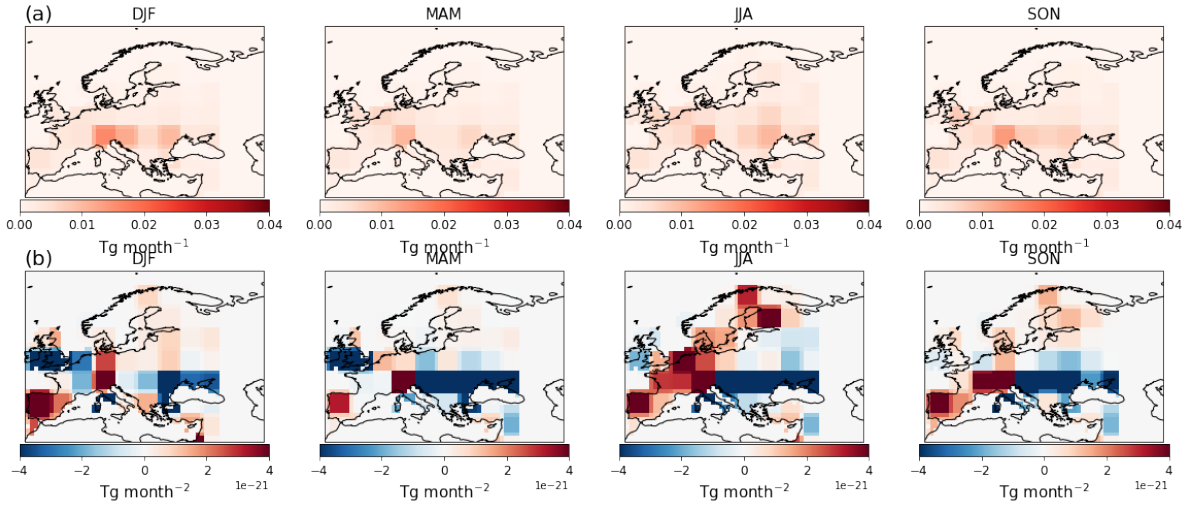

Figure A.10: (a) Seasonal mean emissions (Tg month^{-1}) and (b) seasonal trend in emissions (Tg month^{-2}) over China & Japan between 1995-2020.

A.8 GFED Fire Emissions

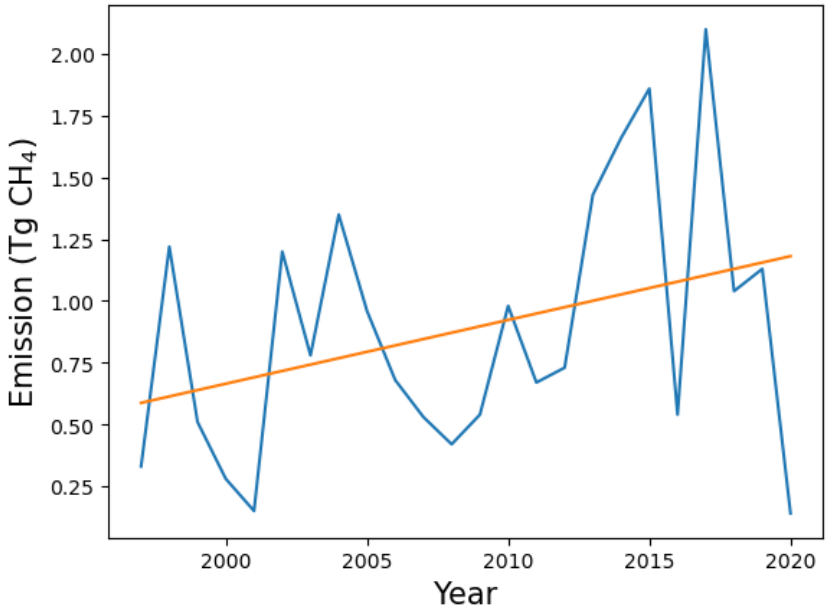

Figure A.11: Emission of CH_4 (Tg CH_4) from fires over Canada between 1997-2020 (blue) and its trend (orange).

A.9 Regional Concentration Contributions to NHL

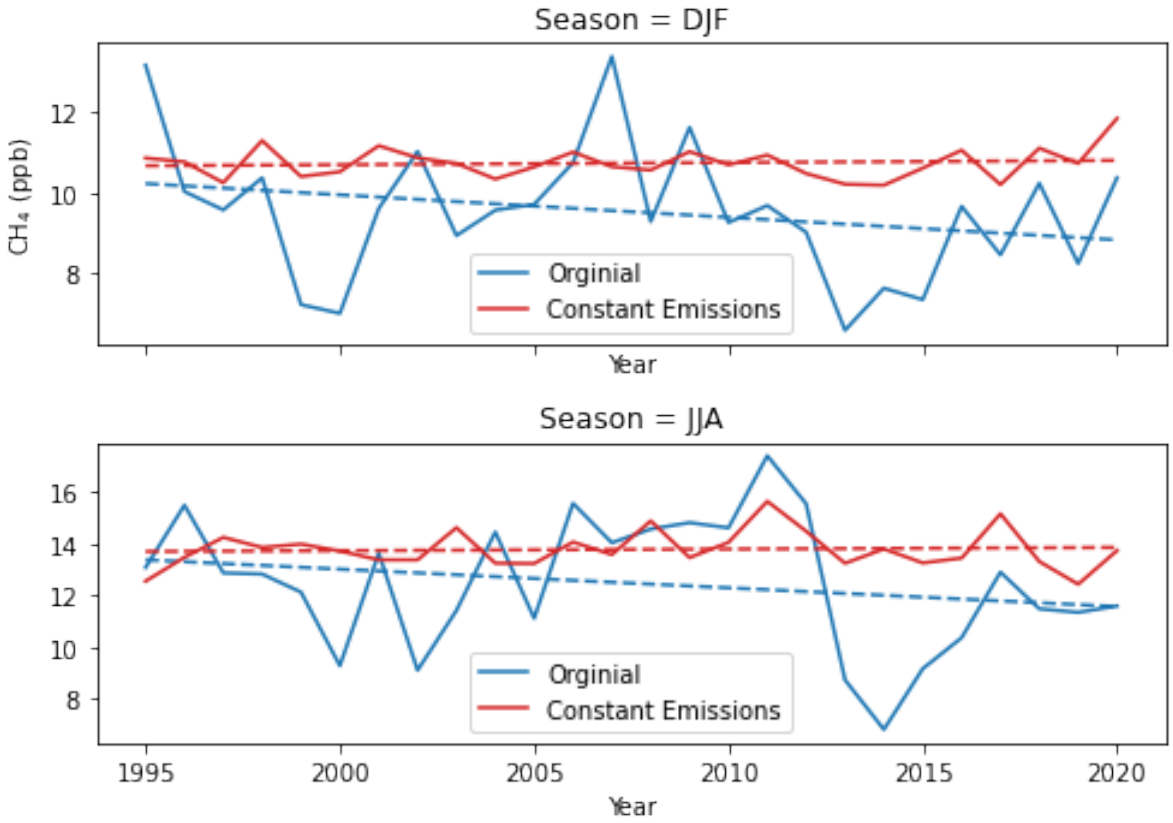

Figure A.12: Mean CH_4 (pbb) contribution across the NHL at the surface (60N-90N) for the TOM_regional simulation (blue) and the TOM_transport simulation (red) from Canada.

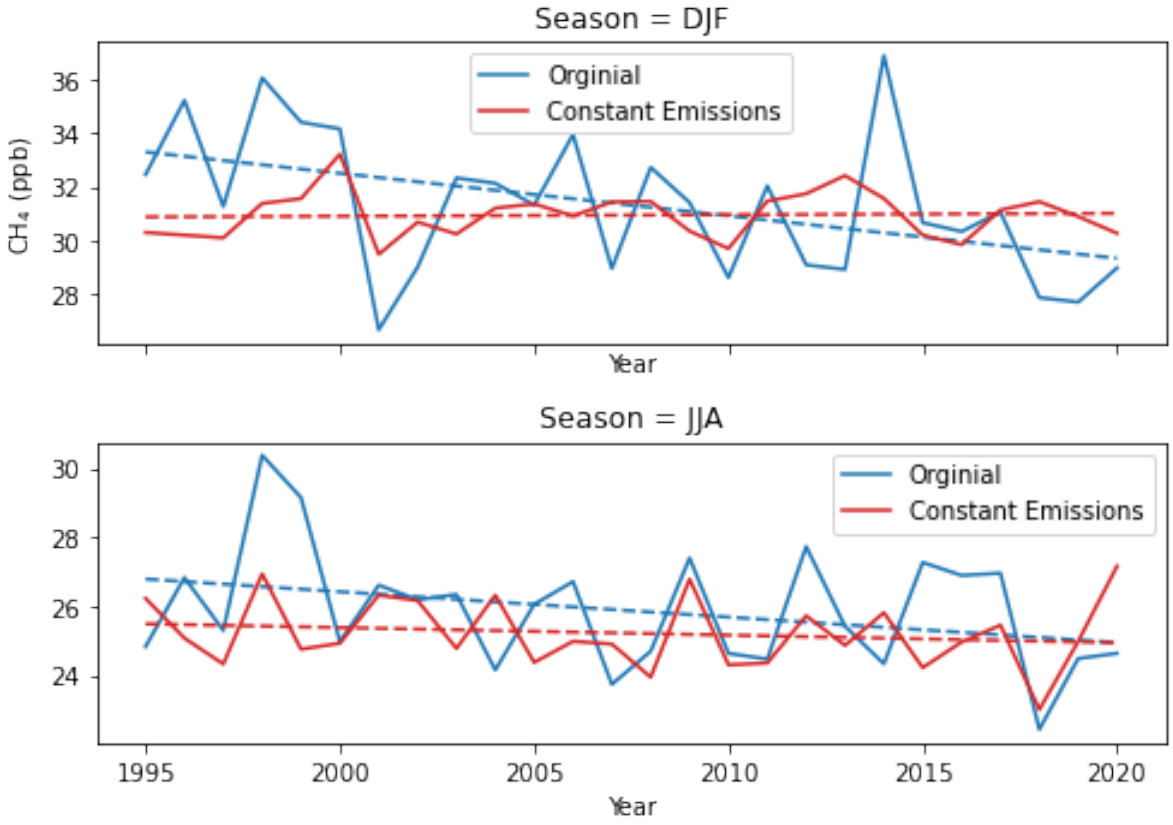

Figure A.13: Mean CH_4 (pbb) contribution across the NHL at the surface (60N-90N) for the TOM_regional simulation (blue) and the TOM_transport simulation (red) from Europe.

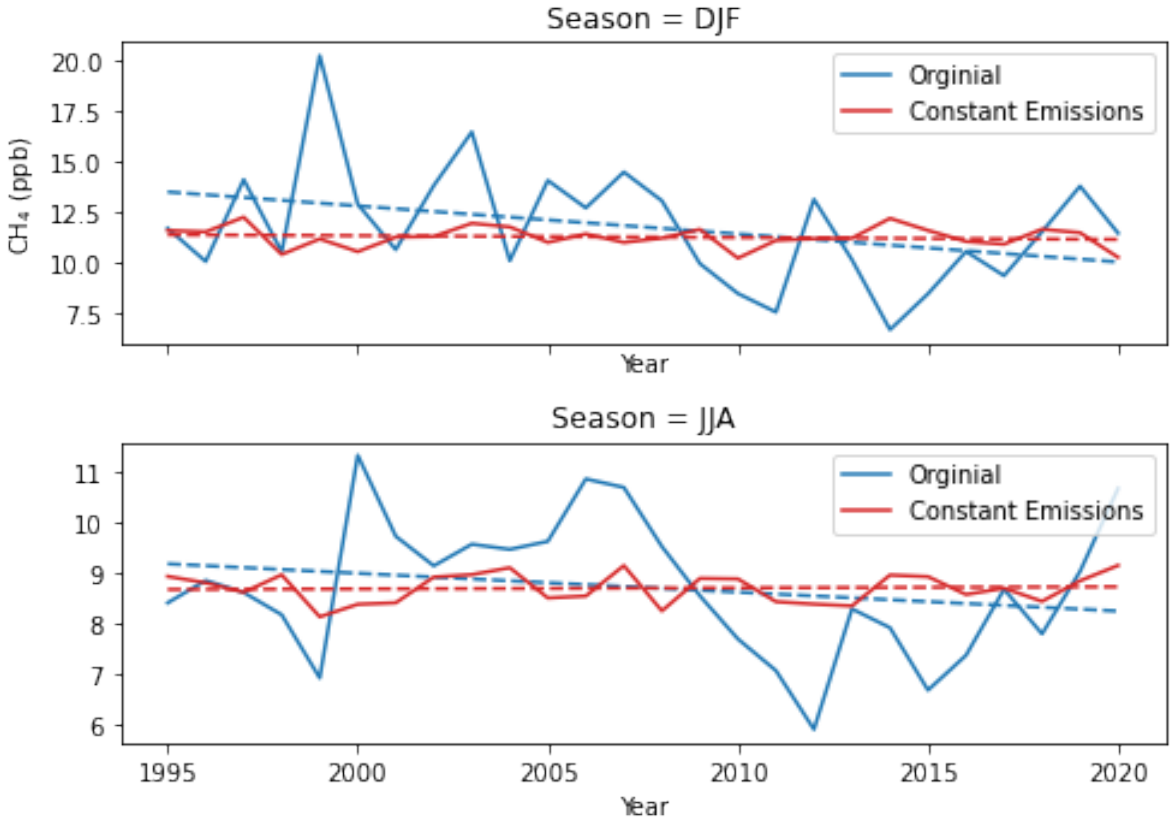

Figure A.14: Mean CH_4 (pbb) contribution across the NHL at the surface (60N-90N) for the TOM_regional simulation (blue) and the TOM_transport simulation (red) from the Middle East.

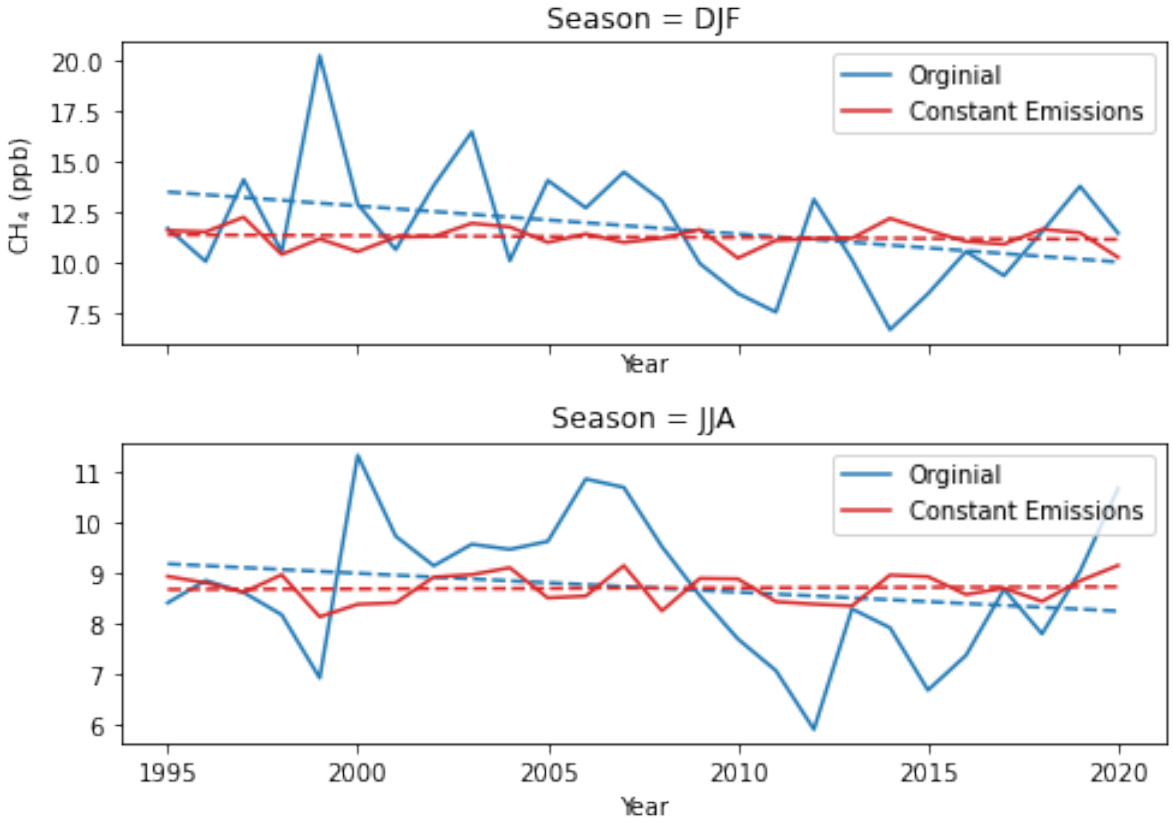

Figure A.15: Mean CH_4 (pbb) contribution across the NHL at the surface (60N-90N) for the TOM_regional simulation (blue) and the TOM_transport simulation (red) from the China & Japan.

Appendix B

Supplement: Paper 3

B.1 Gas Leak Site

Figure B.1: Image of gas leak site works taken on 12th June 2023.

Figure B.2: Image of dead vegetation (circled in red) at gas leak site taken on 12th June 2023.

Figure B.3: ©Google Earth 2023 image of the gas leak site taken in June 2023, showing works being done on the west site of the railway line.

B.2 Leak Location

Table B.1: Location of the gas leak estimated from the satellite observations

Date	Latitude (°N)	Longitude (°W)
27/03/2023	51.95097	2.09956
20/04/2023	51.95098	2.09956
20/05/2023	51.95086	2.09961
22/05/2023	51.95027	2.10012
26/05/2023	51.95079	2.09967

B.3 Flux Estimation Flow Charts

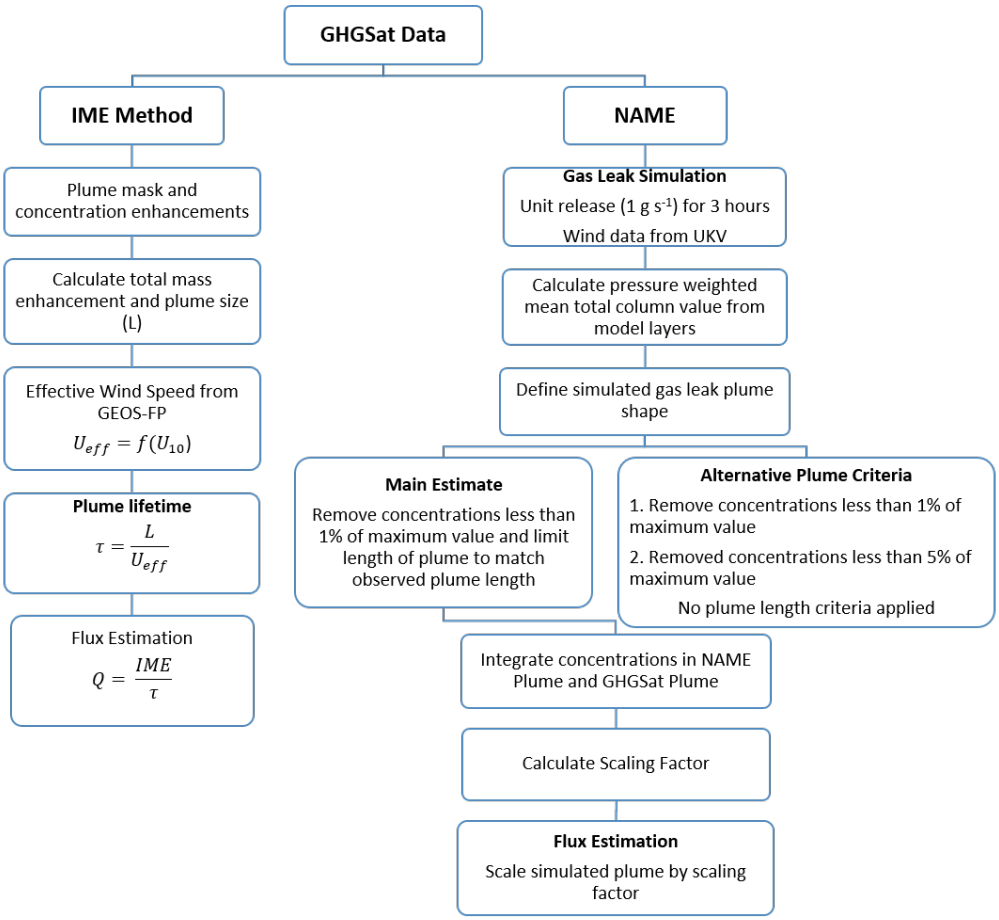

Figure B.4: Flow-chart showing flux estimation methods using GHGSat data. The IME Method flow-chart has been adapted from Varon et al. (2018).

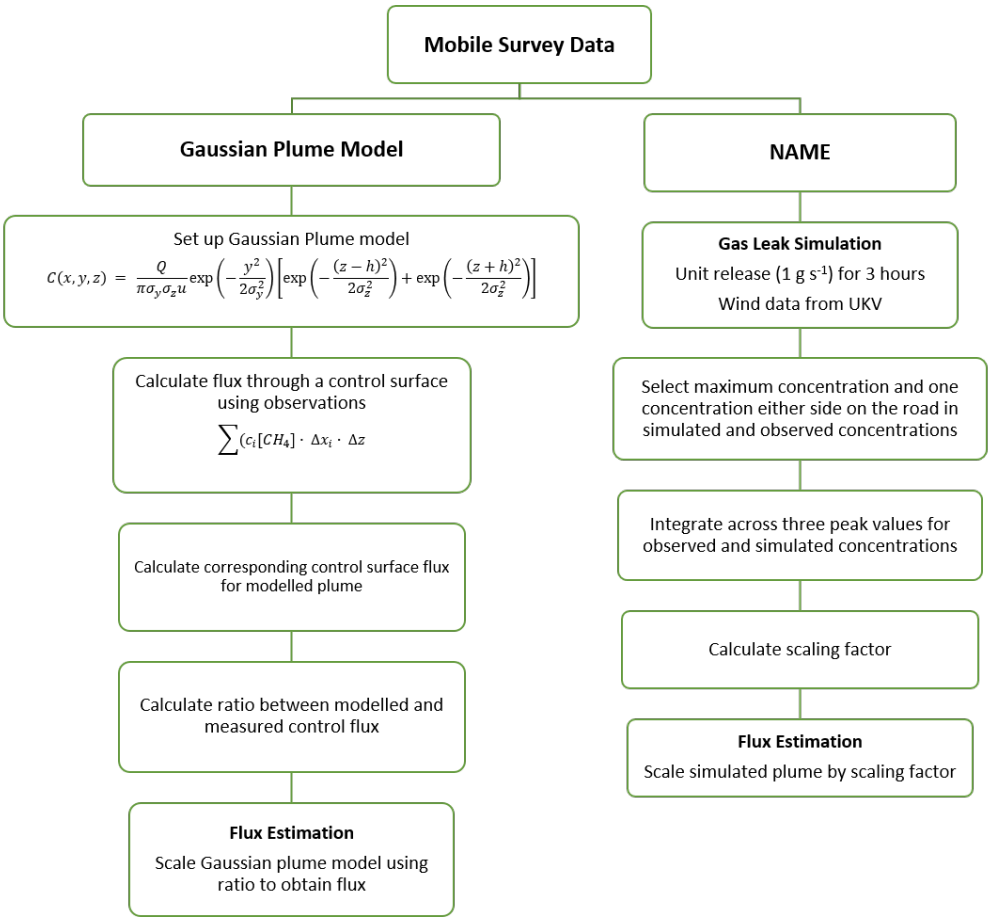

Figure B.5: Flow-chart showing flux estimation methods using mobile survey observations.

B.4 Mobile Survey

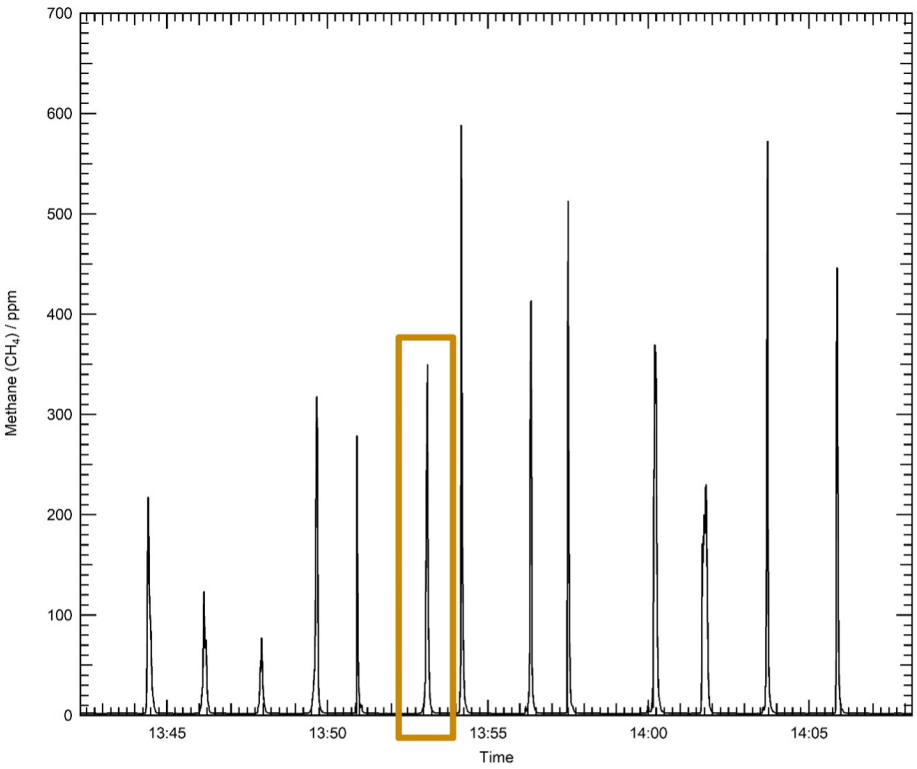

Figure B.6: CH_4 concentrations observed during the 26th May mobile survey transects. The median plume is highlighted by the orange box.

The time-series of CH4 mixing ratio data from the May mobile-survey can be found in the Figure B.6. It shows 13 transects, with the median plume displayed in Figure B.6 shown with the orange outline. The variability in the plume expected to be driven by a combination of meteorology and inconsistent flux rates. This inherent variability in measurements made during mobile transect measurements can be seen in other studies of this nature, such as Caulton et al. (2018). Averaging of the fluxes derived from each individual transect has been demonstrated to be an effective method to estimate a true flux under controlled release conditions to within approximately 40% (Kumar et al., 2021).

Table B.2: Atmospheric stability classification based on wind speed (m s^{-1}) and sky conditions.

	Daytime Insolation			Night-time conditions	
Surface Wind Speed (m s^{-1})	Strong	Moderate	Slight	Thin	cloudiness
< 2	A	A - B	B	E	F
2-3	A - B	B	C	E	F
3-5	B	B-C	C	D	E
5-6	C	C-D	D	D	D
> 6	C	D	D	D	D

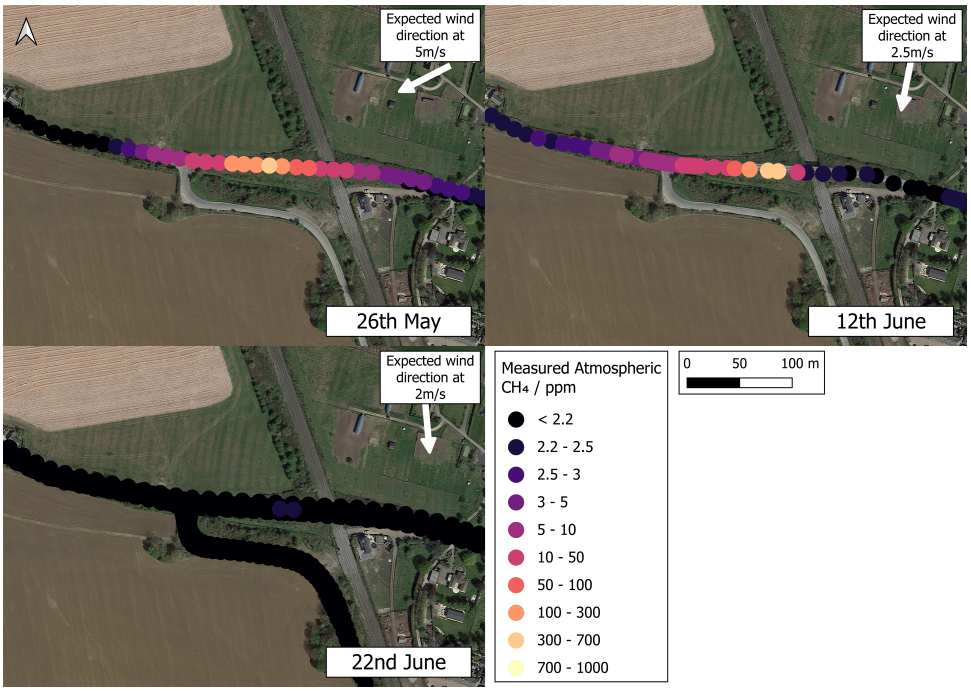

Figure B.7: Median observed concentrations (ppb) during the ground-based mobile surveys. ©Google Maps 2023

B.5 NAME Plume Modelling

We tested different plume criteria for scaling NAME to estimate the flux of the leak from the satellite. Here are the different flux estimates from the different plume criteria.

Table B.3: Comparison between the mobile survey- and GHGSat-derived fluxes (kg h^{-1}) against the equivalent fluxes derived in NAME (kg h^{-1}) with the release location moved by 10m in N/S/E/W directions. The NAME-derived fluxes are shown with the estimation bounds in brackets.

Date	GHGSat Flux (kg h^{-1})	Mobile Survey Flux (kg h^{-1})	NAME Derived Flux (kg h^{-1})	NAME Flux North (kg h^{-1})	NAME Flux South (kg h^{-1})	NAME Flux East (kg h^{-1})	NAME Flux West (kg h^{-1})
27/03/2023	236 ± 157	-	181[135, 329]	199[132,294]	206[132,296]	202[134,314]	208[132,290]
20/04/2023	1071 ± 310	-	745[539, 1376]	732 [560,1808]	769[559,1813]	724 [559,1782]	776 [560,1868]
20/05/2023	1375 ± 481	-	1243 [931, 2322]	1462 [977,3128]	1498[973,3128]	1455[971,3018]	1444[979,3123]
26/05/2023	-	846 ± 453	406 [366,680]	699[513,920]	565[505,860]	402[369,578]	574 [510,823]
22/05/2023	438 ± 215	-	408 [169, 286]	398 [177,395]	432[177, 397]	392[177,396]	432[177,403]
07/06/2023	290 ± 131	-	204 [77, 241]	212 [77,231]	210[76,226]	211 [75,208]	229[76,228]
12/06/2023	-	634 ± 299	512 [498,681]	812 [785,1147]	729 [701,990]	511[502,671]	794[750,1130]

Table B.4: Wind speeds (ms-1) used in flux estimations

Date	GEOS FP Wind Speed (ms^{-1})	GEOS-FP Wind Direction (°)	UKV Wind Speed (ms^{-1})	UKV Wind Direction
27/03/2023	0.8	119 (ESE)	3.8	163 (SSE)
20/04/2023	7.3	45 (NE)	12.0	46 (NE)
20/05/2023	4.9	40 (NE)	7.3	44 (NE)
22/05/2023	5.3	6 (N)	8.6	13 (N)
26/05/2023	-	-	4.4	79 (ENE)
07/06/2023	3.7	66 (ENE)	5.8	76 (ENE)
12/06/2023	-	-	3.1	46 (NE)

B.6 Modelled Concentrations at Ridge Hill

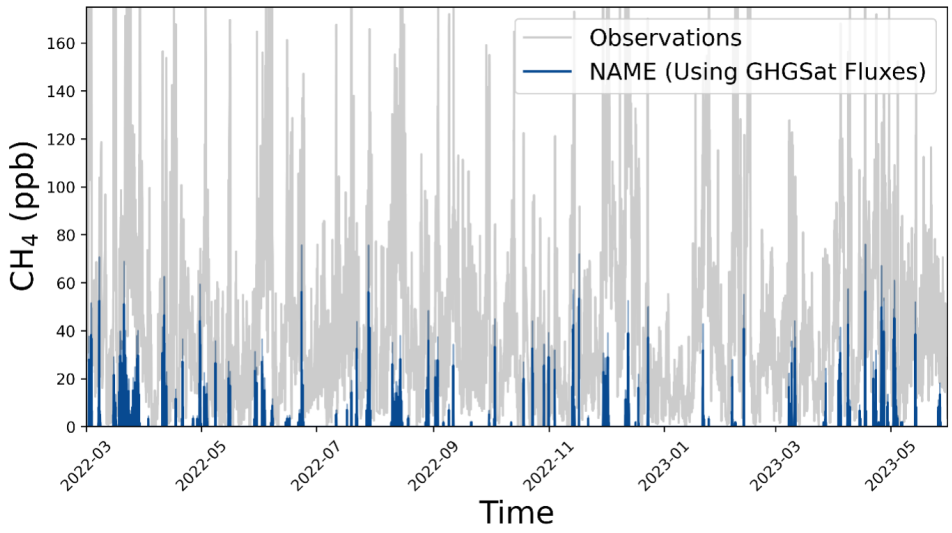

Figure B.8: The NAME_long modelled concentrations at Ridge Hill from GHGSat derived flux rates (ppb, blue) and above-background concentrations at RGL (ppb, grey).

B.7 NAEI

This section includes the most recent National Atmospheric Emissions Inventory (NAEI) emissions maps of the UK. Figure B.9 shows the gridded inventory and Figure B.10 shows the largest 100 point source emitters in the NAEI for 2022. The largest point source is Shearwater in the oil and gas sector and it is estimated to emit 3651 tonnes of CH_4 per year (NAEI, 2024). The second largest point source is Drax power station which is estimated to emit 3434 tonnes of CH_4 per year (NAEI, 2024). If the Cheltenham gas leak emitted CH_4 for one year with a mean emission rate of 754 kg h^{-1}, it would leak a total of 6605 tonnes of CH_4. This is 80% more CH_4 than the UK's largest point source, Shearwater.

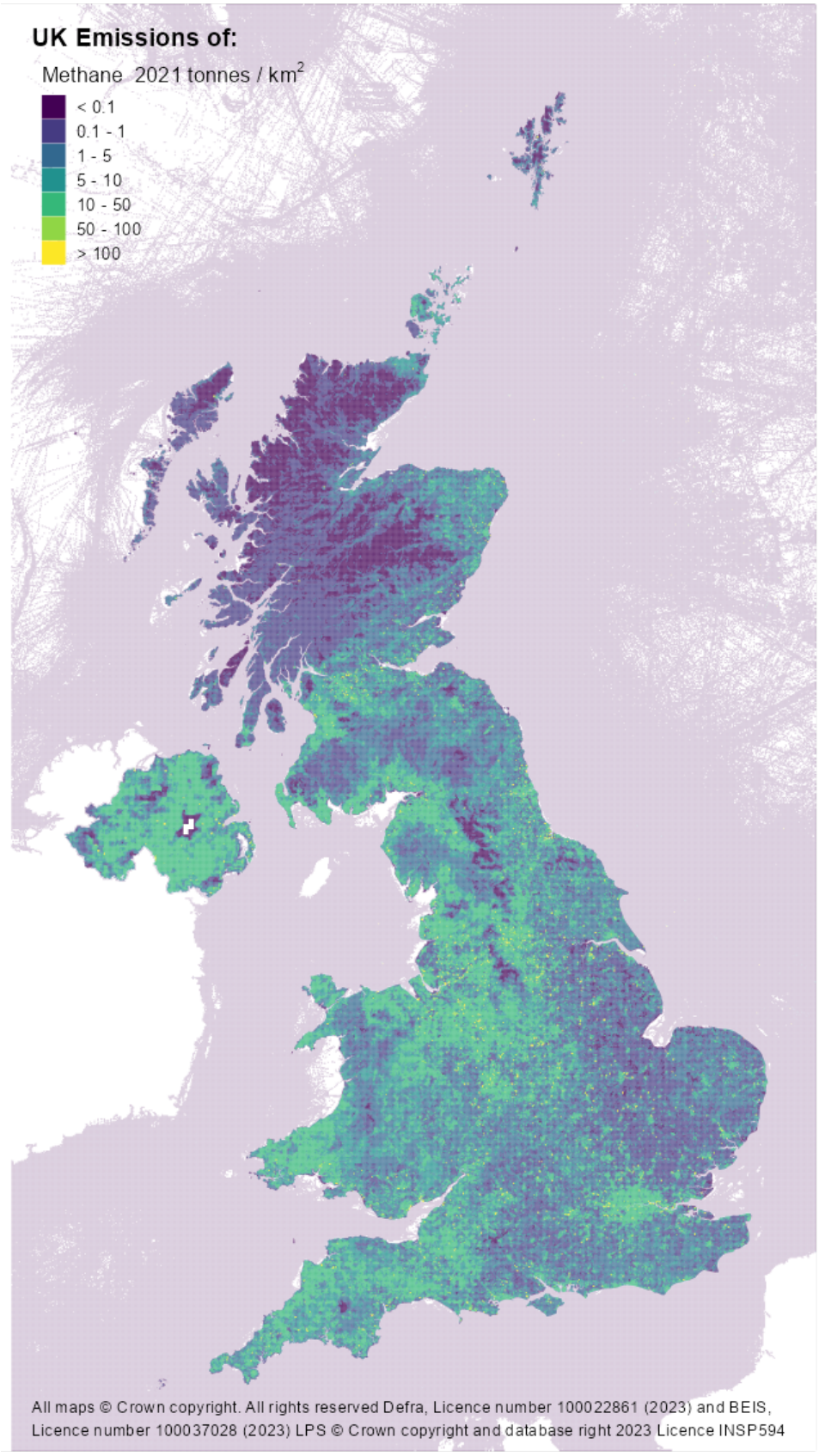

Figure B.9: The NAEI 2021 UK CH_4 gridded emissions inventory (tonnes/ km^2, NAEI (2024)).

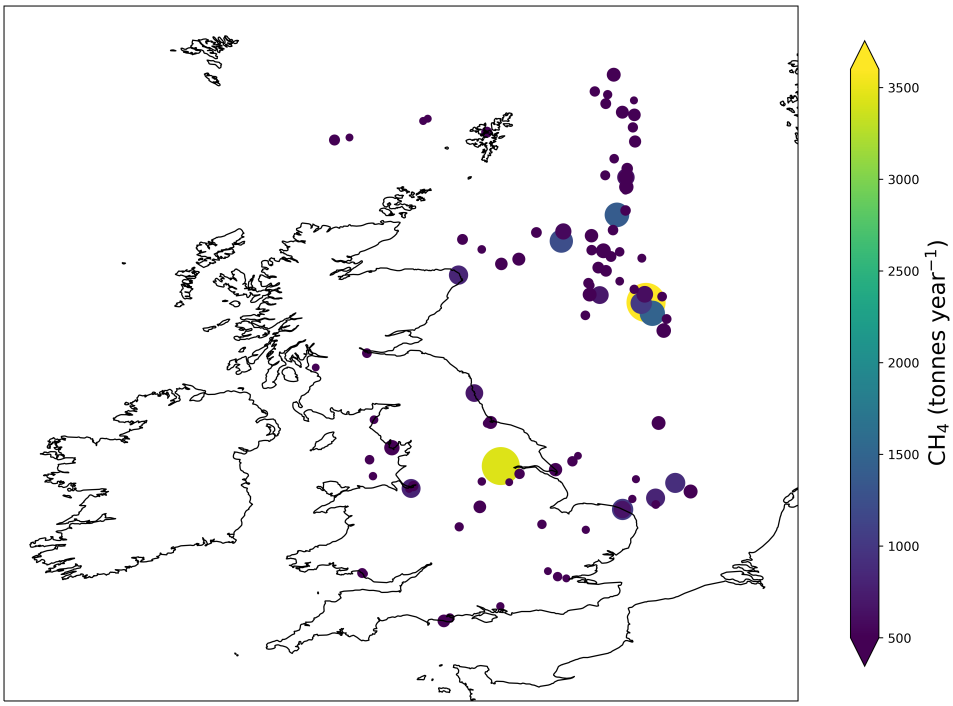

Figure B.10: The NAEI 2021 CH_4 point source emissions (tonnes year $^{-1}$), NAEI (2024)).